UNIVERSITAT DE
BARCELONA

Mechanical and functional properties in magnetic materials

Jaume Calvo de la Rosa

ADVERTIMENT. La consulta d'aquesta tesi queda condicionada a l'acceptació de les següents condicions d'ús: La difusió d'aquesta tesi per mitjà del servei TDX (**www.tdx.cat**) i a través del Dipòsit Digital de la UB (**diposit.ub.edu**) ha estat autoritzada pels titulars dels drets de propietat intel·lectual únicament per a usos privats emmarcats en activitats d'investigació i docència. No s'autoritza la seva reproducció amb finalitats de lucre ni la seva difusió i posada a disposició des d'un lloc aliè al servei TDX ni al Dipòsit Digital de la UB. No s'autoritza la presentació del seu contingut en una finestra o marc aliè a TDX o al Dipòsit Digital de la UB (framing). Aquesta reserva de drets afecta tant al resum de presentació de la tesi com als seus continguts. En la utilització o cita de parts de la tesi és obligat indicar el nom de la persona autora.

ADVERTENCIA. La consulta de esta tesis queda condicionada a la aceptación de las siguientes condiciones de uso: La difusión de esta tesis por medio del servicio TDR (**www.tdx.cat**) y a través del Repositorio Digital de la UB (**diposit.ub.edu**) ha sido autorizada por los titulares de los derechos de propiedad intelectual únicamente para usos privados enmarcados en actividades de investigación y docencia. No se autoriza su reproducción con finalidades de lucro ni su difusión y puesta a disposición desde un sitio ajeno al servicio TDR o al Repositorio Digital de la UB. No se autoriza la presentación de su contenido en una ventana o marco ajeno a TDR o al Repositorio Digital de la UB (framing). Esta reserva de derechos afecta tanto al resumen de presentación de la tesis como a sus contenidos. En la utilización o cita de partes de la tesis es obligado indicar el nombre de la persona autora.

WARNING. On having consulted this thesis you're accepting the following use conditions: Spreading this thesis by the TDX (**www.tdx.cat**) service and by the UB Digital Repository (**diposit.ub.edu**) has been authorized by the titular of the intellectual property rights only for private uses placed in investigation and teaching activities. Reproduction with lucrative aims is not authorized nor its spreading and availability from a site foreign to the TDX service or to the UB Digital Repository. Introducing its content in a window or frame foreign to the TDX service or to the UB Digital Repository is not authorized (framing). Those rights affect to the presentation summary of the thesis as well as to its contents. In the using or citation of parts of the thesis it's obliged to indicate the name of the author.

Program in Engineering and Applied Sciences.
Faculty of Chemistry.
Department of Materials Science and Physical Chemistry.
Materials Science and Engineering Section.

Mechanical and functional properties in magnetic materials

Jaume Calvo de la Rosa

A Dissertation submitted in partial fulfilment of the requirements for the degree of Doctor of Philosophy in the University of Barcelona.

Supervisors:

Dr. Mercè Segarra Rubí.
Department of Materials Science and Physical Chemistry, Faculty of Chemistry.

Dr. Javier Tejada Palacios.
Department of Condensed Matter Physics, Faculty of Physics.

Tutor: Dr. Mercè Segarra Rubí

Publication: September 2019, Barcelona

ACKNOWLEDGEMENTS

This Thesis is, undoubtedly, the result of a teamwork. Many, many people have provided at a certain moment a suggestion, experimental help, an idea, or simply a vital support that has made this work to keep going forward. I would like to devote some lines to thank them, despite it will be shorter than it should be.

Sento que el primer agraïment ha d'anar als meus directors, la Dra. Mercè Segarra i el Dr. Javier Tejada, per ser les dues persones que han fet possible aquesta Tesi.

Javier, no tengo palabras para agradecerte lo que has confiado en mí y todas las oportunidades que me has dado. No solo hablo de esta Tesis, sino de todos los años que he podido trabajar contigo. Todavía recuerdo ir a tu despacho para pedirte hacer el trabajo de final de grado, e irme sorprendido de tu entusiasmo e ilusión por ayudar a la gente joven. Pues de grado a máster, y al final también el doctorado. Estoy muy orgulloso de haber colaborado todos estos años contigo, en los que he aprendido, no solo ciencia, sino también una forma de hacer las cosas. Eres todo un referente para mí. Espero que podamos seguir alargándolo mucho tiempo.

Mercè, també tinc un profund sentiment d'agraïment cap a tu per la teva predisposició i entusiasme cap a aquesta Tesi, des de què ara fa quatre anys vaig entrar al teu despatx (després d'haver parlat amb en Josep Mª Chimenos) buscant fer el doctorat. Malgrat encara pràcticament no havíem tingut relació, em vaig trobar amb una persona entusiasta i convençuda del que anàvem a fer. T'agraeixo totes les reunions *express* (encabides improvisadament a la teva agenda) al teu despatx o a la terrassa, i per ensenyar-me que en molts moments s'ha de ser directe i pragmàtic. Moltes gràcies també per tots aquests últims mails amb correccions a hores intempestives, quan estaves amb cinquanta coses més, que ha "lead TO" la finalització de la memòria. Gràcies de tot cor.

També vull expressar els meus agraïments a la Universitat de Barcelona, tant per haver-me permès realitzar el doctorat, com també per l'assignació de la beca *Ajuts a la Docència i a la Recerca* (*ADR*) que he pogut gaudir durant tres anys i m'ha permès iniciar-me en les tasques docents a la Universitat. En aquest sentit, vull agrair als dos grups de recerca, DIOPMA i Grup de Magnetisme, haver pogut formar part del seu equip i haver-me aportat tots els recursos necessaris per a realitzar aquesta Tesi.

Una de les grans avantatges d'haver format part de dos grups de recerca és que he pogut conèixer el doble de gent única. Haver conegut tota aquesta gent és del més gran que m'enduc d'aquesta etapa.

Pel que fa a la gent de DIOPMA, hi ha un grup de persones a qui he tingut la sort de tenir primer com a professors, i ara com a companys. Chema, Inés, Mònica, Elena i Camila, gràcies perquè sempre que m'ha fet falta he pogut picar la vostra porta sabent que hi trobaria ajuda i orientació en moments en els que he anat perdut. Padi, sens dubte la persona més vital, amb més energia i més *chorreosa* del grup: malgrat perdre'm la bata, gràcies per ensenyar-me a fabricar mufles! Després, aquells amb qui he compartit més *tuppers* i anècdotes: Esther, la persona que tot ho sap i que en incomptables ocasions m'ha ajudat i solucionat problemes, gràcies; Joan & Jessica, gràcies per haver-me tractat tant bé des del primer dia i haver-vos preocupat per mi, gairebé com a "germans grans". Per cert Joan, compra't ja la Play i canvia d'ocellet, que en Neymar no ha arribat; Alex, m'alegro molt de què haguem compartit pràcticament tot aquest camí. Et desitjo molta sort i ànims, que ara t'arriba a tu la part divertida! Un altre grup a qui em vull dirigir són els que es van incorporar ara farà un parell d'anys: Sergio, Adela i Pol. Si això ho està llegint algú acabat d'arribar al grup... vigila, són perillosos! Tot i que també són molt bona gent per compartir un Dunkin. Als nous fixatges i incondicionals dels caps de setmana, Rebeca i Jofre: tota la sort del món i força amb el vostre doctorat! Ja es creuran que no surten, però els he deixat pel final: els meus companys de zulín. Dra. Gonçalves, muito obrigado por las agradables conversaciones que hemos tenido sobre el futuro y tu siempre optimista punto de vista. Alejandro, mi compañero de escritura, sufrimiento, y reciente papeleo: gracias por presentarme a Panic Monster, me ha hecho mucha compañía todo este verano. Jose, ànims que ja ho tens!! I perquè no a en Ricardo, la Judit i en Miki que, malgrat només haver coincidit durant l'inici de la Tesi, m'alegro d'haver-los conegut.

D'altra banda, tots els companys del Grup de Magnetisme. Potser no hem compartit tantes hores de despatx o dinars, però sempre m'heu acollit i tractat sensacionalment. Joan Manel, Toni i Ferran, sou gent genial i us agraeixo que sempre que m'ha calgut he trobat la vostra ajuda o consell. Amb qui més hores de laboratori he compartit ha estat amb en Joan Manel; gràcies per les innumerables vegades que m'has solucionat problemes experimentals, segurament aquesta Tesi no tindria la meitat dels resultats sense la seva ajuda. También, al ya Dr. Nahuel Statuto, ha sido fantástico compartir esta etapa contigo, de inicio a fin. Te deseo mucha suerte para tu postdoc y espero que nos volvamos a ver en un futuro. Al *manager* Sergi, la persona amb més capacitat per memoritzar noms russos del món, és impressionant. Gràcies per la teva vitalitat, optimisme i energia. També vull fer una referència molt especial a en Chen Chao, amb qui durant els últims anys he treballat colze a colze. Et desitjo la millor de les sorts en aquesta nova aventura que estàs començant, vals molt!! També vull recordar-me'n d'aquells que em vau acollir quan tot just arribava al grup: Ricardo, Sergi, Diego i Gianluca. Gràcies perquè al grup vaig trobar un grup humà excel·lent.

Voldria afegir un agraïment a diferents persones del Departament. Primer al PAS, sobretot a l'Esther Vilalta i Silvia Mestre, per la quantitat de vegades que he hagut de recórrer a la vostra ajuda i sempre m'he trobat amb la vostra millor predisposició. També a d'altres professors com la Núria Llorca, Antoni Roca, Montserrat Cruells, Irene García o Sergi Dosta. No hem compartit recerca, però sí bastantes hores de classes, controls d'exàmens i reunions de docència. De tots n'he après.

També al personal dels CCiT-UB què més m'han hagut d'aguantar a mi i a les meves mostres durant aquests anys, com el Ricard Álvarez o la Maria Barba. A qui voldria fer una menció molt especial és a en Xavier Alcobé. Infinites gràcies per tota la teva ajuda, quan no hi tenies cap mena d'obligació. De les hores amb tu davant de l'ordinador fent ajustos de perfil no només m'enduc el coneixement tècnic, sinó tota la passió amb la que ho fas. Sens dubte, sumo a la meva motxilla una eina per a seguir treballant, quan d'inici no m'ho hagués imaginat mai.

Also, I would like to thank David S. Citrin and Alexandre Locquet for opening me the doors of their research group and GTL. There, I could live a unique professional and personal experience, and I am looking forward to keep working together! Moreover, I would like to thank a group of awesome people that I had the opportunity to meet there: Joe, Georges, Min, Shariful, and Charbel. Thank you because you received me as one more in the group and you made me feel at home during the five months I spent in Metz. Oh, Metz… what a beautiful city, and exceptional *croissants au chocolat*!

Furthermore, during these years I have also had the opportunity to collaborate with brilliant people, such as Eugene Chudnovsky, Serghej Prischepa, Arturo Lousa, Joan O'Callaghan, Mark Dougan, "nano" JJ, Pilar and Jesús. Thanks for all the interesting conversations we have had discussing experiments and results. Also, I am grateful because working with you have opened me new opportunities to work in fields that before were completely unknown for me.

A molt bons amics, com el Carlos, l'Hector i l'Albert. El sacrifici que aquesta Tesi comporta molts cops ens ha dificultat veure'ns tot el que m'hagués agradat, però sempre heu estat allà. Gràcies.

Per acabar, aquells més importants, a qui encara que els "parlés en xinès" m'han escoltat, m'han recolzat i s'han preocupat pel que feia. A tota la meva família, des de sogres, cunyada i l'àvia, fins a cosins, tiets, i indubtablement avis, Ana i Pablo. Sou el millor entorn que un podria tenir. També, escrivint aquestes línies no puc evitar recordar-me'n de tu, iaia Carmen. Sé que ho estaràs veient i que estaràs molt orgullosa. Va per tu.

Als meus pares, Ricardo i Mercè, que m'heu inculcat els valors del treball, l'esforç i la perseverança, i m'ho heu donat tot per a què pugui fer tot el que em proposi. He arribat a complir aquesta fita gràcies a vosaltres. A la meva germana, única i especial, Neus. Gràcies per tot el que hem compartit junts, i tot el que t'he pogut "xintxar". Ho seguiré fent. Ara para, pensa bé i lluita per complir els teus somnis, que en tens molts i estic convençut de què els compliràs si t'ho proposes.

Tot el que aquí pugui escriure no tindria cap significat sense un nom: Judith. La meva parella, companya de viatge, d'alegries, de bons i mals moments, però sobretot de projectes i d'il·lusió comú. Ets la primera persona que ha pagat el preu i sacrifici de fer aquesta Tesi i sempre m'has recolzat. Fins i tot en decisions difícils per als dos. T'ho agraeixo tot, no puc especificar res. Aquesta Tesi no pot portar el teu nom a la portada, però també és teva. T'estimo.

ABSTRACT

This doctoral Thesis contains the main obtained results during the four doctoral years in which I have conducted research at Universitat de Barcelona. This work has been done in a collaboration between the research groups DIOPMA from the Materials Science and Physical Chemistry Department, and Grup de Magnetisme from the Condensed Matter Physics Department, under the supervision of Dr. Mercè Segarra and Dr. Javier Tejada, respectively. Moreover, this is also the results of many national and international collaborations.

My research has been focused on the preparation of magnetic materials by different methods, the characterization of their structural characteristics, and the understanding of their mechanical and magnetic properties. Furthermore, a big effort has been paid to investigate the frequency-dependent functional properties of different materials, which are increasingly demanded in novel technological applications. Moreover, this work presents this characterization in a wide range of frequencies, from the kHz to the THz.

In the first chapter, the reader will find an introduction to the topic and the state of the art of those materials that have been synthesized and developed in this Thesis. Then, the general goals of our research are described. However, a more detailed description of the objectives will be found at the beginning of each chapter in order to deepen in the targets before discussing the results.

Chapter II provides all the needed fundamental theory to accomplish with the previously stated goals. The concepts exposed here will be used later in the following chapters where the results will be shown and discussed. Moreover, this chapter does not only pretend to give the essential notions used in the following chapter, but we also aim to provide a useful guide to anyone who starts working on this field.

All the materials, devices, software, and experimental conditions used in this Thesis are described in Chapter III. Here, we describe these aspects in detail in order to allow an agile discussion in the following chapters. Only the relevant and personally done works are here described; the others are specified in each experimental section.

The first experimental chapter is Chapter IV, where the synthesis of copper ferrite nanoparticles by mean of sol-gel and co-precipitation is described. The sol-gel process is optimized through of design of experiments (DoE) approach. Also, the differences between each approach and their repercussion on the prepared material are discussed. The results of the mechanical and magnetic characterization of solid pellets fabricated with the previously synthesized nanoparticles are also shown in this chapter. Finally, by using statistical methods a direct experimental correlation between the mechanical and magnetic properties is found in this material.

Another material, a carbon nanotube–based nanocomposite, is studied in Chapter V. This novel material is first structurally characterized in order to understand its magnetic properties. A big effort is paid on the study of the magnetic relaxation of this material, which has not been previously reported as far as we know.

The investigation of soft magnetic materials (SMM) and composites (SMC) can be found in Chapter VI. The actual SMCs are first structurally and magnetically characterized. Their magnetic properties in the kHz

and MHz frequency range are also investigated, showing the better performance of the SMC at high frequencies. In the second part of the chapter, the development on new SMC's formulations is described. The developed materials are potentially useful for applications in the kHz and MHz frequency range.

The frequency is raised in Chapter VII. Terahertz time-domain spectroscopy (THz-TDS) is used to investigate the optical and dielectric properties of two different semiconductor oxides from 180 GHz to 3 THz. The signal processing and the interpretation of the effect that different characteristics of the sample may have on the observed properties are discussed. In this chapter, magnetic materials are not investigated because the Fresnel model – which is the base of this technique - assumes a non-magnetic response of the material.

The work described in Chapter VIII is completely different from the previous ones. In this case, we investigate the manipulation of the magnetic moments by using surface acoustic waves (SAWs). The experiments done in this chapter lead to interesting observation about the potentiality of the use of SAWs to accelerate the magnetic moment reversal in magnetic nanoparticles.

Finally, Chapter IX contains a brief summary of the main conclusions obtained from this Thesis. Although the conclusions are commented in detail in each chapter, here I wanted to make a more general consideration to not only have an overview of the obtained results in this Thesis, but also a clear statement: the relationship between the composition, the physical characteristics and the final properties of materials allows us to understand and design materials with novel or improved properties.

RESUMEN

Esta Tesis Doctoral contiene los principales resultados que he obtenido durante los cuatro años de doctorado en los que he realizado investigación en la Universitat de Barcelona. Este trabajo se ha realizado en colaboración con los grupos de investigación DIOPMA del Departamento de Ciencia de los Materiales y Química Física, y el Grupo de Magnetismo del Departamento de Física de la Materia Condensada, bajo la supervisión de la Dra. Mercè Segarra y el Dr. Javier Tejada, respectivamente. Además, este es también el resultado de numerosas colaboraciones, tanto nacionales como internacionales.

Mi investigación se ha centrado en la preparación de materiales magnéticos a través de diferentes métodos, la caracterización de sus propiedades estructurales, y la comprensión de sus propiedades mecánicas y magnéticas. Además, se ha hecho especial énfasis en la investigación de las propiedades funcionales dependientes de la frecuencia para distintos materiales, los cuales son cada vez más demandados en aplicaciones tecnológicas punteras y novedosas.

Además, esta caracterización se presenta en un amplio rango de frecuencias, desde el kHz hasta el THz.

De este modo, en el primer capítulo, el lector puede encontrar una introducción al campo de investigación, así como también el estado del arte de aquellos materiales que se han sintetizado y desarrollado en esta Tesis. Posteriormente, y a pesar de que cada capítulo contiene sus objetivos particulares, se describen los objetivos generales que han marcado la dirección de la investigación realizada.

En el Capítulo II se aportan todos los conceptos teóricos necesarios para lograr los objetivos definidos en cada uno de los capítulos. Estos conceptos serán posteriormente necesarios cuando se muestren y discutan los resultados. Asimismo, este capítulo no solo pretende dar las nociones indispensables para poder seguir fácilmente los siguientes capítulos, sino que también busca ser una guía útil para cualquier persona que empiece a formarse o a trabajar en este campo de investigación.

Por otro lado, todos los materiales, dispositivos, software y condiciones experimentales utilizados durante el desarrollo de esta investigación están descritos en el Capítulo III. En este capítulo pretendemos hacer una descripción detallada de todos los procesos que permita, después, desarrollar de forma ágil la discusión de resultados. Por último, en este capítulo solo se encuentran aquellas tereas relevantes y realizadas personalmente; las demás se detallan de forma particular en la parte experimental que convenga.

El Capítulo IV es la primera parte experimental de la Tesis, y en la que se describe la síntesis de nanopartículas de ferrita de cobre vía sol-gel y coprecipitación. También se analizan las diferencias entre cada método y su impacto en el material preparado. En este sentido, se ha usado el método estadístico de Diseño de Experimentos (*DoE*, en inglés) para optimizar la síntesis. Además, se estudian las propiedades magnéticas y mecánicas en pastillas sólidas preparadas a partir de las nanopartículas anteriormente sintetizadas. Finalmente, mediante el uso de métodos estadísticos, se estudia la correlación experimental directa entre las propiedades mecánicas y magnéticas de dicho material.

El Capítulo V está dedicado al estudio de un nuevo material: un nanocompuesto magnético basado en nanotubos de carbono. Al ser un material novedoso, en este capítulo hemos querido estudiar y entender las propiedades magnéticas haciendo, primero, una caracterización química y estructural del material. Por último, nos hemos centrado en comprender la relajación magnética de este nanocompuesto, estudio que hasta nuestro conocimiento no se ha realizado con anterioridad.

Por otro lado, en el Capítulo VI, se muestra la investigación realizada en relación con los materiales y compuestos magnéticamente blandos. En primer lugar, se realiza una caracterización estructural y magnética de los compuestos reales para, posteriormente, investigar sus propiedades magnéticas en el rango de frecuencia de kHz y MHz. Es aquí donde se observan las virtudes del material compuesto. En la segunda parte del capítulo, desarrollamos nuevas formulaciones de compuestos blandos a escala de laboratorio. Los materiales desarrollados son potencialmente útiles para aplicaciones en el rango de las frecuencias del kHz y MHz.

La frecuencia se eleva en el Capítulo VII. En otras palabras, la espectroscopía de terahercios (THz-TDS) se ha utilizado para investigar las propiedades ópticas y dieléctricas de dos óxidos semiconductores diferentes, en el rango de 180 GHz a 3 THz. Aquí se muestra el análisis de la señal y se discute el efecto que las diferentes características de la muestra pueden tener sobre las propiedades deducidas. Cabe añadir que, en este capítulo, los materiales magnéticos no se han investigado ya que el modelo de Fresnel, base fundamental de esta técnica, implica una respuesta no magnética del material.

En el Capítulo VIII se muestra un trabajo completamente distinto a las anteriores partes de la memoria. En este caso, se ha explorado la manipulación del momento magnético mediante el uso de ondas acústicas superficiales (*SAW*, por sus siglas en inglés). Los experimentos realizados en este capítulo proporcionan una interesante observación y abren la puerta a nuevos métodos de manipulación del momento magnético sin necesidad de usar campo.

Finalmente, el Capítulo IX contiene un breve resumen de las principales conclusiones obtenidas en esta investigación. Aunque las conclusiones también se comentan en detalle en cada capítulo, aquí se hace una consideración más general para, no solo tener una visión global de los resultados obtenidos, sino también para llegar a una idea clara: la relación entre la composición, las características fisicoquímicas, y las propiedades finales de los materiales nos permiten comprender y diseñar materiales con propiedades novedosas o mejoradas.

TABLE OF CONTENTS

CHAPTER I

INTRODUCTION AND GOALS

1. CONTEXT AND MATERIALS’ STATE OF THE ART

The term “nano” has its origin in the Greek word “nanos”, which means “dwarf”. Actually, the Cambridge Dictionary [1] defines the prefix “nano-“ as *‘one billionth of the stated unit*’. Moreover, when it is grammatically used to build complex nouns it commonly refers to ‘*extremely small*’. Therefore, the same reference defines the term “nanotechnology” as ‘*an area of science that deals with developing and producing extremely small tools and machines by controlling the arrangement of separate atoms*’. Nevertheless, it is important to point out that nanotechnology, or nanoscience, does not only care about the development of devices and machines; this field is specially focused on the study of the phenomena occurring when the matter is of the nanometre scale. Commonly, this scale is defined from 1 to 100 nm.

The interest paid on nanotechnology is growing day by day. The novelty of the properties that materials exhibit at the nanoscale, as well as the increasing capacity that humans have for designing and manipulating matter of this size, results in an increasing potential of this technology.

Despite there are already common devices using nanotechnology in our lives, it is expected to have even a greater impact in the future and to become an authentic revolution. Due to these expectations, lot of research efforts are actually paid to develop new materials and devices to accomplish with future humanity goals. Health [2]–[4], energy [5]–[7] or environment [8]–[10] are some fields where nanotechnology is having a key role. As an illustration of the increasing research interest in this field, Figure 1. 1 shows the number of published articles during the last 20 years with the term "nanotechnology" in the title.

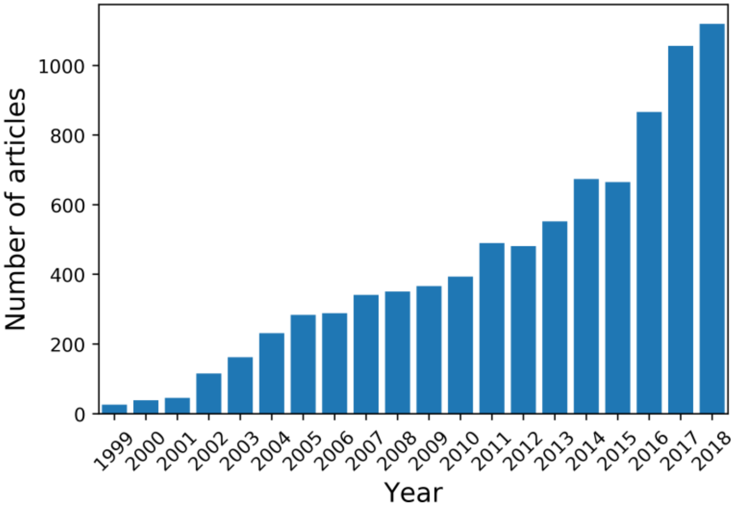

Figure 1. 1. Number of publications containing the term "nanotechnology" in the last 20 years. Data extracted from Science Direct database.

The growth has been almost exponential during last years. This fast analysis is confirmed by recently published bibliometric analysis [11]. The expectations for the future are to keep the same tendency and to make nanotechnology an affordable solution for daily circumstances [12].

More specifically, material science is exploring new routes for designing materials of nanometric size with novel properties. There are two main strategies followed when looking for changing materials' properties in the nanometric scale: (i) appearance of quantum effects due to size reduction or (ii) fabrication of nanocomposites with combined properties. In the first case, the reduction of the matter to nanometric sizes may lead to a change in properties due to the presence of quantum effects. Electron confinement in quantum dots [13], [14] or the formation of magnetic single domain particles [15] are some examples of quantum effects that appear when materials' size is reduced to the nanometric size. The second case looks for the combination of two or more materials in the nanometric scale in order to mix their properties and to fabricate a new composite with specific properties. Some examples of these designs are the core-shell or functionalized nanoparticles applied in biomedicine [16]–[18]. Here, the core gives the main mechanical, magnetic, electric or optical properties, meanwhile the shell (or the functionalization) controls the interaction of the nanomaterial with the surrounding media or biological system. Furthermore, apart from the two specific routes just described, it is worth to point out that when reducing the size, the ratio between the surface and the volume of the particle increases. The increase of this ratio leads to, for example, a higher reactivity of nanoparticles compared with bulk materials of the same composition.

Spinel ferrite nanoparticles have been previously prepared by a wide range of methods, from solid state reaction [19]–[21] to wet chemical methods such as co-precipitation [22], [23], thermal decomposition [24], [25], sonoshemical [26], or solvothermal [27], [28]. Solid state methods are simple to perform, but they have a low degree of control over the variables involved and then it is difficult to obtain materials with tunned properties. Moreover, in order to activate the solid-state reaction, the needed temperatures are large, thus allowing the particles to grow and making difficult to obtain nanosized particles. On the other hand, wet chemical methods usually have a high degree of control and allow to produce nanoparticles with a specific shape, functionalization and composition. However, they tend to be difficult and costly processes, making them difficult to be scaled up. In an intermediate point the sol-gel and gel combustion methods [29]–[32] appear, which have a good balance between the control over the synthesis parameters and production capacity.

More specifically, copper ferrite ($CuFe_2O_4$) is an inverse spinel ceramic material which, apart from the common applications of all spinel ferrites in fields as electronics [33], telecommunications, or medicine [34], [35], has recently shown an intense interest as electrochemical capacitive [36], or as good catalyst for organic degradation [37]–[39], or for water pollutants removal [40]. The sol-gel or gel combustion synthesis of

$CuFe_2O_4$ has been previously reported by various authors. For instance, Zhuravlev *et al*. [31] published an article studying the tetragonal and cubic formation in samples calcinated at different temperatures. This is an excellent reference in the study of the formation of each phase. They obtained a maximum purity of a 95% in their samples, and also reported agglomeration and sintering of the formed nanoparticles at micrometric scale. The work from López-Ramón *et al*. [30], which provides a precise study of the ferrite formation during calcination, reports the formation of tetragonal $CuFe_2O_4$ with a Scherrer crystallite size of 22 nm. However, the purity in these samples did not reached the 88% and presented an important presence of CuO and Fe_2O_3. Finally, a recently published review by Masunga *et al*. [41], summarizes the results obtained by different authors working in this field. In this work they report the wide range of properties that can be obtained at different conditions by using the same approach. Despite the large number of publications about $CuFe_2O_4$ synthesis - where results are consistent for the specific conditions used - there is not a clear reference where the results are analysed in a wide range of conditions, or the effect of each variable in the synthesis process is discussed.

However, the technological evolution to every time higher working frequencies, and its associated efficiency reduction [42], results in a growing interest paid on the development of materials with improved capabilities under these conditions. In this regard, soft magnetic materials (SMMs) are an excellent option due to their low anisotropy and coercivity, leading to small hysteresis losses. Some of the most classical SMMs are classified as first and second generation SMMs [43]. The first generation consists on pure Fe [44], or intermetallic structures such as Fe-P, Fe-Si, Fe-Ni, Fe-Co, or larger combinations [45]–[47]. The intermetallic structures look for reducing the coercivity of the material, or to slightly increase the electrical resistivity [43]. The second generation consists on amorphous and high-resistivity crystalline materials [48], [49], which have better ac properties.

Despite the low hysteresis losses that these materials have, their metallic nature results in the generation of electrical currents between particles when an ac field is applied. These currents, also known as eddy currents, lead to an increase of the power losses. Therefore, soft magnetic composites (SMCs), which have an isolating shell around the ferromagnetic core, have emerged as a real solution. Consequently, the soft magnetic properties of the core are maintained, and the eddy currents are reduced. The isolating shell can be made of different materials, from inorganic oxides or phosphates, to organic epoxy resins or polyester [50]–[53], for instance.

As described in different works [53]–[55] and patents [56], [57], the micrometer iron-based cores are usually prepared by water-atomizing methods. Then, the isolating coating can be added to the cores by mixing orthophosphoric acid and an organic solvent (ethanol, methanol, isopropyl alcohol or acetone for instance) with the iron cores. Another approach is to directly spray the orthophosphoric acid and the organic solvent on the iron particles. At the end the insulating coating should be between 0.1 and 1.2% of the iron particles' weight.

SMCs are actually applied in a large number of applications, such as alternators, generators, electric motors [58], reactor cores for hybrid electric vehicles [44], solenoid valves and reactors for high capacity power supplies or check-coils and noise filters for small power supplies [59]. Ueno and co-workers stated that these materials may have a bigger importance in next-generation semiconductor devices, meanwhile other reports [50] highlight their potential applications in automobiles and aerospace.

2. OBJECTIVES

The main goal of this Thesis is to prepare and to investigate the properties of different magnetic materials, in order to have a full understanding in how they are influenced by the fabrication conditions and their structural characteristics. The mechanical and magnetic properties are those primary investigated, but we also aim to explore their functional properties over a wide frequency range.

The first goal is to synthesise our own copper ferrite magnetic nanoparticles in order to conduct all the properties' characterization. The ambition is to use an easy and scalable up process as sol-gel, and to optimize it according to our requirements. Furthermore, we want to explore the co-precipitation method as an alternative to sol-gel and observe the main advantages of each process. Finally, we pretend to use these nanoparticles to fabricate solid pellets in order to characterize their mechanical and magnetic properties. In this regard, we aim to experimentally correlate them, which could be of interest in design and materials' selection processes.

We also want to study the magnetic properties of a novel nanocomposite consisting of carbon nanotubes (CNTs) and iron-based nanoparticles. The target here is to investigate its general magnetic properties, and to relate them to its physical characteristics. The investigation of its magnetic relaxation is also of interest, as there is a lack of literature regarding this type of measurements.

Another important objective in this work is to analyse the structural characteristics and magnetic properties – static and dynamic - of the currently used SMMs and SMCs, in order to determine the role that each element plays in the composite. Once having a complete understanding of these materials, we aim to develop our own SMCs base through easy and scalable up processes.

The characterization at frequencies up to the terahertz (THz) is also of interest. We aspire to measure the optical and dielectric properties of different oxides in this frequency range, and to discuss how the experimental procedure and physical characteristics of the sample may affect to the results.

Contrary to the previous cases, where the mechanical and functional properties are characterized, our last objective is to manipulate the magnetic moment by means of mechanical stimulus. More specifically, our purpose is to experimentally observe if there is a change on magnetization by using surface acoustic waves (SAWs).

3. REFERENCES

[1] "Cambridge Dictionary." [Online]. Available: https://dictionary.cambridge.org/. [Accessed: 23-Jun-2019].

[2] R. Keçili, S. Büyüktiryaki, and C. M. Hussain, "Advancement in bioanalytical science through nanotechnology: Past, present and future," *TrAC - Trends Anal. Chem.*, vol. 110, pp. 259–276, 2019.

[3] M. Saeedi, M. Eslamifar, K. Khezri, and S. M. Dizaj, "Applications of nanotechnology in drug delivery to the central nervous system," *Biomed. Pharmacother.*, vol. 111, no. December 2018, pp. 666–675, 2019.

[4] A. M. Cryer and A. J. Thorley, "Nanotechnology in the diagnosis and treatment of lung cancer," *Pharmacol. Ther.*, vol. 198, pp. 189–205, 2019.

[5] H. peng Feng *et al.*, "Core-shell nanomaterials: Applications in energy storage and conversion," *Adv. Colloid Interface Sci.*, vol. 267, pp. 26–46, 2019.

[6] J. Mei, T. Liao, G. A. Ayoko, J. Bell, and Z. Sun, "Cobalt oxide-based nanoarchitectures for electrochemical energy applications," *Prog. Mater. Sci.*, vol. 103, no. February 2018, pp. 596–677, 2019.

[7] G. Kumar, T. Mathimani, E. R. Rene, and A. Pugazhendhi, "Application of nanotechnology in dark fermentation for enhanced biohydrogen production using inorganic nanoparticles," *Int. J. Hydrogen Energy*, vol. 44, no. 26, pp. 13106–13113, 2019.

[8] G. N. Hlongwane, P. T. Sekoai, M. Meyyappan, and K. Moothi, "Simultaneous removal of pollutants from water using nanoparticles: A shift from single pollutant control to multiple pollutant control," *Sci. Total Environ.*, vol. 656, pp. 808–833, 2019.

[9] W. Zhang, D. Zhang, and Y. Liang, "Nanotechnology in remediation of water contaminated by poly- and perfluoroalkyl substances: A review," *Environ. Pollut.*, vol. 247, pp. 266–276, 2019.

[10] S. T. Khan and A. Malik, "Engineered nanomaterials for water decontamination and purification: From lab to products," *J. Hazard. Mater.*, vol. 363, no. September 2018, pp. 295–308, 2019.

[11] J. Youtie, A. L. Porter, P. Shapira, and N. Newman, “Lessons From 10 Years of Nanotechnology Bibliometric Analysis,” in *Nanotechnology Environmental Health and Safety*, 2018, pp. 11–31.

[12] M. Berger, *Nanotechnology The Future is Tiny*. Cambridge: Royal Society of Chemistry, 2016.

[13] Y. Zhang, Y. Li, Y. Liu, H. Li, and J. Fan, “Quantum confinement luminescence of trigonal cesium lead bromide quantum dots,” *Appl. Surf. Sci.*, vol. 466, no. July 2018, pp. 119–125, 2019.

[14] T. Han, H. Zhao, and X. Peng, “Enhancement of electrons confinement in AlGaN / AlN / GaN heterostructure using BGaN buffer with a small B-content,” *Superlattices Microstruct.*, vol. 126, no. December 2018, pp. 57–62, 2019.

[15] V. H. Ojha and K. M. Kant, “Temperature dependent magnetic properties of superparamagnetic CoFe2O4 nanoparticles,” *Phys. B Condens. Matter*, vol. 567, no. May, pp. 87–94, 2019.

[16] M. Zu, L. Ma, X. Zhang, D. Xie, Y. Kang, and B. Xiao, “Chondroitin sulfate-functionalized polymeric nanoparticles for colon cancer-targeted chemotherapy,” *Colloids Surfaces B Biointerfaces*, vol. 177, no. November 2018, pp. 399–406, 2019.

[17] S. E. Minaei, S. Khoei, S. Khoee, F. Vafashoar, and V. P. Mahabadi, “In vitro anti-cancer efficacy of multi-functionalized magnetite nanoparticles combining alternating magnetic hyperthermia in glioblastoma cancer cells,” *Mater. Sci. Eng. C*, vol. 101, no. August 2018, pp. 575–587, 2019.

[18] S. Rajkumar and M. Prabaharan, “Multi-functional core-shell Fe 3 O 4 @Au nanoparticles for cancer diagnosis and therapy,” *Colloids Surfaces B Biointerfaces*, vol. 174, no. September 2018, pp. 252–259, 2019.

[19] Z. Zhang, G. Yao, X. Zhang, J. Ma, and H. Lin, “Synthesis and characterization of nickel ferrite nanoparticles via planetary ball milling assisted solid-state reaction,” *Ceram. Int.*, vol. 41, no. 3, pp. 4523–4530, 2015.

[20] C. A. Palacio Gómez, C. A. Barrero Meneses, and A. Matute, “Structural parameters and cation distributions in solid state synthesized Ni-Zn ferrites,” *Mater. Sci. Eng. B Solid-State Mater.*

Adv. Technol., vol. 236–237, no. December, pp. 48–55, 2018.

[21] Y. Cao, H. Qin, X. Niu, and D. Jia, "Simple solid-state chemical synthesis and gas-sensing properties of spinel ferrite materials with different morphologies," *Ceram. Int.*, vol. 42, no. 9, pp. 10697–10703, 2016.

[22] M. Salavati-Niasari, T. Mahmoudi, M. Sabet, S. M. Hosseinpour-Mashkani, F. Soofivand, and F. Tavakoli, "Synthesis and Characterization of Copper Ferrite Nanocrystals via Coprecipitation," *J. Clust. Sci.*, vol. 23, no. 4, pp. 1003–1010, 2012.

[23] M. Kanagaraj, P. Sathishkumar, G. K. Selvan, P. Kokila, and S. Arumugam, "Structural and magnetic properties of CuFe 2 O 4 as-prepared and thermally treated spinel nanoferrites," *Indian J. Pure Appl. Phys.*, vol. 52, no. February 2016, pp. 124–130, 2014.

[24] I. Sharifi, A. Zamanian, and A. Behnamghader, "Synthesis and characterization of Fe0.6Zn0.4Fe2O4 ferrite magnetic nanoclusters using simple thermal decomposition method," *J. Magn. Magn. Mater.*, vol. 412, pp. 107–113, 2016.

[25] R. Al-Gaashani, B. Aïssa, M. Anower Hossain, and S. Radiman, "Catalyst-free synthesis of ZnO-CuO-ZnFe2O4 nanocomposites by a rapid one-step thermal decomposition approach," *Mater. Sci. Semicond. Process.*, vol. 90, no. September 2018, pp. 41–49, 2019.

[26] W. Lv, B. Liu, Z. Luo, X. Ren, and P. Zhang, "XRD studies on the nanosized copper ferrite powders synthesized by sonochemical method," *Jorunal Alloy. Compd.*, vol. 465, no. 3, pp. 261–264, 2008.

[27] A. Kalam *et al.*, "Modified solvothermal synthesis of cobalt ferrite (CoFe 2 O 4) magnetic nanoparticles photocatalysts for degradation of methylene blue with H 2 O 2 /visible light," *Results Phys.*, vol. 8, pp. 1046–1053, 2018.

[28] J. Kurian and M. J. Mathew, "Structural, optical and magnetic studies of CuFe2O4, MgFe2O4 and ZnFe2O4 nanoparticles prepared by hydrothermal/solvothermal method," *J. Magn. Magn. Mater.*, vol. 451, pp. 121–130, 2018.

[29] L. B. Zakiyah *et al.*, "Up-scalable synthesis of size-controlled copper ferrite nanocrystals by thermal treatment method," *Mater. Sci. Semicond. Process.*, vol. 40, pp. 564–569, 2015.

[30] M. V. López-Ramón, M. A. Álvarez, C. Moreno-Castilla, M. A. Fontecha-Cámara, Á. Yebra-Rodríguez, and E. Bailón-García, "Effect of calcination temperature of a copper ferrite synthesized by a sol-gel method on its structural characteristics and performance as Fenton catalyst to remove gallic acid from water," *J. Colloid Interface Sci.*, vol. 511, pp. 193–202, 2018.

[31] V. A. Zhuravlev, R. V. Minin, V. I. Itin, and I. Y. Lilenko, "Structural parameters and magnetic properties of copper ferrite nanopowders obtained by the sol-gel combustion," *J. Alloys Compd.*, vol. 692, pp. 705–712, 2017.

[32] C. Mahapatra *et al.*, "Sol–gel based materials for biomedical applications," *Prog. Mater. Sci.*, vol. 77, pp. 1–79, 2016.

[33] X. L. Tang, H. W. Zhang, H. Su, Y. Shi, and X. D. Jiang, "High-frequency micro-inductor fabricated on NiCuZn ferrite substrates," *J. Magn. Magn. Mater.*, vol. 293, no. 2, pp. 812–815, 2005.

[34] K. Atacan, M. Özacar, and M. Özacar, "Investigation of antibacterial properties of novel papain immobilized on tannic acid modified Ag/CuFe2O4 magnetic nanoparticles," *Int. J. Biol. Macromol.*, vol. 109, pp. 720–731, 2018.

[35] K. Elayakumar *et al.*, "Enhanced magnetic property and antibacterial biomedical activity of Ce 3+ doped CuFe2O4 spinel nanoparticles synthesized by sol-gel method," *J. Magn. Magn. Mater.*, vol. 478, no. January, pp. 140–147, 2019.

[36] B. Saravanakumar, S. P. Ramachandran, G. Ravi, V. Ganesh, R. K. Guduru, and R. Yuvakkumar, "Electrochemical performances of monodispersed spherical CuFe2O4 nanoparticles for pseudocapacitive applications," *Vacuum*, vol. 168, no. May, p. 108798, 2019.

[37] Z. Cao, C. Zuo, and H. Wu, "One step for synthesis of magnetic CuFe2O4 composites as photo-fenton catalyst for degradation organics," *Mater. Chem. Phys.*, vol. 237, no. April, p. 121842, 2019.

[38] P. Ye, D. Wu, M. Wang, Y. Wei, A. Xu, and X. Li, "Coating magnetic CuFe2O4 nanoparticles with OMS-2 for enhanced degradation of organic pollutants via peroxymonosulfate activation," *Appl. Surf. Sci.*, vol. 428, pp. 131–139, 2018.

[39] Z. Li *et al.*, “Heterogeneous catalytic degradation of organic pollutants by peroxymonosulfate activated with nitrogen doped graphene oxide loaded CuFe2O4,” *Colloids Surfaces A Physicochem. Eng. Asp.*, vol. 577, no. March, pp. 202–212, 2019.

[40] D. Miao, J. Peng, M. Wang, S. Shao, L. Wang, and S. Gao, “Removal of atorvastatin in water mediated by CuFe2O4 activated peroxymonosulfate,” *Chem. Eng. J.*, vol. 346, no. December 2017, pp. 1–10, 2018.

[41] N. Masunga, O. K. Mmelesi, K. K. Kefeni, and B. B. Mamba, “Recent advances in copper ferrite nanoparticles and nanocomposites synthesis, magnetic properties and application in water treatment: Review,” *J. Environ. Chem. Eng.*, vol. 7, no. 3, p. 103179, 2019.

[42] A. M. Leary, P. R. Ohodnicki, and M. E. Mchenry, “Soft magnetic materials in high-frequency, high-power conversion applications,” *Jom*, vol. 64, no. 7, pp. 772–781, 2012.

[43] J. A. Bas, J. A. Calero, and M. J. Dougan, “Sintered soft magnetic materials. Properties and applications,” *J. Magn. Magn. Mater.*, vol. 254, no. 255, pp. 391–398, 2003.

[44] N. Igarashi, M. Uozumi, T. Kosuge, A. Sato, K. Kusawake, and K. Yamaguchi, “Pure iron based soft magnetic composite core that enables downsizing automotive reactors,” *SEI Tech. Rev.*, no. 80, pp. 98–103, 2015.

[45] C. Wu, H. Chen, H. Lv, and M. Yan, “Interplay of crystallization, stress relaxation and magnetic properties for FeCuNbSiB soft magnetic composites,” *J. Alloys Compd.*, vol. 673, pp. 278–282, 2016.

[46] P. Gramatyka, A. Kolano-Burian, R. Kolano, and M. Polak, “Nanocrystalline iron based powder cores for high frequency applications,” *J. Achiev. …*, vol. 18, no. 1, pp. 99–102, 2006.

[47] T. H. Kim, K. K. Jee, Y. B. Kim, D. J. Byun, and J. H. Han, “High-frequency magnetic properties of soft magnetic cores based on nanocrystalline alloy powder prepared by thermal oxidation,” *J. Magn. Magn. Mater.*, vol. 322, no. 16, pp. 2423–2427, 2010.

[48] C. Chang, Y. Dong, M. Liu, H. Guo, Q. Xiao, and Y. Zhang, “Low core loss combined with high permeability for Fe-based

amorphous powder cores produced by gas atomization powders," *J. Alloys Compd.*, vol. 766, pp. 959–963, 2018.

[49] R. Hasegawa, "Present status of amorphous soft magnetic alloys," *J. Magn. Magn. Mater.*, vol. 215, pp. 240–245, 2000.

[50] K. J. Sunday and M. L. Taheri, "Soft magnetic composites: recent advancements in the technology," *Met. Powder Rep.*, vol. 72, no. 6, pp. 425–429, 2017.

[51] V. Girman, "Characterization of composite materials based on Fe powder (core) and phenol – formaldehyde resin (shell) modified with nanometer- sized SiO 2," vol. 37, no. 2, pp. 167–177, 2014.

[52] D. Liu, S. Gao, Y. Zhang, S. Yu, and F. Wang, "Microstructural and compositional evolution of core-shell FeSiAl composites during high-temperature annealing," *Ceram. Int.*, no. July, pp. 0–1, 2019.

[53] A. H. Taghvaei, H. Shokrollahi, and K. Janghorban, "Properties of iron-based soft magnetic composite with iron phosphate-silane insulation coating," *J. Alloys Compd.*, vol. 481, no. 1–2, pp. 681–686, 2009.

[54] D. Nikas, "Characterization of electrically insulating coatings for soft magnetic composite materials by means of surface sensitive analytical techniques," Chalmers University of Technology, 2013. PhD Dissertation.

[55] C. Oikonomou, "On Surface Characteristics and Microstructural Development of Soft Magnetic Composite Powder and Components," Chalmers University of Technology, 2015. PhD Dissertation.

[56] L.-A. L. Patricia Jansson, "Phosphate coated iron powder and method for the manufacturing thereof," US 6,348,265 B1, 2002.

[57] Z. Ye and B. Skarman, "Soft Magnetic Powder," US 2010/0038580 A1, 2010.

[58] H. Shokrollahi and K. Janghorban, "Soft magnetic composite materials (SMCs)," *J. Mater. Process. Technol.*, vol. 189, no. 1–3, pp. 1–12, 2007.

[59] T. Ueno, H. Tsuruta, T. Saito, A. Watanabe, T. Ishimine, and K. Yamada, "Practical and potential applications of soft magnetic powder cores with superior magnetic properties," *SEI Tech. Rev.*, no. 82, pp. 9–15, 2016.

CHAPTER II

FUNDAMENTALS

The preparation, structural analysis and functional characterization of magnetic nanoparticles requires a wide group of concepts coming from fields like chemistry, physics, materials science, crystallography, or statistics, for instance. This first chapter is therefore devoted to expose and explain all the theoretical framework needed to perform and discuss the experimental results that will be presented in the following chapters.

The main goal is therefore to introduce the different needed concepts in a logical and ordered way. However, it does not pretend to define just the precise theory that will be later applied: this chapter aims to be a useful reference to any reader who wants to start working in this field, or simply to get enrolled in these topics. For this reason, the fundamentals of this PhD Thesis will be exposed, despite they will be also connected to other related ideas that allow to give them a complete meaning.

1. OXIDES AND MAGNETIC FERRITES

Oxygen (O) is the most abundant chemical element in earth with 21% abundance in atmosphere and around 47% in Earth crust [1]. It is mainly present in the form of complex aluminosilicates that make up the vast proportion of igneous rocks. Oxygen can form at least one binary oxide with virtually all the known elements due to its high reactivity. This capacity comes from its high electronegativity (3.5 in the Pauli scale), its elevated electron affinity, and its capability for form strong chemical bonds (either ionic or covalent, depending on the electronegativity of the combining element).

The three–dimensional (3D) structures that oxide materials can form are usually defined by space filling models, in which ions are treated as hard spheres with a defined radius. The most efficient and stable formation is the one that fills most of the space and maximizes the density. From a two–dimensional (2D) point of view, the most suitable way is to form an equilateral triangular arrangement of spheres in each layer, in which each sphere is surrounded by six other spheres. Depending on the position where the above layers are placed, it is possible to define different configurations. Two of the more relevant are: (i) "…ABABAB…" configuration, where the third layer is placed above the first one and forms what is known as *Hexagonal Close-Packed* (HCP) structure; (ii) "…ABCABC…" configuration, where the third layer is placed on the free interstice and generates the called *Cubic Close-Packed* (CCP). Both configurations are graphically represented in Figure 2. 1.

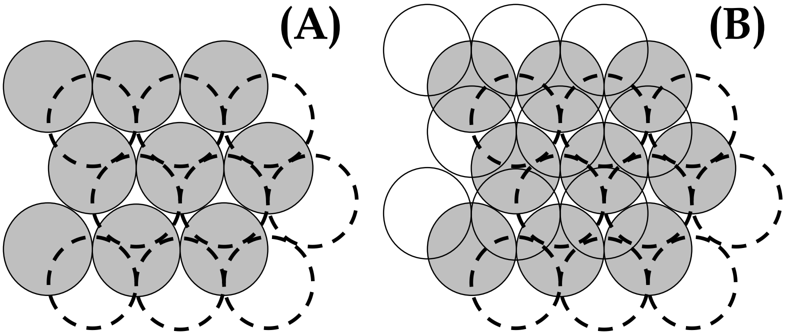

Figure 2. 1. Graphic representation of the (A) HPC and (B) CCP configurations in 2D. Adapted from [1].

However, these basic structures may lead on other crystal arrangements by considering small modifications. For instance, two other common cubic structures are the *body-centered cubic* (BCC), where there is an extra atom in the centre of the cube, or the *face-centered cubic* (FCC), which has an additional half atom (it is shared between two different unit cells) in the faces of the cube. In all these configurations, further atoms – which are usually of smaller size compared with those forming the structure - may be allocated in the free spaces between the main atoms, referred as *interstitial positions*. An interstitial atom is known to occupy an octahedral hole (h_O) or site when the surrounding atoms form an octahedron, giving a number of coordination of six. On the other hand, tetrahedral holes (h_T) have a coordination number of four [2].

As it has been indicated before, oxygen has an elevated facility to combine with one or more elements. Despite more structures for specific ions exist, the next classification allows to differentiate the general structures that oxides present.

1.1. Binary oxide structures

Binary oxides are the simplest from a structural point of view as they are built up just from one type of metal ion bonded with oxygen atoms. Here, different configurations can be differentiated:

- MO. This is the basic structure of NaCl. Anions are arranged in a CCP structure and all h_O are perfectly filled for both, the cation and the anion.
- MO_2 and M_2O. Typical examples of these configurations are fluorite (adopted by CaF_2, CeO_2, or high temperature ZrO_2, for instance), which has CCP arrangement with all h_T filled by anions, or rutile structure (found in TiO_2, SnO_2, or PbO_2, for example) which forms an HCP structure while half of the h_O in each layer are filled following a specific array.
- M_2O_3. Oxygen atoms are arranged in HCP, and only two-thirds of h_O are filled by cations.
- MO_3. Oxygen in CCP with a quarter of h_O filled in an ordered manner, while a quarter of the oxygen atoms are removed in a

similar fashion. It results in a 3D octahedron, in which all vertices are shared with other octahedrons.

1.2. Ternary oxide structures

1.2.1. Perovskite, ABO_3

B ions form the perovskite cubic lattice and form an octahedron with six oxygen atoms, and an *A* element occupies the centre of eight octahedrons. Cation *A* is larger than cation *B*, which are typically transition metals. The radii of the atoms in a perovskite need to fulfil Equation 2. 1, where R_A, R_B, and R_0 are the radii of elements *A*, *B* and oxygen, respectively, and t is the tolerance factor, which must have a value between 0.75 and 1.

$$t = \frac{R_A + R_0}{\sqrt{2(R_B + R_0)}} \qquad \text{Equation 2. 1}$$

Perovskite contain numerous oxygen vacancies, which can be filled with outer oxygen anions (O^{2-}). These absorbed oxygen ions can oxidize the *B* elements [3]. Moreover, perovskites can substitute oxygen atoms by halides ions (I^-, Cl^-, Br^-), which are known as *halide perovskites* [4].

1.2.2. Spinel, AB_2O_4

This structure has its origin on the mineral spinel ($MgAl_2O_4$). Spinel materials crystallize in the cubic space group Fd3m [5]. The unit cell consists of eight FCC units built up by the oxygen atoms. Thus, there are 32 oxygen ions, 32 h_O and 64 h_T. *A* ions fill an eight of h_T (8) and *B* ions occupy a half of the h_O (16). Overall it really has a $A_8B_{16}O_{32}$ structure.

Spinel oxides are used as catalysts, magnets and semiconductors.

1.2.3. Inverse Spinel, $B[AB]O_4$

It is a modification of the normal spinel structure. In this case, *A* ions occupy h_T (8), with half of the *B* ions (8). The other half of the *B* ions are placed in h_O (8).

The conversion, from the normal to the inverse spinel, is often not complete. For this reason, spinel structures can also be noted as $A_{1-\lambda}B_{\lambda}[A_{\lambda}B_{2-\lambda}]O_4$, where λ is the conversion degree with values between zero and the unit. When $\lambda = 0$ it represents the normal spinel, and when $\lambda = 1$ it is the complete inverse spinel.

There are different complex factors that determine the normal or inverse character that a spinel will have. The most important factors are the elastic energy – which is the degree of distortion of the crystal structure due to the difference in ionic radii -, the electrostatic energy (also known as *Madelung energy*), the crystal field stabilization energy, and the polarization effects [6].

1.2.4. Garnet, $A_3B_2T_3O_{12}$

Sometimes are called "rare-earth garnets", and their structure comes from the semiprecious garnets ($3MnO \cdot Al_2O_3 \cdot SiO_2$). *A* are large cations with coordination numbers larger than six and occupying dodecahedral sites, *B* are octahedral cations, and *T* are small cations in h_T. The basic building blocks consist on BO_6 octahedron and TO_4 tetrahedron. It results in a $B_2T_3O_{12}$ framework with dodecahedral cavities that can accommodate *A* cations. All the polyhedral in garnets are distorted and twisted. Each octahedron shares six edges with dodecahedra and only corners with tetrahedral. Each tetrahedron shares two edges with dodecahedra, while octahedral and dodecahedra share only corners. Each dodecahedron shares two edges with tetrahedral, four with octahedral and four with other dodecahedra.

As introduced before, in this chapter only the main structures have been defined, but there are many other possible structures in which oxide materials can arrange, such as Pyrochlore ($A_2B_2O_7$) or Scheelite (ABO_4) structures.

Ferrites are a family of oxide materials commonly known for their interesting magnetic properties. They are basically complex oxides made by the combination of iron oxide and one binary oxide. They can adopt different structures of those previously presented for general oxides. For instance, spinel ferrites have a basic structure MFe_2O_4 (or $MO \cdot Fe_2O_3$) where *M* is a divalent ion (such as Fe^{2+}, Ni^{+2}, Co^{2+}, Zn^{2+}, Mn^{2+}, Mg^{2+} or Cu^{2+}). In addition, spinel garnets have the structure $M_3Fe_5O_{12}$ (or $3M_2O_3 \cdot 5Fe_2O_3$) where *M* is typically yttrium or a rare-earth ion.

Magnetic ferrites have been present throughout the history, from raw magnetite to the most modern complex electronic circuitry. Their versatility (due to the different crystal structures it can adopt and the capacity to introduce different cations in the structure) gives them a wide range of properties that make them suitable for many different applications, from permanent magnets [7] to soft magnetic cores [8]. Furthermore, in the second case, magnetic ferrites are gaining more importance for microwave applications due to their good properties at elevated frequencies.

The control over ferrites chemistry and microstructure is crucial for designing materials with the desired properties for specific applications. For example, in order to increase the bulk magnetization of the material one can use metal ions with the highest magnetic moment (Fe^{3+} and Mn^{2+} have a moment of $5\mu_B$ [6], for instance). Also, considering the antiparallel alignment of the magnetic moments between the h_T and h_O it is also interesting to use non-magnetic ions (such as Zn^{2+}) whose preference to h_T disproportionate the number of Fe^{3+} ions on the two states, giving a bigger overall magnetic moment [5]. An example of these ferrites is $M_{1-x}Zn_x[Fe_2]O_4$ (*M* can be Mn^{2+}, Co^{2+}, Ni^{2+} or Mg^{2+}, for instance) where the substitution of non-magnetic zinc in h_T increases the global magnetic moment at values of x up to 0.5 [5]. If the goal is to increase the permeability (μ) in soft ferrites it is possible to use ions like Zn^{2+} that minimize the magnetocrystalline anisotropy and the magnetostriction, or to create a microstructure with large grains and a lower degree of defects. To improve the high frequency operation, it is recommendable to have small grains with high-resistive grain boundaries in order to avoid having eddy current losses [5], [9]. On the other hand, permeability is a linear function of grain size [6].

Despite their properties can be modulated by controlling their obtention, generally the saturation magnetization (M_S) of ferrites is around a 25% of the one of metals, the Curie temperature (T_C) is also lower, and their μ is lower than Ni – Fe alloys, but comparable with other materials [5]. On the other hand, their electrical resistivity (ρ) is from six to twelve orders of magnitude lower than metals, what makes them unique for high frequency applications [9]. From an economical point of view, their cost is generally lower than metals, and they can be easily moulded in a wide range of shapes, leading to flexible and economic pieces.

Some important fields where magnetic ferrites have a big importance are permanent magnets (loudspeakers, field magnets in motors, …), telephony and telecommunications (broadband transformers, LC circuits, …), power suppliers (high frequency transformers for computers, microprocessors, …), magnetic recording (recording heads, hard disks, …), or microwave components (satellite communications, radar absorbing tiles and paints, …), for instance.

2. SYNTHESIS METHODS

The evolution in technology has always gone directly related to the capacity that humans have had to produce new materials. Furthermore, the increasingly control over the production processes have led to the ability to model materials with new functionalities.

In this chapter, different commonly used strategies or approaches for the synthesis of oxide materials are described. The criteria used to classify them changes depending on the reference consulted, such as the media where the reaction takes place, the physical characteristics of the product or the range of needed temperatures. The selected criteria here is the physical state in which the reaction takes place (solid, liquid or gas). Moreover, despite there are lots of additional methods and processes, we will define some of the more common techniques used for the preparation of the materials that are under study in this Thesis [1], [5].

2.1. Solid – phase synthesis

This is the oldest method and the most used for the conventional preparation of oxides. Stoichiometric amounts of the precursors (either oxides, carbonates or hydrates) are mixed together and forced to react forming the desired oxide. It is an easy strategy from a technical point of view, and it often allows the production of big amounts of oxide materials. Nevertheless, as the reaction takes places in solid state, it is necessary to apply big amounts of energy to make them react. It usually leads to a non-completely pure product due to the difficulty of achieving a complete reaction.

2.1.1. Conventional ceramic synthesis

This is the approach to which one commonly refers when talking about solid-state production of oxides. In this method, the reactants are mixed together in powder form and heated up to make them react. As the reaction takes place in solid state, it is required a good homogeneity and intimate contact of the powder, as well as considerable high temperatures (usually higher than 1000 °C) in order to achieve high conversion rates from the precursors to the products. Repeated cycles of mechanical grinding and calcination are a commonly used mechanism with the goal of promoting homogeneity. Moreover, reactants are often pressed into pellets in order to increase the contact between the particles and, hence, facilitate the reaction.

Despite this is a simple process from a technical point of view, it has some important drawbacks that limit its use for some applications. First, due to the continuous grinding processes there are usually chemical impurities introduced into the sample. Also, it is extremely difficult to achieve an intimate contact and chemical homogeneity of the starting powder. Finally, it is also important to point out that powder aggregations are often produced if the mixture of the reactants is not perfect.

2.1.2. Mechanosynthesis or mechanochemistry

Milling processes have been traditionally understood as size reduction methods of solid particles even to the nanometric range, but they are also initiators or accelerators of solid-state chemical reactions [10]. Actually, mechanochemical method is widely recognized as an efficient and simple alternative to traditional solid-state ceramic processes [11]. This synthesis method uses high mechanical pressures to force the solids to combine each other, and to assume crystal structures and coordination numbers in which they are commonly unstable. Powder reactants (often the elemental oxides) are stoichiometrically mixed and milled for several hours, while the kinetic energy is transferred to the powder trapped between the colliding balls, or between the container and the balls. There is a balance between the coalescence and fragmentation of particles during the process, leading to a final stable particle size. In order to obtain the desired phase and microstructure it is important to optimize some variables in the process as: type of mill, milling container, milling speed, milling time, ball-to-powder weight ratio or the milling atmosphere, for instance [12].

This approach allows the formation of oxides with novel oxidation states and the low-temperature production of those oxides commonly prepared via the conventional ceramic method. On the other hand, some disadvantages are the long reaction times that are required, the presence of impurities coming from the balls or the container, or the high degree of structural and surface disorder. Low temperature annealing treatments have been demonstrated [10], [11] to be effective for redistributing the cations to their equilibrium position and lowering defect concentration.

2.2. Liquid – phase synthesis

The general idea of this approach is to achieve a much better chemical homogeneity of the precursors by diluting them in a liquid media before starting the chemical reaction. Then, depending on the specific conditions in which this reaction takes place, it is possible to distinguish between different specific techniques than are described below.

Independently of the specific method used, liquid–phase synthesis is an option that offers better homogeneity and purity than solid–state methods, and reactions take place at much lower temperatures. On the other hand, reactants are often more complex, the process has more technical requirements, and the production rate is lower compared with solid–state methods.

2.2.1. Precipitation or co-precipitation method

Co-precipitation is one of the most used methods for the preparation of homogeneous and high–purity nanoparticles [13]. The aqueous solutions of the metal precursors (usually chlorides, nitrates or sulphates) are stoichiometrically mixed. By the increase of the pH (adding NaOH, for example), they simultaneously precipitate forming hydroxides. Finally, the precipitate is filtered, washed and dried, before performing a final thermal treatment to form the pure oxide [6].

The agglomeration of the formed hydrous forms is an undesired stage in the process when the goal is to synthesize fine particles. In order to ward off this effect, it is crucial to avoid local supersaturation of the reactants and slowly generate the precipitating agent. In this regard, organic dispersant agents (also known as *surfactants*) are often used to separate the different nucleating points and avoid particles' growth.

2.2.2. Sol – Gel

In this process, the molecular precursors are mixed and converted into a sol or a gel through a chemical reaction. Then, solid materials can be obtained by drying and densifying. This allows the production of high purity single or multicomponent materials with the desired physical properties and microstructure at lower temperatures than solid–phase methods.

More specifically, a traditional sol-gel process consists on a five-steps process: hydrolysis, condensation, polymerization, aging and drying [14]. Metal alkoxides are often used as reactant agents because they easily react with water, producing *hydrolysis*. In this reaction, a hydroxyl ion becomes attached to the metal atom, as is represented in Equation 2. 2.

$$Si(OR)_4 + H_2O \rightarrow HO - Si(OR)_3 + ROH \qquad \text{Equation 2. 2}$$

where *R* represents a proton or other ligand, and the bar (—) is sometimes used to indicate the presence of a chemical bond. The hydrolysis process may go to completion (where all the OR groups are replaced by OH) or stop while the metal is only partially hydrolysed, depending on the amounts of catalyst and water present. Then, two partially hydrolysed compounds can link each other in a *condensation* process, as described in Equation 2. 3:

$$(OR)_3Si - OH + HO - Si(OR)_3 \rightarrow (OR)_3Si - O - Si(OR)_3 + H_2O \qquad \text{Equation 2. 3}$$

This reaction can continue in a *polymerization* process building up larger molecules. A substance is considered as a *gel* if its molecules reach macroscopic dimensions so that it extends throughout the solution. The time needed to form the last bond that completes this giant molecule is known as *gel point*. The formed gel consists on a solid skeleton containing a continuous liquid phase, both of colloidal dimensions. It is possible to make objects with a desired shape if this polymerization (or also known as *gelation*) process occurs after casting the sol into a mold. Despite the formation of bonds during the polymerization, there is still some movement allowed in the network. With the aging process, the structure and properties of the gel definitely change by further bonds formation and condensation. Finally, elimination of the remaining liquid by the drying process usually causes shrinkage of the gel network due to the rise of capillary pressure. The obtained gel, known as *xerogel* (*xero* means *dry*) is often reduced 5 or 10 times in volume. If the goal is to obtain a nonporous material, it is necessary to heat the material to high temperatures in order to produce sintering.

Another interesting approach is the called polymer–assisted sol–gel method [15], [16]. The main idea of this mechanism is to form a gel spreading the solution with the metal precursors. In this method, the gel is not a part of the desired product and it is only a polymer matrix that isolates the different nucleating points where the particles will later be formed. By avoiding this contact between each nucleation point the particle growth is diminished, so it becomes a very suitable option for synthesizing fine particle sized transition metal oxides containing two or more metal ions.

From an experimental point of view, the polymer precursors (citric acid and ethylene glycol, in the pure *citrate* or *Pechini* method [17]–[19]) are mixed and stirred together with the metal precursors (usually nitrates or chlorides) in an aqueous solution. Then, by a slightly heating, the polymer precursors react forming a gel containing a uniform mixture of metal ions. Finally, the gel is fired to be eliminated and the final product is obtained.

Overall, sol-gel method appears to be as an easy and cheap process that allows the synthesis of relatively big amounts of a wide range of different oxide nanomaterials.

2.2.3. Hydrothermal methods

This is a very suitable process to produce good quality monodisperse ceramic powders and large amounts of polycrystalline powders.

In this approach, an aqueous solution with the salt precursors is placed in a sealed system under hydrothermal conditions, i.e. at temperatures slightly above of the critical point of the solvent (usually around 350 °C or 400 °C) and high pressures (about 100 MPa). Hydrothermal autoclaves are placed in a furnace where a temperature gradient produces these conditions on the solution.

The main advantages of this method are the good quality of the products and the use of lower temperatures than those required for producing the same chemical reactions without the hydrothermal conditions. On the other hand, dilute cation concentrations (10^{-2} M) are required for the formation of monosized particles.

2.2.4. Thermal decomposition

This method is one of the simplest methods for preparing nanoparticles. It is based on the thermal decomposition of an organometallic precursor in the presence of organic solvents and surfactants [20]. The temperature needed for the decomposition depends on the type of precursor used, but they are all around 500 °C or 600 °C [21], [22].

2.3. Gas – phase synthesis

Gas–phase reactions allow having an initial mixture of the reactants at the molecular level, thus maximizing the homogeneity. In addition, reactions between solids and gases are also considered in this method, which is commonly used for the synthesis of monoxide ceramics.

Experimental efforts have been paid on the development of heating methods that allow the control of the nucleation, growth and aggregation of the particles from a supersaturated gas phase. This family of processes usually work with quick heating and cooling rates, and hence small reaction times, ensuring homogeneous nucleation.

2.3.1. Chemical Vapour Deposition (CVD)

In CVD processes two or more volatile compounds react in gas phase, and the solid-state product is deposited on a substrate. It is especially suitable for producing thin films, multilayers and composite materials for applications in microelectronics, optoelectronics and energy conversion devices [23]. Nevertheless, it is also possible to use this method for the preparation of nanoparticles [24].

Some advantages of CVD processes are the good layer uniformity, wide flexibility in terms of chemical precursors, the possibility of depositing at relatively low temperatures, the capacity for controlling the crystal structure, the adjustment of the deposition rate, and ultra-high vacuum conditions are not required. Some drawbacks are their technical complexity compared to other gas–phase methods, and the toxic, flammable or explosive behaviour of some reactants needed [25].

2.3.2. Physical Vapour Deposition (PVD)

The PVD process consist on the sputtering or evaporation of the precursor transition metal - by means of an electron beam or plasma heating - which reacts with a low-pressure gas to produce a layer [1]. Although this process allows to produce 2D ferrites for microwave applications [26], it is commonly used to produce hard coatings made of carbonitrides, carbides nitrides, or oxides.

3. DESIGN OF EXPERIMENTS

The classical perception of the utility of statistical methods on experimental processes is related to the conception of a useful tool for processing big batches of data and to extract overall conclusions. Nevertheless, the implantation of statistics in science can also have a large benefit in the experiments' planning process and the maximization of the conclusions that can be extracted from the experimental data.

3.1. Concept and definition

Chemometrics is a field of knowledge that applies multivariate statistics and mathematical modelling in the field of chemistry [27]. More specifically, *Design of Experiments* (DoE) is defined as a planned approach for determining cause and effect relationships [28]. This method consists on:

- Reduce the number of needed experiments.
- Verify all factors that affect an experiment.

- Define a strategy to obtain reliable solutions after a set of experiments.

DoE is a multivariate method, i.e. it considers that more than one variable can be affecting the results obtained in the experiments. It has sense considering that most of the processes in our lives are governed by multiple variables at the same time. Nevertheless, for a long time, science has worked modifying just one variable of the experiment when a phenomenon was studied. This method is known as one variable at a time (OVAT) [29]. Therefore, the possible effects that other variables may have on the experiments are suppressed, as well as any possible interaction between them. By considering a proper distribution of samples, it is possible to obtain more information than by individually considering each variable [27]. Moreover, by using the DoE methodology, the number of experiments is minimized, and suitable experimental conditions are defined to maximize the obtained information and to determine the interaction between variables. The obtained data can be mathematically processed by specific models to obtain the *response surface*, which simulates the results in all the experimental domain. By this way, results can be predicted by doing a minimum number of experiments.

3.2. Methodology

The key of a good DoE is to design the more adequate set of experiments to obtain the desired information [30]. At this point, despite it might seem obvious, the more important aspect is to determine the research goal. The experiment responses that may be representative of the properties that are pretended to be evaluated must be identified, as well as all the possible variables that can affect the results.

Different approximations and models can be chosen in a DoE. Each model can be interpreted as a different geometrical shape investigating the experimental domain through a specific *response function* (Y). The coefficients of this function can be obtained from the experimental results. Once the coefficients are obtained, Y can be used for predicting the result of the experiment in the experimental domain, which is called the *response surface.* The area where the response surface is constructed is known as *factor space* [28]. For instance, when two variables (X_1 and X_2) are explored in an experiment, the resulting factor space is the one represented in Figure 2. 2:

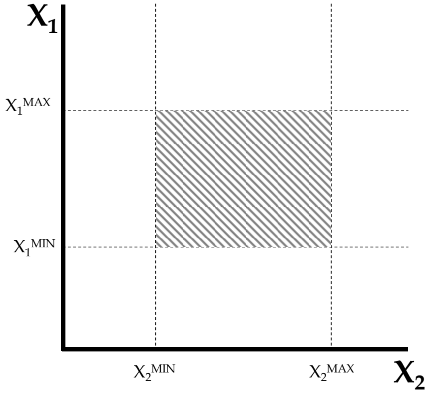

Figure 2. 2. Representation of the experimental domain investigation when two variables (X_1 and X_2) are considered. The area filled with diagonal lines represents the factor space.

The response surface allows predicting the result of the experiment in an untested condition, but also to find the conditions where the optimum response (maximum or minimum) might be obtained.

3.3. Functions and models

The most suitable approach depends on the number of variables considered (k), and the capacity to fabricate samples or to perform experiments. The most common models are described below.

3.3.1. Full Factorial Design, 2^k

This is the case where all the possible combinations of levels of factors are performed and the statistical analysis is applied to process the experimental results. This is also called the experiment of 2^k type, because the number of trials (N) is determined by 2^k. Here the total number of experiments may be large; thus, this is an appropriate approach when working with a reduced number of variables, and a high degree of control in the regression is needed.

As stated before, each model can be interpreted as a different geometrical inspection of the experimental domain. In the case of the Full Factorial Design, all the corners of the combinations between maximum and minimum variable values (X_i^{MIN} and X_i^{MAX}) are tested. Figure 2. 3 shows the geometrical interpretation when $k = 2$ and $k = 3$ models are applied.

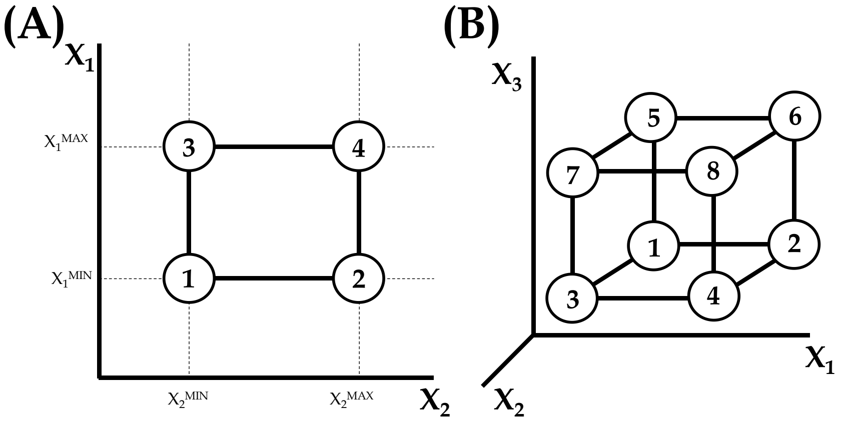

Figure 2. 3. Geometrical distribution of the experiments in a k-dimension experimental domain. (A) $k = 2$, and (B) $k = 3$. Adapted from [31].

In this figure, it is possible to see how the experiments are placed in the vertexes of a rectangle or a cube in a two and three variables design, respectively. This geometry evolves to higher dimensions for higher k values.

In this design each variable has two levels (-1 or +1), which can be either quantitative or qualitative. These levels refer to the minimum and maximum values of each variable, respectively. Once these boundaries have been defined, the *experimental matrix* can be constructed. By this matrix all the experiments – corresponding to all the combinations of properties – are planned before performing the experiments. Table 2. 1 and Table 2. 2 show the experimental matrix for the case of $k = 2$ and $k = 3$, respectively. As can be seen in these tables, the matrix is obtained by varying for each variable the -1 and the +1 value each 2^{n-1} positions, where n is the number of the planned variables.

Table 2. 1. Experimental matrix when *k* = 2.

Experiment	X_1 value	X_2 value
1	-	-
2	+	-
3	-	+
4	+	+

Table 2. 2. Experimental matrix when *k* = 3.

Experiment	X_1 value	X_2 value	X_3 value
1	-	-	-
2	+	-	-
3	-	+	-
4	+	+	-
5	-	-	+
6	+	-	+
7	-	+	+
8	+	+	+

Here “-“ and “+” symbols represent X_i^{MIN} and X_i^{MAX}, respectively.

Experiments must be randomly run in order to avoid considering the effect of exterior variables in the experiments [29]. The output of each of these experiments (Y_i^{EXP}) is later computed by a model to simulate the response at any point of the factor space. The response function is a polynomial function of *k*-degree, as described by Equation 2. 4.

$$Y = b_0 + \sum_{i}^{k} b_i X_i + \sum_{i}^{k} b_{ij} X_i X_j \qquad \text{Equation 2. 4}$$

where Y is the response value, b_i are linear regression coefficients, b_{ij} are regression coefficients of double factor interactions, and $X_{i,j}$ are specific conditions on the factor space. For instance, Equation 2. 5 shows the response function for a two-variable (*k* = 2) system.

$$Y = b_0 + b_1 X_1 + b_2 X_2 + b_{12} X_1 X_2 \qquad \text{Equation 2. 5}$$

where b_0 is the free coefficient, b_1 and b_2 are the linear regression coefficients for each variable, and b_{12} is the regression coefficient of the double interaction.

Once the experiments have been performed and the output measured, the *model matrix* can be built up. This matrix collects the coefficients of each regression values and the output, for each experiment. As an example, Table 2. 3 shows the model matrix for a k = 2 example.

Table 2. 3. Model matrix for a k = 2 design.

Experiment	b_0	b_1	b_2	b_{12}	Y_i^{EXP}
1	+	-	-	+	Y_1^{EXP}
2	+	+	-	-	Y_2^{EXP}
3	+	-	+	-	Y_3^{EXP}
4	+	+	+	+	Y_4^{EXP}

For each coefficient, its column is multiplied point to point by the corresponding response, and they are added up. Finally, the average of this sum is calculated. For instance, for the example shown in Table 2. 3, the coefficients would be calculated following Equation 2. 6, Equation 2. 7, Equation 2. 8, and Equation 2. 9.

$$b_0 = \frac{1 \cdot Y_1^{EXP} + 1 \cdot Y_2^{EXP} + 1 \cdot Y_3^{EXP} + 1 \cdot Y_4^{EXP}}{4} \quad \text{Equation 2. 6}$$

$$b_1 = \frac{-1 \cdot Y_1^{EXP} + 1 \cdot Y_2^{EXP} - 1 \cdot Y_3^{EXP} + 1 \cdot Y_4^{EXP}}{4} \quad \text{Equation 2. 7}$$

$$b_2 = \frac{-1 \cdot Y_1^{EXP} - 1 \cdot Y_2^{EXP} + 1 \cdot Y_3^{EXP} + 1 \cdot Y_4^{EXP}}{4} \quad \text{Equation 2. 8}$$

$$b_{12} = \frac{1 \cdot Y_1^{EXP} - 1 \cdot Y_2^{EXP} - 1 \cdot Y_3^{EXP} + 1 \cdot Y_4^{EXP}}{4} \quad \text{Equation 2. 9}$$

As can be appreciated, b_0 directly corresponds to the mean value of the measured responses. Once the coefficients are obtained, Equation 2. 5 can be applied to obtain the response surface on the experimental domain. Furthermore, the magnitude of the linear and quadratic coefficients gives information about the significance of the effect that variables and interactions have on the measured output. Lineal coefficients are representative of the effect of each variable, meanwhile the quadratic (or higher) coefficients show the importance of the interaction between the two variables involved.

3.3.2. Fractional Factorial Design

The number of experimental trials needed to perform a Full Factorial Design increases rapidly with the number of variables involved. Thus, when k is really elevated, a Full Factorial Design may become an unaffordable option. It is neither the best option when there are limitations for performing the experiments, such as technical, economic or time restrictions. In these cases, reducing the total number of experimental runs and performing a factorial design is an interesting option. The possibility to reduce the number of experiments and keep obtaining valuable information is supported by two main arguments [30]:

i. Usually high-order interactions have small values and, consequently, no practical importance. The main effects (first order) tend to be larger than the second order ones, which at the same time are more important than the third-order ones. If their importance is low, there is no reason for performing all the runs to complete factorial design to estimate their values.
ii. As the number of factors increases, the probability that one of these variables do not affect the experiment also increases.

Nevertheless, it is often impossible to predict which variables will significantly affect the response. In order to avoid the risk of excluding important factors, it is recommended to use the maximum number of possible factors. Fractional Factorial Design can do that without increasing the number of experiments.

The reduced model used in this case is defined by 2^{k-n}, where n are the degrees excluded of the design. The selection of design arrangement, in terms of number of points, as well as the coordinate settings of the points, depends on the form of the combined model to be fitted. For further information and details, references [28], [30] give the specific criteria as well as some examples of the application of this methodology.

For instance, Plackett-Burman Design uses only few experiments equal to the first multiple of 4 greater than the number of variables. This model only considers the constant and lineal terms. This type of design can be very useful when the goal is to detect the most relevant variables (or those which are non-relevant) to later perform a Full Factorial Design with a lower number of variables involved [29].

3.3.3. Central Composite Design (CCD)

Generally, a CCD with k variables consists on the following parts:

- A factorial (i.e. cubic) part, where the coordinates correspond to the +1 or -1 values of each variable. The number of points (N_{fact}) is defined by the 2^k rule.
- An axial (or star) part formed by $N_{ax} = 2k$ points. In these points all the coordinates are null except for one that has a certain α (or -α) values.
- A total (N_{cen}) of central points, where all the variables' values are set to 0 (i.e., the medium value between the maximum and the minimum one).

These aspects will define the design used. Hence, the number of cubic points, the α value, and the number of replicates on the central point are the three that must be defined before starting the design. If $\alpha = 1$, the axial points are placed in each of the faces between the cubic points, whereas if $\alpha = \sqrt{k}$ the design has a spherical shape. Figure 2. 4 represents these two possible options in the case where $k = 3$. The total number of experiments is 2^k+2k+N_{cen}.

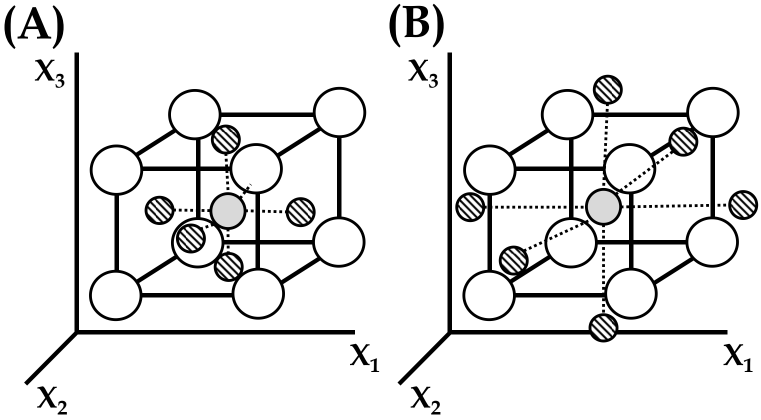

Figure 2. 4. Geometrical representation of the central composite design when *k* = 2. (A) α = 1, and (B) $\alpha = \sqrt{2}$. White spheres represent the cubic points, dashed spheres are the axial points, and the grey one is the central point. Adapted from [31].

The quadratic model, which allows estimating the linear, interactions, and quadratic terms for a CCD, is described in Equation 2. 10:

$$Y = b_0 + \sum_{i}^{k} b_i X_i + \sum_{i}^{k} b_{ii} {X_i}^2 + \sum_{i<j}^{k} \sum_{j}^{k} b_{ij} X_i X_j \qquad \text{Equation 2. 10}$$

In case where *k* = 2, Equation 2. 10 results in Equation 2. 11:

$$Y = b_0 + b_1 X_1 + b_2 X_2 + b_{12} X_1 X_2 + b_{11} {X_1}^2 + b_{22} {X_2}^2 \qquad \text{Equation 2. 11}$$

3.3.4. Doehlert Design

This design, as in the case of CCD, allows to estimate the linear, interaction, and quadratic terms. On the other hand, the number of experiments ($N = k^2 + k + N_{cen}$) is lower than in CCD. This makes this design interesting when it is important to reduce the number of experiments and the quadratic terms are needed. Moreover, in this case *N* is not the same for all the variables: with *k* = 2, the first has five levels, meanwhile the second one has three levels; with *k* = 3 the number of levels is seven, five and three [29]. Figure 2. 5 shows the geometrical interpretation of this model when *k* = 2 and 3. As it is seen, it is a hexagon when exploring two dimensions.

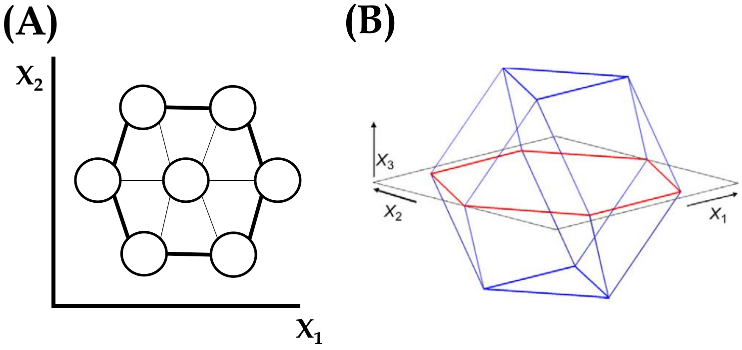

Figure 2. 5. Geometrical representation of the Doehlert Design when (A) *k* = 2, and (B) *k* = 3 [29].

Perhaps the most important aspect of this design is its capacity to be performed sequentially in order to extend the explored domain. The previous experiments can be combined with the new ones to build a new structure and explore more promising regions [29], [30]. For instance, Figure 2. 6 shows three examples of combinations between sets of different designs to explore the experimental domain.

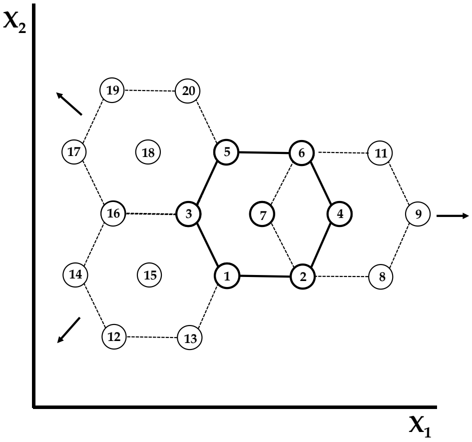

Figure 2. 6. Geometrical representation of the capacity of the Doehlert Design to chain experiments and expand the tested experimental domain. Adapted from [31]

3.3.5. D-Optimal Design

D-Optimal Design is an interesting option because it provides the maximum accuracy in estimating the regression coefficients. Nevertheless, this is not a common method due to the elevated number of tests required [28].

By this method, only those terms which maximize the confidence of the calculated model are considered. Considering X as the model matrix and X′ its transposed, the matrix X′X is the information matrix, and its inverse $(X'X)^{-1}$ is the dispersion matrix. The product between the experimental variance and the values in the diagonal of the dispersion matrix corresponds to the variances of the coefficients, whereas the covariance of the coefficients is obtained when multiplying the experimental variance by the extradiagonal values. By minimizing the determinant of $(X'X)^{-1}$ the confidence volume is minimized [30]. Therefore, it is possible to predict which subset of experiments is better, before performing the experiments [29].

This calculation is usually done with specific software, which can find the best subset of experiments once the number of experiments and a list with all the candidate points are defined. It is only possible to make direct comparisons for matrices having the same number of experiments: from a mathematical point of view the quality of the design increases as more experiments are performed. To compare experimental matrices having a different number of experiments, the normalized determinant is used. This determinant (*M*) is described in Equation 2. 12.

$$M = \frac{det(X'X)}{N^p} \qquad \text{Equation 2. 12}$$

where *N* is the number if experiments, and p the number of parameters.

When *N* increases, both the numerator and the denominator increase. Then, the value of *M* will increase if the numerator increases more than the denominator; this may only happen when by adding an experiment, the quality of the information increases more than the experimental effort [29].

4. X – RAY DIFFRACTION (XRD)

The term X-ray refers to electromagnetic radiations that have a wavelength range of 10^{-3} nm to 10 nm, which were discovered in 1895 by W. Röntgen [32] . This wavelength range corresponds to energies from $1.24 \cdot 10^{6}$ eV to 124 eV and frequencies from $3 \cdot 10^{20}$ Hz to $3 \cdot 10^{16}$ Hz.

X-rays have been used for imaging materials which are opaque at visible frequencies. In this regard, they have been widely used in medical radiography, security scanners or computed tomography. Moreover, they can reveal information of materials, such as the crystal structure, microstrain, or orientation.

To study the structure of matter, the so-called *hard* X-rays are used for two main reasons (i) they deeply penetrate on the material, despite the penetration depth depends on each substance; (ii) they have a much shorter wavelength (between 0.1 and 0.2 nm) compared to visible light, which is similar to the atoms size and, thus, diffracts with those atoms periodically arranged [32].

Diffraction is a phenomenon that occurs when a wave encounters an obstacle or a slit. In this case, when the X-ray faces a periodic structure it is split into different waves traveling in different directions. Crystalline matter contains a variety of planes with different orientations and spacings. Each one of these planes of ordered atoms acts as a diffraction centre. The diffraction pattern, which is characterized by the intensity and direction of the diffracted beam, is then defined by the distribution of planes in the material (i.e. its crystalline structure). Consequently, the diffraction pattern obtained is characteristic of the matter and its internal structure. X-ray diffraction (XRD) has become nowadays a powerful non-destructive technique for the analysis of materials.

4.1. X-rays generation

X-rays are produced by rapidly decelerating electrons which were previously accelerated to very high speeds. This process is typically done in an X-Ray tube, where two metals, the cathode and the anode, act as the source and target of electrons, respectively. The anode is maintained at high negative voltage (-V), meanwhile the anode is at ground potential [32], [33]. The cathode is made up of a tungsten filament which is heated by applying high electric potentials (20 – 60 kV) and accelerates electrons. When the electrons impact the target, they lose their kinetic energy (E_K) and this loose of energy is emitted as X-rays. Figure 2. 7 shows a scheme of the system.

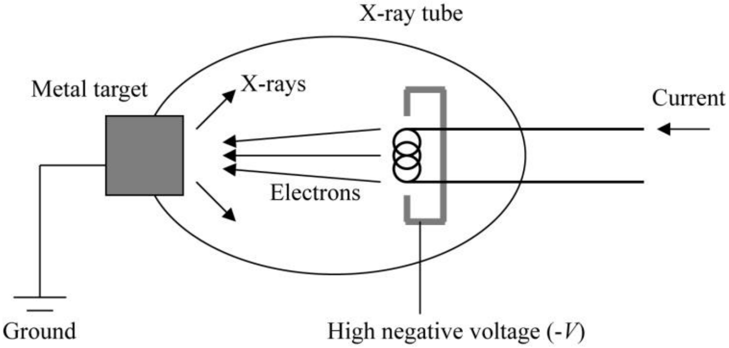

Figure 2. 7. Schematic representation of the generation of X-rays in an X-ray tube [32].

The E_K (in eV) that electrons have in the moment of collision against the target is defined by Equation 2. 13 [34].

$$E_K = \frac{1}{2}mv^2 \qquad \text{Equation 2. 13}$$

where m is the mass of the electron ($9.11 \cdot 10^{-31}$kg) and v is the speed before the impact. The generation of X-rays is a really inefficient process; only about a 1% of the energy consumed by the tube is transferred into X-rays. The maximum X-ray frequency and minimum wavelength that X-rays could have in case of a 100% of energy transformation is defined in Equation 2. 14.

$$h\nu_{max} = h\frac{c}{\lambda_{min}} \qquad \text{Equation 2. 14}$$

being ν the frequency, λ the wavelength, and c the speed of light. However, most of the electrons suffer multiple collisions and lose part of their energy. For this reason, the E_K at which electrons reach the target is not the same and, hence, there is a range of wavelengths (and frequencies) emitted by the X-ray tube. This effect is known as *white radiation*. The higher the voltage applied in the anode, the higher the intensity of the emitted X-rays, as can be seen in Figure 2. 8. Furthermore, as it can be appreciated in this figure, sharp peaks appear at certain frequencies. They are known as *characteristic lines* and only depend on the target material. These peaks correspond to the ejection of an electron from the inner shells of the target atom [32].

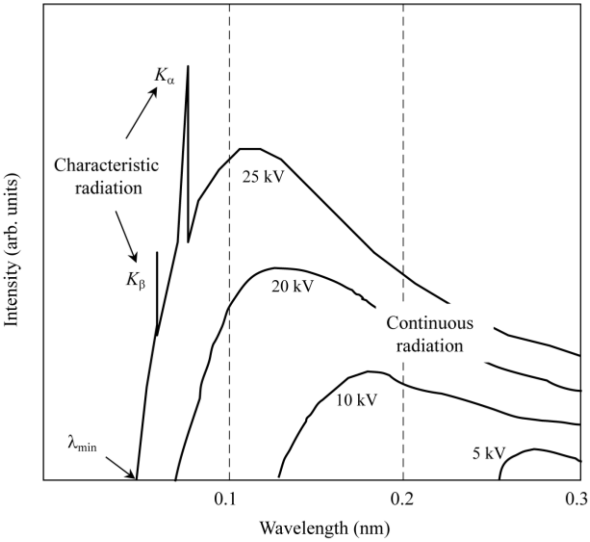

Figure 2. 8. X-Ray spectrum for a molybdenum target [32].

While the continuous radiation is caused by the loss of E_K of the electrons, the characteristic radiations are originated by the ejection of an electron of the inner shells of the target material. When an electron with enough energy impacts to the target material, an electron of the K shell can be ejected. Then, an electron from an outer shell can occupy this vacant, and there is an emission of an X-ray photon equal to the difference in energy. Then, the wavelength (i.e. the energy) of the radiation is defined by the specific transition of the electron between energy levels. For instance, the term α represents the transition between two adjacent levels, meanwhile in the case of *β* there is a two-level transition. Following this notation, K_α radiation is emitted when an electron from the L shell occupies the vacant in the K shell, whereas K_β radiation is emitted when the electrons travel from the M shell to the K one [32], [34].

In XRD experiments only the characteristic lines are used, except for the Laue method in which the white spectrum is required. K lines are the most interesting due to their wavelengths [32]. In Table 2. 4 the most characteristic lines of common targets are listed.

Table 2. 4. Characteristic lines' wavelength of common target materials.

	Cu	**Mo**	**Fe**	**Co**	**Cr**
K_α	1.542 Å	0.711 Å	1.937 Å	1.790 Å	2.261 Å
K_β	1.392 Å	0.632 Å	1.757 Å	1.621 Å	2.085 Å

The specific line can be selected by choosing the appropriate filter, whose absorption lies between K_α and K_β. Also, all elements produce two K_α lines: $K_{\alpha1}$ and $K_{\alpha2}$. As they have very similar wavelengths, they are often difficult to distinguish. $K_{\alpha1}$ has a shorter wavelength and about double intensity compared with $K_{\alpha2}$.

4.2. Radiation – matter interaction

When an electromagnetic wave encounters a material, different phenomena may occur depending on the characteristics of the material and the way the wave contacts the sample. When a wave is incident from the free space into the matter, its frequency remains unchanged but its speed v is reduced depending on the specific refractive index n of the substance (see Equation 2. 15).

$$n = \frac{c}{v} = \frac{\lambda_0}{\lambda} \qquad \text{Equation 2. 15}$$

where c and λ_0 are the speed and the wavelength of light in vacuum, whereas v and λ are the same magnitudes in the matter. Notice that when the wave travels through the vacuum, $n = 1$. Thus, as higher is n in the incident substance, slower will be the movement of the wave. Moreover, the difference of n between both media also determines how the light is refracted. Refraction is a phenomenon that occurs when light changes its propagation direction when crossing the boundary between two media.

This effect is described by the Snell's law of refraction, shown in Equation 2. 16.

$$n_1 \sin\theta_1 = n_2 \sin\theta_2 \qquad \text{Equation 2. 16}$$

where θ_1 and θ_2 are, respectively, the incidence and refracted angles. It is worth to notice that there is refraction ($\theta_2 \neq 0$) only if the incidence angle is different from zero, i.e. the waves do not arrive perpendicularly to the surface. Figure 2. 9 schematizes the principle described in Equation 2. 16. As can be seen, there is a fraction of the incident light that reflects with the same incident angle when encounters the surface. These processes are governed by Fresnel equations [35].

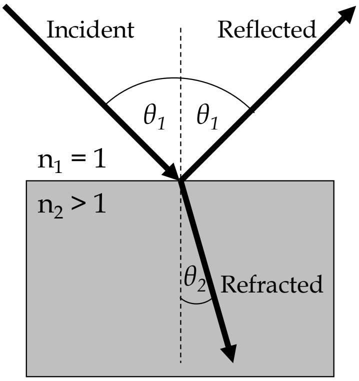

Figure 2. 9. Scheme of the phenomena occurring when a wave encounters an interface between two media. Adapted from [32].

Nevertheless, *n* is not a constant property and it varies with the frequency. All materials present n ≈ 1 at X-ray frequencies, what facilitates the analysis because the incident beam is not refracted in the interface.

When an electromagnetic wave propagates inside a material, each atom interacts with the primary wave front by splitting it into several beams traveling in specific directions. This phenomenon is known as *diffraction* and is based on the scattering of an incident beam by the atoms in the material. Scattering occurs in all directions, but the amplitude of the scattered waves depends on the direction.

The way diffraction occurs drastically changes depending on the arrangement of the atoms of the irradiated material. If the material under study has an amorphous structure, i.e. atoms are randomly distributed, diffraction occurs in all directions from each atom. Since the scattered rays have a randomly phase relationship, the scattering intensity is NE_0^2, where N is the number of scattered rays and E_0 the amplitude of the wave [32]. On the other hand, in crystalline materials – where atoms are periodically arranged in a set of discrete parallel planes – the diffracted waves may interact constructively at certain directions where they are perfectly in phase, whereas the destructive interference is predominant in the others. Thus, it will produce a pattern of peaks in specific directions, which will be determined by the way atoms are arranged in the material.

In 1913, W.L. Bragg and his father W.H. Bragg [36] published a simple mathematical condition for X-ray diffraction. They found that at certain wavelengths and incident angles, X-rays diffracted from crystals produced intense peaks, known as *Bragg peaks*. Furthermore, they proposed that these peaks corresponded to those diffracted waves with constructive interference, what happens when the difference in phase is a multiple of 2п. Figure 2. 10 shows a scheme of the principle proposed by Bragg.

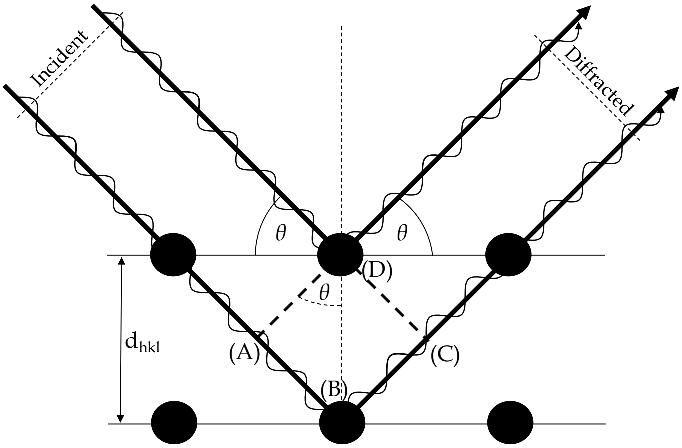

Figure 2. 10. Bragg's condition for X-ray diffraction. The interference of the diffracted waves must be constructive in order to produce a peak.

In this figure, it is possible to see how atoms are arranged in a simple but periodic way. Two waves, coming from the same X-ray beam, irradiate the crystalline material and, after scattering with the atoms, diffracted signals are produced to all the directions of the space. However, only for those in the specific direction (θ) shown in Figure 2. 10, the interference is constructive, and a peak is observed.

Deducing the condition for having constructive interaction becomes a geometrical problem. As incident X-rays are in-phase, the difference in path between both waves must be a multiple of the wavelength λ in order to remain in-phase. Then, $\overrightarrow{ABC}$ length for the lower wave must be a multiple of λ, in order to maintain the same phase as the upper wave after scattering with atom (D). With this consideration, and applying simple geometric calculations, *Bragg's law* is defined as Equation 2. 17:

$$n\lambda = 2d_{hkl}\sin\theta \qquad \text{Equation 2. 17}$$

where n is an integer, and d_{hkl} is the interplanar spacing between one specific family of planes with *{hkl}* indices. n indicates the order of reflection, i.e. the specific plane inside a determined family of planes. Thus, a n^{th} order reflection represents the reflection from the plane (*nh nk nl*) of the family of planes {*hkl*}. Here it is important to stress that the reflection corresponding to each order of reflection is equivalent: for instance,$\lambda = 2d_{001}\sin\theta_1 \equiv 2\lambda = 2d_{001}\sin\theta_2 \equiv \lambda = 2d_{002}\sin\theta_2$. For this reason, usually $n = 1$ is taken for practical reasons. On the other hand, d_{hkl} is defined by the crystal structure of the material, the lattice parameter (a) and, of course, the plane *{hkl}* under consideration. For example, for a cubic structure the d_{hlk} is defined by Equation 2. 18 [32], [34].

$$d_{hkl} = \frac{a}{\sqrt{h^2 + k^2 + l^2}} \qquad \text{Equation 2. 18}$$

Bragg's law gives information about the position where peaks appear in a specific structure. But, what about the intensities? Despite it is a function of many variables, it is mainly dependent on the arrangement and nature of atoms in the unit cell [32]. Furthermore, although Bragg's law may predict a peak at certain θ value, {001} family of planes do not show a peak in BCC structure. The reason is that there is an extra plane of atoms between the {001} planes with half-wavelength difference in path compared with the wave diffracting with atoms places in {001} planes: thus, the diffracted beams are 180° out of phase and their interference is completely destructive. Moreover, the nature of the atom must be also considered, as different atoms have different scattering strength.

When an electromagnetic wave – such as X-rays - encounters an atom, its varying electric field exerts a force on the electrons of the atoms, which start to oscillate around a mean position. As a consequence, these atoms emit *coherent scattered* radiation of the same frequency and wavelength as the primary beam. The intensity I of the radiation at specific point P, which is at a distance R from the electron is defined by *Thomson equation* (Equation 2. 19), which was postulated in 1906.

$$I = I_0\left(\frac{\mu_0 e^2}{4\pi m R}\right)^2\left(\frac{1+cos^2 2\theta}{2}\right) \qquad \text{Equation 2. 19}$$

where I_0 is the intensity of the primary beam, μ_0 is the magnetic permeability in vacuum ($4\pi \cdot 10^{-7}$ m kg C^{-2}), e is the electron charge, m is the electron mass, and 2θ is the angle between the incident radiation and the direction where scattering is observed. The term $(1+\cos^2 2\theta)/2$ is known as *polarization factor* for an unpolarised primary beam, and it is different if the beam is polarized. Although one may notice that the relative signal at a certain small distance is weak - what would complicate the detection of diffracted X-rays - it is worth to notice that this represents the intensity of the scattering produced by just one electron.

When the electromagnetic wave collides with an atom, the nucleus does not play any role in the scattering, and all this effect is only generated by its surrounding electrons. Hence, the net scattering effect is the sum of the waves scattered by each of the electrons. All the waves scattered in the same direction are in phase, but there is a phase difference between those waves traveling in different directions. The interaction between these waves leads to a reduction of the amplitude of the resulting signal. The ratio between the amplitude of the scattered wave by an electron and the amplitude of a wave scattered by the whole atom in the same direction is known as *atomic scattering factor f* [32], [34]. This factor is of importance as it is used to calculate the *structure factor F* for a given Bragg peak. This concept will be later defined.

In crystalline materials the atoms are periodically arranged in the space. If the interaction between the scattered waves at angle θ of the different atoms is out of phase, the peak may not appear despite Bragg's law is satisfied. Thus, the phase relationship between the scattered waves by individual atoms in the crystal structure is a dominant factor affecting the diffraction intensity. By considering each of the waves as a complex number with phase δ, and by adding the contribution of each of the scattered waves, the resulting scattered signal by all of the atoms of the unit cell is given by Equation 2. *20*.

$$F = f_1 e^{i\delta_1} + f_2 e^{i\delta_2} + \cdots + f_N e^{i\delta_N} \qquad \text{Equation 2. 20}$$

being F the structure factor and N the total number of atoms in the unit cell. For (*hkl*) reflection, it can be expressed as Equation 2. 21 [34], [37].

$$F_{hkl} = \sum_{n=1}^{N} f_n e^{2\pi i (hu_n + kv_n + lw_n)} \qquad \text{Equation 2. 21}$$

where f_n is the atomic scattering factor of the n^{th} atom, and u_n, v_n and w_n represent its coordinates. The magnitude of the resultant wave $|F|$ corresponds to the ratio of the amplitude of the scattered waves by all atoms in a unit cell, and the amplitude of the scattered wave by a single electron. As it is shown in Equation 2. *22*, the diffraction intensity is proportional to $|F|^2$ when Bragg's law is satisfied. Then, one can consider the position of the atoms for each crystal structure and predict which families of planes {*hkl*} will interact constructively and, consequently, will produce a diffraction peak. Therefore, the following rules can be deduced for each type of structure [32], [34]:

- CS: All families of planes are satisfied (there are not intermediate planes).
- FCC: All planes indices (*h*, *k* and *l*) must be even or odd.
- BCC: When the sum of (*h*+*k*+*l*) is even, scattered rays are in phase.

Following the criteria used before, lets now consider the arrangement of N unit cells forming a small single crystal. The diffraction intensity I_P from this small single crystal is defined by Equation 2. 22.

$$I_P = I_0|F|^2N^2 \qquad \text{Equation 2. 22}$$

This is the intensity corresponding to an ideal case, which obviously will not be the one experimentally measured. The presence of defects or systematic imperfections on the crystal, as well as instrumental factors, may broaden the observed diffraction profile.

The term *powder diffraction* refers to the use of XRD to analyse powder or microcrystalline samples [32]. This technique is mainly used for phase identification and quantification, what is often required in materials science. Here, instead of having a single crystal, an enormous number of small crystals are randomly oriented, and therefore a large number of grains are in the Bragg position at the same time [33]. Therefore, for every set of planes, there will be a small percentage of crystallites that are properly oriented to diffract. This method involves the use of monochromatic X-ray beam, usually Cu K_α.

4.3. Phase Identification and basic information extraction

4.3.1. Phase identification

Possibly, the most common use of powder XRD is the phase identification. In materials science research, it is crucial to identify the phases that form the substance under study, especially when working in synthesis or modifying the initial structure of a material.

The most common identification method relies on the comparison of the experimental pattern with a database with a large set of already known diffraction patterns. The first studies involving this phase identification method were published by J.D. Hanawalt [38], [39]. Each one on these patterns is known as Powder Diffraction File (PDF) and contains all the crystallographic information of the phase. Actually, the International Centre for Diffraction Data (ICDD) is the responsible of continuously updating the PDFs [33]. There are PDFs of a large number of different materials, from pure elements, to metals, alloys, or ceramics. Most of the PDFs are obtained with Cu K_α radiation, unless for those containing Fe because this element is extremely absorbent at the wavelength of Cu K_α [32].

Actually, there are powerful software which are able to compare the experimental patterns with these large databases. Each PDF contains a list with the expected 2θ positions and the relative intensity of each of the peaks for this phase, and they are compared with the positions and the intensities of the measured spectra. There are many methods for doing the comparison, but often the most intense peaks are first identified, and the software looks for PDFs which contains these peaks. Then, the system keeps comparing in decreasing intensity order [33]. A successful identification of a substance can be achieved by the comparison of the three most intense peaks [32], [33].

According to the above discussion, each crystal structure has a specific imprint when is characterized by XRD. When one or multiple PDFs are matched with the experimental pattern, the crystallographic information of each one can be obtained from each PDF. Thus, a correct phase identification may provide information about which are the phases that form the analysed substance and what their crystal structure is.

4.3.2. Semi-quantitative analysis

Once the crystalline phases present in the sample have been identified, it is possible to do some basic calculations to extract further information about the sample.

First, the relative presence of each phase can be deduced from the relative intensity of the peaks. It is not possible to do a direct relationship between the relative intensity of the peaks corresponding to one of the phases and the sample composition, because of the different absorption coefficients of each phase. One solution consists on introducing a known amount of a reference crystalline phase – which is not present in the sample – and to measure again the relative intensities. By considering the change in intensity due to a known reduction in composition, it is possible to approximate then the composition of the sample [33].

Nevertheless, another approach is often used in research. With high quality data, the *reference intensity ratio* (RIR) method becomes a fast tool to obtain semi-quantitative data. As commented in the first approach, the relative intensity (I_α/I_β) is proportional to the weight fraction of each phase ($X_{\alpha,\beta}$), according to Equation 2. 23 [40]. Here, instead of having to re-measure the sample with a reference material, the weight fraction of each phase is calculated from the relative intensity and the RIR coefficient provided in the PDF of each phase. This coefficient has been previously obtained by the author of the PDF by mixing the pure phase with a reference crystalline phase. Therefore, this constant of proportionality considers the absorption of each phase and allows to directly compare the relative intensity of the different phases in the sample. This facilitates the process as no further measurements are required.

$$\frac{I_\alpha}{I_\beta} = \frac{RIR_\alpha}{RIR_\beta}\frac{X_\alpha}{X_\beta}$$ Equation 2. 23

being α and β two different crystalline phases present in the powder sample.

4.3.3. Microstructural analysis

In addition to the intensity of the peaks, their width also provides interesting information about the microstructure of the analysed material. It is well known that – considering Voigt / pseudo-Voight functions – the diffraction profile width can be determined from Equation 2. 24 and Equation 2. 25 [41].

$$H_{Gh}^2 = H_{Gf}^2 + H_{Gg}^2$$ Equation 2. 24

$$H_{Lh} = H_{Lf} + H_{Lg}$$ Equation 2. 25

where H represents the *full width at half maximum* (also known as FWHM), G and L refer respectively to the Gaussian and Lorentzian contributions, while h, f, and g refer to the observed, intrinsic, and instrumental profiles.

The contribution of the sample to the peak width is calculated from the intrinsic factor. It can be obtained after comparing the observed and the instrumental profiles. The instrumental contribution can be obtained by measuring an appropriate reference sample – usually a large single crystal – which does not generate intrinsic peak broadening. Then, by fitting the experimental data with the Gaussian and Lorentzian distributions it is possible to deduce the two intrinsic factors that may generate peak broadening: crystal size and microstrains [41].

It has been previously demonstrated how the number of unit cells N in the crystal contributes to the intensity of the diffracted signal, but it also affects its widths. When N is lowered, the peak intensity decreases but the width increases, as shown in Figure 2. 11.

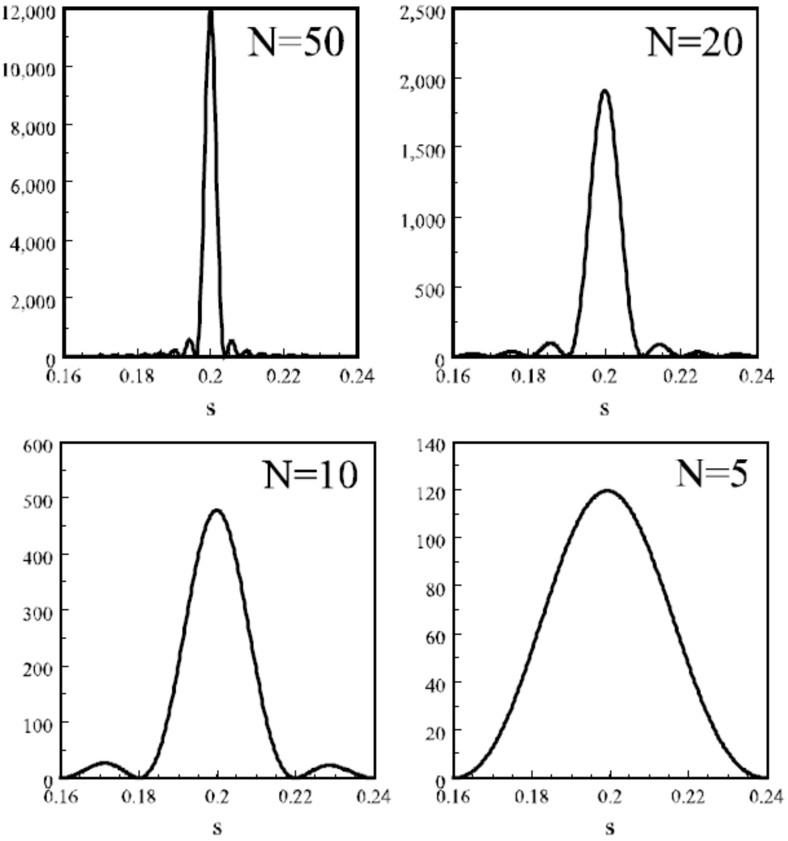

Figure 2. 11. Peak intensity and width as a function of the number of unit cells N in the crystal [33].

P. Scherrer, in 1918 [42], postulated the mathematical relationship between the intrinsic size peak broadening (β_L) due to the crystal size (L). The commonly known *Scherrer equation*, which is described in Equation 2. 26, states that the peak width is inversely proportional to the crystal size.

$$\beta_L = \frac{K\lambda}{L\cos\theta} \qquad \text{Equation 2. 26}$$

being K the *shape factor* or *Scherrer constant*, which is ~1.

On the other hand, the effect of microstrains was first published by A. R. Stokes and A. J. C. Wilson in 1942. Equation 2. 27 shows the Stokes-Wilson equation for peak broadening (β_ε) due to microstrain (ε).

$$\beta_\varepsilon = C\varepsilon \tan\theta \qquad \text{Equation 2. 27}$$

where *C* is a constant which is often assumed as 4.

With these equations it is possible to calculate the crystal size and the microstrains of the system from the peak broadening, but at this point one should be extremely careful of not using the FWHM value for each calculation. First, as has been commented before, it is crucial to remove the instrumental contribution by an appropriate calibration; then, the intrinsic peak width might be originated by both, size and strain effects. Notice that the dependence of width on size and on microstrain is $1/\cos\theta$ and $\tan\theta$, respectively. Thus, each contribution must be discriminated by using Fourier series to analyse the peak profile [33].

4.4. Rietveld refinement

The Rietveld method (H. M. Rietveld in 1969, [43]) was first designed as a refinement tool for crystal and magnetic structures measured by powder neutron diffraction, but it was rapidly extended to XRD. The use of Rietveld method in powder XRD has been a revolution in the methodologies for the quantitative phase analysis because of its wide range of options and reduced error sources. The novelty on Rietveld's conception is to operate with the intensity in each point of the profile and to compare it with a calculated intensity. By this way the whole profile is adjusted, what is an important improvement compared with classical methods which only consider one or few reflections. Moreover, its application has been favoured as it can be easily programmed [44].

Nowadays, Rietveld refinement method is used for applications such as:

- Refinement of crystal structures.
- Quantitative phase analysis and of the amount of amorphous phase.
- To reveal previously unknown structures.
- To approximate the crystal size and shape.
- To study the microstrain and stresses in the system.

The basic principle of Rietveld refinement is to minimize the difference between the observed intensities (y_i^{obs}) and the calculated ones (y_i^{cal}). Then, the parameter S_y in Equation 2. 28 must be minimized.

$$S_y = \sum_i w_i \left| y_i^{obs} - y_i^{cal} \right|^2 \qquad \text{Equation 2. 28}$$

being w_i the weight factor of each point.

The observed intensities are, of course, those experimentally measured, meanwhile the parameters in the calculated profile are constantly adjusted in order to fit them to the observed ones as best as possible. The calculated intensity in each Bragg position $2\theta_i$ is calculated as the sum of all the reflections k at this point, plus the background contribution [41], [44].

$$y_i^{cal} = b(2\theta_i) + S_\alpha \sum_k m_k |F_k|^2 \Omega(2\theta_i - 2\theta_k) Lp\,(2\theta_i) P_k \qquad \text{Equation 2. 29}$$

In Equation 2. 29, $b(2\theta_i)$ is the background contribution at this point, S_α is the scale factor of the pure phase α, k represents the Miller indices for an specific reflection, m_k is the multiplicity of the reflection k, $\Omega(2\theta_i\text{-}2\theta_k)$ describes the distribution of intensities around the Bragg position, $Lp(2\theta_i)$ contains Lorentzian and polarization correction values, and P_k is a function that contains the correction factors due to preferred orientation, absorption, and extinction coefficients. F_k is the structure factor, which has been previously defined in Equation 2. 21 and gives information about the reflection amplitude for each unit cell.

In case of having a sample with more than one phase, this equation may be modified as it is in Equation 2. 30, where m phases are considered.

$$y_i^{cal} = b(2\theta_i) + \sum_{i=1}^{m} S_i \sum_k m_k |F_k|^2 \Omega(2\theta_i - 2\theta_k) Lp\,(2\theta_i) P_k \qquad \text{Equation 2. 30}$$

From all these coefficients, the phase scale factor S_i is the one that adjusts the relative intensity between the different phases in the mixture as a function of their volume fraction. By considering the density of the mixture (ρ_m) and the density of one specific phase α (ρ_α), the scale factor can be expressed as in Equation 2. 31 [44].

$$S_\alpha = \frac{W_\alpha}{\rho_\alpha} K \frac{\rho_m}{2\mu_m} \qquad \text{Equation 2. 31}$$

where W_α is the weight fraction of the phase α, and K is a constant that does not depend on the sample. Density values are calculated considering the volume of the unit cell V, the number of molecules per unit cell Z, and the molecular mass M.

It is important to have in mind that the sum of the weight fractions of all the phases must be the unit, i.e. $\sum W_i = 1$. Then, the weight fraction of each phase may be calculated from the scale factor of each phase obtained from the refinement, and the corresponding calculated density. For instance, considering a n-phases system, the weight fraction of one of the phases is calculated by Equation 2. 32. This is the parameter to be obtained – for each phase - when the goal is to do quantitative analysis.

$$W_\alpha = \frac{S_\alpha \cdot \rho_\alpha}{\sum_{j=1}^{n} S_j \cdot \rho_j} = \frac{S_\alpha \cdot (ZMV)_\alpha}{\sum_{j=1}^{n} S_j \cdot (ZMV)_j} \qquad \text{Equation 2. 32}$$

Calculating properly the 2θ positions and the relative intensities of the peaks is of great importance in order to extract, respectively, structural and compositional information. Nevertheless, as it has been stated before, the shape of the peaks can reveal interesting information regarding the crystal size and residual stresses in the structure. Thus, considering the appropriate peak shape is a key step when refining the profile. Moreover, it must be taken into account that - contrary to what happens in traditional methods where just one peak is fitted - the peak shape may change along the profile as a function of 2θ. There are different functions which can be used, but here focus on the pseudo-Voigt distribution, which is the most common, and it has a Gaussian and a Lorentzian contribution [44]. The contribution of each distribution is defined by the parameter η. This parameter can have values between 0 and 1: when η is close to 0, the Gaussian contribution is predominant; when η tends to 1, it is closer to a Lorentzian function. The Gaussian component (H_G) is shown in Equation 2. 33.

$$H_G^2 = U\tan^2\theta + V\tan\theta + W + \frac{P}{\cos^2\theta} \qquad \text{Equation 2. 33}$$

where U, V and W are the classical Caglioti [45] parameters that depend on instrumental contribution. In modern diffractometers, where resolution is high, the Gaussian contribution is low. Furthermore, when refining high quality data of crystalline samples it is enough to refine only the W parameter [44]. On the other hand, P is a parameter that considers the Scherrer broadening due to crystal size.

The Lorentzian contribution, which is much more dependent on the sample contribution than the Gaussian one, is defined in Equation 2. 34:

$$H_L = X\tan\theta + \frac{Y}{\cos\theta} \qquad \text{Equation 2. 34}$$

where X is the parameter considering the microstrain in the material, and Y the one due to the size of the crystals.

There are different parameters to evaluate the quality of the fit between the observed intensities and the calculated ones [41], [44]. The most relevant ones for this work are presented below.

First, the *weight profile R-factor* (R_{WP}) is probably the most used and is defined by Equation 2. 35. The calculation is performed for all the points in the profile.

$$R_{WP}(\%) = 100 \cdot \sqrt{\frac{\sum_{i=1}^{n} w_i\left(y_i^{obs} - y_i^{cal}\right)^2}{\sum_{i=1}^{n} w_i\left(y_i^{obs}\right)^2}} \qquad \text{Equation 2. 35}$$

The evolution of this parameter during the refinement is of great interest as it shows if the changes in the model are improving the refinement or not. On the other hand, one should consider that this factor may not be completely representative of the adjustment of the reflections, as it also considers the background. The R_P and R_F disagreement factors are similar approximations in which the absolute differences of the non-weighted intensities y_i and the structure factors F_k are computed, respectively.

Ideally the R_{WP} value should be close to the *expected R-factor* (R_{exp}), which can be calculated by Equation 2. 36.

$$R_{exp}(\%) = 100 \cdot \sqrt{\frac{N - P + C}{\sum_{i=1}^{n} w_i \left(y_i^{obs}\right)^2}} \qquad \text{Equation 2. 36}$$

where N is the number of independent observations, P the number of refined parameters, and C the number of restricted equations in the refinement. The quotient between R_{WP} and R_{exp} is called *goodness of fit* ($\chi2$) (see Equation 2. 37).

$$\chi^2 = \frac{R_{WP}}{R_{exp}} \qquad \text{Equation 2. 37}$$

Finally, another interesting factor is the *intensity R-factor* (R_I) or *Bragg R-factor (R_B)*, which computes the difference in intensities of the reflections I_i. This factor is defined in Equation 2. 38.

$$R_I(\%) = R_B(\%) = 100 \cdot \frac{\sum_{hkl} \left| I_i^{obs} - I_i^{cal} \right|}{\sum_{hkl} I_i^{obs}} \qquad \text{Equation 2. 38}$$

5. NANOMECHANICS

Mechanical properties are determined by the chemical composition and crystal structure of the materials. In many applications, mechanical properties play a capital role, even more than the primary functional property (electrical, optic or biological, for instance) because this is the one that determines if the material can operate under certain conditions without failure [2].

More specifically, indentation or hardness (*H*) testing has been widely used as a characterization and quality control method of materials. In this test, a hard tip with known mechanical properties touches the material under interest, whose properties are unknown [46]. The output H is a measure of the relative penetration depth of the indenter into the sample under a certain load P [47]. Furthermore, indentation methods may provide information about other mechanical properties than H by properly controlling and studying the loading, unloading, and the residual impression on the sample.

5.1. Mechanical properties of materials

Before starting to discuss the technical aspects of nanoindentation test, it is important to first have some important concepts in mind. Here, some basic concepts about the mechanical properties and behaviour of materials are presented.

5.1.1. Elastic behaviour

The strength of a material is related with the strength of the chemical bonds between atoms. The electrostatic Coulomb repulsion at short distances is compensated by the long-range attractions due to the lower energy states that arise due to filling of electrons shells, leading in an equilibrium position with the lower potential energy. The necessary force (F) to separate one atom from another depends on the specific chemical bond nature, but generally there is the linear force-distance relationship shown in Equation 2. 39.

$$F = kx$$ Equation 2. 39

where x is the distance, and k the proportionality constant. This law, commonly known as *Hooke's Law*, works well for very short distances, but for higher deformations the behaviour is influenced by neighbouring atoms and bulk character. The constant of proportionality k depends on intrinsic values of the material, such as the maximum force required to break the chemical bond (F_{max}), or the distance from the equilibrium position (L) [48]. This relationship is represented in Equation 2. 40.

$$F = \left[\frac{F_{max}\pi}{2L}\right]x \qquad \text{Equation 2. 40}$$

Then, by considering the force distributed over a unit area (σ) and the strain produced ($\varepsilon = x/L_0$), this expression leads to Equation 2. 41.

$$\frac{\sigma}{\varepsilon} = \left[\frac{L_0\pi\sigma_{max}}{2L}\right] = E \qquad \text{Equation 2. 41}$$

being σ_{max} the *tensile strength* of the material. Everything inside the brackets is a constant that depends on the material, and thus can be represented by the *elastic modulus* or *Young's modulus* (E). This modulus represents the stiffness of the material, i.e. the constant of proportionality between the stress and strain. This proportionality is present until a maximum strain value, known as *yield strength* (σ_Y), where the plastic deformation starts.

When a longitudinal stress is applied to a material there is a lateral contraction as the material tries to keep a constant volume. The ratio between the lateral ($\varepsilon_{\perp}$) and longitudinal ($\varepsilon_{\parallel}$) deformations is considered in the *Poisson's ratio* (ν), which is defined in Equation 2. 42. This parameter can reach a maximum value of 0.5 [48].

$$\nu = \frac{\varepsilon_{\perp}}{\varepsilon_{\parallel}} \qquad \text{Equation 2. 42}$$

Once E and ν are known, it is possibly to define the *shear modulus* (G) and the *bulk modulus* (K), which are respectively represented in Equation 2. 43 and Equation 2. 44. The first indicates the resistance of the material to shear stress, while the second is a measure of its compressibility.

$$G = \frac{E}{2(1+\nu)} \qquad \text{Equation 2. 43}$$

$$K = \frac{E}{3(1-2\nu)} \qquad \text{Equation 2. 44}$$

5.1.2. Plasticity

If the applied stress is higher than the yield strength, then the deformation is irreversible. In this regime, the material exhibits strain ε at constant stress σ; the total ε depends on the length of time the stress is applied, leading in a *plastic flow* [48]. The resistance to flow is determined by the *viscosity coefficient* (η), as defined in Equation 2. 45.

$$\sigma_{zy} = \eta \frac{d\gamma_{zy}}{dt}$$ Equation 2. 45

where γ is the *sharing angle*, i.e. the change in angle between two planes (z, y) that were initially orthogonal. Then, the rate of change of strain in each direction of the space can be expressed by Equation 2. 46, Equation 2. 47, and Equation 2. 48.

$$\dot{\varepsilon}_x = \frac{1}{2\eta}[\sigma_x - \sigma_m]$$ Equation 2. 46

$$\dot{\varepsilon}_y = \frac{1}{2\eta}[\sigma_y - \sigma_m]$$ Equation 2. 47

$$\dot{\varepsilon}_z = \frac{1}{2\eta}[\sigma_z - \sigma_m]$$ Equation 2. 48

being σ_m the mean stress.

5.1.3. Fracture mechanics

This field of mechanics studies the resistance of a materials to fracture, i.e. its *toughness*. In real world, bulk materials do not have an ideal and continuous structure, but there are usually cracks, notches or corners that tend to concentrate stresses. The *stress concentration factor* κ is defined by Equation 2. 49, and gives information about the increase of stress in an elliptical hole inside a material [48].

$$\kappa = 1 + 2\sqrt{\frac{c}{\rho}}$$ Equation 2. 49

where c is the hole radius, and ρ is the radius curvature of the tip of the hole. Notice that for a narrow elliptical hole, κ may be much greater than one. The minimum crack length that is not self-propagating, known as *critical crack length* (c_c), is defined in Equation 2. 50. This will not happen until the strain energy rate becomes equal to the surface energy requirement.

$$c_c = \frac{2\gamma}{\pi\sigma_a^2}$$ Equation 2. 50

where σ_a is the applied stress, and γ is the *fracture surface energy* of the solid, which is usually greater than the intrinsic surface energy due to dissipative mechanisms around the crack tip [48].

In 1957, George R. Irwin [49] formulated that the stress field in the vicinity of an infinitely sharp crack tip depends on the magnitude of the stress and its distribution. The magnitude of the stress is defined by the *stress intensity factor* (K_I), described in Equation 2. 51.

$$K_I = \sigma_a Y\sqrt{\pi c}$$ Equation 2. 51

where c is the crack semi-length, and Y is a geometry factor constant for a specific crack system: therefore, the magnitude of the stress only depends on σ_a and $\sqrt{c}$. There is a critical value for K_I (known as K_{IC}) which characterizes the fracture strength of each material. Thus, K_{IC} provides quantitative information of the *toughness* of materials. When $K_I = K_{IC}$, the energy balance is satisfied and the crack may extend [48].

5.2. Nanoindentation

Nanoindentation is an indentation technique in which the penetration is of the order of magnitude of nanometres, instead of micrometres or millimetres as in conventional hardness tests. Moreover, another peculiarity is the indirect method for measuring the contact area, i.e. the area of contact between the indenter and the sample [46]. In this case, it is not needed to visualize the imprint, what simplifies the extraction of mechanical properties [47]. Furthermore, this is a depth-sensing technique, what means that it is possible to obtain the mechanical properties as a function of the indentation depth.

Additionally to H, nanoindentation may also be used to calculate E, K_{IC}, and viscoelastic properties [46]. These mechanical properties are measured from submicron indentations with small deformation volumes associated, which allow to do a really local characterization of the material. Moreover, the amount of load P used in the measurement does not only affects to the size of the deformed region, but also on the elastic-plastic response and the atomic mechanisms of deformation [47].

A typical nanoindentation test consists of two stages that are represented in Figure 2. 12.A: loading and unloading. First, the tip is placed into contact with the flat surface of the specimen and then the load P continuously increases. During this loading process, the material responds elastically at the beginning and plastically at higher loads. The load and the penetration are continuously recorded until reaching the maximum load (P_{max}). Then, the load is removed and, if the yield has occurred, a residual impression is left in the specimen surface (h_r). The depth of penetration for a particular load, together with the slope of the unloading curve (dP/dh) measured as the tangent at P_{max}, allow to determine the H and E of the sample [46]. In the case of a viscoelastic material (Figure 2. 12.B), there is not a linear dependence between the applied load and the strain. As has been previously introduced, the penetration depends on the load application rate, as well as the magnitude of the load itself. Nanoindentation allows to determine the solid (or liquid) like behaviour of the sample. Finally, in the case of brittle materials cracking may occur (see Figure 2. 12.C), especially when using pyramidal indenters. The length of these cracks can be used to calculate the K_{IC} [46].

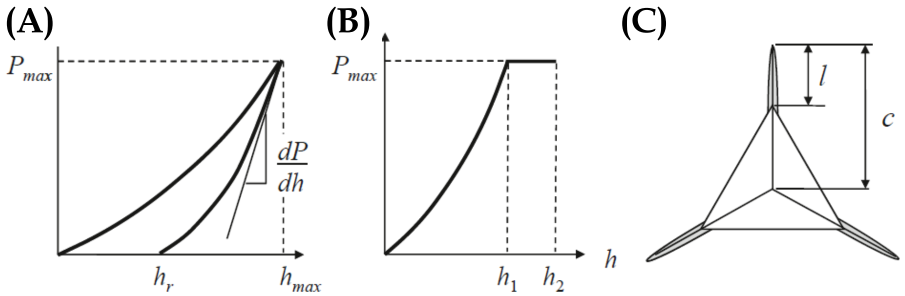

Figure 2. 12. *P-h* curve for (a) elastic – plastic solid, and (b) viscoelastic solids, and (c) cracks from the corners of the residual impression in a brittle material [46].

5.2.1. Contact mechanics

The interest upon depth-sensing indentation techniques is continuously increasing, with the principal goal of extracting the hardness H and the elastic modulus E of the material. The forces involved for performing these measurements are in the range of milinewtons (10^{-3} N), with a resolution of few nanonewtons (10^{-9} N), while penetration depths are of some microns (10^{-6} m), with a resolution of less than a nanometre (10^{-9} m) [46].

H. Hertz [50], [51] first related the elastic properties of the tested material with the *contact circle radius* a, the indenter radius R, and the applied load P. This relationship is expressed in Equation 2. 52.

$$a^3 = \frac{3}{4}\frac{PR}{E_{eff}}$$ Equation 2. 52

The term E_{eff} is known as *reduced modulus* or *effective modulus* and combines the elastic moduli of the indenter and the specimen. It is defined as:

$$\frac{1}{E_{eff}} = \frac{(1-\nu^2)}{E} + \frac{(1-{\nu_i}^2)}{E_i}$$ Equation 2. 53

where the subscript i corresponds to the indenter properties. The assumption that the indenter has or not a rigid behaviour, as well as the tip geometry, changes the way the tip contacts the specimen. In Figure 2. 13 it is possible to see how these variables affect the contact.

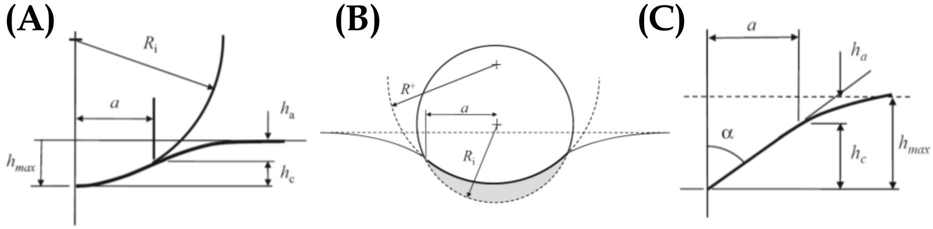

Figure 2. 13. Indenter – sample contact with a spherical tip assuming a (A) rigid indenter and a (B) non-rigid indenter, and (C) a conical indenter. Figures obtained from [46].

Here, h_c refers to the *penetration contact depth*, R_i to the spherical indenter radius, and R^+ to the *equivalent indenter radius* when it is assumed to be non-rigid. R^+ depends on the applied P and the E and ν of the sample material [46].

In a classical test, the parameters that must be measured are [47]: i) maximum applied load, P_{max}; ii) maximum penetration depth, h_{max}; iii) *final penetration depth*, h_f; and iv) the elastic unloading stiffness, S. The analysis of the P-h curves is different if it is a loading curve (which can be elastic or elasto-plastic) or an unloading curve (where elastic recovery happens). Figure 2. 14 shows the scheme of the unloading process used for the calculation of H and E considering that a Berkovich tip can be modelled as a conical indenter.

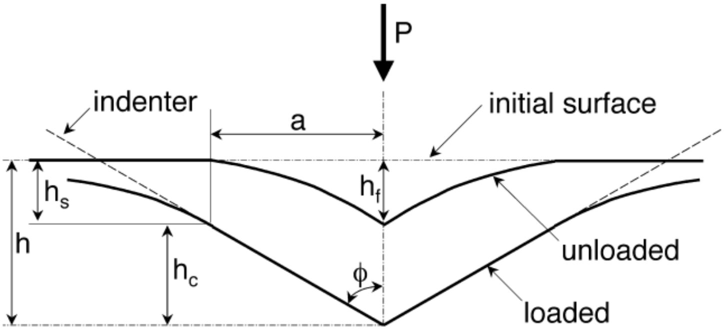

Figure 2. 14. Scheme of the unloading processes with a conical indenter indicating the parameters used to characterize the contact geometry [52].

The *H* and *E* are calculated from the unloading curve as a function of the penetration depth using the Oliver and Pharr method [52]. In elastic models the total amount of sink-in h_s is defined as:

$$h_s = \varepsilon \frac{P}{S} \qquad \text{Equation 2. 54}$$

where ε parameter depends on the indenter geometry, and *S* is the S*tiffness*, which is the curve slope (*S*=*dP/dh*). The penetration contact depth h_c can then be calculated as the difference between the maximum and the skin-in depths.

$$h_c = h_{max} - h_s = h_{max} - \varepsilon \frac{P}{S} \qquad \text{Equation 2. 55}$$

Once these depth parameters are defined, the *projected area A* of the indentation may be calculated. It depends on the specific intender tip used in the test. In Table 2. 5 the equations to calculate *A* for each type of indenter type are defined.

Table 2. 5. Projected area and semi-angle contact of each kind of indenter tip. Values extracted from [46].

Indenter type	Projected area, A	Semi-angle θ (deg)
Sphere	$\pi 2Rh_c$	N/A
Berkovich	$3\sqrt{3}h_c^2\tan^2\theta$	65.27
Vickers	$4h_c^2\tan^2\theta$	68
Knoop	$2h_c^2\tan\theta_1\tan\theta_2$	θ_1=86.25, θ_2=65
Cube corner	$3\sqrt{3}h_c^2\tan^2\theta$	35.26
Cone	$\pi h_c^2\tan^2\alpha$	α

where α represents the cone semi-angle, which depends on the tip geometry.

The accurate determination of S and A is crucial for the characterization of E and H. Oliver and Pharr method [52] starts fitting the unloading curve to a power-law relation, as described in Equation 2. 56.

$$P = BA\left(h - h_f\right)^m \qquad \text{Equation 2. 56}$$

where B and m are the power law fitting parameters [53]. Considering that $S = dP/dh$ at $h = h_{max}$, then:

$$S = Bm\left(h_{max} - h_f\right)^{m-1} \qquad \text{Equation 2. 57}$$

Once these two parameters (S and A) are determined, E_{eff} can be easily calculated by means of Equation 2. 58.

$$E_{eff} = \frac{1}{2}\frac{dP}{dh}\frac{\sqrt{\pi}}{\sqrt{A}} = \frac{1}{2}S\frac{\sqrt{\pi}}{\sqrt{A}} \qquad \text{Equation 2. 58}$$

From the analysis of the slope of the load–depth curve, and by applying Equation 2. 58 it is possible to deduce the reduced modulus E_{eff}. Then, by means of Equation 2. 53, the elastic modulus of the sample may be obtained. In this calculation, the Poisson's coefficient ν of the tested material is assumed to be known.

Hardness H can be calculated as the ratio between the maximum applied load P_{max} and the projected area A.

$$H = \frac{P_{max}}{A(h_c)}$$ Equation 2. 59

In contrast with the expression in Equation 2. 59, where P_{max} and A are used, Vickers hardness (H_v) is measured from the residual imprint after unloading. This last approximation leads to error due to the elastic relaxation that occurs after unloading. This phenomena can be especially relevant in ceramic materials [47].

Considering all the above exposed, the typical procedure to analyse the elastic curve consists on the following steps [54]:

- Plot the *P-h* curve. The initial loading part of the curve may be successfully fitted with the Hertz equation; any deviation from this behaviour would indicate an elasto-plastic transition.
- Determine the contact point. The contact radius a can be calculated by means of Equation 2. 60.
- Plot the indentation σ-ε curve by using Equation 2. 61. The left hand of the equation corresponds to the indentation stress (known as Meyer's hardness), and the term in the parenthesis in the right side refers to the indentation strain.

$$a = \sqrt{2R_i h_c - h_c^2}$$ Equation 2. 60

$$\frac{P}{\pi a^2} = \frac{4}{3\pi} E_{eff} \left(\frac{a}{R_i}\right)$$ Equation 2. 61

Indentation tests will usually result in both elastic and plastic deformation of the tested material. In brittle materials, plastic deformation usually occurs when using pointed indenters (such as Vickers diamond pyramid), meanwhile in ductile materials plastic deformation can be induced by a "blunt" indenter (as an sphere or cylinder, for instance) [46], [47].

5.2.2. Fracture toughness

When nanoindentation tests are performed on brittle materials, such as ceramics, cracking of the material can occur emerging from the corners of the imprint [54]. The length of these cracks and the applied load are related with K_{IC}. Despite that Vickers is the most common indenter, cube-corner is used to produce cracks at small loads due to its more acute angle. Pharr [55] proposed the following relationship for a cube corner indenter.

$$K_{IC} = \xi_R \left(\frac{E}{H}\right)^{\frac{1}{2}} \frac{P}{c^{\frac{3}{2}}} \qquad \text{Equation 2. 62}$$

being c the crack length measured from the centre of the indenter corners, and ξ = 0.016. Nevertheless, Laugier formulation [56] works better for high K_{IC} materials.

$$K_{IC} = \chi^p \left(\frac{l}{a}\right)^{\frac{-1}{2}} \left(\frac{E}{H}\right)^{\frac{2}{3}} \frac{P}{c^{\frac{3}{2}}} \qquad \text{Equation 2. 63}$$

where l represents the crack length measured from the indentation corners, a is half of the diagonal of the indentation imprint, and X^p is a constant which depends on the indenter type.

5.3. Equipment – Nanoindenter

Nanoindentation instruments typically measure the penetration depth using an inductance or capacitance displacement sensor with a resolution less than 0.1 nm. The applied force may be of several nanonewtons, which can be electrostatically applied, by the expansion of a piezoelectric element, or the movement if a coil in a magnetic field [46].

In order to have a high degree of control and to apply the load in a continuous and smooth manner, nanoindenters use electromagnetic load coils instead of the traditional dead weight systems. The indenter is supported by springs to prevent lateral movement, with a permanent magnet or an electromagnet on the top. When current is applied, the electromagnet generates a magnetic field that interacts with the permanent magnet and the indenter is forced towards the sample. Other methods consist on producing an electrostatic attraction between multiple parallel plates, or via the expansion of a PZT ceramic elements when a voltage is applied. The applied force is rarely directly measured; often the applied voltage is measured, and the one needed for deflecting the support string is subtracted. To have a precise control over the applied force, it is needed to do an appropriate calibration by measuring the current needed to move the indenter without touching the sample. On the other hand, the displacement is measured with sensors based on two or three place capacitors, or a variable differential transformer (also known as LVDT). These sensors achieve sub-nanometer resolutions. Then, the contact point with the sample is determined as the depth point where the force sensor makes contact. Finally, samples are placed in a XY stage, which has a stepper motor to move in both directions in a controlled manner. This movement allows to indent different places in the sample and, thus, allows to indent large sets of indentations in defined positions [46]. Figure 2. 15 shows a general scheme of the arrangement of all these components in a nanoindenter.

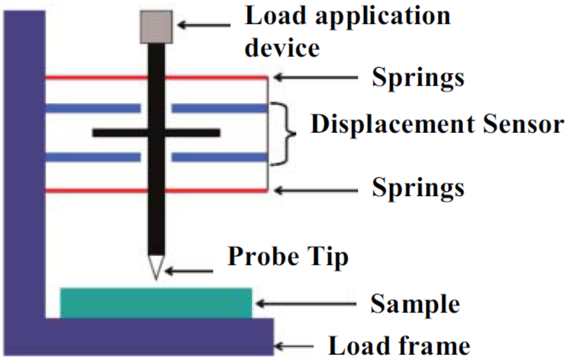

Figure 2. 15. Schematic representation of the different components in a nanoindenter [47].

5.4. Indenter geometries

As it has been previously introduced, there are different types of indenter tips which produce different deformations and interactions with the tested material. Moreover, the projected area A – which is needed for the calculation of H and E – is a function of the type of indenter used.

There are three main categories of indenters [46], [47]:

- **Spherical.** The contact stress is initially small and produces only elastic deformation. Later, the elastic-plastic transition occurs, and the full σ-ε curve can be recreated.
- **Conical.** Interesting due to the high concentration of σ at the edge. On the other hand, their use is limited in nanoindentation due to their difficulty to be fabricated.
- **Pyramidal.** The basic structure of these indenters is a three or four-sided pyramid. The number of sides and their relative angles lead to different types of pyramidal indenters:
    - Vickers. This a square diamond pyramid indenter specially used in micromechanical works.
    - Berkovich. It is a three-sided pyramid with the same depth-to-area relation as the four-sided Vickers pyramid. This is the more common indenter used because of its precise control over the indentation process. It is used for the calculation of E, H and K_{IC}.
    - Cube-corner. This is a three-sided pyramid with mutually perpendicular faces arranged, as in the corner of a cube. It has a sharper corner compared with other pyramidal tips, which produce higher σ and ε in the contact region. This is useful to produce well defined cracks to estimate K_{IC}.
    - Knoop. It has almost the same geometry as the classical Vickers indenter with the main difference that it has unequal edges, resulting in two different diagonal lengths. This is an interesting option for measuring very hard materials, because the length of the diagonal is more easily measured.

Figure 2. 16 shows a schematic representation of the three main families of indenters. On the other hand, Figure 2. 17 shows three SEM images of

the more common pyramidal indenters, where the difference in the edge angle can be clearly appreciated.

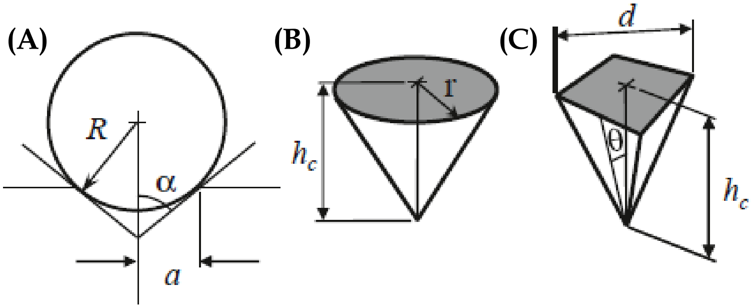

Figure 2. 16. Schematic representation of (A) spherical, (B) conical, and (C) pyramidal indenters. The pyramidal indenter corresponds, on this case, to a Vickers tip [46].

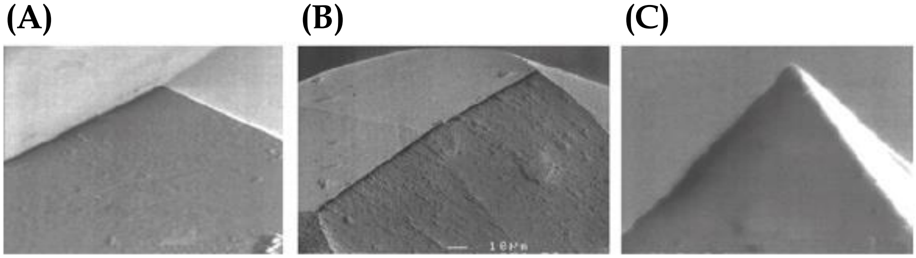

Figure 2. 17. SEM images of (A) Berkovich, (B) Knoop, and (C) cube-corner indenters [46].

6. MAGNETISM

6.1. Magnetic moment

The elemental entity in magnetism is the magnetic moment dm, which in terms of electromagnetism may be equivalent to a current I around an oriented loop of area |dS|. It is also equivalent to a magnetic dipole, which consists in two monopoles of opposite magnetic charge separated by a small distance along the direction of the vector dS. The magnetic moment dm is normal to the plane of the current loop and its orientation depends on the direction of the electrical current. The total magnetic moment *m* in loop of finite size can be calculated by using Equation 2. 64 [57], [58].

$$m = \int dm = I \int dS$$ Equation 2. 64

The electron is an elementary particle with two different sources of angular momentum: one associated with the orbital motion around the nucleus (*angular momentum*, $\ell = m_e r \times v$), and the other is the spin (*s*, which can take values of ± ½) [59]. These two sources of angular momentum are computed in the *total angular momentum quantum number* (*J*), which is defined in Equation 2. 65.

$$J = s + \ell$$ Equation 2. 65

According to the Bohr model (see Figure 2. 18), an electron (with charge –*e* and mass m_e) circulating on its orbit at a distance *r* and velocity *v* is equivalent to a current loop of opposite direction. The magnetic moment associated *m* can be expressed as [59]:

$$m = -\frac{e}{2m_e}\ell$$ Equation 2. 66

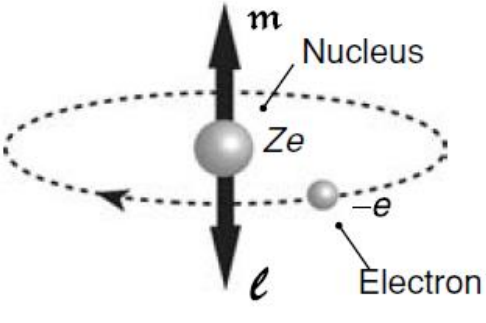

Figure 2. 18. The Bohr atoms. The electron moves in circular orbit around the nucleus [59].

The constant term $-(e/2m_e)$ is known as *gyromagnetic ratio* (γ). Thus, the proportionality between m and ℓ can be expressed as in Equation 2. 67. This relationship is demonstrated by the Einstein-de Haas effect [60], [61], which is a rotation effect induced by magnetization.

$$m = \gamma\ell$$ Equation 2. 67

Despite protons, neutrons, and electrons have all an intrinsic angular momentum $\frac{1}{2}\hbar$ (where $\hbar$ is Plank's constant h divided by 2π), the nuclear magnetism (μ_p) can be often neglected and are the electrons (μ_e) the main source of magnetic moment in solids, as $\mu_p = \frac{\hbar}{2}\frac{e}{m_p} \ll \mu_e = \frac{\hbar}{2}\frac{e}{m_e}$.

If we consider a single electron describing a circular orbit around the nucleus, the magnetic moment of the electron is:

$$m = -\frac{e\hbar}{2m_e} = -\mu_B$$ Equation 2. 68

where μ_B is the *Bohr magneton* ($9.274 \cdot 10^{-24}$ Am^2) and is a useful unit to describe the atomic magnetic moment.

When a magnetic field B is applied, the magnetic moment m rotates around the field direction with a deviation of θ, in a movement commonly known as *precession*. The energy E of a magnetic moment is defined by Equation 2. 69. Notice that the energy minimizes when the magnetic moment lies along the field direction [57].

$$E = -m \cdot B = -mB\cos\theta$$ Equation 2. 69

The frequency at which m rotates around B is called as *Larmor precession frequency (ω_L)*, which depends on γ as described in Equation 2. 70.

$$\omega_L = \gamma B$$ Equation 2. 70

The *magnetization* (M) is defined as the magnetic moment per unit volume. Its vector quantity is considered a continuum approximation of the individual atomic moments. Then, M can be considered a smooth vector field which is continuous everywhere unless in the borders of the material. In free space there is no magnetization, and:

$$B = \mu_0 H \qquad \text{Equation 2. 71}$$

where H is the *magnetic field strength*. B and H are related by μ_0, which is the *magnetic permeability of the free space* ($4\pi \cdot 10^{-7}$ Hm^{-1}). In a magnetic material, which magnetizes when B is applied, this relationship is not as direct and M must be considered [57]–[59].

$$B = \mu_0 (H + M) \qquad \text{Equation 2. 72}$$

For the simplest materials, which are isotropic and homogeneous, M may be directly proportional to H, as described in Equation 2. 73.

$$M = \chi H \qquad \text{Equation 2. 73}$$

being χ a dimensionless quantity known as *magnetic susceptibility*. Then, a linear relationship between B and H may be defined.

$$B = \mu_0 (1 + \chi) H = \mu_0 \mu_r H = \mu H \qquad \text{Equation 2. 74}$$

where μ is the *magnetic permeability*, and $\mu_r = \mu / \mu_0 = 1 - \chi$ is the *relative magnetic permeability* of the material [57], [59].

By analysing the magnetic susceptibility, it is possible to differentiate two main magnetic behaviours: paramagnetism (χ>0) and diamagnetism (χ<0). Diamagnetic materials are those that magnetize oppositely to the applied magnetic field that caused it. This is an entire quantum mechanics phenomenon in materials with no unpaired electrons, which increases with the number of electrons in the outer shell of an ion. This effect is present in all materials, but it has a weak effect and it tends to be ignored. On the other hand, paramagnetic materials align parallel to the applied field. In this case, it appears in atoms that have a net magnetic moment due to unpaired electrons. The random orientation of these magnetic moments in a solid ends with the application of a magnetic field, which lines them up [57].

When J is a positive integer or a half-integer, the magnetization in a paramagnetic material is well defined by the *Brillouin function $B_J(y)$*, as expressed in Equation 2. 75 [57], [59]:

$$M = M_s B_J(y) \tag*{Equation 2. 75}$$

where M_S is the *saturation magnetization*, i.e. the maximum magnetization than can be achieved when all the magnetic moments are aligned. This magnitude can be considered as $M_S = ng\mu_0 J$, where n denotes the number of magnetic moments per unit volume and g refers to the *g-factor*. Then, the *Brillouin function $B_f(y)$* can be defined as:

$$B_J(y) = \frac{2J+1}{2J}\coth\left(\frac{2J+1}{2J}y\right) - \frac{1}{2J}\coth\frac{y}{2J} \tag*{Equation 2. 76}$$

being $y = g\mu_0 JB/k_B T$.

In 1905, Paul Langevin postulated the classical theory of paramagnetism, which is in the limit of quantum theory ($J \rightarrow \infty$) [57], [59]. It considers a set of atoms or particles with macroscopic magnetic moment m, which can take any orientation relative to the applied field. *Langevin function, $L(y)$,* is defined in Equation 2. 77.

$$L(y) = \coth y - \frac{1}{y} \tag*{Equation 2. 77}$$

where $y = \mu B/k_B T$, and k_B is the Boltzmann constant ($1.38 \cdot 10^{-23}$ m^2 kg s^{-2} K^{-1}). The saturation magnetization can be defined as $M_S = n\mu$. Then, the ratio of the magnetization to the saturation magnetization is:

$$\frac{M}{M_S} \approx \frac{\mu B}{3k_B T} \tag*{Equation 2. 78}$$

Finally, by considering that $\chi = M/H \approx \mu_0 M/B$, we have:

$$\chi = \frac{n\mu_0\mu^2}{3k_BT}$$ Equation 2. 79

This expression demonstrates that χ is inversely proportional to the temperature, which is known as *Curie's law*.

Figure 2. 19 shows a comparison of two *B_J(y)* functions, considering J = ½ and J = 2, compared with the *L(y)* function. Here it is clearly seen that $B_\infty(y) = L(y)$.

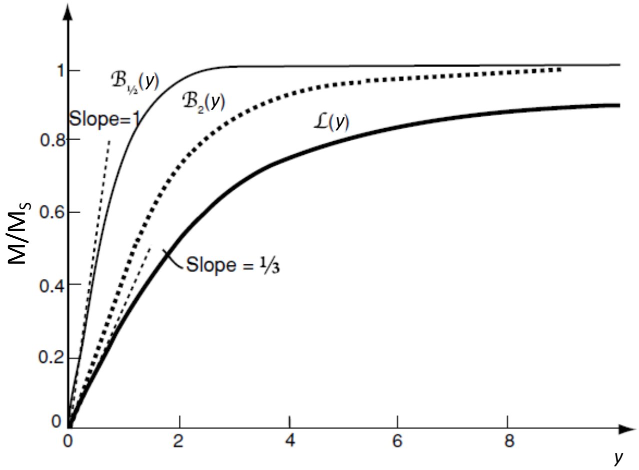

Figure 2. 19. Comparison of Langevin *L(y)* and Brillouin $B_J(y)$ functions. J has been considered as ½ and 2 for each $B_J(y)$ function. Figure adapted from [59].

6.2. Magnetic order

In a solid material, it can be exchange interaction of electrons between atoms due to the overlap of their wave functions. The term J_{ex} is the *exchange energy*, which refers to the possibility of exchange between electrons. Electrons are indistinguishable, except for their spin. Their relative orientation is the most important factor: if they are parallel, J_{ex} is positive, meanwhile J_{ex} is negative for an antiparallel alignment. Depending on these interactions, different magnetic ground states can be defined:

- **Ferromagnetism.** The most characteristic feature of ferromagnetic materials is their spontaneous magnetization due to the alignment of the magnetic moments located on the crystal structure [57], [59]. The magnetization tends to be parallel aligned to an easy axis direction, which depends on the crystal structure and sample shape. Magnetic order in a crystal may influence the lattice parameters and elastic modulus. Thus, ferromagnetism influences thermal, electrical and optical properties of solids [59].
- **Antiferromagnetism.** In antiferromagnetic systems the magnetic moments lie antiparallel to one another. This usually happens when the crystal lattice is divided into two or more atomic sublattices, which order in such a way that the global magnetic moment is zero. Single transition-metal oxides and fluorides are frequently antiferromagnetic [59].
- **Ferrimagnetism.** This is similar to antiferromagnetism but, in this case, the magnetic moments of the two sublattices are not equal, and therefore the global magnetic moment is not cancelled. Most oxides which possess a net magnetic moment are ferrimagnets. For instance, ferrites have two types of lattice sites: tetrahedral and octahedral holes. The cations filling these holes are antiparallel in magnetic moment [6]. As the number of octahedral and tetrahedral sites is unequal, together with the fact that different cations can fill these spaces, the global sum of magnetic moment is unbalanced. The total magnetic moment will depend on the specific cations introduced in the structure, as well as their distribution in these sites [57], [59]. See Table 2. 6 where the net magnetic moment of different spinels are summarized.
- **Spin glasses.** These structures consist on a random distribution of magnetic atoms in a nonmagnetic matrix. These structures do not show phase transitions at any particular temperature. Then, they can be understood as a random, magnetic system with mixed spin interactions at a well-defined *freezing temperature* T_f. Below this temperature, a metastable state appears without long-range order [57], [59].

Table 2. 6. Magnetic moment of different spinel ferrites. The term in brackets refers to the cations in octahedral positions. Adapted from [6].

Spinel	Calculated Magnetic moment (μ_B)	Experimental Magnetic moment (μ_B)
Fe^{3+} [Fe^{2+} Fe^{3+}]	4	4.1
Fe [Ni Fe]	2	2.3
Fe [Co Fe]	3	3.7
Fe [Cu Fe]	1	1.3

6.2.1. Anisotropy and magnetostriction

Magnetization is not isotropic in a crystal because its energy depends on its orientations with respect to the crystal structure. The direction where the energy is minimum is known as *easy direction*, which are usually the axes $\langle 100 \rangle$ and $\langle 111 \rangle$ in cubic structures. On the other hand, the magnetization vector has higher energy in a *hard direction*. This phenomenon, known as magnetocrystalline anisotropy, is extremely important because it plays a key role in the magnetisation process [6]. In a cubic structure, the energy E_K needed to deviate the magnetization from the easy direction is defined in Equation 2. 80.

$$E_K = K_1(\alpha_1^2\alpha_2^2 + \alpha_2^2\alpha_3^2 + \alpha_3^2\alpha_1^2) + K_2(\alpha_1^2\alpha_2^2\alpha_3^2) + \cdots \qquad \text{Equation 2. 80}$$

where α are the angle cosines, and K_1 and K_2 are the magnetocrystalline anisotropy constants. The anisotropy constants are found to be highly dependent on temperature and tend to be smaller in lattices with higher symmetry. Magnetocrystalline anisotropy results from spin-orbit interactions and a partial quenching of the orbital angular momentum [6], [57]. A common representation of the anisotropy of a system is made by the anisotropy field H_K, which is defined as a fictive field exerting a torque equal to anisotropy on the magnetic moment [6]. In Table 2. 7 both are defined, the anisotropy constant K_1 and the anisotropy field H_K for different ferrites.

Table 2. 7. Anisotropy constants K_1 and anisotropy field H_K for different ferrites at 300 K. The easy or hard direction determines the sign of K_1. Adapted from [6].

Ferrite	K_1 (kJ/m^3)	H_K (kA/m)
Fe_3O_4	-11	24.3
$NiFe_2O_4$	-6.2	24.4
$CoFe_2O_4$	200	500
$MnFe_2O_4$	-3	8

6.2.2. Domains and domain walls

One may concern that in daily situations there are magnetic materials, such as two pieces of Fe, which do not experiment magnetic forces between them, despite they are ferromagnetic materials even at room temperature. This phenomenon can be explained by the existence of magnetic *domains*, which are regions of the bulk ferromagnet with the same magnetic orientation but different to their neighbours. Each domain has a spontaneous magnetization, but as the magnetization direction of each domain is different, they compensate each other and there is not net magnetic moment [6]. Furthermore, between two magnetic domains there is a region – known as *domain wall* - where the magnetization rotates from the orientation of one domain to the orientation of the other [59]. When a magnetic field is applied, it makes all the domains to align following the direction of the magnetic field, that can be achieved by the *domain wall motion* process [57].

In the saturated situation, i.e. when there is just one magnetic domain, the exchange and anisotropy energies are minimum. Nevertheless, the magnetic flux outside the sample represents an additional magnetic energy, known an *magnetostatic* energy E_m. This energy - defined in Equation 2. 81 – is a function of the magnetization M and the demagnetisation factor N_d, which depends on the sample shape.

$$E_m = \frac{1}{2} N_d M^2 \qquad \text{Equation 2. 81}$$

When M is reduced by the formation of domains, E_m decreases. It keeps decreasing as more domains are formed until being virtually eliminated by forming closure domains, which retain all the magnetic flux within the sample (see Figure 2. 20).

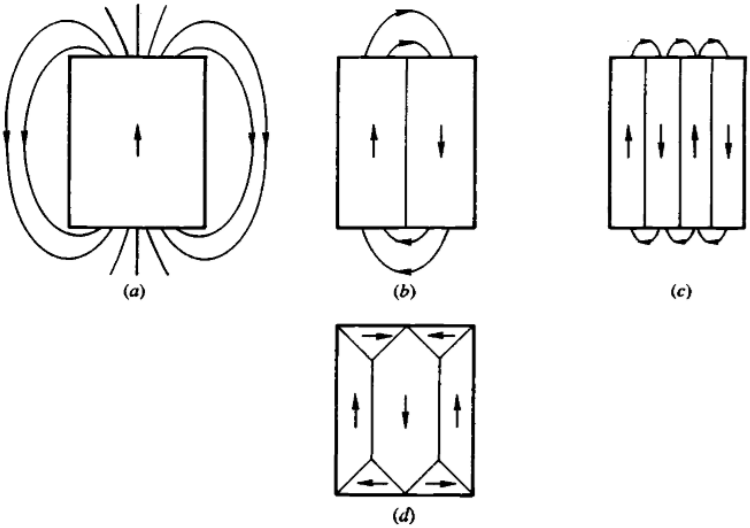

Figure 2. 20. Domain structure and magnetic flux evolution during the demagnetization process [6].

Despite the magnetic moment prefers to be aligned in the easy axis in the domains, it has to rotate in the domain wall, and a component lies in the hard axis, leading to an energy cost [57]. The exchange energy E_{ex} in a domain wall is defined by Equation 2. 82 [6].

$$E_{ex} \approx -2Js^2 + Js^2\theta^2$$ Equation 2. 82

The first term is constant, while the right term is inversely proportional to the number of spins in the wall. Then, exchange energy promotes thick walls, whereas the anisotropy energy favours thin walls in order to have most of the spins pointing to the easy direction. With all that, the *domain wall width* (λ_W) can be defined as [6]:

$$\lambda_w = a\sqrt{\frac{E_{ex}}{E_K}}$$ Equation 2. 83

Where term *a* refers to the unit cell parameter. Consequently, each material has a particular value of λ_W.

For small particles, there is a critical diameter below which the formation of a domain wall results in a energy contribution larger than the magnetostatic energy of a single domain configuration. Therefore, a particle smaller than λ_W does not contain any domain wall and all the spins point to the same direction. These particles are known as *single domain particles* (SDP) and have a single total spin $\vec{S}$. The energy barrier that prevents the spin of a single domain particle to rotate between two antiparallel states (*up* and *down* positions) can be empirically expressed as:

$$U = KV \qquad \text{Equation 2. 84}$$

where U is the energy barrier, K is the anisotropy constant, and V is the particle volume. It is therefore more energetically expensive to rotate big and anisotropic particles. Nevertheless, here it is important to mention that, under certain conditions, transitions between both states can occur due to *quantum tunnel effect* [62], [63]. The transition probability (Γ) is:

$$\Gamma \propto e^{-\frac{U}{k_B T}} \qquad \text{Equation 2. 85}$$

being $k_B T$ the thermal energy of the system. Finally, the inversion time of a single domain particle is defined in Equation 2. 86.

$$\mathrm{t} = t_0 e^{\frac{U}{k_B T}} \qquad \text{Equation 2. 86}$$

where t_0 is the attempt time, and $1/t_0$ the attempt frequency. When the thermal energy is much greater than the energy barrier, the inversion frequency between both states is extremely high. This behaviour is known as *superparamagnetism*.

6.2.3. Magnetization process and hysteresis

It should be considered the multidomain structure present in a bulk ferromagnet. Without any magnetic field applied, all the magnetic domains are randomly oriented, and the sum of their magnetic moments is null. For this reason, it is considered that the material is initially non-magnetized. When a magnetic field is applied to a specific direction, the magnetic moments of these domains tend to re-orient in order to follow the direction of the field. When the spins start to be oriented in the direction of the field, the total magnetic moment is not yet cancelled and appears a net magnetic moment. The relative magnetic permeability μ_r, which has been previously introduced in Equation 2. 74, is here an important parameter to evaluate the magnetic response. Materials with high (μ_r) are highly sensitive to the magnetic field and magnetize early. This response at low fields is mainly due to domain wall movement, because spins inside the domains are still highly affected by the magnetocrystalline anisotropy as they are oriented to an easy direction. At higher fields starts the rotation of those magnetic moments which have easy directions non-parallel with the magnetic field, in order to be aligned with the easy direction closer to the field direction. Finally, there is a coherent rotation of the magnetic domains to the field direction, independently of the easy or hard magnetization direction [6], [57]. When all the magnetic moments are oriented to the field direction, the saturation magnetization M_S is reached. The magnetization curve (M vs H) shows a different behaviour if the field is applied in the easy or hard magnetization direction, as can be appreciated in Figure 2. 21.

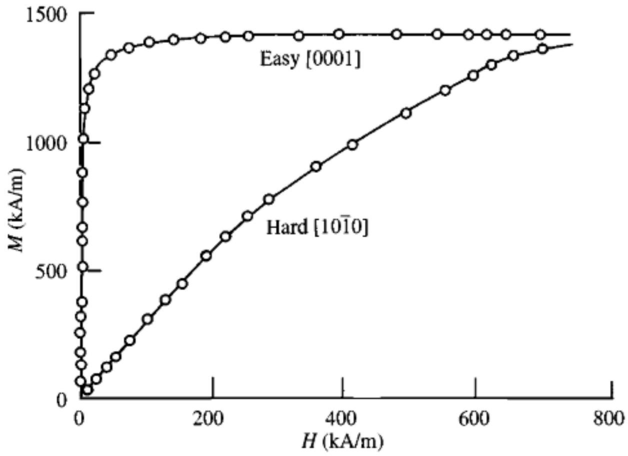

Figure 2. 21. Comparison of the first magnetization curve when the field is applied in the easy or hard magnetization directions [6].

Once the magnetic field is removed, the material keeps some *remanent magnetization* (M_R), instead of going directly to zero magnetization. Domain walls keep pinned due to the energy balance between the reduction of magnetization and the cost of generating them. Thus, some domains are still completely or partially aligned with the field. Of course, this is related to the decay of M_R to zero in the absence of the external magnetic field, leading in greater M_R at higher switching field frequencies. In order to overcome M_R and demagnetize the material, it is needed to apply an opposite magnetic field, which is known as *coercive field* (H_C). If the magnitude of this opposite magnetic field increases, the material starts to magnetise in the field direction, until reaching again the saturation. As the magnetization and demagnetization curves are not perfectly reversible, there is an area involved when the material is magnetized in one and the opposite direction; this is what is known as *hysteresis cycle* or *hysteresis loop*.

In Figure 2. 22.A, the above commented mechanisms for the first magnetization curve until the saturation are represented, whereas in Figure 2. 22.B the main parameters in a full hysteresis cycle are specified.

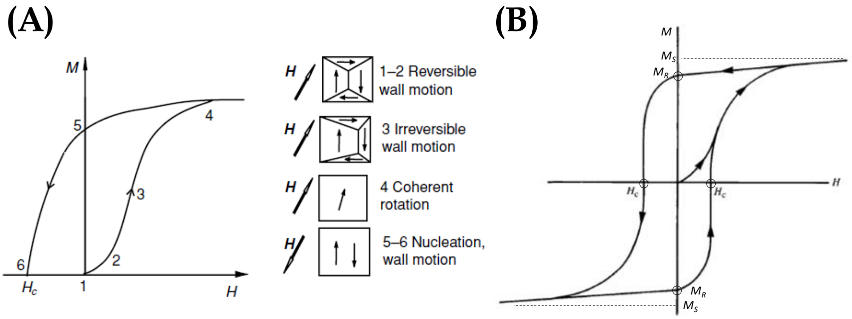

Figure 2. 22. (A) First magnetization and demagnetization curves with the representation of the corresponding mechanism, and (B) full hysteresis cycle with the main parameters indicated. Figures adapted from (A) [59], and (B) [6].

Based on their response in these *M*(*H*) measurements, it is possible to differentiate between two main families of magnetic materials:

- **Soft Magnetic Materials (SMMs).** These materials are characterized by an elevated permeability and a reduced hysteresis area. Consequently, these materials magnetize easily, and their magnetic moment can be switched with a very small energy consumption. These materials are specially interesting in high frequency applications where energy loses must be minimized [64], [65].
- **Hard Magnetic Materials (HMMs).** This family of materials is characterized for having two extremely stable magnetic states, up and down. Their elevated M_R and H_C ensure that both saturation states will not be spontaneously lost. The ideal hysteresis cycle for a HMM is squared-shaped, and they have many applications as permanent magnets in memory devices, for instance [7], [66].

6.2.4. Magnetic relaxation

A material is saturated when the anisotropy field H_K is applied, as the field is so strong than can overcome the anisotropy energy and allows the spins to rotate in the field direction. However, there is not an instantaneous demagnetization when the field is removed. Despite the absolute minimum energy state corresponds to the zero magnetization, there is a balance between this tendency and the energy required to produce domain walls. The system first tends to a *critical state*, which leads to a time-dependent process of magnetization reduction that is known as *magnetic relaxation*. In fact, the presence of these metastable states is what results in magnetic hysteresis. All materials presenting hysteresis are expected to slowly relax towards the minimum energy state. In contrast with other relaxation mechanisms, magnetic relaxation is a non-linear effect and its large duration is due to the exponentially large lifetimes of metastable states [63].

As stated before, the magnetization first reduces to a critical value M_C, where pinning occurs, and domain walls stop. From this moment, the relaxation is governed by thermal processes and has a ln(t) dependence as is shown in Equation 2. 87.

$$M(t) = M(t_0)\left[1 - \frac{T}{U_0}\ln\left(\frac{t}{t_0}\right)\right] \qquad \text{Equation 2. 87}$$

where $M(t_0) \approx M_C$ and U_0 is the energy barrier. The term in front of ln(t) is called the *magnetic viscosity* (S) and gives rise about the velocity at which the material relaxes. This parameter can be defined as:

$$S = -\frac{1}{M(t_0)}\frac{\partial M}{\partial \ln(t)} \qquad \text{Equation 2. 88}$$

This model predicts that S must tend to zero when temperature reduces. Nevertheless, some studies have detected deviations from this prediction at lower temperatures. In this new regime, relaxation is still logarithmic with time, but viscosity becomes independent with temperature. This non-thermal relaxation indicates the presence of quantum tunnelling of the magnetization below the critical temperature T_C. Thus, relaxation experiments can also provide information about the thermal-quantum transition of the decay of metastable magnetic states [63]. In Figure 2. 23, an example of the *S(T)* dependence and the appearance of quantum relaxation mechanisms at low temperatures is shown.

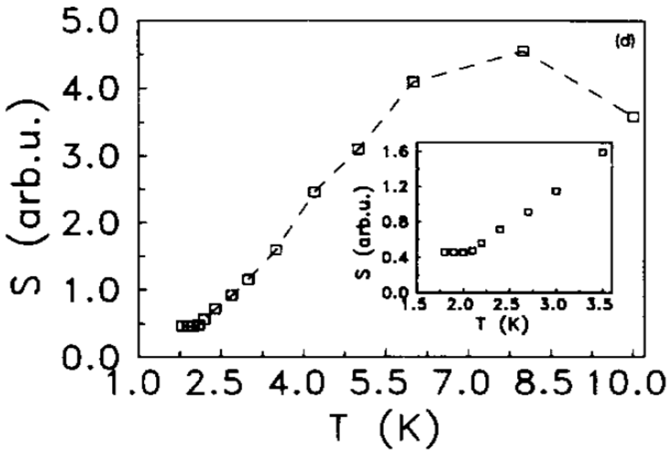

Figure 2. 23. Temperature dependence of the magnetic viscosity of antiferromagnetic ferritin particles with H_1 = 100 Oe and H_2 = - 100 Oe [67].

Let's now consider a system on non-interacting particles with a distribution of volumes *f(V)*, then Equation 2. 87 can be replaced by:

$$M(t) = M(t_0) - \left[M(t_0) - M_{eq}(H)\right] \frac{\int_0^{V_B} dVf(V)V}{\int_0^{\infty} dVf(V)V} \qquad \text{Equation 2. 89}$$

where the term V_B is the blocking volume. The particles which are smaller than V_B have already relaxed, meanwhile those bigger are still blocked in the initial direction. As the observation time is running, the system faces greater barriers which are more difficult to overcome, and for this reason the relaxation may be understood as ln*(t)* dependent. Then, it is also possible to characterize the system in terms of the *blocking temperature,* $T_B = KV_0/\ln(\nu t)$, where ν is the attempt frequency, and t the characteristic measuring time of the instrument. Typical values of νt in macroscopic relaxation experiments are $\nu t \simeq 10^{11} - 10^{15}$. In this scale, the transitions on most of the particles unfreeze above T_B. The condition $T \ll T_B$ is mathematically equivalent to $V_B \ll V$. Moreover, an important conclusion is that the thermal relaxation, *M* depends on time only through the combination *T* ln*(νt)*.

Considering Equation 2. 89, the condition of viscosity *S* in the case of non-interacting particles at $H \ll H_K$ is:

$$S=-\frac{1}{M_0-M_{eq}}\frac{dM}{d\ln(t)}=\frac{T}{K\langle V\rangle}\frac{V_B f(V_B)}{\int_0^\infty dV f(V)} \qquad \text{Equation 2. 90}$$

where $\langle V\rangle=\int_0^\infty dV f(V)V/\int_0^\infty dV f(V)V$. Finally, it should be mentioned that in the case of having a system in which the particles interact, the conception of the critical state (Equation 2. 87 and Equation 2. 88) are more useful than those later derived [63].

6.2.5. Zero Field Cooled – Field Cooled

The zero-field-cooled (ZFC) $M(T)$ measurement is an appropriate source of information to study a system of magnetic clusters of different sizes. By this method, it is possible to study the distribution of energy barriers, which is originated by the presence of a distribution of sizes.

Consider a non-magnetized system (M=0) which is cooled to a very low temperature at H = 0. In this situation, all the magnetic moments are still randomly orientated. Then, a small magnetic field ($H \ll H_K$) is applied and the temperature dependence of M is studied. At a certain temperature, the particles of volume $V < V_B$ are superparamagnetic, whereas those which are bigger ($V > V_B$) are still blocked in their initial state [63]. As temperature raises, the thermal energy increases and bigger particles unblock. By considering the distribution function *f(V)*, the total ZFC moment is:

$$M(T,H,t)=\frac{m_0^2 H}{2T}\int_0^{V_B(T,t)} dV f(V)V^2 \qquad \text{Equation 2. 91}$$

where m_0 is the magnetization of the material of the particle. At $T > T_B$ (or $V_B > V_0$) Equation 2. 91 becomes constant and proportional to $1/T$. This is the limit where all the particles are superparamagnetic. Below this temperature, the temperature dependence of the total moment depends on the distribution function [63].

From an experimental point of view, the magnetization initially increases as temperature raises because more and more particles are unblocked, and can be oriented in the field direction. This tendency is maintained upon a maximum value, at $T = T_B$, where all the particles have enough energy to overcome the energy barrier. Above this temperature the system enters in the superparamagnetic state and, as the magnetic moment can be in any of both states, the magnetization decreases. In the presence of quantum relaxation, the ZFC should increase proportionally to $1/T$ at $T < T_C$. The different behaviours in the ZFC can be observed in Figure 2. 24.

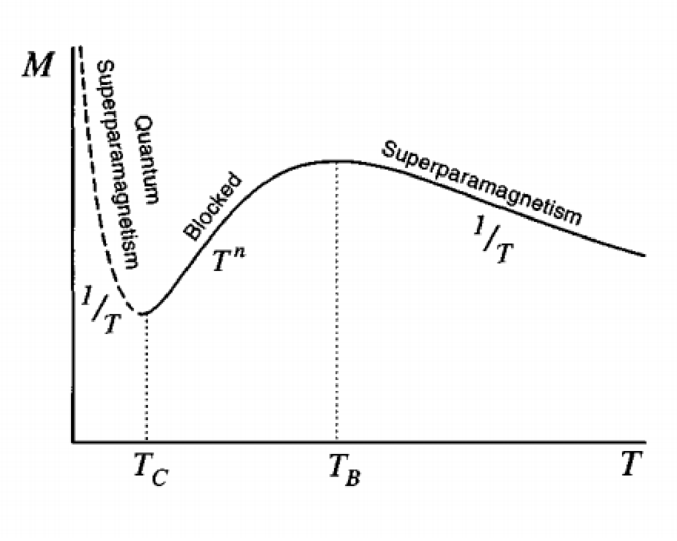

Figure 2. 24. Magnetic behaviour in a ZFC as a function of the temperature [63].

Finally, once at room temperature, field-cooled (FC) starts. In this case, the applied magnetic field is kept, and the cooling starts. In this process the bigger particles start to block in the direction favoured by the field, so the magnetization may increase following the Curie law. From the difference between the FC and ZFC curves, it is possible to calculate the distribution of energy barriers, as T_B for each particle is proportional to the energy barrier U.

6.3. Equipment – SQUID Magnetometer

SQUID is the acronym of *Superconducting Quantum Interference Device*. A schematic representation of a SQUID magnetometer is represented in Figure 2. 25. It basically consists on a helium dewar, a cryostat with a superconducting solenoid, the tube where the sample is placed and connected with the exterior, a set of superconducting pick-up coils, and the SQUID itself at the bottom. This device allows to work at ultra-low temperatures (down to 1.8 K) and high magnetic fields (up to 5 T).

The sample is mounted in a non-magnetic holder and connected at the end of a non-magnetic sample rod. The sample is moved between the pick-up coils, which are connected to one or two (depending if it is a RF or DC SQUID, respectively) Josephson junctions. The relative movement between the sample and the coils generated an induced current in the coils, which can be converted to magnetic moment after fitting this signal to the theoretical signal, and applying iterative or linear regression algorithms [68], [69].

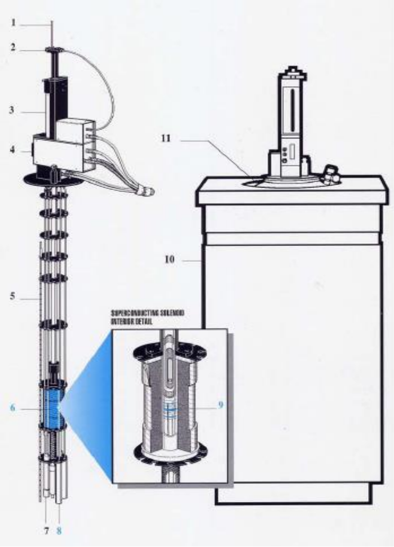

Figure 2. 25. Scheme of a SQUID magnetometer. Superconducting elements are shown in blue. The components are: (1) sample rod, (2) sample rotator, (3) sample transport, (4) probe assembly, (5) helium level sensor, (6) superconducting solenoid, (7) flow impedance, (8) SQUID capsule with magnetic shield, (9) superconducting pick-up coil, (10) Dewar isolation cabinet, (11) Dewar [68].

7. FREQUENCY – DEPENDENT MAGNETIC PROPERTIES

The study of the magnetic properties when an alternating field is applied is of growing interest for electronics or radar applications. For instance, novel soft magnetic alloys and ferrites [8], [65], [70]–[72] are continuously under investigation due to their high permeability and electrical resistance, respectively, for applications in the kHz or MHz frequency (ν) range. In this regard, characterization methods such as impedance spectroscopy [73], [74] can provide useful information about the frequency dependence of their properties.

7.1. Complex magnetic permeability

The magnetic permeability has been previously defined in Equation 2. 74 as the linear relationship between the B and H. Moreover, it has also been defined the relative permeability as $\mu_r = \mu/\mu_0 = 1 - \chi$. Thus, high μ_r materials are easily magnetizable. However, magnetic permeability can be expressed as a frequency–dependent complex magnitude according to Equation 2. 92.

$$\hat{\mu}_r(\omega) = \mu_r'(\omega) - j\mu_r''(\omega) \qquad \text{Equation 2. 92}$$

where ω is the angular frequency ($\omega = 2\pi\nu$), while μ_r' and μ_r'' are the real and imaginary components, respectively. The real and imaginary parts represent, respectively, the stored and lost contributions. Thus, the loss tangent [*tan(δ)*] is commonly used to compare the ratio between the lost and the stored parts.

$$tan(\delta) = \frac{\mu_r''(\omega)}{\mu_r'(\omega)} \qquad \text{Equation 2. 93}$$

being δ the angle between the real and imaginary components.

Complex permeability is generally related to two different mechanisms: spin rotation magnetizing $\chi_{sp}(\omega)$ and domain wall motion $\chi_{dw}(\omega)$ [75]. Therefore, the magnetic permeability can also be expressed as:

$$\mu(\omega) = 1 + \chi_{sp}(\omega) + \chi_{dw}(\omega) \qquad \text{Equation 2. 94}$$

The first mechanism is of relaxation type, and it is described by the Snoek's law [76]. This mechanism depends on the gyromagnetic ratio γ, the anisotropy field H_k, and the saturation magnetization M_S, as it is described by the Snoek's product in Equation 2. 95 [72].

$$(\mu_S - 1) \cdot \nu_r = \frac{\gamma}{3\pi} M_S \qquad \text{Equation 2. 95}$$

being μ_S the static permeability, and ν_r the relaxation frequency ($\nu_r = \gamma \cdot H_k/2\pi$), i.e. the frequency at which μ'' is maximum.

On the other hand, domain wall motion is a resonance mechanism, and depends on the square of the frequency. It is sensitive to microstructure characteristics of the material, such as the grain size [72], [75]. Despite both mechanisms can contribute to the complex permeability spectra, it has been determined that it is spin rotation the one that makes major contributions to magnetic loss [77], [78].

7.2. Relaxation models

Relaxation processes are common in different physics properties, which monotonically evolves to a stational state after a temporal stimulus has been applied. The evolution is time-dependent, and can be usually expressed in the form:

$$M(t) = M_0 \left(1 - e^{-t/\tau}\right) \qquad \text{Equation 2. 96}$$

where M represents the physical magnitude under study, and τ is the characteristic relaxation time.

There exist different models for studying the relaxation phenomena in materials, and some of the more important are described below. The presented models are commonly used to describe dielectric and magnetic relaxation mechanisms. Here, due to the goal if this Thesis, are adapted to the magnetic relaxation.

7.2.1. Debye

This is the standard and simplest model, which was defined by Debye in 1912 [79]. This model describes an exponential decay in time with a characteristic relaxation time [80]. The real component $\mu'(\omega)$ monotonically decreases when increasing ω, and the imaginary part $\mu''(\omega)$ shows a maximum at $\omega_r = 1/\tau$. According to this model, the complex permeability can be defined as in Equation 2. 97.

$$\hat{\mu}(\omega) = \mu_\infty \frac{\mu_S - \mu_\infty}{1 + j\omega\tau} \qquad \text{Equation 2. 97}$$

where μ_S is the static permeability (i.e. the constant permeability at zero frequency), μ_∞ is the infinite permeability (i.e. the permeability value at high frequencies, after the relaxation), and τ is the characteristic relaxation time. From this expression, the real and imaginary components described in Equation 2. 98 and Equation 2. 99 can be obtained.

$$\mu'(\omega) = \mu_\infty \frac{\mu_S - \mu_\infty}{1 + \omega^2\tau^2} \qquad \text{Equation 2. 98}$$

$$\mu''(\omega) = \frac{(\mu_S - \mu_\infty)\omega\tau}{1 + \omega^2\tau^2} \qquad \text{Equation 2. 99}$$

As it has been previously commented, the relaxation frequency is inversely proportional to τ. Figure 2. 26 shows the typical morphology of a Debye relaxation, as well as the effect of τ. In the bottom part of the figure, the dependence of the real and imaginary components with frequency is plotted, whereas in the bottom part it can be found the Cole – Cole diagram, where the real and imaginary components are compared.

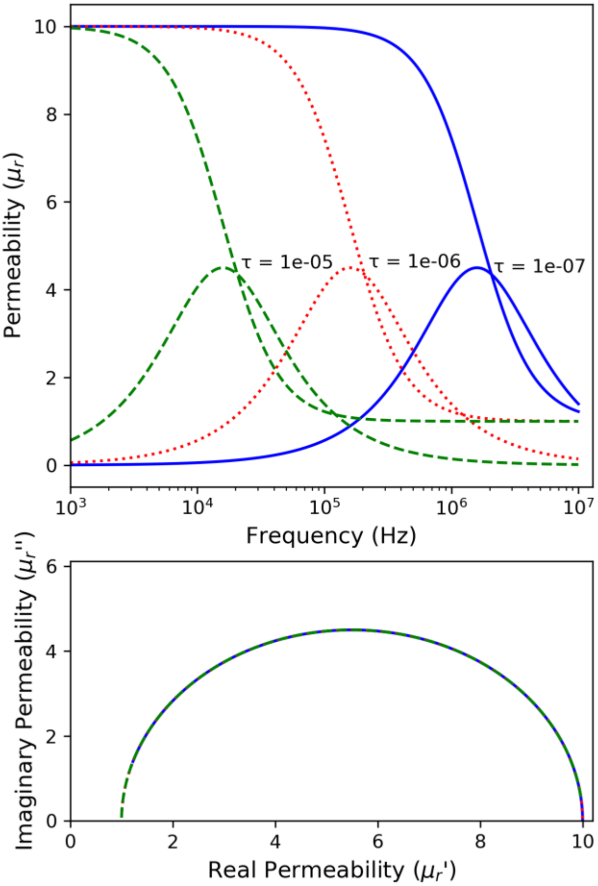

Figure 2. 26. Debye relaxation simulation with different τ values (10^{-7} s in the solid line, 10^{-6} s in the dotted line, and 10^{-5} s in the dashed line). The top part of the figure shows the frequency dependence of permeability, while the bottom corresponds to the Cole-Cole diagram. For this simulation it has been considered $\mu_S = 10$ and $\mu_\infty = 1$.

As can be appreciated, there is a single relaxation centred at ν_r depending on τ value, and all the plots form a semi-sphere in the Cole-Cole diagram.

This model is often non satisfactory for real materials, and advanced non-exponential models (also known as *anomalous relaxation* models) are required [80].

7.2.2. Cole – Cole (CC)

This model was first described by K. S. Cole and R. H. Cole in two different papers [81], [82] in 1941 and 1942. This model defines a non-exponential relaxation behaviour, which usually happens in compounds with rigid molecules in the pure liquid state [80], such as polar liquids or amorphous solid materials with ionic conductivity. This model assumes a distribution of τ instead of a single value, so it can be understood as a superposition of Debye relaxations with different τ.

The complex permeability is defined as Equation 2. 100.

$$\hat{\mu}(\omega) = \mu_\infty \frac{\mu_s - \mu_\infty}{1 + (j\omega\tau)^{1-n}} \qquad \text{Equation 2. 100}$$

where n is a mathematical parameter that defines the nature of the relaxation and can only take values between 0 and 1. For $n = 0$, it corresponds to the classical Debye relaxation, while as n increases it starts to consider every time a wider distribution of τ. For $n > 0$, the relaxation softens, and the slope reduces, as every τ relaxes at a different ω_r. The real and imaginary component of Equation 2. 100 can be defined as:

$$\mu'(\omega) = \mu_\infty + (\mu_s - \mu_\infty) \frac{1 + (\omega\tau)^{1-n} \sin n\pi/2}{1 + 2(\omega\tau)^{1-n} \sin n\pi/2 + (\omega\tau)^{2(1-n)}} \qquad \text{Equation 2. 101}$$

$$\mu''(\omega) = (\mu_s - \mu_\infty) \frac{1 + (\omega\tau)^{1-n} \cos n\pi/2}{1 + 2(\omega\tau)^{1-n} \sin n\pi/2 + (\omega\tau)^{2(1-n)}} \qquad \text{Equation 2. 102}$$

Figure 2. 27 corresponds to a calculation of μ' and μ'' with different n values and fixed τ. Here it is possible to observe the graphical difference with the Debye and the effect of the n parameter in the relaxation.

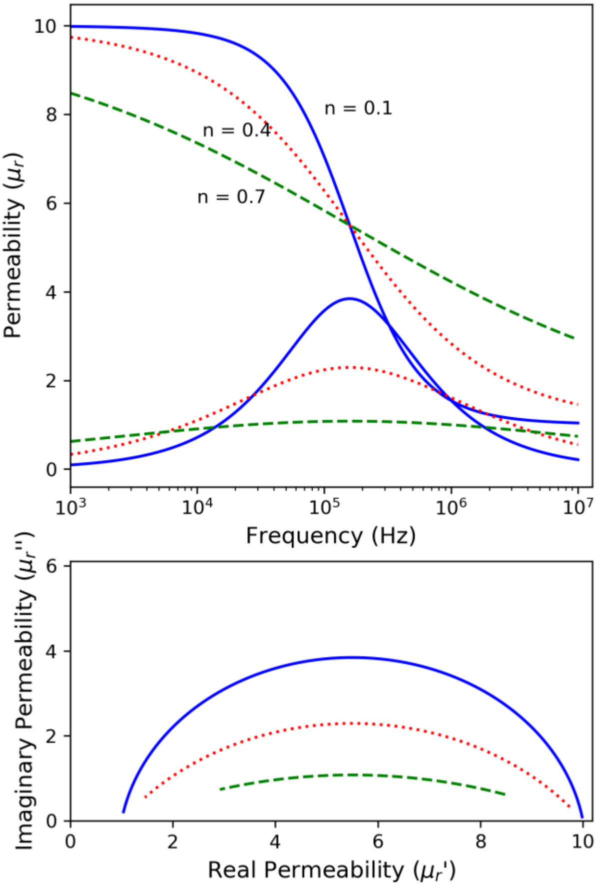

Figure 2. 27. Cole - Cole relaxation simulation with different *n* values (0.1 in the solid line, 0.4 in the dotted line, and 0.7 in the dashed line). The top part of the figure shows the frequency dependence of permeability, while the bottom corresponds to the Cole-Cole diagram. For this simulation it has been considered $\tau = 10^{-6}$ s, $\mu_S = 10$ and $\mu_\infty = 1$.

In this case, the parameter *n* changes the slope of the relaxation (by increasing the distribution of τ) and keep centered at $\omega_r = 1/\tau$. The Cole-Cole diagram shows how the semi-sphere keeps centred independently of the *n* value, but it is displaced when *n* is changed. Despite it has not been again represented, a change in τ would only affect on the relaxation frequency.

7.2.3. Davidson – Cole (DC)

This model was introduced in 1950 – 1951 by D. W. Davidson and R. H. Cole [83], [84] in order to fit the broader range of dispersion observed at high frequencies in some materials [80]. In this case, the complex permeability is defined as:

$$\hat{\mu}(\omega) = \mu_{\infty} \frac{\mu_s - \mu_{\infty}}{(1 + j\omega\tau)^{1-n}} \qquad \text{Equation 2. 103}$$

This model also assumes a distribution of τ determined by the n parameter. However, in this case, the spectrum in not centred at $\omega_r = 1/\tau$ and becomes asymmetric. The real and imaginary components can be expressed as follows:

$$\mu'(\omega) = \mu_{\infty} + (\mu_s - \mu_{\infty}) \frac{\cos[(1-n) arctan(\omega\tau)]}{[1 + (\omega\tau)^2]^{1-n/2}} \qquad \text{Equation 2. 104}$$

$$\mu''(\omega) = (\mu_s - \mu_{\infty}) \frac{\sin[(1-n) arctan(\omega\tau)]}{[1 + (\omega\tau)^2]^{1-n/2}} \qquad \text{Equation 2. 105}$$

Again, it has a Debye character when n tends to 0, and the DC influence increases as n turns to 1. A graphical simulation of the DC with different n values (the same used for CC) is shown in Figure 2. 28.

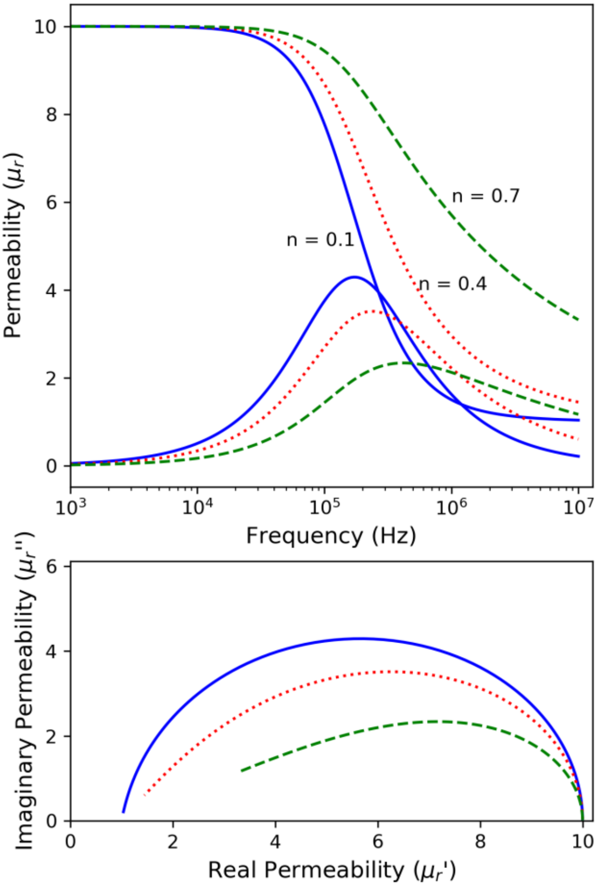

Figure 2. 28. Davidson - Cole relaxation simulation with different n values (0.1 in the solid line, 0.4 in the dotted line, and 0.7 in the dashed line). The top part of the figure shows the frequency dependence of permeability, while the bottom corresponds to the Cole-Cole diagram. For this simulation it has been considered $\tau = 10^{-6}$ s, $\mu_S = 10$ and $\mu_\infty = 1$.

As it has been commented before, n parameter reduces the slope of the relaxation and makes the spectrum asymmetric. Regarding the Cole-Cole diagram, it can be seen how it shifts from the semi-sphere (observed in the Debye and CC models) when $n \rightarrow 0$, to an asymmetric "pear" shape at higher n values.

8. TERAHERTZ TIME-DOMAIN SPECTROSCOPY (THz – TDS) AND IMAGING

The terahertz (THz) portion of the electromagnetic spectrum expands from approximately 100 GHz to 10 THz, i.e. wavelengths in the range between 3 mm to 30 µm. It is placed between microwaves and infrared radiation in the full electromagnetic spectrum, as it is shown in Figure 2. 29. In this frequency range, the wave can penetrate non-metallic materials that are opaque at other frequencies. Moreover, it has a non-ionizing character and therefore it is a safe characterization technique [85]. Unlike to other well know frequency bands (as infrared, microwaves, or optical, for instance) there are many fundamental research opportunities because this is a relatively novel field which started to be explored only some decades ago [86]. Since the mid-70s, advances in electronics and photonics have provided new materials and devices that make the THz band accessible and accelerated the progress in this field, both fundamental and for applications [87], [88]. It is attracting the attention of the technological sector due to the wavelengths' range used, which provides an interesting penetration depth scale with good resolution. Even in spintronics interesting advances have been done working with THz and antiferromagnetic insulators [89], [90].

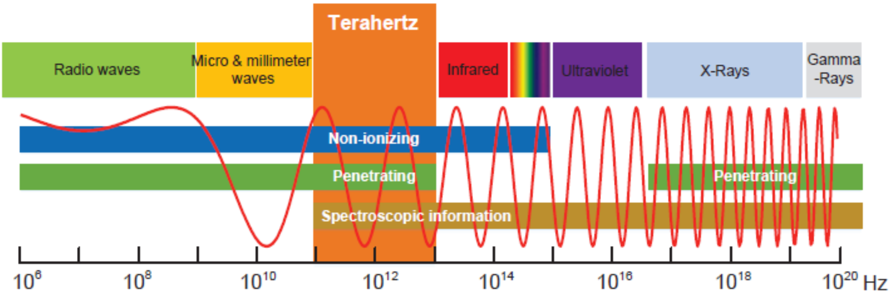

Figure 2. 29. Complete electromagnetic spectrum representation. THz portion is found between microwaves and infrared radiation [85].

8.1. Generation and detection of THz

The generation of broadband THz pulses is based on the excitation of different materials with ultrashort laser pulses. Different mechanisms have been explored to produce this generation, like photocarrier acceleration in photoconducting antennas (PCA), second-order non-linear effects in electro-optic crystals, plasma oscillations, and electronic non-linear transmission lines. The physical mechanism of THz generation in a PCA, which is the most common approach, starts with an ultrafast laser pulse (with a wavelength approximately equal to the semiconductor bandgap [91]) that creates an electron-hole pair in the semiconductor [88]. Mode-locking is a technique for producing short, high-power, and periodic laser pulses [91]. The generated carriers then accelerate in the static bias field to form a transient photocurrent and radiates electromagnetic waves. Different parameters of the materials define the intensity and bandwidth of the emitted THz radiation [88].

The detection of THz pulses is another active research area. The low power of the THz sources combined with high levels of thermal background noise make indispensable to have highly sensitive detectors. Current detection systems use different technologies - such as thermal absorbers, pyroelectric infrared detectors, extremely sensitive superconducting bolometers, or single electron transistors - depending on the specific needs [88], [91].

A typical configuration of the THz system from the generation to the signal detection is described in Figure 2. 30. The femtosecond laser pulse is split in two parts: one part is directly conducted to the THz detector and generates a single-cycle of THz radiation, which is known as *pump*; the other, referred as *probe*, is directed through a variable time delay before being focused to the sample [91]. The timing difference between the pump and probe beams is controlled, so the response of the sample to the pump beam as a function of time can be measured very precisely [87].

The system can be also set in two different configurations: transmission or reflection. The basic difference between them is the relative position between the emitter and the receiver. In the transmission mode the emitter and the receiver are placed in the opposite sides of the sample, while they are placed in the same one in the reflexion mode. In order to measure in the reflexion mode, it is necessary to place the sample on a metallic plate to ensure a full signal reflexion after passing through the sample.

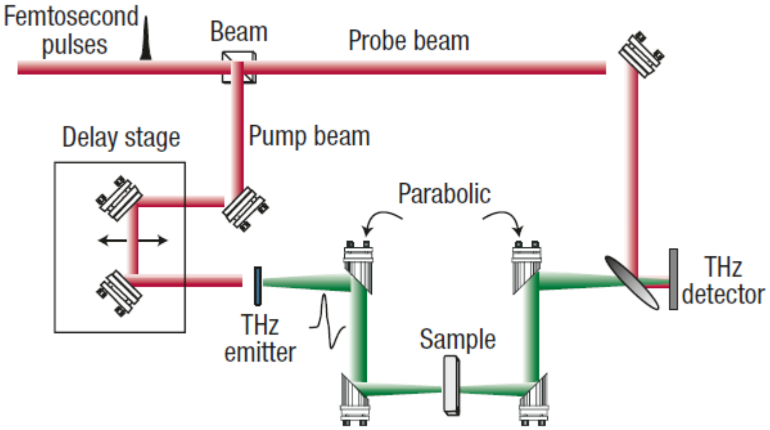

Figure 2. 30. THz System configuration from the signal generation to the detection, passing through the sample. This corresponds to the transmission configuration. Red lines define the laser paths, while the greens are the THz ones [88].

8.2. Measuring modes

The basic idea of *terahertz time-domain spectroscopy* (THz-TDS) systems is to irradiate the sample with a THz pulse and then to analyse the changes caused in the signal to deduce the physical properties of the material. However, it is possible to perform two different kinds of measurements depending on the information that wants to be extracted from the sample: spectroscopy or imaging.

8.2.1. THz - TDS

The spectroscopic side of the THz characterization pretends to deduce the optical and dielectric properties of the material under study. This method has been used to study a wide range of different materials, such as ceramics, semiconductors, pollutants, chemical mixtures and gases [92]. Most of these materials have been largely studied by FT-IR, but their fingerprint in the THz range varies and may provide important advantages.

The spectroscopic THz measurements are usually performed in transmission mode and in a single point in the sample. In this approach the variation of the intensity and time delay of the THz pulse are studied when it passes through the material. The variation of signal intensity is related with the absorption of the material, while the time delay is due to a change on refractive index between the air and the sample. A more detailed explanation about these relationships and the calculations performed to deduce the functional properties of the sample is provided in section 9.3.

8.2.2. THz imaging

This working mode is performed by doing successive measurements in different points of the sample surface in an ordered way. Each measurement point is a pixel, and the distance between pixels determine the image resolution. Then, by analysing a specific criterion (the time delay or the signal amplitude, for instance) and comparing in between the different pixels, a 2D image can be constructed. This type of measurements is usually done in reflection mode.

This is an extended technique for non-destructively analyse multilayer materials. The thickness or physical properties can be evaluated because each interface produces one reflection peak due to the change in refractive index. The penetration depth – which depends on the absorption coefficient of each material – determines the maximum thickness that can be detected, while the wavelength determines the maximum resolution of the system. In the case of an extremely thin layer – a nanometric one, for instance – the two reflection peaks superpose, and it is not possible to differentiate them. However, algorithms and signal deconvolution strategies have been recently published [85], [93] to distinguish both signals and to allow the characterization of thinner structures.

This non-destructive imaging technique has been already applied for characterizing multilayer systems [93], polymer reinforced polymers [94], [95], graphene and carbon-based structures [96], [97], or even for cultural heritage [98].

8.3. Signal processing and properties calculation

Once the measurements have been performed, it is needed to analyse the obtained signal in order to relate the observed changes with the physical properties of the material characterized.

We begin by reviewing the relationship between various optical constants [99], [100]. We shall only consider the linear optical properties and shall assume that the bulk material constituents are isotropic. Despite the measurement is carried out in the time-domain (TD), this signal can be converted to the frequency–domain (FD) by means of a discrete Fourier transformed (DFT). Then, the transmittance $T(\nu)$ can be calculated by considering the ratio between the electric field transmitted though the sample (E_S) and the reference one (E_R) at the same ν (see Equation 2. 106). E_R is previously determined by performing one measurement without sample. From this ratio, it is possible to extract the frequency-dependent relative amplitude $A(\nu)$ and phase ϕ (ν) of the transmitted field.

$$T(\nu) = \frac{E_S(\nu)}{E_R(\nu)} = A(\nu)e^{i\phi(\nu)} \qquad \text{Equation 2. 106}$$

The refractive index $n(\nu)$ is calculated from the propagation delay related to the difference in phase caused during transmission, while the absorption coefficient $\alpha(\nu)$ is also related to the reduction in amplitude:

$$n(\nu) = 1 + \frac{c}{2\pi\nu}\phi(\nu) \qquad \text{Equation 2. 107}$$

$$\alpha(\nu) = -\frac{2}{d}\ln\left[A(\nu)\frac{(n(\nu)+1)^2}{4n(\nu)}\right] \qquad \text{Equation 2. 108}$$

where c is the in-vacuo speed of light and d is the sample thickness. Equation 2. 108 accounts for the transmission and reflection at both interfaces of the pellet. The absorption coefficient is directly proportional to the extinction coefficient κ, which corresponds to the absolute value of the imaginary part κ of the complex refractive index $n - j\kappa$. This coefficient is defined by Equation 2. 109.

$$\kappa = \frac{\alpha\lambda_0}{4\pi} \qquad \text{Equation 2. 109}$$

In this equation, λ_0 is the wavelength in vacuum, i.e., $\lambda_0 = c/\nu$. The complex permittivity $\hat{\varepsilon} = \varepsilon' + \varepsilon''$ can be calculated from n and α by using Equation 2. 110 and Equation 2. 111 below. The real part of the permittivity is related to the stored energy, while the imaginary part is related to attenuation:

$$\varepsilon' = n^2 - \kappa^2 = n^2 - \left(\frac{\alpha\lambda_0}{4\pi}\right)^2 \qquad \text{Equation 2. 110}$$

$$\varepsilon'' = 2n\kappa = \frac{\alpha n\lambda_0}{2\pi} \qquad \text{Equation 2. 111}$$

Moreover, the electrical conductivity σ can be calculated from the imaginary part of the permittivity by:

$$\sigma = 2\pi\nu\varepsilon'' = 2\pi\nu\varepsilon_0\varepsilon_r'' \qquad \text{Equation 2. 112}$$

where ε_0 is the vacuum permittivity (8.85x10^{-12} F/m) and ε_r'' the imaginary component of the relative permittivity ($\varepsilon_r = \varepsilon/\varepsilon_0$).

8.4. Effective Medium Models (EMMs)

Due to the high attenuation of the typically measured materials, it is needed to disperse the powder samples in a THz-transparent polymer matrix in order to permit significant overall transmission through the sample and thus a large signal-to-noise-ratio (SNR). For this reason, the properties deduced using the above equations do not directly represent the properties of the sample itself, but rather the macroscopic properties of the combination of the polymer matrix and the powder sample. As one may expect, the amount of oxide dispersed into the polymer affects the observed properties.

In order to deduce the intrinsic properties of the sample from the measured mixture, various *Effective Medium Models* (EMMs) have been developed [101]. Despite these are general models that may be applied in many research and technological fields, here we present them as an indispensable tool to obtain significant information from the THz-TDS measurements.

Two of the most popular models (Maxwell–Garnett and Bruggeman's) are described below. Despite many other models with peculiar considerations [91], [102]–[106] have been postulated, here we will present the two which are more common and adequate for the materials analysed in this Thesis. Each of these models considers differently the dependence of the effective permittivity of the mixture with the oxide filling factor.

8.4.1. Maxwell – Garnett (MG) theory

One of the most common approximations is MG theory [107], [108], which assumes that the electric field within each particle is a combination of the external field and the field caused by other particles [91], [102], [109]. This approximation leads to Equation 2. 113.

$$\frac{\varepsilon_{eff} - \varepsilon_h}{\varepsilon_{eff} + \eta\varepsilon_h} = f_v \frac{\varepsilon_i - \varepsilon_h}{\varepsilon_i + \eta\varepsilon_h} \qquad \text{Equation 2. 113}$$

where ε_{eff}, ε_h, and ε_i represent the permittivity of the effective medium (measured mixture), the host material, and the inclusions (powder), respectively; f_v is the volume filling factor, i.e., the volume ratio that the inclusions occupy; and η is the shape factor ($\eta = 2$ for spherical inclusions, and $\eta = 1$ for cylinders with the axis perpendicular to the probing electric field) [91].

Despite the fact that this model was developed for spherical particles, it can be assumed to be valid for any shape as long as the medium is electrodynamically isotropic [109]. In addition, MG theory assumes a distribution of noninteracting particles, avoiding percolation effects. For this reason, it is an accurate approximation when working with low f_v (< 50 %) samples, and the host and inclusions' volumes are not comparable. In cases with higher f_v, other theoretical approaches (such as Bruggeman's) may be employed. Finally, scattering is not accounted for, so inclusions and the distances between them should be much smaller than the wavelengths within the THz pulse bandwidth [26,27]. With this in mind, MG theory is used here to infer the permittivity of the oxide inclusions.

8.4.2. Bruggeman's (BG) model

The BG model [110] is another popular EMM used to deduce the dielectric properties in a composite medium. The main difference with the MG is that this model takes into account the possible percolation of both components, so it is a convenient option for describing systems close to the percolation threshold [91]. It is an useful approximation when it is not possible to distinguish the dielectric inclusions embedded in the matrix [103], or when the f_V is close to a 50%.

The relationship between f_V and the permittivity of each of the phases in the BG model is defined by Equation 2. 114.

$$f_v \frac{\varepsilon_i - \varepsilon_{eff}}{\varepsilon_i + \eta\varepsilon_{eff}} + (1 - f_v) \frac{\varepsilon_h - \varepsilon_{eff}}{\varepsilon_h + \eta\varepsilon_{eff}} = 0 \qquad \text{Equation 2. 114}$$

Therefore, each one of these models considers differently the dependence of ε_{eff} with respect f_V, for fixed ε_h and ε_i values. In Figure 2. 31 it is graphically shown the behaviour of these models. Moreover, it is also represented a simple linear proportionality between ε_h and ε_i as a function of f_V. It can be appreciated that MG and BG work similarly in the low-f_V region (< 15%) but differ for higher contents.

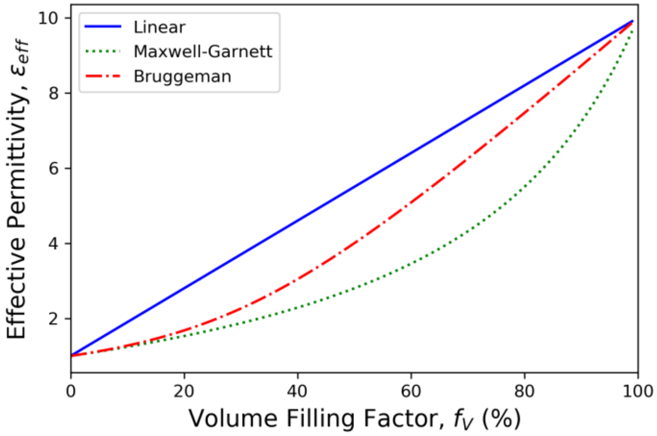

Figure 2. 31. Simulation of the $\varepsilon_{ff} - f_V$ dependence following a linear relationship (solid line), Maxwell-Garnett (dotted line), and Bruggeman's (dash-dotted line) models. The values used for this simulation are ε_h = 1, and ε_i = 10.

9. REFERENCES

[1] R. B. King, *Encyclopedia of inorganic chemistry*. West Sussex: John Wiley & Sons, 2005.

[2] D. R. Askeland, P. P. Fulay, and W. J. Wright, *The Science and Engineering of Materials*, 6th ed. Cengage Learning, Inc, 2010.

[3] H. Nan, X. Hu, and H. Tian, "Recent advances in perovskite oxides for anion-intercalation supercapacitor: A review," *Mater. Sci. Semicond. Process.*, vol. 94, no. February, pp. 35–50, 2019.

[4] A. Hossain, S. Roy, and K. Sakthipandi, "The external and internal influences on the tuning of the properties of perovskites: An overview," *Ceram. Int.*, vol. 45, no. 4, pp. 4152–4166, 2019.

[5] D. Bloor, R. J. Brook, M. C. Flemings, and S. Mahajan, *The encyclopedia of advanced materials*. Pergamon, 1994.

[6] R. Valenzuela, *Magnetic Ceramics*. Cambridge University Press, 1994.

[7] O. Mounkachi *et al.*, “Exploring the magnetic and structural properties of Nd-doped Cobalt nano-ferrite for permanent magnet applications,” *Ceram. Int.*, vol. 43, no. 16, pp. 14401–14404, 2017.

[8] Y. Gao, Z. Wang, J. Pei, and H. Zhang, “Structural, elastic, thermal and soft magnetic properties of Ni-Zn-Li ferrites,” *J. Alloys Compd.*, vol. 774, pp. 1233–1242, 2019.

[9] S. Tokatlidis, G. Kogias, and V. T. Zaspalis, “Low loss MnZn ferrites for applications in the frequency region of 1–3 MHz,” *J. Magn. Magn. Mater.*, vol. 465, no. June, pp. 727–735, 2018.

[10] V. Šepelák, S. Bégin-Colin, and G. Le Caër, “Transformations in oxides induced by high-energy ball-milling,” *Dalt. Trans.*, vol. 41, no. 39, pp. 11927–11948, 2012.

[11] V. G. Harris and V. Šepelák, “Mechanochemically processed zinc ferrite nanoparticles: Evolution of structure and impact of induced cation inversion,” *J. Magn. Magn. Mater.*, vol. 465, no. June, pp. 603–610, 2018.

[12] C. Suryanarayana, “Mechanical alloying and milling,” *Prog. Mater. Sci.*, vol. 46, pp. 1–184, 2001.

[13] K. K. Kefeni, T. A. M. Msagati, and B. B. Mamba, “Ferrite nanoparticles: Synthesis, characterisation and applications in electronic device,” *Mater. Sci. Eng. B Solid-State Mater. Adv. Technol.*, vol. 215, pp. 37–55, 2017.

[14] C. J. Brinker and G. W. Scherer, *Sol-Gel Science: The physics and chemistry of sol-gel processing*. 1990.

[15] C. Mahapatra *et al.*, “Sol–gel based materials for biomedical applications,” *Prog. Mater. Sci.*, vol. 77, pp. 1–79, 2016.

[16] J. García Capdevila, “Síntesis de cerámicos tecnológicos mediante métodos de combustion de geles de acrilamida,” Universitat de Barcelona, 2007.

[17] S. V. Motloung, P. Kumari, L. F. Koao, T. E. Motaung, T. T. Hlatshwayo, and M. J. Mochane, “Effects of annealing time on the structure and optical properties of ZnAl2O4/ZnO prepared via citrate sol-gel process,” *Mater. Today Commun.*, vol. 14, no. January, pp. 294–301, 2018.

[18] J. R. Salasin, S. E. A. Schwerzler, M. R. Koehler, D. J. Keffer, and C. J. Rawn, "The effect of process parameters on the amorphous citrate sol-gel synthesis of Cu-doped Ca12Al14O33," *Materialia*, vol. 4, no. November, pp. 466–477, 2018.

[19] P. Manju, M. R. Ajith, and D. Jaiswal-Nagar, "Synthesis and characterization of BaZrO 3 nanoparticles by citrate-nitrate sol-gel auto-combustion technique: Systematic study for the formation of dense BaZrO 3 ceramics," *J. Eur. Ceram. Soc.*, vol. 39, no. December 2018, pp. 3756–3767, 2019.

[20] K. K. Kefeni, T. A. M. Msagati, and B. B. Mamba, "Ferrite nanoparticles: Synthesis, characterisation and applications in electronic device," *Mater. Sci. Eng. B Solid-State Mater. Adv. Technol.*, vol. 215, pp. 37–55, 2017.

[21] E. M. M. Ibrahim, L. H. Abdel-Rahman, A. M. Abu-Dief, A. Elshafaie, S. K. Hamdan, and A. M. Ahmed, "The synthesis of CuO and NiO nanoparticles by facile thermal decomposition of metal-Schiff base complexes and an examination of their electric, thermoelectric and magnetic Properties," *Mater. Res. Bull.*, vol. 107, no. August, pp. 492–497, 2018.

[22] N. Zare, A. Zabardasti, A. Mohammadi, and F. Azarbani, "Synthesis of spherical Fe3O4 nanoparticles from the thermal decomposition of iron (III) nano-structure complex: DFT studies and evaluation of the biological activity," *Bioorg. Chem.*, vol. 80, no. April, pp. 334–346, 2018.

[23] B. Lee and S. Komarneni, *Chemical Processing of Ceramics*, vol. 80, no. 1. Taylor & Francis, 2005.

[24] R. Nagarajan and T. A. Hatton, *Nanoparticles: Synthesis, stabilization, passivation and functionalization*. ACS Symposium Series, 2008.

[25] Y. Xu and X.-T. Yan, *Chemical Vapor Deposition*, vol. 1. Springer, 2010.

[26] V. G. Harris, "Modern microwave ferrites," *IEEE Trans. Magn.*, vol. 48, no. 3, pp. 1075–1104, 2012.

[27] C. K. Bayne and S. J. Haswell, *Practical Guide to Chemometrics*, vol. 37, no. 2. 2006.

[28] Z. R. Lazic, *Design of Experiments in Chemical Engineering*. Wiley-VCH, 2004.

[29] R. Leardi, “Chemometrics in Food Chemistry,” in *Chemometrics in Food chemistry*, 1st ed., F. Marini, Ed. Amsterdam: Elsevier, 2013, pp. 9–53.

[30] R. E. Bruns, I. Scarminio, and B. Barros Neto, *Statistical Design – Chemometrics*, vol. 25. 2006.

[31] R. Leardi, “Experimental design in chemistry: A tutorial,” *Anal. Chim. Acta*, vol. 652, no. 1–2, pp. 161–172, 2009.

[32] M. Lee, *X-Ray Diffraction for Materials Research. From Fundamentals to Applications*. Apple Academic Press, 2016.

[33] R. Guinebretière, *X-ray diffraction by polycrystalline materials*. London: ISTE, 2007.

[34] B. D. Cullity, *Elements of X-Ray Diffraction*, 2nd ed. Addison-Wesley Publishing Company INC, 1978.

[35] A. I. Lvovsky, “Fresnel Equations,” in *Encyclopedia of Optical Engineering*, no. August, New York: Taylor & Francis, 2013, pp. 37–41.

[36] W. H. Bragg and W. L. Bragg, “The Reflection of X-rays by Crystals,” *R. Soc.*, vol. 17, pp. 428–438, 1913.

[37] A. A. Hernández-Hernández *et al.*, “Optimization of microwave-solvothermal synthesis of Fe3O4 nanoparticles. Coating, modification, and characterization,” *Mater. Chem. Phys.*, vol. 205, pp. 113–119, 2018.

[38] J. D. Hanawalt and H. W. Rinn, “Identification of Crystalline Materials,” *Ind. Eng. Chem.*, vol. 8, no. 4, pp. 244–247, 1936.

[39] J. D. Hanawalt, H. W. Rinn, and L. K. Frevel, “Chemical Analysis by X-Ray Diffraction: Classification and Use of X-Ray Diffraction Patterns,” *Ind. Eng. Chem. - Anal. Ed.*, vol. 10, no. 9, pp. 457–512, 1938.

[40] S. A. Speakman, “Basics of X-Ray Powder Diffraction.” MIT Materials Research Laboratory.

[41] X. Alcobé, “Calibratges instrumentals de difractòmetres de raigs x

de pols," Universitat de Barcelona, 2007.

[42] P. Scherrer, "Bestimmung der Grösse und der inneren Struktur von Kolloiteilchen mittels Röntgenstrahlen," *Nachrichten von der Gesellschaft der Wissenschaften zu Gottingen Math. Phys.*, vol. 1, no. 2, pp. 96–100, 1918.

[43] H. M. Rietveld, "A profile refinement method for nuclear and magnetic structures," *J. Appl. Crystallogr.*, vol. 2, no. 2, pp. 65–71, 1969.

[44] J. M. Amigó *et al.*, *El método de Rietveld*. Publicacions de la Universitat Jaume I, 2006.

[45] G. Caglioti, A. Paoletti, and F. P. Ricci, "Choice of collimators for a crystal spectrometer for neutron diffraction," *Nucl. Instruments*, vol. 3, no. 4, pp. 223–228, 1958.

[46] A. C. Fischer-Cripps, *Nanoindentation*, 3rd ed., vol. 36. London: Sprin, 2011.

[47] J. J. Roa Rovira, "Mechanical Properties of Htsc At Micro / Nanometric Scale," University of Barcelona, 2010.

[48] A. C. Fischer-Cripps, *Introduction to Contact Mechanics*, 2nd ed. Springer, 2006.

[49] G. R. Irwin, "Analysis of stresses and strains near the end of a crack traversing in a plate," *J. Appl. Mech.*, vol. 24, pp. 361–364, 1957.

[50] H. Hertz, "On the contact of elastic solids," *J. Reine Angew- Math*, vol. 92, pp. 156–171, 1881.

[51] H. Hertz, "On hardness," *Ver. Beförderung Gew. Fleisses*, vol. 61, p. 410, 1882.

[52] W. C. Oliver and G. M. Pharr, "Measurement of hardness and elastic modulus by instrumented indentation: Advances in understanding and refinements to methodology," *J. Mater. Res.*, vol. 19, no. 01, pp. 3–20, 2004.

[53] W. C. Oliver and G. M. Pharr, "An improved technique for determining hardness and elastic modulus using load and displacement sensing indentation experiments," *Mater. Res. Soc.*, vol. 7, no. 6, pp. 1564–1583, 1992.

[54] A. Tiwari and S. Natarajan, Eds., *Applied Nanoindentation in Advanced Materials*. John Wiley & Sons Ltd, 2017.

[55] G. M. Pharr, "Measurement of mechanical properties by ultra-low load indentation," *Mater. Sci. Eng. A*, vol. 253, pp. 151–159, 1998.

[56] M. T. Laugier, "New formula for indentation toughness in ceramics," *J. Mater. Sci. Lett.*, vol. 6, no. 3, pp. 355–356, 1987.

[57] M. T. Dove, J. Singleton, A. M. Fox, S. J. Blundell, J. F. Annett, and R. A. L. Jones, *Magnetism in Condensed Matter Physics*. Oxford Master Series in Condensed Matter Physics, 2001.

[58] J. Stöhr and H. C. Siegmann, *Magnetism. From Fundamentals to Nanoscale Dynamics*. Springer Series, 2006.

[59] J. M. D. Coey, *Magnetism and Magnetic Materials*. Cambridge University Press, 2009.

[60] O. W. Richardson, "A mechanical effect accompanying magnetization," *J. Phys.*, vol. 4, p. 678, 1905.

[61] A. Einstein and W. J. de Haas, "Experimental proof of the existence of Ampère's molecular currents," *K. Akad. van Wet.*, vol. 18, pp. 696–711, 1915.

[62] J. R. Friedman, M. P. Sarachik, J. Tejada, and R. Ziolo, "Macroscopic measurement of resonant magnetization tunneling in high-spin molecules," *Phys. Rev. Lett.*, vol. 76, no. 20, pp. 3830–3833, 1996.

[63] E. M. Chudnovsky and J. Tejada, *Macroscopic Quantum Tunneling of the Magnetic Moment*. Cambridge University Press, 1998.

[64] T. Ueno, H. Tsuruta, T. Saito, A. Watanabe, T. Ishimine, and K. Yamada, "Practical and potential applications of soft magnetic powder cores with superior magnetic properties," *SEI Tech. Rev.*, no. 82, pp. 9–15, 2016.

[65] C. Chang, Y. Dong, M. Liu, H. Guo, Q. Xiao, and Y. Zhang, "Low core loss combined with high permeability for Fe-based amorphous powder cores produced by gas atomization powders," *J. Alloys Compd.*, vol. 766, pp. 959–963, 2018.

[66] O. Gutfleisch, M. A. Willard, E. Br??ck, C. H. Chen, S. G. Sankar, and J. P. Liu, "Magnetic materials and devices for the 21st century:

Stronger, lighter, and more energy efficient," *Adv. Mater.*, vol. 23, no. 7, pp. 821–842, 2011.

[67] J. Tejada and X. Zhang, "Experiments in quantum magnetic relaxation," *J. Magn. Magn. Mater.*, vol. 140–144, no. PART 3, pp. 1815–1818, 1995.

[68] D. Villuendas Pellicero, "Magnetic deflagrations in Mn 12 -ac and new techniques and phenomena," Univeristy of Barcelona, 2015.

[69] S. Tumanski, *Handbook of Magnetic Measurements*, vol. 96, no. 2395. CRC Press, 2011.

[70] B. Zhou, Y. Dong, L. Liu, L. Chang, F. Bi, and X. Wang, "Enhanced soft magnetic properties of the Fe-based amorphous powder cores with novel TiO 2 insulation coating layer," *J. Magn. Magn. Mater.*, vol. 474, no. October 2018, pp. 1–8, 2019.

[71] K. J. Sunday and M. L. Taheri, "Soft magnetic composites: recent advancements in the technology," *Met. Powder Rep.*, vol. 72, no. 6, pp. 425–429, 2017.

[72] R. Lebourgeois, C. Le Fur, M. Labeyrie, M. Paté, and J. P. Ganne, "Permeability mechanisms in high frequency polycrystalline ferrites," *J. Magn. Magn. Mater.*, vol. 160, pp. 329–332, 1996.

[73] J. Calvo-de la Rosa, J. Tejada, and A. Lousa, "Structural and impedance spectroscopy characterization of Soft Magnetic Materials," *J. Magn. Magn. Mater.*, vol. 475, pp. 570–578, 2019.

[74] J. R. Macdonald, "Impedance Spectroscopy," *Ann. Biomed. Eng.*, vol. 20, pp. 289–305, 1992.

[75] T. Nakamura, "Snoek's limit in high-frequency permeability of polycrystalline Ni – Zn , Mg – Zn , and Ni – Zn – Cu spinel ferrites," *J. Appl. Phys.*, vol. 88, no. 1, p. 348, 2000.

[76] J. L. Snoek, "Dispersion and absorption in magnetic ferrites at frequencies above one Mc/s," *Physica*, vol. 14, no. 4, pp. 207–2017, 1948.

[77] J. L. Xie, M. Han, L. Chen, R. Kuang, and L. Deng, "Microwave-absorbing properties of NiCoZn spinel ferrites," *J. Magn. Magn. Mater.*, vol. 314, no. 1, pp. 37–42, 2007.

[78] H. J. Kwon, J. Y. Shin, and J. H. Oh, "The microwave absorbing

and resonance phenomena of Y-type hexagonal ferrite microwave absorbers," *J. Appl. Phys.*, vol. 75, no. 10, pp. 6109–6111, 1994.

[79] P. Debye, "Zur Theorie der spezifischen Wärmen," *Ann. Phys.*, vol. 344, no. 14, pp. 789–839, 1912.

[80] R. Garrappa, F. Mainardi, and G. Maione, "Models of dielectric relaxation based on completely monotone functions," *Fract. Calc. Appl. Anal.*, vol. 19, no. 5, 2016.

[81] K. S. Cole and R. H. Cole, "Dispersion and absorption in dielectrics, vol. I. Alternating current field," *J. Chem. Phys.*, vol. 9, no. 4, pp. 341–351, 1941.

[82] K. S. Cole and R. H. Cole, "Dispersion and absorption in dielectrics: II. Direct current characteristics," *J. Chem. Phys.*, vol. 10, no. 2, pp. 98–105, 1942.

[83] D. W. Davidson and R. H. Cole, "Dielectric Relaxation in Glycerine," *J. Chem. Phys.*, vol. 18, no. 10, p. 1417, 1950.

[84] D. W. Davidson and R. H. Cole, "Dielectric Relaxation in Glycerol, Propylene Glycol, and n-Propanol," *J. Chem. Phys.*, vol. 19, no. 12, p. 1484, 1951.

[85] J. Dong, "Terahertz imaging for nondestructive evaluation and material characterization," Georgia Institute of Technology, 2017.

[86] J. C. Wheatcroft, "Terahertz Time-Domain Spectroscopy and Fresnel Coefficient Based Predictive Model," Kent State University, 2012.

[87] Zomega Terahertz Corporation, "The Terahertz Wave eBook Fundamentals of Terahertz Wave," 2012.

[88] B. Ferguson and X. C. Zhang, "Materials for terahertz science and technology," *Nat. Mater.*, vol. 1, no. 1, pp. 26–33, 2002.

[89] R. Cheng, D. Xiao, and A. Brataas, "Terahertz Antiferromagnetic Spin Hall Nano-Oscillator," *Phys. Rev. Lett.*, vol. 116, no. 20, pp. 1–5, 2016.

[90] R. Khymyn, I. Lisenkov, V. Tiberkevich, B. A. Ivanov, and A. Slavin, "Antiferromagnetic THz-frequency Josephson-like Oscillator Driven by Spin Current," *Sci. Rep.*, vol. 7, no. March, pp. 1–10, 2017.

[91] H.-E. Peiponen *et al.*, *Terahertz spectroscopy and imaging*. Springer Series in Optical Sciences The, 2013.

[92] M. Naftaly and R. E. Miles, "Terahertz time-domain spectroscopy for material characterization," *Proc. IEEE*, vol. 95, no. 8, pp. 1658–1665, 2007.

[93] J. Dong, X. Wu, A. Locquet, and D. S. Citrin, "Terahertz Superresolution Stratigraphic Characterization of Multilayered Structures Using Sparse Deconvolution," *IEEE Trans. Terahertz Sci. Technol.*, vol. 7, no. 3, pp. 260–267, 2017.

[94] J. Dong *et al.*, "Visualization of subsurface damage in woven carbon fiber-reinforced composites using polarization-sensitive terahertz imaging," *NDT E Int.*, vol. 99, no. July, pp. 72–79, 2018.

[95] J. Wang, J. Zhang, T. Chang, L. Liu, and H. L. Cui, "Terahertz nondestructive imaging for foreign object detection in glass fibre-reinforced polymer composite panels," *Infrared Phys. Technol.*, vol. 98, no. February, pp. 36–44, 2019.

[96] M. Wang and E. H. Yang, "THz applications of 2D materials: Graphene and beyond," *Nano-Structures and Nano-Objects*, vol. 15, pp. 107–113, 2018.

[97] G. B. Jung *et al.*, "Terahertz spectroscopy of nanocrystal-carbon nanotube and -graphene oxide hybrid nanostructures," *J. Phys. Chem. C*, vol. 114, no. 25, pp. 11258–11265, 2010.

[98] C. Seco-Martorell, V. López-Domínguez, G. Arauz-Garofalo, A. Redo-Sanchez, J. Palacios, and J. Tejada, "Goya's artwork imaging with Terahertz waves," *Opt. Express*, vol. 21, no. 15, p. 17800, 2013.

[99] B. Michael, E. W. Van Stryland, D. R. Williams, and W. L. Wolfe, *Handbook of Optics*, 2nd ed. Optical Society of America, 1995.

[100] W. J. Tropf, M. E. Thomas, and T. J. Harris, "Properties of Crystals and Glasses," in *Handbook of Optics*, 3rd ed., OSA, 2009, p. 100.

[101] M. Scheller, C. Jansen, and M. Koch, "Applications of Effective Medium Theories in the Terahertz Regime," in *Recent Optical and Photonic Technologies*, no. January, 2010, p. 450 pp.

[102] L. Jylhä and A. Sihvola, "Equation for the effective permittivity of particle-filled composites for material design applications," *J.*

Phys. D. Appl. Phys., vol. 40, no. 16, pp. 4966–4973, 2007.

[103] C. F. Bohren, "Applicability of Effective_Medium Theories to Problems of Scattering and Absorption by Nonhomogeneous Atmospheric Particles," *J. Atmos. Sci.*, vol. 43, no. 5, 1985.

[104] G. A. Niklasson, C. G. Granqvist, and O. Hunderi, "Effective medium models for the optical properties of inhomogeneous materials," *Appl. Opt.*, vol. 20, no. 1, p. 26, 2008.

[105] E. P. Parrott, J. A. Zeitler, and L. F. Gladden, "Accurate determination of optical coefficients from chemical samples using terahertz time-domain spectroscopy and effective medium theory," *Opt. Lett.*, vol. 34, no. 23, p. 3722, 2009.

[106] R. Ruppin, "Evaluation of extended Maxwell-Garnett theories," *Opt. Commun.*, vol. 182, no. 4, pp. 273–279, 2000.

[107] J. C. Maxwell Garnett, "Colours in Metal Glasses and in Metallic Films," *R. Soc.*, vol. 203, no. 359–371, pp. 385–420, 1904.

[108] J. C. Maxwell Garnett, "Colours in Metal Glasses and in Metallic Films in Metallic Solutions - II," *R. Soc.*, vol. 205, no. 387–401, pp. 237–288, 1905.

[109] V. A. Markel, "Introduction to the Maxwell Garnett approximation: tutorial," *J. Opt. Soc. Am. A*, vol. 33, no. 7, p. 1244, 2016.

[110] D. A. G. Bruggeman, "Calculation of various physics constants in heterogenous substances," *Ann. Phys.*, vol. 24, pp. 636–664, 1935.

CHAPTER III

EXPERIMENTAL METHODOLOGY AND MATERIALS

1. INTRODUCTION

This chapter is devoted to the description of the methods, materials and devices used to perform the experimental work of this Thesis. This work is essentially experimental, and the data obtained has been always processed and adjusted to physical models in order to better understand the studied properties.

Furthermore, it must be pointed out that this chapter describes the processes that have been personally performed and represent an important contribution to this Thesis. On the other hand, those measurements done by collaborators or sporadically used are commented when used.

2. DESIGN OF EXPERIMENTS (DoE)

The design of experiments approach has been used as a crucial tool, specially in Chapter IV, in order to optimize the synthesis conditions. As it will be later reasoned, two variables are studied: time and temperature of the thermal treatment.

To do so, a Full Factorial Design 2^k has been selected, with $k = 2$. Thus, in each planned DoE, four experiments have been performed in random order. The experimental matrix used in all cases – as a function of the minimum and maximum values for time (t_{min}, t_{max}) and temperature (T_{min}, T_{max}) – has been the one shown in Table 3. 1.

Table 3. 1. Experimental matrix structure used to optimize the synthesis of copper ferrite.

Experiment	Time level (minutes)	Temperature level (°C)
1	t_{min}	T_{min}
2	t_{max}	T_{min}
3	t_{min}	T_{max}
4	t_{max}	T_{max}

The quantified response (Y) in this study has been the copper ferrite content, i.e. its purity. With the result of each experiment, the model described in Equation 3. 1 has been applied in order to simulate the response values in all the factor space.

$$Y = b_0 + b_1 T + b_2 t + b_{12} T t \qquad \text{Equation 3. 1}$$

where t and T represent, respectively, time and temperature values.

3. SYNTHESIS AND PELLETS PREPARATION

The preparation of new materials in this project has been usually made in powder form, but their properties have been evaluated in either powder or bulk. The specifications and conditions of the synthesis of copper ferrite nanoparticles and preparation of new soft magnetic composites will be given later in Chapter IV and Chapter VI, respectively. These processes have been adapted from other references or fully self-developed to accomplish with our targets, and thus are considered as part of the results obtained in this work. However, here are defined the materials, devices and tools used in each kind of material preparation.

3.1. Powder materials fabrication

3.1.1. Copper ferrite nanoparticle's synthesis

For both synthesis methods (sol-gel and co-precipitation) the used metal salt precursors have been the same: iron nitrate ($Fe(NO_3)_3 \cdot 9H_2O$, *Labkem*) and copper nitrate ($Cu(NO_3)_2 \cdot 3H_2O$, *Labkem*). Both reactants have been used as received, without further purification. Distilled water has been always used as the solvent media.

Additionally, other substances have been used in a particular way in each synthesis approach. In the sol-gel process, the gelling agent used has been polyvinylpyrrolidone, *PVP* ($(C_6H_9NO)_n$, *Sigma-Aldrich*). On the other hand, for the co-precipitation synthesis, octanoic acid ($C_8H_{16}O_2$, *Scharlab*) was used in preliminary experiments (it will be later explained in Chapter IV that it was not used for the final samples), and sodium hydroxide (NaOH, *VWR Chemicals*) as basic solution.

In both cases, all the thermal processes (either gel-burning or calcination) have been done in a *Carbolite CWF1300* furnace, while drying processes have been done in a *JP SELECTA* drying oven. The centrifugation processes to clean the co-precipitation samples have been done in an *MSE PACISA* centrifuge.

3.1.2. Soft Magnetic Composites (SMCs) fabrication

For the preparation of novel SMCs, two precursor materials have been used: (i) commercial iron micrometric particles, provided by AMES enterprise; (ii) magnetite nanoparticles (Fe_3O_4, *SigmaAldrich*) with a particle size distribution < 50 nm. Furthermore, ethanol has been used, in the required cases (see Chapter VI), as the liquid media where particles have been dispersed to be mixed by means of ultrasound agitation. Agitation has been done with a *Sanitas SUR 42* ultrasound system.

3.2. Pellets fabrication

In some cases, these powder materials have been processed to fabricate solid pellets in order to perform specific measurements. We have worked with two different shapes: (i) circular and (ii) toroidal shaped pellets.

3.2.1. Compaction

To fabricate them, a certain amount of powder material (usually around 0.5g for ferrites, and 3g for the metallic micrometric particles) is first weighted in an analytical balance before being introduced in the die. In the case of ferrites, the obtained product from sol-gel after the gel burning process is used, without further calcination. The circular-shaped mould has a diameter of 13 mm, while the toroidal-shaped one was self-designed, and has an inner diameter of 7.2 mm and an outer diameter of 13.8 mm. Depending on the material processed, different presses have been used (which are placed in different departments) for practical purposes. Copper ferrite pellets have been pressed in the press shown in Figure 3. *3*.A at 50 bar (5 MPa), while SMC powders have been compacted in the press shown in Figure 3. *3*.B under 700 kg/cm^2 (~ 69 MPa). Due to the low toughness of the ceramic materials, higher pressures could not be applied to the ferrite powders in order to avoid delamination of the green pellet.

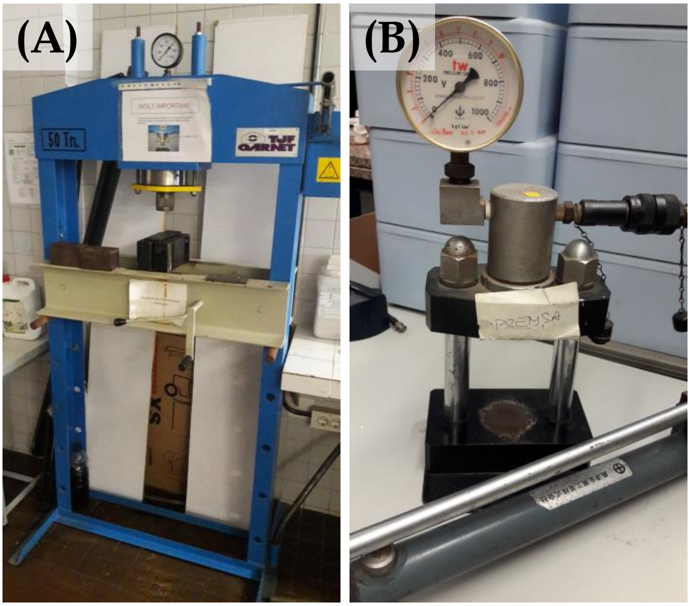

Figure 3. 1. Presses used for pellets preparation. (A) Press used for ferrite powder, located in the Department of Materials Science and Physical Chemistry, and (B) press used to process the metallic powder, which is in the Department of Condensed Matter Physics (Magnetism and Microwaves Laboratory).

At this point, we should point out that a polymeric lubricant (*Dry Lube-F CRC*) was used to process the metallic powder, while it was avoided when conforming the ceramic samples in order to prevent problems with the furnace during the following high temperature processes. Moreover, its absence does not have a big repercussion because of the low degree of adhesion of this material with the die, due to its little ductility.

3.2.2. Thermal processing

Once the powder is pressed, pieces with the desired shape are obtained. However, their properties are still not the desired ones – from a mechanical stability point of view – and are known as “green” pellets. Thermal treatments under certain conditions, which depend on each material, allow to obtain bulk samples with the desired characteristics.

These processes have been different for each sample. In the case of ceramic pellets, copper ferrite in our case, a strong sintering process is necessary to physically bond the particles and form a solid with mechanical integrity. These treatments have been performed in a *HOBERSAL MOD XG3-17* furnace for long periods of time and at high temperatures. The specific conditions are later commented in Chapter IV. The methodology used for the sintering consists on:

- Heating from room temperature to 500 °C at 5 °C/minute and keep this temperature for 2 hours.
- Heating from 500 °C to 800 °C at 5 °C/minute and keep this temperature for 2 hours.
- Heating from 800 °C to the setpoint temperature at 5 °C/minute and keep this temperature for the necessary time.
- Cooling down to room temperature with the slowest rate possible (furnace turned off).

The idea has been to perform a slow heating and cooling process to avoid producing thermal stresses on the sample and to allow it to accommodate the best possible. The first step at 500 °C should allow the sample to eliminate any possible remaining organic matter from the synthesis process. Then, the long time at 800 °C allows the structure to accommodate the generated stresses due to the temperature gradient, and to avoid the generation of defects. Finally, the sample is heated to the desired temperature to produce solid-state atomic diffusion, followed by a slow cooling to room temperature to favour the slow relaxation process.

In the case of the metallic soft magnetic powder, the sintering process is not necessary because of the high ductility of this material. The obtained bulk pieces are mechanically stable by themselves. However, they need to be annealed before being technologically aplied. This process makes the grain grow and reduces the stress induced in the structure produced by the compaction, leading to an increase of the permeability and frequency stability [1], [2]. The annealing conditions were set around 15 minutes at 400 °C in nitrogen atmosphere, following the recommendations provided by AMES enterprise. Other authors have proved that the isolating shell in composite materials decomposes above 500 °C, leading to a decrease of its resistivity and, thus, an increase of the power losses [3], [4]. These annealing processes have been done in the laboratory-made tubular furnace shown in Figure 3. 2, with a nitrogen flow adjusted to ensure an overpressure in the chamber.

Figure 3. 2. Tubular furnace used for the annealing treatments with N_2 atmosphere.

4. X-RAY DIFFRACTION

X-ray diffraction has probably been the most important technique used in this work for revealing the crystal structure of the fabricated materials, and for quantifying the relative composition of each crystalline phase.

4.1. Sample preparation

An adequate sample preparation is crucial to do a successful phase identification and Rietveld refinement. A correct sample preparation should allow to obtain all the desired parameters with the minimum preparation steps [5].

Depending on the physical state of the sample, two types of preparation have been done:

- **Powder samples.** Powder samples have been first manually grounded in order to avoid agglomeration. Then, the powder has been frontally added in a standard rectangular sample holder of 20 mm of length, 15 mm of width and 2 mm of width (PW1172/01). A glass plate has been used to ensure a flat frontal surface. Figure 3. 3 shows the powder finally assembled in the holder.

- **Bulk samples.** Those samples which were previously sintered in bulk form (see Chapter IV) have been directly measured. These samples have been mounted over a handmade glass sample holder and fixed by means of silicon paste. The assembly has been then clamped with the flat bracket stage.

  Bulk samples have been measured with two different morphologies: circular and toroidal shaped. It is important to mention that, in the second case, it is not possible to ensure that the illuminated volume is the same in all samples due to their geometry.

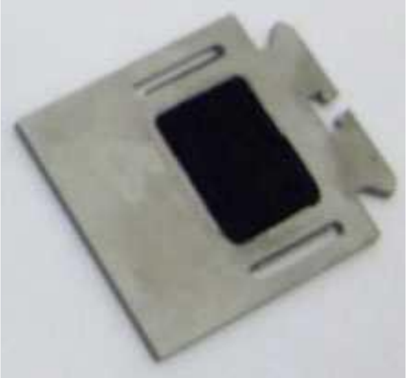

Figure 3. 3. Powder sample prepared in a standard rectangular sample holder. Adapted from [6].

Moreover, for the temperature dependent XRD measurements (see next section for further measurement details) the preparation consisted on a manual pressing of the powder sample, by means of a glass plate, in order to get a flat surface in a cylindrical alumina sample holder of 16 mm of diameter and 0.4 mm of height.

4.2. XRD measurements

All the measurements in this Thesis have been performed by the technicians of the X-ray diffraction unit of *Centres Científics i Tecnològics* of University of Barcelona (CCiT-UB).

All the examined samples have a high Fe content. In order to avoid Fe fluorescence problems, a *PANalytical X'Pert PRO MPD θ/θ Bragg-Brentano* powder diffractometer of 240 millimetres of radius, with a secondary graphite flat crystal monochromator, has been used [6], [7]. Moreover, all the experiments have been done using Cu K_α radiation (λ = 1.5418 Å).

During the various stages of the research, different XRD measurements have been done with different goals. Their characteristics are:

- **Standard.** These measurements have been done routinely in order to verify the crystal structure and crystalline phases in all the prepared samples. The degree of statistics is low, so it is not possible to reveal the microstructure (crystallite size and macrostrain), or to obtain high quality phase quantification by Rietveld refinement. Nevertheless, these measurements have enough quality to reveal the crystal structure and the relative phase composition in each sample.
- **Improved statistics.** These measurements have been extremely interesting in order to have high-quality XRD data to perform deeper Rietveld refinement, and thus to be able to determine the microstructure of the sample. In this case, more and longer measurements have been done, thus giving a higher degree of statistics. This test has only been performed in strategic samples which were considered important to know the formed structure.
- **Temperature dependent.** By these measurements, XRD patterns have been measured as a function of the temperature, allowing to study the formation of crystalline phases during the thermal treatment.

  Here, the sample has been warmed from 28ºC up to 950 ºC, and cooled from 950 ºC to 28 ºC at a constant rate of 60 °C per minute. Measurements have been performed in a *High Temperature Chamber Anton Paar HTK1200N* every 50 °C, in air (oxidant) conditions.

Table 3. 2 additionally specifies the other parameters used for each type of measurement. Notice the longer measurement times for the improved statistics method.

Table 3. 2. Measurement settings used for each of the three measurement strategies used.

Setting	**Standard**	**Improved statistics**	**Temperature dependent**
Illuminated length in the beam direction (variable automatic divergence slit)	10 mm	10 mm	10 mm
Length of the beam over the sample in the axial direction (mask)	12 mm	12 mm	12 mm
Work power	45 kV – 40 mA	45 kV – 40 mA	45 kV – 40 mA
$\theta/2\theta$ scan range	10° – 110°	10° – 152°	10° – 100°
2θ step size	0.017°	0.017°	0.017°
Measuring time	50″	160″	42″
Repeated scans	1	5	1

4.3. Phase identification

The observed XRD data has been analysed by different ways. In the first step, the present crystalline samples have been identified by using the *HighScore X'Pert software* and the *Powder Diffraction Files* (PDF) from the *Crystallography Open Database* (COD).

This process consists of three main steps:

(i) Determine background. A polynomic function is fitted to the experimental background, so this intensity will not be later considered in the peak analysis.
(ii) Search peaks. By doing the derivative of the observed data and looking for zeros, the software proposes where the peaks are. It is crucial to define correctly the minimum intensity and minimum/maximum width values that are required to

consider a peak; otherwise, background or noisy data could be confounded with a peak.

(iii) Phase identification. Once the peaks are identified, their position and relative intensities are used to look in the PDF database for those files with higher coincidence. The coincidence between the experimental data and each PDF is expressed by the software with the *Score (%)* parameter. Even though the candidates are ordered by their *Score (%)*, one must analyse the coincidence between the experimental data and the candidate before accepting it as a phase present in the sample.

4.4. Rietveld refinement

The Rietveld refinement has been done by using *FullProf Suite* software. For doing a refinement, three different files are needed: (i) XRD data file (.xrdml) with the measured data, (ii) Crystallographic Information File (CIF) with all the crystallographic parameters (iii) Instrumental Resolution Function (IRF) to consider the peak broadening due to the instrument.

First the CIF files of the desired phases (those previously identified by *HighScore X'Pert*) have been download from the COD webpage [8]. Then, these CIF files need to be converted to PCR, which are the ones that *FullProf Suite* uses to control the refinement. The IRF file must be loaded to the software at this point, in order to take into account, the instrumental contribution on the observed peaks widths.

A refinement process may be a demanding and tough work, and cannot be simply resumed in a list of tasks which directly drives to a successful refinement. It is needed to continuously evaluate the results in each refinement step, and to decide which variable should be modified. Nevertheless, a basic guidance of the method and the variables involved consists on refining: (i) zero and displacement, (ii) scale factor, (iii) cell parameters (a, b, c, α, β, and γ), (iv) atomic positions (x, y, and z), (v) B-iso parameters (atomic or overall), (vi) occupancy factor, (vii) shape parameters (U, V, W, X, and Y in a Pseudo-Voigt function), (viii) preferred directions (if needed), and (ix) background.

As commented before, this is not a mechanical process and requires a continuous evaluation by the user and re-refining of variables. In this process, there are some direct relationships that need to be considered when doing the refinement.

- Peaks' positions are defined by unit cell dimensions (Bragg's law). Thus, displacements in 2θ must be corrected by adjusting the cell parameters.
- The relative intensity between phases depends on the scale factor.
- The presence of crystallographic preferred orientations can lead to peaks with higher intensities than expected.
- Amplitude of the peaks might be adjusted with the Pseudo-Voigt function parameters.
- An incorrect peak shape definition can generate problems on the relative intensity of the peaks.

Finally, apart from the qualitative human inspection of the profile, the change in statistical parameters such as R_B (%) (Equation 2.38) and χ^2 (Equation 2.37) need to be checked in order to evaluate the mathematical improvement of the fitting.

The improved statistic data have been used to precisely define the crystal structure, which has been later used as a starting point when refining the standard measurements.

5. PARTICLE SIZE DISTRIBUTION

The particle size analysis has been, together with the compositional and crystallographic characterization made by XRD, the other technique used routinely to study the formation of the prepared materials.

5.1. Sample preparation

All the powder samples have been dispersed in distilled water by means of manual and ultrasonic agitation for two minutes prior to the analysis. No dispersing agents have been added due to the good short-term stability of the suspension.

5.2. Laser Diffraction measurements

Laser Diffraction (LD) technique has been used to study the particle size distribution. More specifically, a *Beckman Coulter LS 13 320* analyser from the CCiT-UB has been used with the liquid module configuration. The stability of the particles' suspension has been checked every time by performing three consecutive scans, with an elapsed time of 60 seconds between them.

6. SCANNING ELECTRON MICROSCOPY

Scanning Electron Microscopy (SEM) has been used as a powerful tool to qualitatively check the particles' size and their morphology. Moreover, chemical analysis has been also done by means of Energy Dispersive X-ray Spectroscopy (EDS).

6.1. Sample preparation

Two different sample preparations have been carried out depending on the observation goal. First, when observing the ferrite nanoparticles synthesized in Chapter IV, the powder has been directly deposited on an adhesive sheet placed on the sample holder. Due to the high resistivity of ferrites, all these samples have been covered with a thin carbon layer to avoid retaining electrons (i.e. to charge the sample). On the other hand, the soft magnetic composites are expected to have a core-shell structure

[9]. To view this structure, powder samples have been embedded in the carbon-based conductive resin *PL-RCZ0016* from *Polirresin*. This resin piece has been first ground, and then polished in order to reveal the powder core. The first process has been done with silicon carbide papers, commonly with successive grift levels of 240, 800 and 1200. Polishing has been first done using a suspension of 6 μm diamond particles, and then with another one of 1 μm particles. These samples have not been covered with carbon due to the conductive nature of the core. The isolating shell is expected to be isolating, so by this way its conductive nature may be also corroborated.

6.2. Equipment

The devices used for these observations have been the *Jeol J-6510* (indicated as Jeol in the following chapters), the *ESEM Quanta 200 FEI, XTE 325/D8395* (named Quanta in the following chapters) and the *FESEM JEDL J-7100* (referred as *Field-Emission* in the following chapters), both from CCiT-UB.

7. NANOINDENTATION

Nanoindentation technique has been used to study the mechanical properties (E and H) of various copper ferrite samples prepared under different conditions.

7.1. Sample preparation

The bulk pellets fabricated from the ferrite from have been used for nanoindentation measurements. These pellets have been embedded in PolyFast conductive resin from *Struers* by hot methods. Prior to mechanical characterization, the specimens have been first ground and subsequently polished using silicon carbide papers, followed by diamond suspensions until 3 µm, and a last step using colloidal alumina. After that, the polished specimens have been carefully cleaned ultrasonically with acetone for 10 minutes and dried with pure air. Finally, optical microscopy is used to check the surface. Figure 3. 4 shows an example of one of the prepared samples at the end of this process.

Figure 3. 4. Copper ferrite pellet embedded in resin and prepared for nanoindentation tests.

7.2. Nanoindentation measurements

The samples mounted in resin are mounted in cylindrical aluminium sample holders, which are at the same time settled in the platform shown in Figure 3. 5.A. In this image two fused silica samples can also be seen, which have a known Young's modulus of 72 GPa, and are used to calibrate the tip before each batch of tests. The nanomechanical test has been performed with a *Nanoindenter® XP System* (*MTS*) with a *continuous stiffness measurement* mode (CSM) module incorporated, allowing a dynamic determination of the mechanical properties during the indentation process. 25 imprints (5x5 matrices) have been done in each sample in order to get statistical signification at 2000 nm of maximum displacement into the surface, or until reaching a maximum applied load of 650 mN. Imprints have been separated 50 µm in order avoid overlapping effects. The strain rate has been held constant at 0.05 s^{-1} and the indenter shape has been calibrated for true indentation depth as small as 25 nm by indenting fused silica standard. A Berkovich tip has been used, and *H* and *E* have been calculated by using the Oliver and Pharr model [10]. As the specimen is a ceramic material, its Poisson's ratio ν has been set to 0.3 in all the measurements [11].

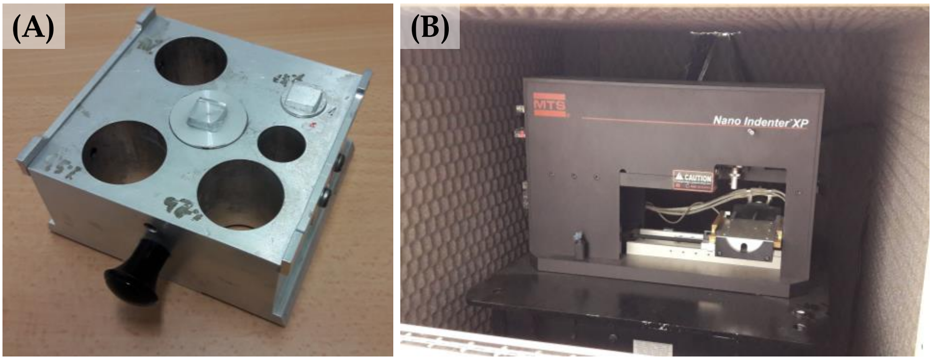

Figure 3. 5. (A) Sample holder with two fused silica (reference) samples, and (B) Nanoindenter® XP System.

8. MAGNETIC MEASUREMENTS

The study of the static magnetic properties has been an important part of the work done in this Thesis. A variety of different measurements, where the magnetization *M* has been studied as a function of the applied magnetic field *H*, the temperature *T*, and time *t*.

8.1. Sample preparation

This type of magnetic measurements can be done to measure both, powder and bulk samples. Furthermore, small amounts of sample are enough to perform the experiment, usually from few to tens of milligrams. The amount of needed sample depends on its magnetization, as it is necessary to ensure that the magnetization during the measurements is in the detection range of the device.

The sample that wants to be measured is placed in a gelatine capsule, which does not interact with the applied magnetic field. It must be ensured that the sample does not move during the measurement due to the forces generated by the magnetic field. To do so, the capsule is usually filled with cotton - which in non-magnetic - to fix the sample position, as it is shown in Figure 3. 6.

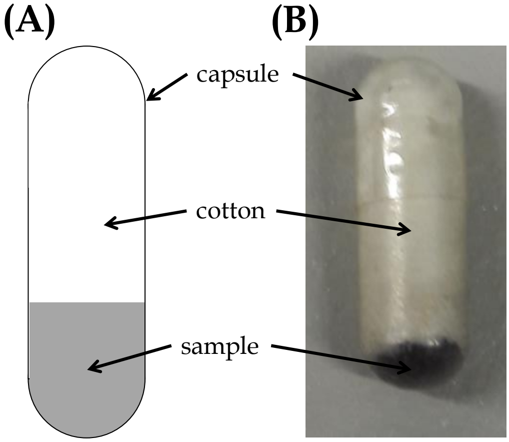

Figure 3. 6. (A) Scheme of the mounting of a sample in a capsule, and (B) real sample prepared for performing magnetic measurements.

8.2. Magnetic measurements

The magnetic measurements have been performed by using a *SQUID MPMS Quantum Design magnetometer*. The results presented in Chapter VIII where obtained with our own SQUID magnetometer from the Grup de Magnetisme (see Figure 3. 7), whereas the SQUID magnetometer from CCiT-UB has been used for the measurements presented in Chapter IV, V, and VI due to technical difficulties. Both devices are the same model of SQUID.

In a typical measurement, the capsule with the sample is introduced in the SQUID by the sample transport system (see Figure 2.25) until it is placed between the superconducting coils. Before starting the measurements, the signal must be examined to perfectly place the sample in the central position between the coils. If not, the measured signal would not be representative of the real magnetization of the sample.

Figure 3. 7. SQUID magnetometer of the Magnetism Group from University of Barcelona.

8.2.1. Measurement protocol

The instructions given to the SQUID magnetometer (i.e. the experimental conditions) for each of the different types of performed measurements are described below.

a) Hysteresis cycle, $M(H)$

In the hysteresis cycle, the dependence of the magnetization M with the magnetic field H is studied at a constant temperature T ($M(H)_T$). Thus, first the desired temperature is set with zero field. Once the temperature is stable, magnetic field is increased up to a maximum defined value, where the saturation magnetization M_S is expected to be reached. M values are recorded as H increases. Once M_S is reached, H is reduced until reaching the value of the maximum magnetic field previously applied but in the opposite direction. Ideally, H is inverted another time until reaching again the first positive maximum magnetic field to measure the whole cycle. However, sometimes in this Thesis we have only measured half of the cycle as it already provides information about M_S, M_R and H_C. Moreover, as the hysteresis cycle is symmetric, the whole curve can be easily calculated from the first half.

b) Zero-Field Cooled – Field-Cooled, ZFC – FC

The ZFC – FC measurements are done when it is desired to investigate the existence of anisotropy energy barriers of the system, as M is studied as a function of T at a constant H ($M(T)_H$).

In these measurements, the temperature is decreased to low values (usually 2 K in our experiments) at H = 0. Once this minimum temperature is reached, a certain H is applied (which must be much smaller than the anisotropy field) and the temperature progressively increases until reaching 300 K. M is recorded during this temperature change. This first curve is called the *zero-field cooled* (ZFC). From this curve, we can deduce the blocking temperature (T_B), which defines the start of the superparamagnetic behaviour. Once 300 K are reached, the temperature is decreased again to the minimum one, keeping the applied H. From the difference between both curves, it is possible to deduce the anisotropy energy barriers of the system and, in case of having single domain particles (SDP), their particle size distribution [12].

c) Magnetic relaxation, $M(t)$

Magnetic relaxation measurements are a type of measurements that allow to determine the demagnetizing behaviour of a material from M_S once H is removed. From these measurements, it is possible to study the dependence of the magnetic viscosity S with T, and to observe the presence of quantum effects such as magnetic tunnelling [13]–[15]. In these measurements, M is recorded as a function of the time t at a constant T and H = 0 ($M(t)_{T,\,H=0}$).

In a typical experiment, the desired temperature is first set at H = 0. Once this temperature is stable, the saturation field H_S (i.e. the needed H to reach M_S) is applied. In the $M(t)$ experiments presented in Chapter V, H_S = 1.5 T (15 kOe). Once the M_S is reached, H is removed, and M is recorded as a function of t. In the experiments presented in Chapter V, a small demagnetizing field is applied contrary to the magnetization in order to overcome the intrinsic remanent magnetization of the SQUID magnetometer.

9. IMPEDANCE SPECTROSCOPY

Impedance spectroscopy measurements have been of immense importance in this work as they have provided information about the frequency dependence of the complex magnetic permeability (μ). The obtained results from these measurements are of technological importance because they test the magnetic response of the material when the magnetic field is switched.

9.1. Sample preparation

In order to perform impedance spectroscopy measurements, it is needed to work with bulk toroidal-shaped samples. To prepare a toroid it is necessary to follow the compacting process previously described in this chapter. Once a toroid is fabricated, a copper wire is wound around it, and this system is at the same time welded into a support to ensure good electrical contact (see Figure 3. 8). The total number of turns has always been close to 15 in order to avoid capacitance problems between them. If the sample is conductive - as it happens with the metallic soft magnetic materials studied in Chapter VI – the toroid is coated with Teflon in order to avoid a short circuit between the sample and the copper wire. The insulating behaviour of the toroid and the good electrical contact with the support are tested with a voltmeter before each experiment.

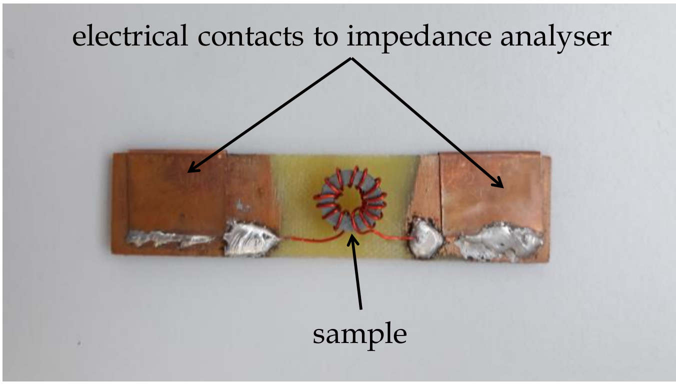

Figure 3. 8. Toroid sample wounded with a copper wire and welded to the contact support.

9.2. Impedance measurements

The device used for the impedance measurements is a *HP 4192 A impedance analyser*, which is shown in Figure 3. 9. The use of this device is a courtesy of Dr. Arturo Lousa, from the Department of Applied Physics and Optics at Universitat de Barcelona. The sample support is connected to the impedance analyser by the contacts located at the bottom left side of the image. This device generates an AC electric current that pass through the copper solenoid, which generates an ac magnetic field on the toroid. This device is usually manually controlled, but in order to improve the precision of the data acquisition, increase the number of measured points, and reduce the measurement time a self-made LabView® program has been developed. This software remotely controls the impedance analyser and defines 165 logarithmically spaced frequencies in the range from 1 kHz to 13 MHz where the measurements are done. In each of these frequencies, the impedance modulus $|Z|$ and phase θ are measured. From these values, the real Z' and imaginary Z'' components of impedance may be deduced by means of Equation 3. 2.

$$Z(\nu) = |Z|e^{i\theta} = Z'(\nu) + Z''(\nu)i \qquad \text{Equation 3. 2}$$

Figure 3. 9. Impedance analyser used for the impedance spectroscopy measurements from 1 kHz to 13 MHz.

9.3. Permeability calculation

The magnitude experimentally measured is impedance (*Z*), but it needs to be converted to permeability (μ) in order to evaluate the magnetic response at these frequencies. It can be easily calculated by means of Equation 3. 3 and Equation 3. 4 [16].

$$\mu_r' = \frac{L'(\nu)}{L_0} = \frac{Z''(\nu)}{\nu L_0} \quad \text{Equation 3. 3}$$

$$\mu_r'' = \frac{L''(\nu)}{L_0} = \frac{Z'(\nu)}{\nu L_0} \quad \text{Equation 3. 4}$$

where μ_r' is the real component of the relative permeability, μ_r'' is the imaginary component, *L* is the complex inductance, and L_0 is the inductance of the empty toroid. L_0 depends on the number of wire turns (*N*) around the toroid, and its dimensions (inner radius r_{in}, outer radius r_{out}, and high *h*), as described in Equation 3. 5. μ_0 is the vacuum permeability.

$$L_0 = \frac{\mu_0 N^2 h \ln\left(\frac{r_{out}}{r_{in}}\right)}{2\pi} \qquad \text{Equation 3. 5}$$

9.4. Relaxation model fitting

The obtained complex permeability values have been fitted to the Davidson-Cole (DC) relaxation model. From this comparison, the parameters μ_S, n, and τ have been calculated for each sample. The adjustment of these parameters to fit the experimental data has been done with a self-developed *Python*® software, which tests all the possible combinations of these values in a previously defined range – in order to ensure physically logic magnitudes - and provides the combination that minimizes the residual function defined by Equation 3. 6. Moreover, the experimental parasite currents (C_P), which affects to the measured *Z''*, have also been determined by this fitting.

$$R = \frac{\sum_{i=}^{n}\left(\mu_i^{exp} - \mu_i^{mod}\right)^2}{n} \qquad \text{Equation 3. 6}$$

9.5. Power losses

Loss tangent ($\tan(\delta) = \mu_r''(\nu)/\mu_r'(\nu)$) is a common calculation to compare the lost and the stored power. However, the dissipated power in each cycle corresponds to Equation 3. 7 [16].

$$\langle P(t)\rangle_t = \frac{1}{2} I_0^2 L_0 \nu \mu_r''(\nu) \qquad \text{Equation 3. 7}$$

being I_0 the intensity. The intrinsic material factor $L_0 \nu \mu_r''(\nu)$ has been calculated for each sample in order to consider their power losses. This factor has units of ohms (Ω), as in the dissipated ac power is $\langle P(t)\rangle_t = \frac{1}{2} I_0^2 R$.

10.TERAHERTZ SPECTROSCOPY

THz time-domain spectroscopy (THz-TDS) has been used in this Thesis to study the optical and dielectric properties of different oxides. With this technique, properties such as the absorption coefficient (α), the refractive index (n), the complex relative permittivity ($\hat{\varepsilon}_r$), and the electric conductivity (σ) are deduced for each material in the THz frequency range, usually from 100 GHz to 10 THz.

This work has been done during an international research stay at Georgia Tech Lorrain in Metz (France). All THz experiments have been carried out in the facilities of the Photonics and Terahertz Group, of the School of Electrical and Computer Engineering of the Georgia Institute of Technology.

10.1. Sample preparation

THz-TDS measurements are usually carried out in transmission mode. The measurement of materials which highly attenuate the signal may lead to a null or poor signal amplitude on the detector side. This is a common problem with oxide materials. To solve that, powder samples are dispersed in a matrix made of a low absorption material in order to increase the transmitted signal. A common host material is polyethylene (PE), which is transparent at THz frequencies.

The studied oxides by THz-TDS have been copper oxide (CuO) and zinc oxide (ZnO), two semiconductor materials. Both oxides have been obtained in powder form from *Inoxia Ltd.* (Cranleigh, UK). PE powder used is *Inducos 13/1* (particle size < 80 µm) purchased from *TeraView Ltd.* (Cambridge, UK).

The sample preparation has been done by Dr. Denis Bouscaud and Dr. Sophie Berveiller from the Laboratoire d'Etude des Microstructures et de Mécanique des Matériaux in Metz. To fabricate the samples, a certain amount of oxide material and 360 g of PE have been weighted in a microbalance and manually mixed. Then, a 13 mm diameter evacuable pellet die from *Specac* has been filled with the mixture and a force of 25 kN has been applied to compact the pellet. An example of the obtained pellets is shown in Figure 3. 10.

Figure 3. 10. 13 mm diameter pellet prepared by mixing the oxide powder and 360g of PE.

Pellets with different amounts of oxides - what is known as *weight filling factor*, f_W - have been prepared for each oxide. As the *effective medium models* (EMMs) operate with the fraction of volume occupied by each phase, the *volume filling factor* (f_V) has been calculated for each sample by applying Equation 3. 8. Moreover, the *porosity* (P) of each pellet has been approximated by considering the density of the host material (ρ_{host}) and the one from the oxide inclusions (ρ_{incl}) (see Equation 3. 9 [17]).

$$f_V = \frac{\frac{f_W}{\rho_{incl}}}{\frac{f_W}{\rho_{incl}} + \frac{1 - f_W}{\rho_{host}}} \quad \text{Equation 3. 8}$$

$$P(\%) = 100 \cdot \left(1 - \frac{\rho_{exp}}{\rho_{ideal}}\right) = 100 \cdot \left(1 - \frac{\rho_{exp}}{f_V \rho_{incl} + (1 - f_V)\rho_{host}}\right) \quad \text{Equation 3. 9}$$

The considered densities have been 0.95g/cm^3 for PE, 5.61 g/cm^3 for ZnO, and 6.31 g/cm^3 for CuO.

10.2. THz-TDS measurements

For performing the experiments, pellets have been placed in the sample holder shown in Figure 3. 11.A, and lately measured by using a *TeraView*

TPS Spectra 3000 in transmission mode (Figure 3. 11.B). The experimental bandwidth (power spectrum of the THz pulses) extends from ~180 GHz to 3 THz. In order to avoid water-vapour absorption lines obscuring the spectra, the entire chamber where the sample holder is placed (Figure 3. 11.A) has been purged with N_2 for 10 minutes at a rate of 5 litres per minute. In each test, 1800 measurements have been averaged and the Blackman-Harris 3-term apodisation method [18] has been used to remove spectral artefact which are not related to sample absorption.

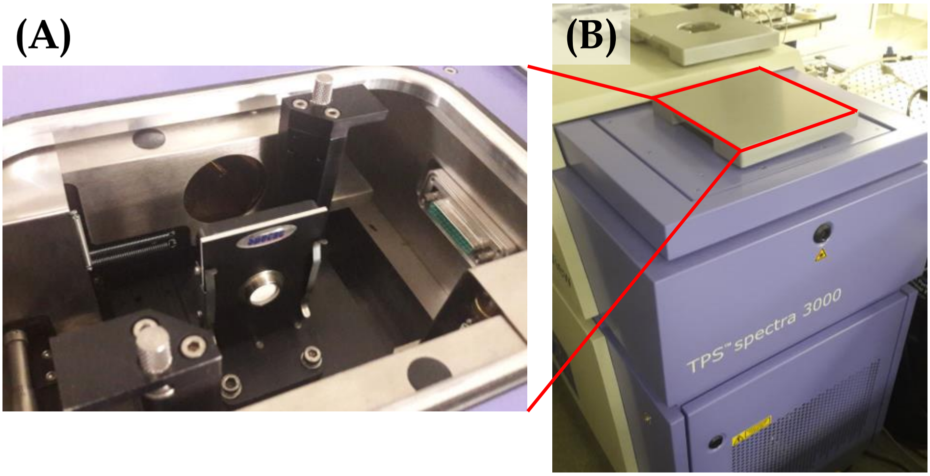

Figure 3. 11. (A)TPS Spectra 3000 device used for the THz-TDS measurements, and (B) cavity where the sample holder is placed, between the emitter and the receiver.

11.REFERENCES

[1] L. Qian, J. Peng, Z. Xiang, Y. Pan, and W. Lu, "Effect of annealing on magnetic properties of Fe/Fe 3 O 4 soft magnetic composites prepared by in-situ oxidation and hydrogen reduction methods," *J. Alloys Compd.*, vol. 778, pp. 712–720, 2019.

[2] X. Xie *et al.*, "Influence of annealing treatment on microstructure and magnetic properties of cold sprayed Ni-coated FeSiAl soft magnetic composite coating," *Surf. Coatings Technol.*, vol. 374, no. April, pp. 476–484, 2019.

[3] D. Liu, S. Gao, Y. Zhang, S. Yu, and F. Wang, "Microstructural and compositional evolution of core-shell FeSiAl composites during high-temperature annealing," *Ceram. Int.*, no. July, pp. 0–1, 2019.

[4] M. Huang, C. Wu, Y. Jiang, and M. Yan, "Evolution of phosphate coatings during high-temperature annealing and its influence on the Fe and FeSiAl soft magnetic composites," *J. Alloys Compd.*, vol. 644, pp. 124–130, 2015.

[5] J. M. Amigó *et al.*, *El método de Rietveld*. Publicacions de la Universitat Jaume I, 2006.

[6] X. Alcobé, "Calibratges instrumentals de difractòmetres de raigs x de pols," Universitat de Barcelona, 2007. PhD Dissertation.

[7] Y. M. Mos, A. C. Vermeulen, C. J. N. Buisman, and J. Weijma, "X-Ray Diffraction of Iron Containing Samples: The Importance of a Suitable Configuration," *Geomicrobiol. J.*, vol. 35, no. 6, pp. 511–517, 2018.

[8] D. Chateigner *et al.*, "Crystallography Open Database." [Online]. Available: http://www.crystallography.net/cod/. [Accessed: 04-Aug-2019].

[9] C. Oikonomou, "On Surface Characteristics and Microstructural Development of Soft Magnetic Composite Powder and Components," Chalmers University of Technology, 2015.

[10] W. C. Oliver and G. M. Pharr, "Measurement of hardness and elastic modulus by instrumented indentation: Advances in understanding and refinements to methodology," *J. Mater. Res.*, vol. 19, no. 01, pp. 3–20, 2004.

[11] J. J. Roa Rovira, "Mechanical Properties of Htsc At Micro / Nanometric Scale," University of Barcelona, 2010. PhD Dissertation.

[12] R. Zarzuela and G. Barbadillo, "Calculo Teorico de las curvas de FC y ZFC," 2013.

[13] J. Tejada and X. Zhang, "Experiments in quantum magnetic relaxation," *J. Magn. Magn. Mater.*, vol. 140–144, no. PART 3, pp. 1815–1818, 1995.

[14] E. M. Chudnovsky and J. Tejada, *Macroscopic Quantum Tunneling of the Magnetic Moment*. Cambridge University Press, 1998.

[15] J. R. Friedman, M. P. Sarachik, J. Tejada, and R. Ziolo, "Macroscopic measurement of resonant magnetization tunneling in high-spin molecules," *Phys. Rev. Lett.*, vol. 76, no. 20, pp. 3830–3833, 1996.

[16] J. Calvo-de la Rosa, J. Tejada, and A. Lousa, "Structural and impedance spectroscopy characterization of Soft Magnetic Materials," *J. Magn. Magn. Mater.*, vol. 475, pp. 570–578, 2019.

[17] H. Namkung, J. Kim, H. Chung, and M. A. Arnold, "Impact of pellet thickness on quantitative terahertz spectroscopy of solid samples in a polyethylene matrix," *Anal. Chem.*, vol. 85, no. 7, pp. 3674–3681, 2013.

[18] T. Lo, I. S. Gregory, C. Baker, P. F. Taday, W. R. Tribe, and M. C. Kemp, "The very far-infrared spectra of energetic materials and possible confusion materials using terahertz pulsed spectroscopy," *Vib. Spectrosc.*, vol. 42, no. 2, pp. 243–248, 2006.

CHAPTER IV

SYNTHESIS AND CHARACTERIZATION OF COPPER FERRITES

1. INTRODUCTION

According to the literature, copper ferrite ($CuFe_2O_4$) is expected to have an inverse spinel structure, either in its tetragonal (space group *I41/amd*) or cubic (space group *Fd-3m*) form [1]–[3]. This material has been selected for this study because of the high capabilities that spinel structures have to modify their structure, with the consequent repercussion on their physical properties. Its two possible crystal arrangements, as well as its inverse nature, allow to see differences on properties when changing the inversion parameter, i.e. the distribution of cations in the structure holes. Moreover, here we are dealing with two cations with really different effective magnetic moment (Cu^{2+} has $\sqrt{3}\,\mu_B$, while Fe^{3+} has $\sqrt{35}\,\mu_B$ [4], [5]), leading in significant magnetic properties change depending on their distribution. On the whole, this material is an excellent candidate to modify its structure and to study the variation on its physical properties.

In this chapter, $CuFe_2O_4$ nanoparticles are prepared by means of two chemical methods: polymer-assisted sol-gel method and co-precipitation. The main work is devoted to the development and optimization of a fast, versatile, easy, and up scalable sol-gel process, whereas in a second step the same particles are synthesized by means of co-precipitation in order to analyse the main advantages and drawbacks that each method has, as well as to determine how these experimental processes influence the physical characteristics of the sample. Sol-gel method is optimized by using DoE multivariable methods, with the main goal of obtaining the purest particles of nanometric size. In addition, the effect of the main variables in the synthesis process are analysed and discussed.

However, for some technological applications, it is important to have a solid piece of material capable to provide both, the needed functional properties and mechanical stability.

The study of the relationship between the mechanical and magnetic properties with the preparation conditions or the microstructural characteristics of the sample are commonly found in literature [6]–[11]. Nevertheless, it is much more difficult to find works directly correlating two properties [12]–[14], what is of major importance for designing novel materials in the industry sector. A direct relationship between the magnetic and mechanical properties – without passing through the chemical composition or microstructure – may provide new criteria in design processes. In materials selection two or more properties are compared at the same time to define which is the material with a better "balance" of properties for a specific application. For this reason, defining a direct correlation between the magnetic and mechanical properties may be of great interest for the design of novel materials for magnetic applications.

In this chapter, bulk pellets have been prepared following the procedure defined in Chapter III.3. In order to inspect how the sintering temperature affects to these properties, five different $CuFe_2O_4$ samples have been prepared at different sintering temperatures. Moreover, we have also prepared samples of each of the precursor oxides (CuO and Fe_2O_3) in order to understand the copper ferrite properties as its formation from both simple oxides.

2. CHAPTER OBJECTIVES

The first objective is to prepare high purity $CuFe_2O_4$ particles of nanometric size by a simple and fast chemical method. In this regard, the understanding of the effect that the different variables involved in the sol-gel synthesis have on the product is a key aspect. Therefore, we aim to define the optimum sol-gel conditions for the preparation of this material.

In addition, we pretend to investigate the co-precipitation synthesis method as an alternative to sol-gel. The main advantages and disadvantages of each process want to be defined, as well as to find the possible differences on the formed $CuFe_2O_4$. If there are differences, we expect to understand why they are produced in each case.

Finally, another important target here is to fabricate bulk samples from the previously produced powder. This process may allow to apply these materials in a wider variety of applications. We want to investigate how the processing affects to their mechanical and magnetic properties. Moreover, we aim to find empirical correlations between the magnetic and mechanical properties of this ferrite, what could become an interesting tool for further design and materials' selection processes.

3. SOL – GEL SYNTHESIS

With this synthesis method we aim to produce high-purity and nano-sized $CuFe_2O_4$ particles. The paper from Zakiyah *et al.* [15] has been considered as an starting point, but then the process has been continuously modified in order to accomplish with our goals, until reaching a final method.

In this section, the developed method for the sol-gel synthesis of $CuFe_2O_4$ nanoparticles is first presented. Then, two DoE cycles are planned in order to find the optimum synthesis conditions to obtain the desired nanoparticles. A first DoE examines a wide experimental domain, in order to clearly detect the effect of each of the variables, whereas the second DoE is focused close to the optimum region with the goal of getting more precise information. The chemical and structural characteristics, particle size, and magnetic properties of the obtained materials are also discussed.

3.1. Synthesis method

For the synthesis of $CuFe_2O_4$ nanoparticles by the polymer-assisted or sol-gel method, a specific amount of PVP (ratio 1:1 with the aimed $CuFe_2O_4$ mass) has been first dissolved in 200 mL of distilled water under stirring at room temperature for 2 hours. Then, stoichiometric amounts of copper and iron nitrate precursors have been added, and the solution has been further stirred at room temperature during 3 additional hours. After this time, the homogeneous solution has been heated at 80 °C for 24 hours in a drying oven in order to dry the sample and let the gelling agent to polymerize. Thus, a solid gel containing a homogeneous distribution of the metal ions is obtained. In order to eliminate the organic matter and obtain the desired oxide, the gel has been burned at 250 °C for 15 minutes in a furnace. The obtained product is further grounded to powder, and finally a thermal treatment is applied to each sample in order to form the complex ferrite under the conditions defined by each DoE plan.

It is worth to mention that one of the main contributions to this process has been the gel burning step. Initially, the gel was burned in a Bunsen burner, but it resulted in a process with low control and high dispersion on the manner each sample fired. It was later substituted by a burning process in an oven at 250 °C for 15 minutes, increasing then the capacity of control over the gel temperature. Moreover, the use of an oven instead of a Bunsen burner ensures a more homogeneous distribution of temperature (i.e. a lower temperature gradient) along the sample. However, the burning time of each sample may slightly change depending on, for example, the amount of water in the solution; despite the initial volume is always the same, some extra water is used when adding each reagent. In all cases, samples have been removed from the oven at their burning time, ranging from 10 to 15 minutes maximum.

3.2. Results and discussion

All the starting experiments have provided important information about the range of synthesis conditions of more interest. After checking that the effect of the amount of gelling agent (PVP in this case) is not as important as others, the time (X_1) and temperature (X_2) of thermal treatment have been defined as the two parameters to be optimized.

3.2.1. First DoE cycle

Considering the above exposed, the experimental matrix described in Table 4. 1 has been defined for the first optimization cycle by means of a 2^k design. The goal of this design is to maximize the purity of $CuFe_2O_4$.

Table 4. 1. Experimental matrix for the first optimization cycle.

Experiment	Time level (minutes)	Temperature level (°C)
1	15	750
2	120	750
3	15	950
4	120	950

a) <u>Structural and compositional analysis</u>

The experiments from Table 4. 1 have been performed in random order, and each one of these samples has been analysed by standard powder XRD measurements. Figure 4. 1 shows the diffraction patterns obtained for each sample.

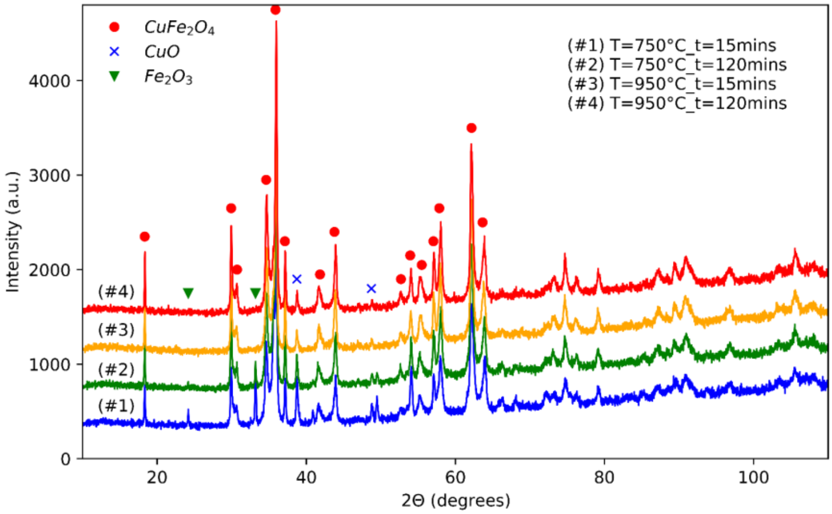

Figure 4. 1. *XRD* patterns of the four experiments corresponding to the first DoE. All the patterns have been intentionally displaced 400 units in intensity to facilitate their simultaneous visualization. The different markers indicate the 2θ positions of the main peaks of the present crystalline phases.

The phase identification process reveals the presence of a predominant tetragonal $CuFe_2O_4$ phase, and less abundant rhombohedral Fe_2O_3 (also known as α-Fe_2O_3, or *hematite*) and monoclinic CuO (also known as *tenorite*). The presence of these secondary phases is in good agreement with those found by other authors [16].

There are some clear tendencies regarding the relative intensity of the peaks of the different phases. For instance, the two Fe_2O_3 peaks decrease or even disappear at harder thermal treatments. However, it is difficult to clearly appreciate the changes in this figure. Figure 4. 2 provides higher magnification images of some of the more representative peaks in order to allow a better comparison.

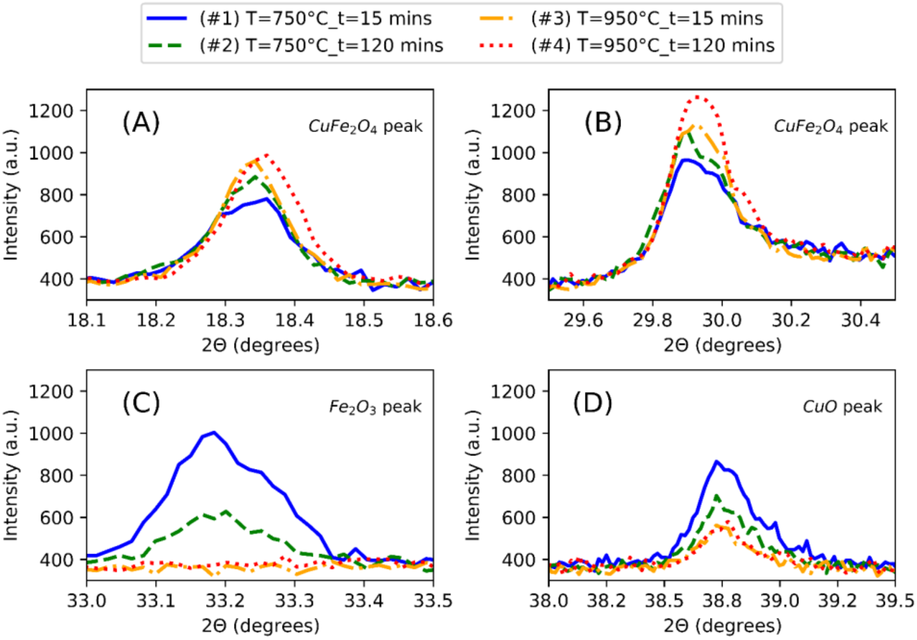

Figure 4. 2. Zoomed representation of some of the more representative peaks of the crystalline phases present in the samples from the first DoE. (A) and (B) are $CuFe_2O_4$ peaks, (C) is a Fe_2O_3 peak, and (D) is a CuO peak.

By analysing Figure 4. 2.A and Figure 4. 2.B one may notice that the intensity of the peaks corresponding to the main $CuFe_2O_4$ tetragonal phase increase at higher temperatures and longer times. Samples are perfectly ordered according to their thermal treatment conditions: sample #4 is the more intense, sample #1 is the one with lower $CuFe_2O_4$ content, meanwhile #2 and #3 have intermediate intensities. By focusing the attention in the two intermediate samples, we can see that the sample prepared at 950 °C (#3) is more intense than the one at 750 °C (#2), even though the treatment time in #2 is considerably larger than in #3; it suggests that the effect of temperature is stronger than the one of time, and thus high purity samples might be obtained by using short treatments at high temperatures. The same trends are observed in an opposite way when studying the intensity of the peaks of Fe_2O_3 and CuO. Figure 4. 2.C shows how Fe_2O_3 completely disappears at 950 °C, whereas Figure 4. 2.D still shows some contents of CuO at this temperature.

These samples have been also refined by the Rietveld method in order to obtain more accurate information about their crystal structure and relative phase composition. Figure 4. 3 shows the results obtained for one of these samples.

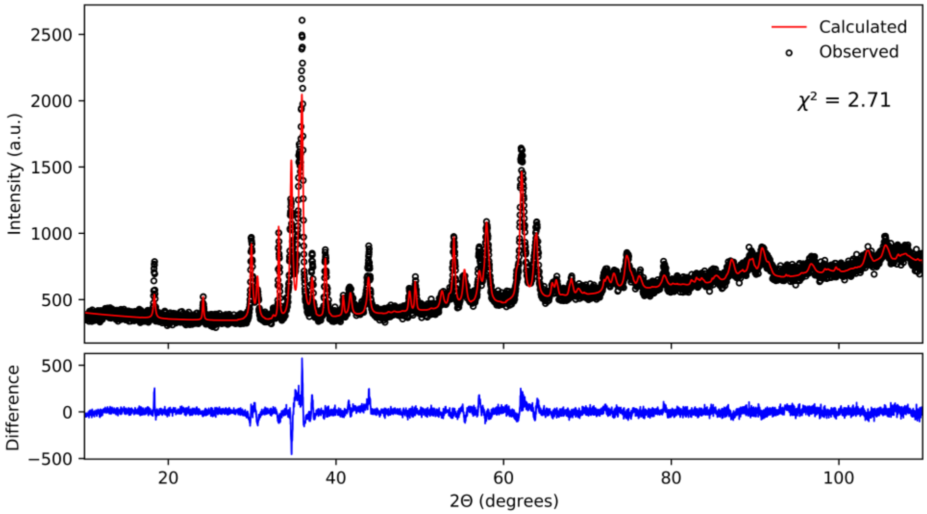

Figure 4. 3. Rietveld refinement for sample #1 of the first DoE. The top figure shows the observed and calculated data, meanwhile the bottom one represents their difference.

As can be observed, the relative intensity between peaks of the same phase is not accurate. This might be due to the presence of preferred crystallographic orientation (which are unexpected in a powder sample), or because the considered structural model for the calculation is not fully strict with the reality. Nevertheless, as the scale factor, peak shape, and unit cell parameters are correctly adjusted, the results are rigorous with the relative composition of each sample. The predominant $CuFe_2O_4$ tetragonal phase has unit cell dimensions of approximately a = b = 5.83 Å and c = 8.65 Å. Table 4. 2 summarizes the qualitative composition results and the obtained χ^2 values for each Rietveld refinement.

Table 4. 2. Samples' compositions obtained from the Rietveld refinement for each of the samples from the first DoE.

Experiment	$CuFe_2O_4$ (%)	CuO (%)	Fe_2O_3 (%)	χ^2
1	70.3	8.4	21.3	2.71
2	83.3	5.7	11.0	2.87
3	95.5	4.5	0.0	3.02
4	96.0	4.0	0.0	3.08

Again, the formation of $CuFe_2O_4$ and consumption of CuO and Fe_2O_3 at high temperatures and long times is confirmed, as could be expected from a thermodynamic point of view.

Once the % of $CuFe_2O_4$ is known, Equation 2.5 can be applied in order to obtain the response model. The obtained values are b_0 = 86.3, b_1 = 3.4, b_2 = 9.5, and b_{12} = - 3.1. Then, it is possible to predict the product purity (Y) at any point in the area between the tested experimental points. A graphical representation of these coefficients, as well as the simulation of the expected purity, are shown in Figure 4. 4.

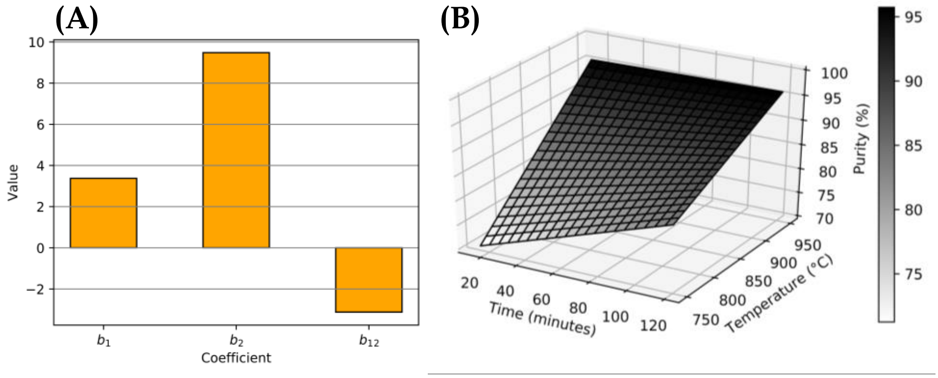

Figure 4. 4. (A) Obtained parameters for b_1, b_2 and b_{12}; (B) simulated values with the model, for the first DoE.

By analysing the coefficients' values it is possible to extract two main conclusions: (i) the temperature at which the calcination is done (b_2) has approximately three times the impact on the chemical composition than the time (b_1), as was predicted analysing the XRD pattern in Figure 4. 2; (ii) the magnitude of the interaction variable (b_{12}) is of the order of magnitude of b_1, so - apart from the individual effects - there is a considerable interaction between both variables.

b) Particle size and morphology

In order to study the effect that these variables have on the particle size, Figure 4. 5 shows the number and volume particle size distributions for each sample obtained by LD.

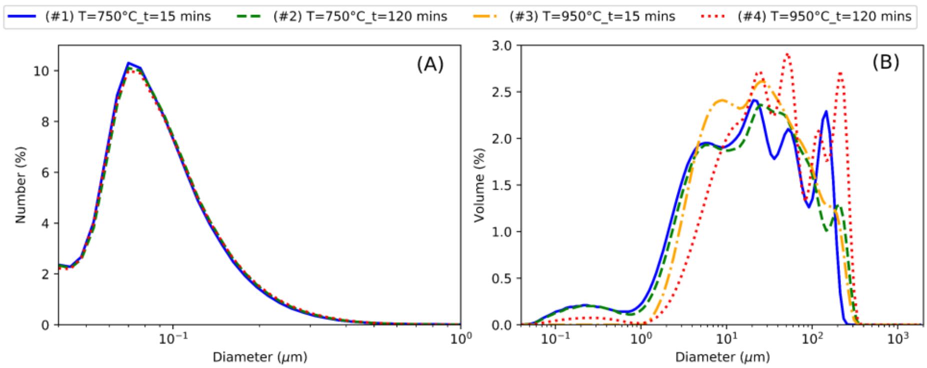

Figure 4. 5. Particle size distribution of the first DoE: (A) represented as a function of the number of particles, and (B) as the percentage of volume that each diameter represents in the whole sample.

We can consider all the samples to be of nanometric size as the number distribution (i.e. most of the particles) is centred under 100 nm. On the other hand, the major part of the volume of the sample is occupied by micrometer-sized particles. We can attribute this double effect to two different origins: (i) most of the particles are nanometric, but there are others (much lower in number) which are orders of magnitude bigger and have a greater influence when representing the volume fraction (it would happen in a synthesis process with an extremely low degree of control); (ii) nanoparticles have been formed but then they get attached to each other by thermal processes (i.e. sintering) forming micrometric clusters. The shape of the volume distribution indicates that different distributions coexist in the sample. This effect suggests that the formation of clusters is the origin of these micrometric bodies. Otherwise, if micrometric particles would have been formed, a more continuous distribution should be expected. Moreover, as LD principles assume having spherical particles, the different superposed peaks could also be originated by irregular-shaped particles, something common when agglomeration is present.

The physical aspect of the particles is inspected by SEM. Figure 4. 6 shows some of the obtained images, where it is possible to get information about the formation of these particles.

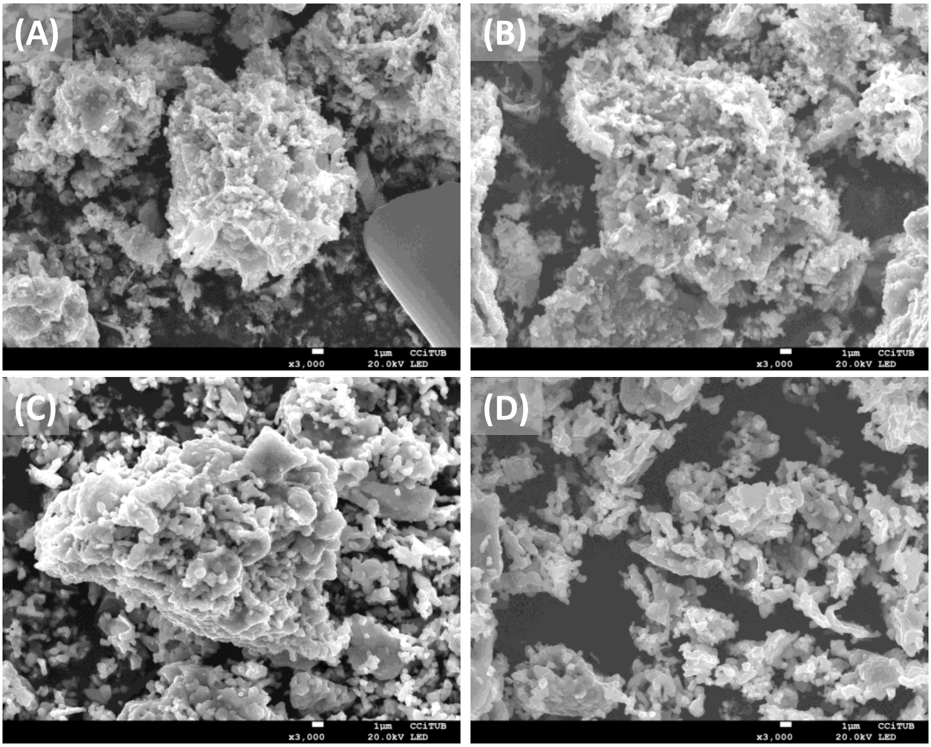

Figure 4. 6. SEM images with secondary electrons at x3000 magnification of all the powder samples of the first DoE: (A) sample #1, (B) sample #2, (C) sample #3, and (D) sample #4.

There is a common trend present in the four samples: the formation of micrometric clusters by the agglomeration of submicrometric particles. The morphology of these clusters suggests sintering between the smaller particles, forming physical bridges between them. This effect is much more clearly seen in Figure 4. 7, which is an image at higher magnification of sample #1.

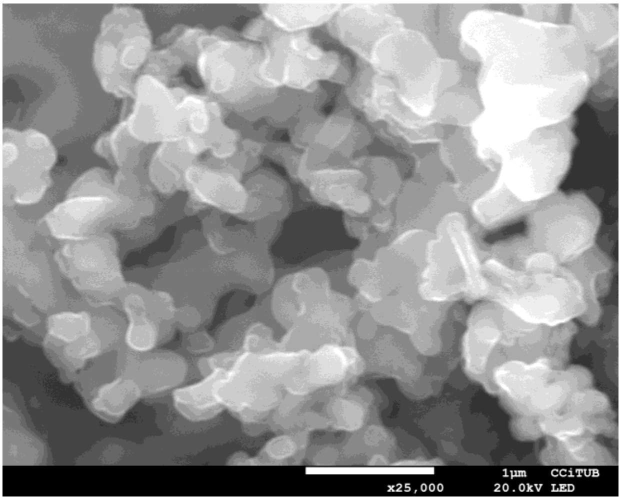

Figure 4. 7. SEM image obtained with secondary electrons at x25000 magnification of sample #1 of the first DoE.

Here, the nanometric particles sintering each other forming solid 3D clusters, is more clearly seen. These results verify the arguments previously presented from LD results. Also, in each one of the samples the size distribution of aggregates is wide, and their shape is irregular, in good agreement with the volume LD results.

Now it is clear that small particles have been synthesized, but due to the thermal treatment effect they act as building blocks that sinter each other forming bigger agglomerates. Furthermore, by looking below the big aggregates (back in Figure 4. 6) it is possible to find a distribution of particles which is smaller in size than the individual particles that form the agglomerates. This smaller distribution may be representative of those nanometric particles that have not sintered with others, keeping by this way their original size. Despite the shape of the aggregates is irregular, individual nanoparticles seem to be spherical-shaped.

All these results are in good agreement with those from the LD particle size analysis and have been already observed in previously mentioned works [16]–[19]. Therefore, number % distributions can be understood as a representation of the size of the formed particles, meanwhile the volume % distribution gives information about the sintering process between the previously formed nanoparticles.

Once the real meaning of each representation has been checked, it is time to come back to Figure 4. 5. In the number % representation there is almost no difference between the size distribution of the nanoparticles prepared at different conditions. The resolution of the measurement is bigger than the difference produced by the different conditions. The mean value of these distributions is 93.3 ± 0.7 nm. On the other hand, by studying the volume % distributions it is clearly seen how the distribution is progressively shifted to bigger diameters as the calcination intensifies. Despite it consists in the superposition of different peaks, the main distribution has a clear dependence on the thermal treatment conditions. Consequently, the effect that it has on the sintering between particles is demonstrated, which increases at higher temperatures and longer times.

With all these results, it has been seen the inverse effect that these conditions have on the final goal of this work: when the thermal treatment is more intense, purity and sintering between particles increases; for soft thermal treatments, the sintering is lower but less pure ferrites are obtained. Therefore, it is needed to find an optimum balance between both variables in order to have high purity products and, at the same time, reduce as much as possible the sintering between nanoparticles.

c) Magnetic properties

Finally, the magnetic hysteresis cycle has been measured. As can be appreciated in Figure 4. 8, only the first magnetization curve and the demagnetization from the positive to the negative saturations have been measured. As the hysteresis cycle has a symmetric behaviour when the magnetic field is reversed, these conditions are enough for determining the interesting properties here.

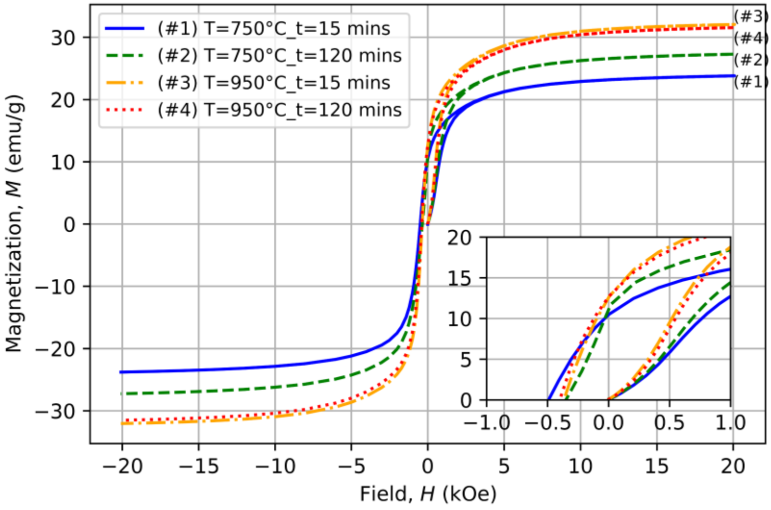

Figure 4. 8. $M(H)$ measurements at 300 K for the samples of the first DoE. The inner plot is a zoomed representation of the data close to the origin of coordinates, in order to better visualize μ, M_R, and H_C.

These results clearly show how M_S, M_R, and μ increase for harder thermal treatments, according to the formation of $CuFe_2O_4$ detected by XRD. There is a strong dependence on the treatment time for all these magnetic properties when the sample is prepared at 750 °C, meanwhile there is a weaker or inexistent time dependence when the sample is prepared at 950 °C. Additionally, H_C has the same increasing tendency, except for the case of sample #1, which shows the larger coercivity value. All the quantitative results are summarized in Table 4. 3.

Table 4. 3. Magnetic properties of the samples of the first DoE.

Experiment	M_S (emu/g)	M_R (emu/g)	H_C (Oe)
1	23.7	10.5	491.3
2	27.2	11.1	349.6
3	31.9	12.6	365.8
4	31.4	12.7	400.3

3.2.2. Second DoE cycle

With these results in mind, another DoE has been planned to get more detailed information in the region close to the optimum. Considering that there are not significant differences in the size of the formed nanoparticles, and the results from the DoE represented in Figure 4. 4.B, the region where higher purities have been found is zoomed. The new conditions are defined in Table 4. 4.

Table 4. 4. Experimental matrix for the first optimization cycle.

Experiment	Time level (minutes)	Temperature level (°C)
1	30	850
2	120	850
3	30	950
4	120	950

d) <u>Structural and compositional analysis</u>

Again, all the samples have been first characterized by XRD in order to reveal their composition and crystal structure. The results are compared in Figure 4. 9.

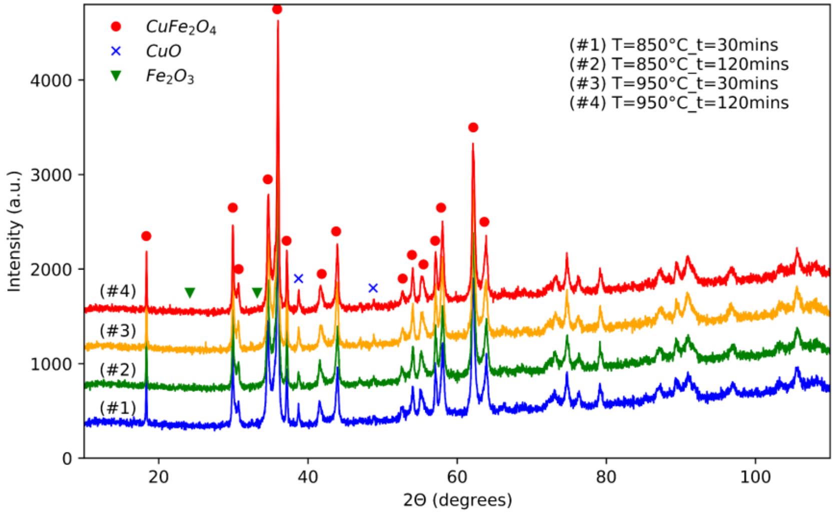

Figure 4. 9. XRD patterns of the four experiments corresponding to the second DoE. All the patterns have been intentionally displaced 400 units in intensity to

facilitate their simultaneous visualization. The different markers indicate the 2θ positions of the main peaks of the present crystalline phases.

All the analysed samples have the same predominant tetragonal $CuFe_2O_4$ phase described for the first batch, but with smaller traces of CuO and Fe_2O_3. It is worth to notice that the characteristic peaks of these undesired phases have considerably been reduced and are difficult to be detected with this view. Again, in order to make a better comparison between the different synthesis conditions, some peaks are zoomed and shown in Figure 4. 10. The selected peaks are the same than those in Figure 4. 2.

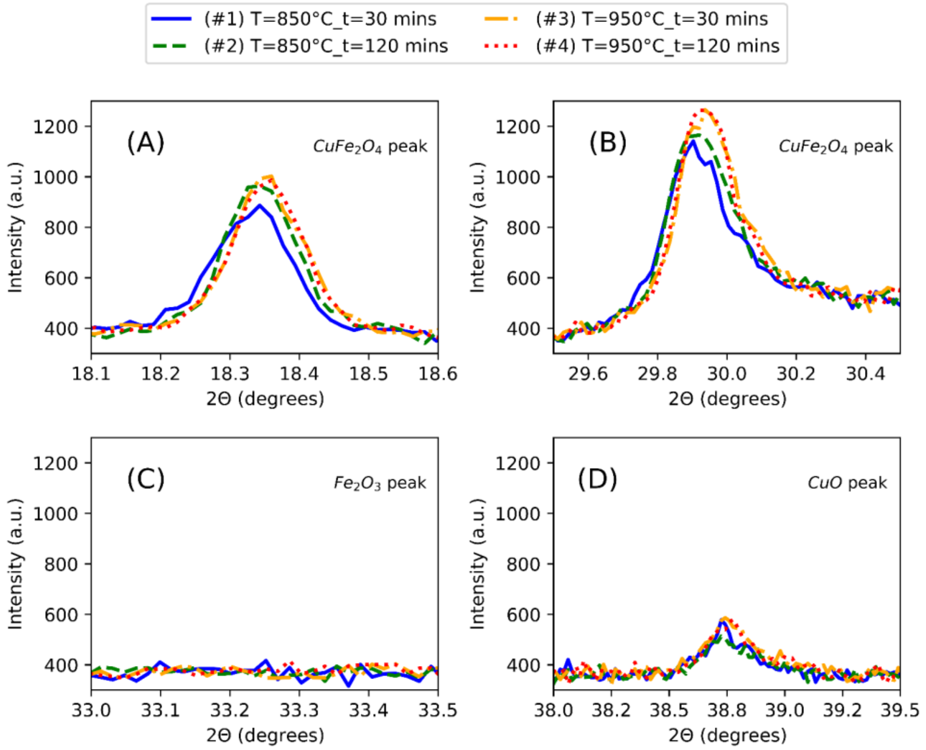

Figure 4. 10. Zoomed representation of some of the more representative peaks of the crystalline phases present in the samples from the second DoE. (A) and (B) are $CuFe_2O_4$ peaks, (C) is a Fe_2O_3 peak, and (D) is a CuO peak.

By analysing Figure 4. 10.A and Figure 4. 10.B, it can be seen than all the $CuFe_2O_4$ peaks are almost equally intense, despite for the case of sample #1. Additionally, when looking in more detail, one may see that sample #2 is slightly less intense than those prepared at 950 °C (#3 and #4), even though the differences are not large. In these samples prepared at 950 °C, the intensity is roughly the same, independently of the thermal treatment time. The intensity in Figure 4. 10.C, which corresponds to a Fe_2O_3 peak, is inexistent for the four samples, giving a good idea about the purity improvement in this batch. Finally, Figure 4. 10.D indicates that all the samples still have some CuO traces, which are almost the same in all of them. In order to have more detailed information, the samples have been refined by the Rietveld method. Figure 4. 11 shows the profile fitting done for one of the samples, and Table 4. 5 contains the refined values.

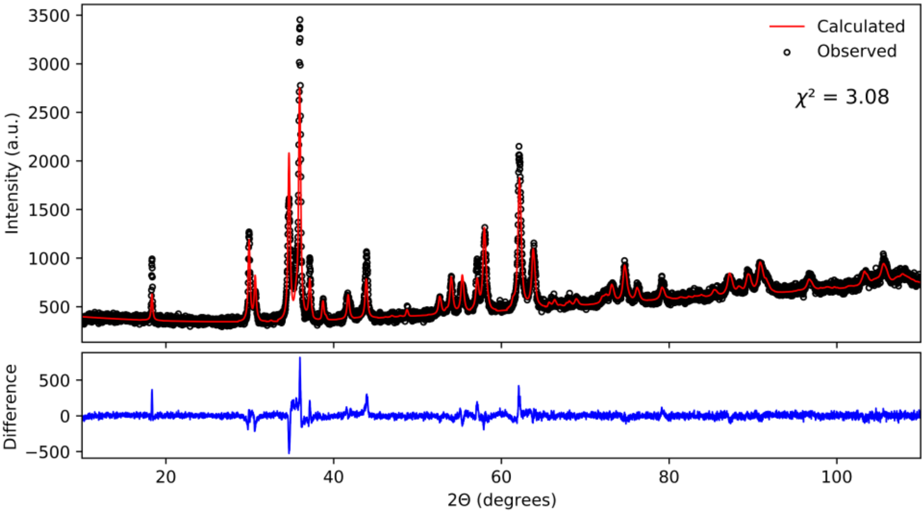

Figure 4. 11. Rietveld refinement for sample #4 of the second DoE. The top figure shows the observed and calculated data, meanwhile the bottom one represents their difference.

Table 4. 5. Samples' compositions obtained from the Rietveld refinement for each of the samples from the second DoE.

Experiment	$CuFe_2O_4$ (%)	CuO (%)	Fe_2O_3 (%)	χ^2
1	96.1	3.9	0.0	3.22
2	96.4	3.6	0.0	3.18
3	95.8	4.2	0.0	3.26
4	96.0	4.0	0.0	3.08

Rietveld refinement confirms what was suggested before: the purity is excellent in all the samples and all the values are extremely similar. These small differences are not significant and are influenced by the small differences on the profile fitting quality. The mean purity value is 96.1 ±

0.2 %. The similarity in these results suggests that, in this conditions range, a maximum purity is reached.

When these experimental responses are used to deduce the model described in Equation 1.5, the parameters obtained are: b_0 = 96.1, b_1 = 0.1, b_2 = - 0.2, and b_{12} = 0.0. The graphical representation of these values, and the simulation done with them, are represented in Figure 4. 12:

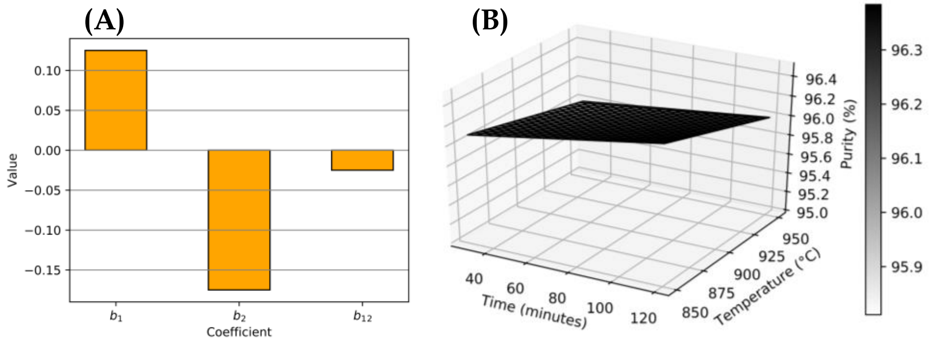

Figure 4. 12. (A) Obtained parameters for b_1, b_2 and b_{12}; (B) simulated values with the model, for the second DoE.

In this second design of experiments, the obtained coefficients are substantially lower than those obtained for the first design. In contrast with the first batch, now the relative value of b_{12} compared to b_1 and b_2 is much lower. These results are consistent with the fact that the chemical composition is almost constant in this range. Moreover, the surface represented in Figure 4. 12.B is almost constant between the studied conditions. Despite it may seem that there is some slope, it should be considered the small differences in ferrite purity, indicated in the vertical axis. Finally, in order to check the obtained model results, an extra sample with intermediate conditions has been prepared and characterized. This sample has been prepared at 900 °C for 60 minutes, and the purity obtained by Rietveld refinement is of 96.1% with χ^2 = 3.01. This chemical composition is in excellent accordance with the predicted values under the same conditions (96.1%) and, hence, the model is validated.

Our purity results are higher than those maximum values reported in the literature for similar synthesis methods [16], [19], [20]. However, it should be mentioned here that the processes described in these references achieve maximum temperatures of 800 °C, whereas the minimum one in this second DoE is of 850 °C. As has been previously proved, an increase of the temperature between 750 °C and 850 °C can lead to an increase of the ferrite conversion %. Nevertheless, with this second DoE we prove that a plateau in composition is reached at 850 °C. On the other hand, all these works agree on the formation of the tetragonal phase of $CuFe_2O_4$ under these conditions range.

e) <u>Particle size and morphology</u>

The particle size distribution has also been analysed by means of LD, as Figure 4. 13 shows.

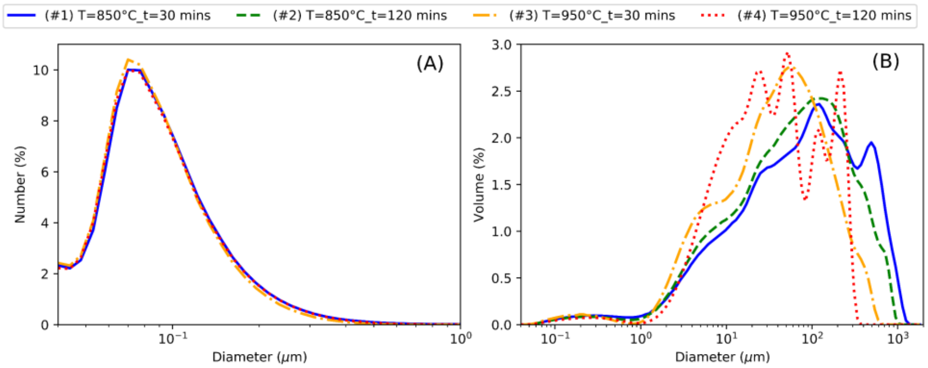

Figure 4. 13. Particle size distribution of the second DoE: (A) represented as a function of the number of particles, and (B) as the percentage of volume that each diameter represents in the whole sample.

Again, the nanometric nature of these particles is confirmed because the number % distribution is centred below 100 nm in all cases. No clear differences are detected between samples, which have a mean value of 93.1 ± 1.4 nm. These results are of the same order than those obtained for the first batch. Regarding the volume % distribution, it is seen a curious behaviour: those samples prepared at lower temperatures (#1, #2) are displaced to bigger sizes. The inverse tendency has been seen in the previous set of samples. On the other hand, the aspect of the patterns suggests that the distributions are more homogeneous when the sample is prepared at lower temperatures, which corresponds to a lower degree of particles' sintering and agglomeration.

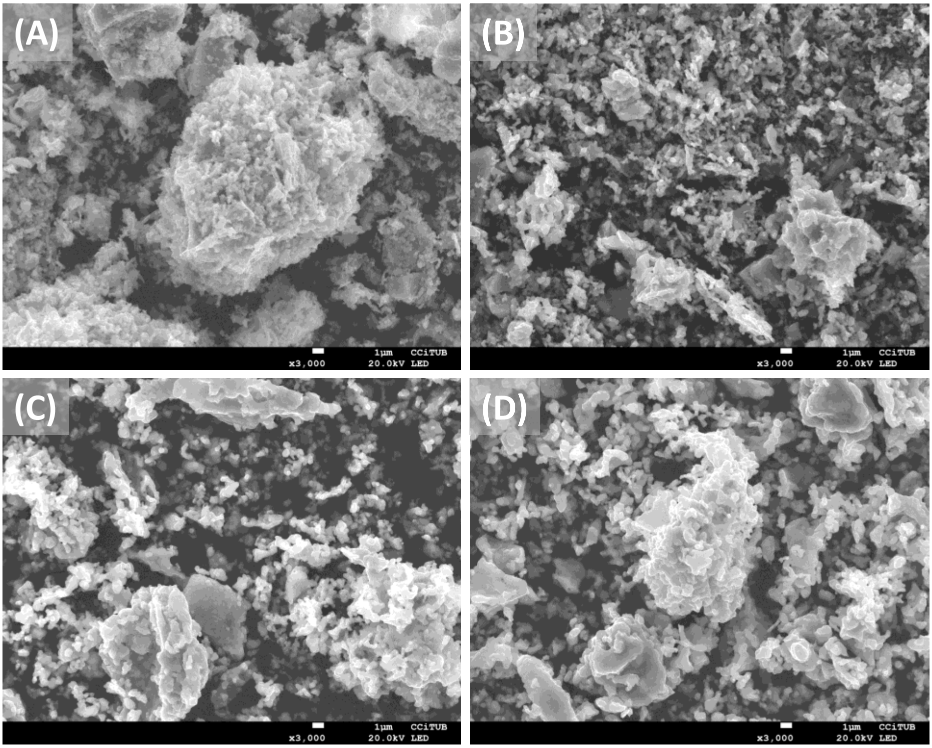

Figure 4. 14. SEM images with secondary electrons at x3000 magnification of all the powder samples of the second DoE: (A) sample #1, (B) sample #2, (C) sample #3, and (D) sample #4.

SEM images shown in Figure 4. 14 reveal a similar behaviour than the ones seen for the samples prepared in the first DoE. Spherical-shaped nanoparticles seem to be formed, but they sinter each other forming bigger micrometric clusters. Hence, it is needed to find an equilibrium to maximize the ferrite purity and to avoid sintering effects. Once the maximum purity is achieved, as happens in this second batch, it is recommended to use the minimum necessary temperature and time (850 °C for 30 minutes), in order to reduce the agglomeration.

f) Magnetic properties

Finally, the hysteresis cycle of this set of samples has also been measured by SQUID magnetometry. Results are shown in Figure 4. 15.

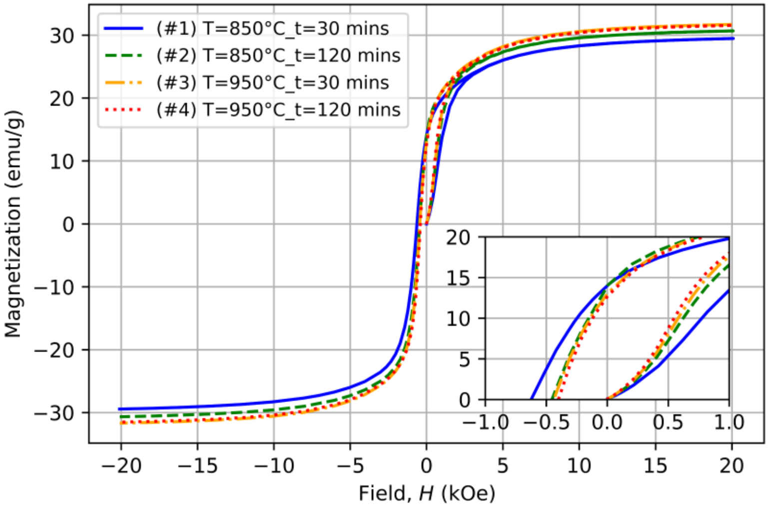

Figure 4. 15. $M(H)$ measurements at 300 K for the samples of the second DoE. The inner plot is a zoomed representation of the data close to the origin of coordinates, in order to better visualize μ, M_R, and H_C.

The magnetic behaviour, as could be expected from the XRD results, is really similar in all cases. A small increase of μ and M_S is seen in those samples prepared at 950 °C (#3 and #4), according to their slightly higher content of $CuFe_2O_4$. Looking in detail, one may see that the tendency of M_R and H_C is contrary to the one seen for the first batch of samples. Nevertheless, the magnitude of the difference is small and may be in the error range of the measurement. The main magnetic properties extracted from Figure 4. 15 are listed in Table 4. 6.

Table 4. 6. Magnetic properties of the samples of the second DoE.

Experiment	M_S (emu/g)	M_R (emu/g)	H_C (Oe)
1	29.3	14.0	623.6
2	30.6	13.9	453.4
3	31.7	13.0	437.1
4	31.4	12.7	400.3

The obtained M_S values are greater than those previously reported for $CuFe_2O_4$ nanoparticles prepared by similar methods [16], [20], [21] which show values between 20 and 28 emu/g. In samples treated at 800 °C, López-Ramón *et al*. reported much softer magnetic properties, with approximately M_R values of 0.8 emu/g, and H_C of 30 Oe. Anandan *et al.* obtained a similar remanence and coercivity values (M_R of 12 emu/g and H_C of 631 Oe), meanwhile Sumangala *et al.* results show a harder behaviour (H_C around 1 kOe). IN the paper published by Yadav *et al.* [22] are reported values of M_S = 25 emu/g, M_R = 8 and H_C = 218 Oe when the tetragonal phase is completely formed. These results are of the same order of magnitude as ours, but with a softer behaviour.

Table 4. 7 provides an overall comparison of our results with those previously reported by other authors. The sample prepared at 850°C has been used for the comparison due to its similar conditions with references, and because it may be considered to represent the optimal conditions found in the second DoE. Only references with the same crystal structure have been considered for a more rigorous comparison.

Table 4. 7. Comparison of the results obtained in this work with literature. "-" symbol indicates unknown information.

Reference	Calcination temperature (°C)	Calcination time (minutes)	Spinel crystal structure	Purity (%)	M_S (emu/g)
This work	850	30	Tetragonal	96	31
[16]	800	180	Tetragonal	88	25
[19]	800	240	Tetragonal	95	-
[20]	800	-	Tetragonal	95	28
[21]	900	180	Tetragonal	-	21
[22]	1100	120	Tetragonal	-	25

The dependence of M_S and M_R with the $CuFe_2O_4$ content is shown in Figure 15. All the samples from both batches have been represented. As can be clearly seen, both magnitudes increase as $CuFe_2O_4$ content increments. For high-purity samples the values are almost constant, with a certain degree of deviation. These values can be assumed as those corresponding to the pure $CuFe_2O_4$ phase. Overall, the formation of the ferrite from its former oxides increases M_S but it is accompanied by a slightly increase on M_R.

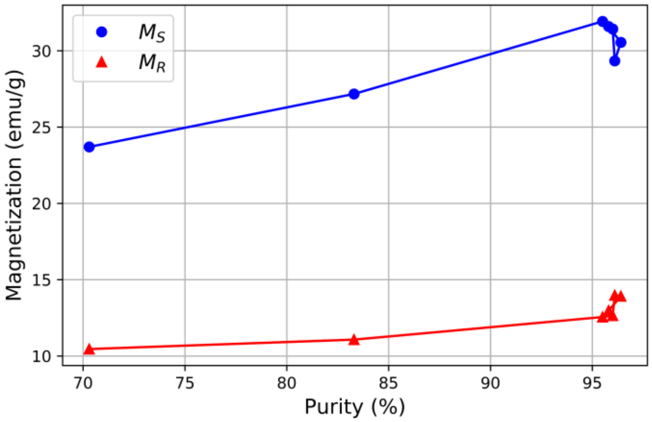

Figure 4. 16. M_S and M_R dependence with the purity for all the sol-gel prepared samples.

4. CO-PRECIPITATION SYNTHESIS

The co-precipitation method has also been investigated as an alternative approach for the synthesis of magnetic nanoparticles. The main goal has been to define another easy process and to compare it with the principal approach used in this Thesis, i.e. the sol-gel method. For this reason, in this section the results from the characterization of some magnetic nanoparticles prepared by co-precipitation are directly compared with the results obtained by sol-gel. We aim to determine which are the main advantages and drawbacks of each method in order to design nanoparticles with the desired characteristics.

To do so, here we have synthesized a set of co-precipitation and sol-gel samples under the same thermal conditions. The objective is to study how the technical differences between both processes affect the nanoparticles' properties in such a way that the calcination effect can be neglected. Moreover, as it has been previously demonstrated that temperature is the variable with a higher influence on the properties change, two different samples have been prepared at different temperatures by each method. The temperature region has been chosen to be around the optimum synthesis conditions previously found for the sol-gel method (850 °C). In Table 4. 8 the four new samples are defined, where the term "SG" and "CP" refers to the samples prepared by the sol-gel and co-precipitation methods, respectively. The thermal treatment time is of 1 hour in all cases.

Table 4. 8. Samples' description for the comparison of the sol-gel and co-precipitation methods.

Sample	Synthesis method	Temperature (°C)
SG1	Sol-gel	800
SG2	Sol-gel	900
CP1	Co-precipitation	800
CP2	Co-precipitation	900

4.1. Synthesis method

The co-precipitation synthesis method has been based on the work reported by Salavati *et al.* [23]. Nevertheless, some aspects have been modified and adapted to improve the method according to our needs.

In the co-precipitation preparation of $CuFe_2O_4$, the iron and copper nitrate salt precursors are dissolved in distilled water by stirring for 1 hour. A 1.5 M solution of NaOH is added dropwise until pH reaches a value of 10 and precipitation starts. The solution is then heated up to 80 °C and stirred for 1 additional hour, before leaving it cooling down to room temperature. In order to remove the remaining ions (such as Na^+ or NO^{3-}) the product is washed four times with ethanol and water, decanting the supernatant liquid after centrifugation at 3000 rpm during 10 minutes in each cycle. The obtained product is then dried at 80 °C for 24 hours. The thermal treatment is finally done – according to the values from Table 4. 8 - to allow the ferrite formation.

The use of a surfactant agent (octanoic acid in [23]), which is commonly used in co-precipitation methods, has been supressed. In preliminary experiments we tested the effect of the surfactant agent: there were not found meaningful differences in particle size or composition compared with those samples prepared without surfactant. Moreover, the removal of the surfactant is not an easy task, and it can lead to organic impurities in the samples. Thermal processes were discarded in order to avoid particle growth, and the above explained centrifugation process still led to small traces of surfactant in the final product. As one of our goals is to define an easy and scalable processes, the addition of surfactant has been thus suppressed.

4.2. Results and discussion

4.2.1. Structural and compositional analysis

g) Standard XRD measurements – Phase identification

The crystal structure of these samples has been examined by XRD. The obtained patterns are compared in Figure 4. 17. It is obvious that by the co-precipitation method the obtained crystal structure is different compared with sol-gel samples. Some differences between the obtained pattern by each method are the existence of doublets at around 30° and 50° in the case of sol-gel samples, meanwhile co-precipitation ones have a single peak in these positions, for instance. There are other clear differences at higher angles.

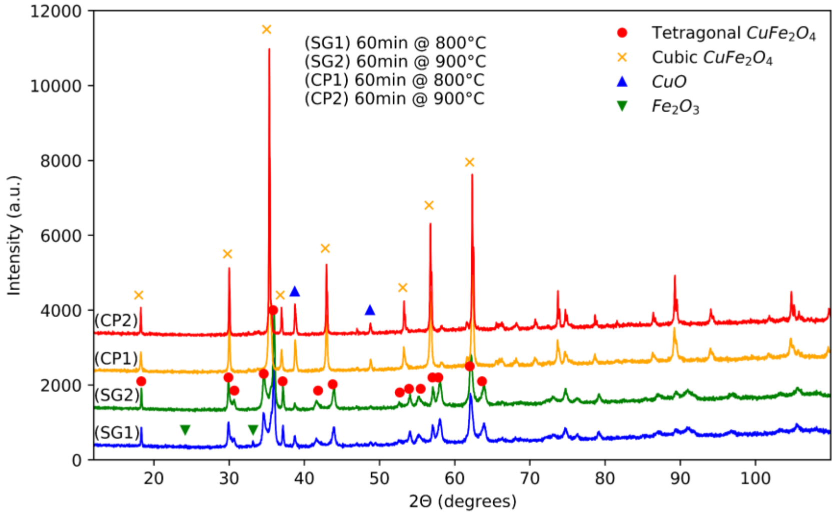

Figure 4. 17. XRD patters of the four samples, two prepared by sol-gel (SG) and two by co-precipitation (CP).

The predominant phase in all samples is $CuFe_2O_4$. It has a tetragonal structure in sol-gel samples, in good agreement with the results obtained in the previous section, whereas it is configured in a cubic structure when co-precipitation synthesis is used. The discussion of the formation of these phases will be given in section 5. All samples contain traces of monoclinic CuO, but they are more intense in CP samples. Rhombohedral Fe_2O_3 is only detected in sample SG1.

For a better comparison of the formed phases, some specific peaks have been zoomed in Figure 4. 18.

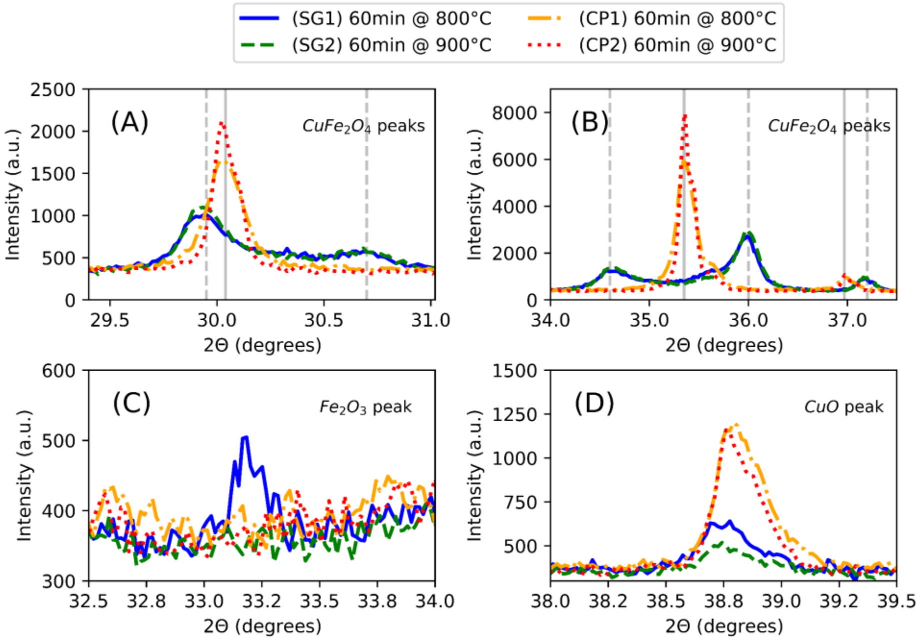

Figure 4. 18. Zoomed regions of the XRD patterns. (A) and (B) contain tetragonal and cubic $CuFe_2O_4$ peaks, (C) contains a Fe_2O_3 peak, and (D) a CuO peak. Vertical continuous lines represent the 2θ positions where cubic $CuFe_2O_4$ peaks are expected, meanwhile dashed lines represent the tetragonal $CuFe_2O_4$ positions.

Figure 4. 18.A and Figure 4. 18.B both represent 2θ regions where tetragonal and cubic $CuFe_2O_4$ peaks are present. Here, it is possible to easily confirm that sol-gel samples follow the tetragonal patterns, whereas the co-precipitation ones fit with the cubic pattern. Additionally, we notice that there is a minimum difference in intensity between sol-gel samples, whereas the $CuFe_2O_4$ intensity notably increases with

temperature in co-precipitation prepared powders. Figure 4. 18.C confirms that the only sample that contains Fe_2O_3 is SG1, which disappears at higher temperatures, and Figure 4. 18.D verifies that all samples still contain a small amount of CuO. In this regard, one can also notice that co-precipitation samples have a higher amount of CuO impurities than those samples prepared by sol-gel, despite it reduces when increasing temperature.

h) Rietveld refinement

Rietveld refinement has then been performed with the goal of obtaining quantitative information about the chemical composition of each sample. In Figure 4. 19, the profile refinements for those samples prepared at 800 °C are represented, and

Table 4. **9** summarizes the values obtained for all the synthesized samples.

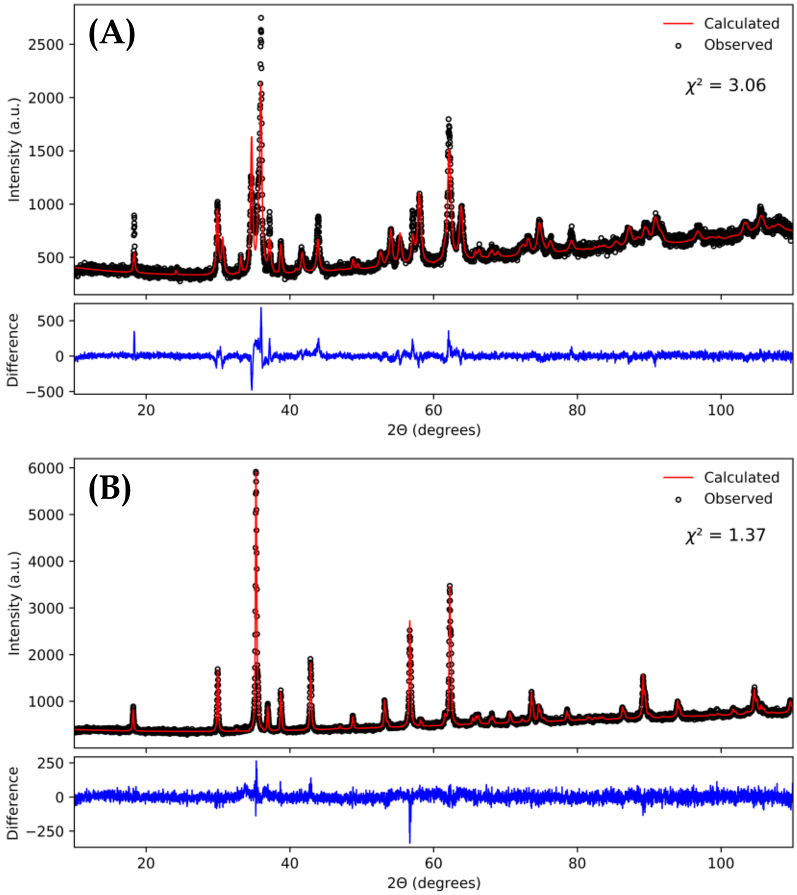

Figure 4. 19. Rietveld refinement of the two samples prepared at 800 °C, (A) SG1 and (B) CP1. Circles represent the measured data, meanwhile the continuous red line shows the calculated model. The difference between both values is represented in the bottom plot.

Table 4. 9. Composition obtained from Rietveld refinement for the four samples. "T" refers to the tetragonal structure, and "C" to the cubic one.

Sample	**T - $CuFe_2O_4$ (%)**	**C - $CuFe_2O_4$ (%)**	**CuO (%)**	**Fe_2O_3 (%)**	**χ^2**
SG1	87.5	- - -	5.7	6.8	3.06
SG2	96.1	- - -	4.3	0.0	3.01
CP1	- - -	88.3	11.7	0.0	1.37
CP2	- - -	88.4	11.6	0.0	1.53

By analysing the sol-gel samples, the small quantity of Fe_2O_3 only present in the sample prepared at 800 °C is confirmed. When increasing the temperature, the purity raises up to 96.1% and the traces are reduced. These results are in good agreement with those obtained in the section about the sol-gel optimization in this same chapter. Co-precipitation samples do not contain Fe_2O_3 and only an excess of CuO is found. The amount of $CuFe_2O_4$ do not significantly increase with temperature. When comparing the sol-gel and co-precipitation results, apart from the difference in crystal structure, it should be noticed that the purity values that are achieved by the sol-gel method are considerably higher than those obtained by co-precipitation.

4.2.2. Particle size and morphology

The four samples have been measured by LD in order to compare the particle size produced by each method under the same thermal conditions. The results are shown in Figure 4. 20.

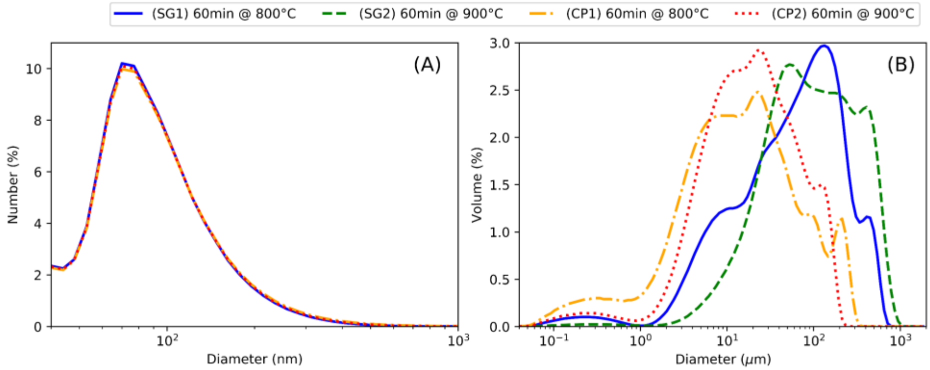

Figure 4. 20. Particle size distribution of the four samples: (A) represented as a function of the number of particles, and (B) as the percentage of volume that each diameter represents in the hole sample.

In both cases the number % distribution is under 100 nm, meaning that most of the synthesized particles can be considered as nanoparticles. It is not possible to differentiate the difference in size in Figure 4. 20.A due to measurement resolution. The average particle size is of 94.0 ± 0.8 nm. On the other hand, Figure 4. 20.B shows the volume fraction that is occupied by each particle size. There, the first remarkable aspect is the difference in particle size between the samples prepared by each chemical method: smaller sizes are achieved by co-precipitation, with a difference of one order of magnitude when comparing the centre of their distributions. Moreover, by comparing the two samples prepared by the same approach, it is possible to see how the distributions are displaced to bigger diameters in those specimens treated at higher temperatures, especially in the sol-gel case. These results are coherent with what could be expected from a particle growth point of view.

Figure 4. 21 shows x5000 magnification SEM images of the prepared samples in order to detect morphology differences. It is possible to see the sintering and growth behaviour of each kind of particles under the same conditions.

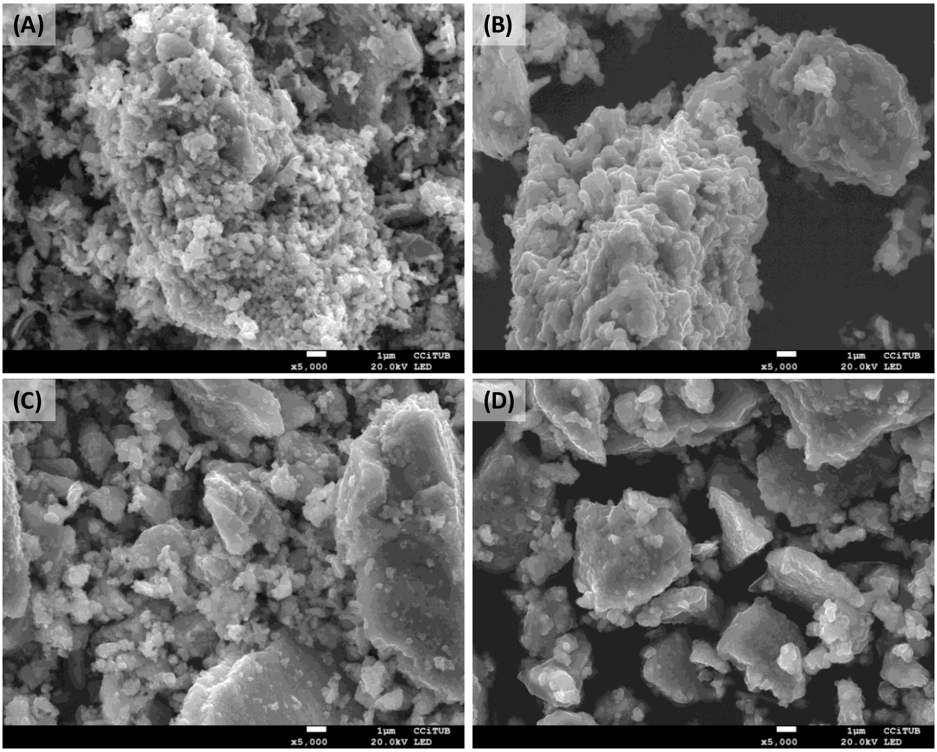

Figure 4. 21. SEM secondary electrons images at x5000 magnification of (A) SG1, (B) SG2, (C) CP1, and (D) CP2 samples.

In all cases, there is agglomeration and sintering of the nanometric particles forming micrometric clusters. The diameter of each individual particle is roughly the same in all samples, being always under the micron in size. On the other hand, the volume of the micrometric clusters – formed by the sintering of small particles – seems to be qualitatively bigger for sol-gel than co-precipitation samples. This is in really good agreement with the results previously obtained by LD. As has been previously done with the sol-gel samples, the sintering between nanoparticles has been also checked for co-precipitation products at higher magnification. Figure 4. 22 shows an image taken at x20000 magnification where nanoparticles are well resolved, and it is possible to see how they also sinter forming the micrometric clusters.

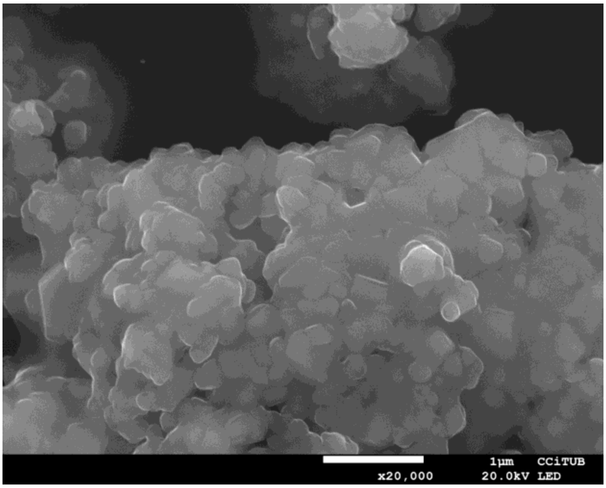

Figure 4. 22. SEM image obtained by secondary electrons of the sample CP2 at x20000 magnification.

4.2.3. Magnetic properties

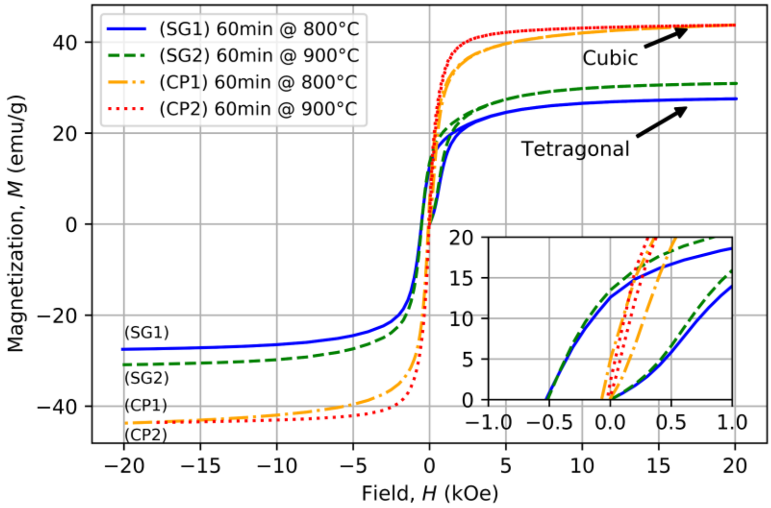

Figure 4. 23. $M(H)$ measurements at 300 K of sol-gel (SG) and co-precipitation (CP) samples. The inner plot is a zoomed representation of the data close to the origin of coordinates, in order to better visualize μ, M_R, and H_C.

Figure 4. 23 shows the hysteresis cycles measured at room temperature for the four samples. It is clear that the materials prepared by each chemical method (i.e. each crystal structure) have a different magnetic behaviour. First, M_S is greater for cubic samples compared with the tetragonal ones. This behaviour is in good agreement with previous works [24], which state that this higher saturation magnetization of the cubic phase, compared to the tetragonal one, is an indication of the migration of Cu^{2+} ions to octahedral holes during the tetrahedral distortion. It might prove that the inversion parameter is different in each structure. Especially in the case of the cubic structure, the obtained magnetic values are considerably above than those reported for $CuFe_2O_4$ prepared by similar methods [16], [20], [21]. The hysteresis area, which is directly related to the energy needed for sweeping the magnetic moment between both states, is also completely different for each structure. In this regard, cubic samples present a softer behaviour compared with the tetragonal ones, with lower M_R and H_C values. This soft behaviour makes the cubic phase to be an excellent candidate for high frequency applications [25]. In Table 4. 10 the specific values for each property are specified.

Table 4. 10. Magnetic properties of the four prepared samples.

Sample	M_S (emu/g)	M_R (emu/g)	H_C (Oe)
SG1	27.4	12.6	526.6
SG2	30.8	13.9	513.6
CP1	43.5	4.8	70.8
CP2	43.6	2.1	24.4

As well as in the case of the chemical composition, the magnetic results are in good agreement with those obtained in the sol-gel optimization section, confirming the reproducibility of the results.

5. SOL-GEL vs. CO-PRECIPITATION: TETRAGONAL AND CUBIC PHASES

In this work, the formation of the tetragonal and cubic phases by, respectively, the sol-gel and co-precipitation methods has been experimentally proved. Nonetheless, explaining the reason why each phase is formed is not a straightforward task.

5.1. State of the art

According to the literature, $CuFe_2O_4$ has two possible crystal structures: the tetragonal one (space group *I41/amd*) which is stable below 700K (427 °C), and the cubic one (space group *Fd-3m*), that appears above this temperature. The transformation is less defined in the case of nanoparticles, as Zhang *et al.* [26] determined that the transformation temperature may be reduced linearly with particle size. The structural transition between them may be explained by the Jahn – Teller effect, which arises from the octahedral Cu^{2+} ions. This effect leads to the elongation of the octahedron, and the spinel lattice is tetragonally distorted. Above the transition temperature, part of Cu^{2+} ions move into tetrahedral sites, so the oxygen environment of copper ion becomes distorted and the orbital degeneration of electron states is removed. Consequently, the total energy of the system is reduced and the phase transition tetragonal-to-cubic appears [1], [27]. There is not a clear criterion in literature regarding the fact of a possible change in the spinel inversion parameter during the transition. Experimental data suggest that it depends on the synthesis method, and the annealing and cooling rates [28], [29].

Recent articles, focused on the study of the phase transition in sol-gel process [16], [19], have obtained a cubic dominant structure just after the gel calcination, which tends to disappear when samples are calcined at higher temperatures. With treatments in the range between 350 °C and 400 °C, and subsequent cooling to room temperature, authors start to obtain the tetragonal phase. The later phase is completely dominant when $CuFe_2O_4$ is processed at or above 800 °C. Furthermore, it has been also reported that traditional ceramic methods also produce the tetragonal phase [16] in similar temperature conditions. In our case, we are working at 800 °C and 900 °C, so our results are in perfect accordance with these references. Zhuravlev *et al.* [19] suggested that the reason why in their sol-gel samples the cubic phase was stable after burning the gel is the fast cooling rate. This really acts as a quenching process and, hence, stabilizes the high temperature structure. Khemthong *et al.* [3] have recently published an interesting paper where they study the crystallization of the spinel structure during sol-gel combustion by means of in situ X-ray absorption. They conclude that, in the case of sol-gel, the energy of the combustion may be enough to initiate the $CuFe_2O_4$ formation, and the subsequently calcination helps to ensure the crystallinity and phase purity. These conclusions are also in good agreement with Zhuravlev’s results.

On the other hand, there are papers [29]–[31] reporting the formation of cubic phase by using hydrothermal and co-precipitation methods, working under and above the transition temperature. This is in good agreement with the results obtained in this work by means of co-precipitation. Finally, the cubic structure has also been prepared by means of solid-state reaction under N_2 atmosphere [32]. However, there is not a clear explanation of why the cubic structure is stable at room temperature instead of transforming to the tetragonal one.

In the previous sections we have reported an experimental evidence of the formation of the two phases by working at the same thermal conditions, so it should not be simply considered as a temperature-dependent effect or an oxidation control by atmosphere.

5.2. Temperature – dependent XRD

The final calcination process in both of our methods has been exactly the same, so we can assume the same cooling rate in both samples. In order to know how these phases are formed and how the chemical reaction behaves during the thermal treatment, temperature dependent XRD measurements have been performed to each sample.

In the case of the sol-gel sample, the measurement has been done after burning the gel, in order to ensure not to fire it inside the diffractometer and to simulate exactly the same process performed to prepare the nanoparticles. The sample prepared by co-precipitation was measured after the drying process, without any further thermal treatment. Each sample has been measured from room temperature (28 °C) to the maximum temperature used in the work (950 °C).

5.2.1. Sol-gel sample

Figure 4. 24 represents the XRD patterns obtained at some of the measured temperatures. Only some of the measurements are shown in this figure for practical purposes. It is important to consider that these temperatures are those where the XRD patterns are in-situ measured, and must not be confused with various samples calcinated at different temperatures and later measured at room temperature.

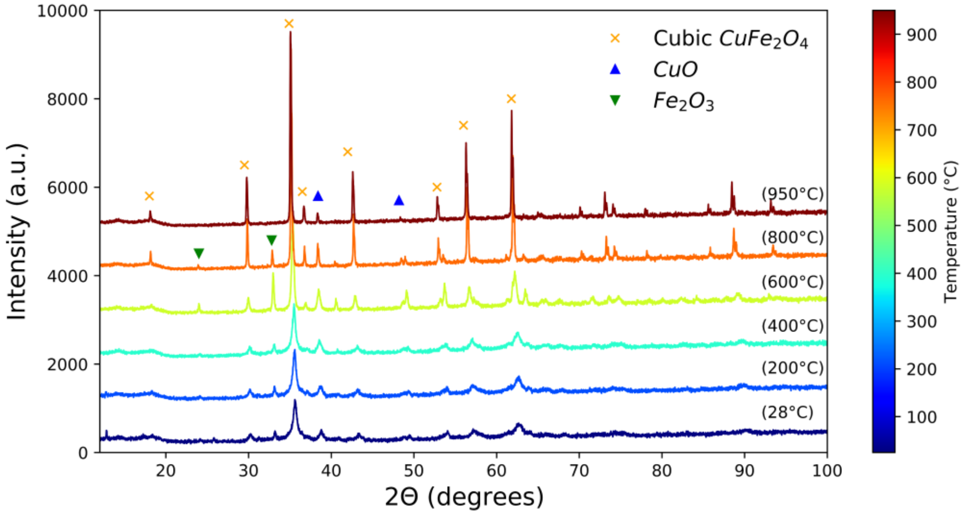

Figure 4. 24. Temperature-dependent XRD patterns for one sample prepared by sol-gel. These measurements correspond to the heating process. All the patterns have been intentionally displaced 1000 units in intensity to facilitate their simultaneous visualization. The different markers indicate the 2θ positions of the main peaks of the present crystalline phases.

The pattern obtained at room temperature (28°C), which corresponds to the product obtained after the gel burning, describes a structure with a low degree of crystallinity. An important aspect is that the cubic $CuFe_2O_4$ phase can be already detected, what is in good agreement with Zhuravlev [19] and Khemthong [3], who also observed that this previous process could lead to ferrite formation. Additionally, smaller quantities of monoclinic CuO and rhombohedral Fe_2O_3 are also present. The low crystallinity degree keeps until 600 °C where there is an abrupt increase of the peak intensity in all phases and a background reduction, that can be understood as an increase of the crystallinity without a meaningful ferrite conversion. Above this temperature, the cubic $CuFe_2O_4$ peak intensity grows while the precursor oxides' one reduces until the maximum temperature. At this point, only small quantities of CuO are detected, apart from the main ferrite. It is known that high-temperature techniques always lead to the presence of CuO as second phase [27]. In order to have a better idea and more precise information about this process, Figure 4. 25 provides magnified images of different characteristic peaks for each one of the present phases.

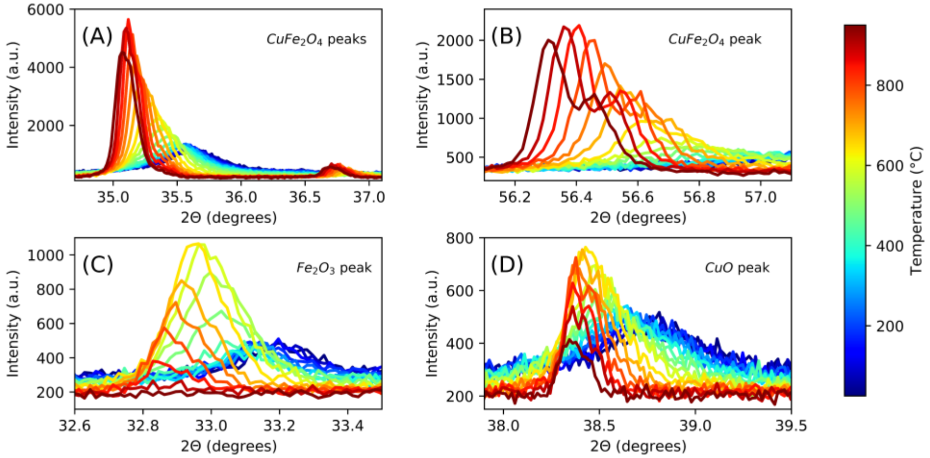

Figure 4. 25. Zoomed regions of the XRD patterns for the sol-gel prepared sample. (A) and (B) contain tetragonal and cubic $CuFe_2O_4$ peaks, (C) contains a Fe_2O_3 peak, and (D) a CuO peak. These measurements correspond to the heating process.

All the measurements done during the heating process are here represented. Figure 4. 25.A, which corresponds to a cubic $CuFe_2O_4$ peak, shows the presence of a low-intensity peak just above 35.5 ° that remains constant until 500 °C. Above this temperature, this peak starts to considerably increase and to shift to lower 2θ, what is attributed to an increase of the unit cell parameters (dilatation) at high temperatures. However, the change in 2θ position cannot be directly related to the change in the unit cell parameter, as during the dilatation/contraction process the dimensions of the sample vary, and thus the height where the X-rays contact the sample also change. This effect can be corrected by an appropriate correction of the *zero* and *displacement* parameters during the Rietveld refinement. The formation of a smaller peak around 36.7 °C can be also appreciated. In Figure 4. 25.B it is possible to see exactly the same behaviour, but here it is better observed how the doublet corresponding to $K_{\alpha1}$ and $K_{\alpha2}$ signals is better defined at higher temperatures, where there is a better crystallinity. Moreover, it can be seen how the intensity of the peak slightly reduces above 850 °C, which could also be intuited in Figure 4. 25.A.

Figure 4. 25.C shows the behaviour of the rhombohedral Fe_2O_3 phase. Again, the intensity abruptly increases at 500 °C due to the improvement of crystallinity until reaching a maximum at 650 °C. Above this temperature the intensity reduces until completely disappear at 900 °C.

CuO behaves in a similar way. As can be appreciated in Figure 4. 25.D, the peak is better defined above ~ 500 °C, and then starts to reduce at 650 °C. Thus, this temperature is at which the transformation from the copper and iron oxides starts to form the ferrite. In this case, CuO is not completely consumed as there is some remaining intensity at 950 °C.

As could be expected, the cubic $CuFe_2O_4$ is the dominant phase at high temperatures. Nevertheless, during the cooling process back to room temperature, the tetragonal phase is formed (see Figure 4. 26).

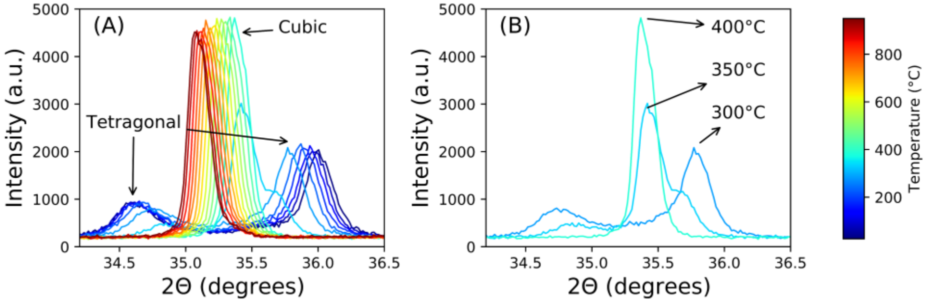

Figure 4. 26. Temperature-dependent XRD patterns for the sol-gel prepared sample. These measurements correspond to the cooling process. In (A) all the measurements done are shown, whereas in (B) only those patterns close to the cubic to tetragonal transition are plotted.

During the cooling process, the cubic $CuFe_2O_4$ peaks only experiment a shift on 2θ due to the change on the cell parameter and sample height due to compression, as explained before. However, at 350 °C the cubic peak suddenly reduces, and a doublet starts to grow. This doublet corresponds to two different tetragonal $CuFe_2O_4$ peaks. At 300 °C the transformation is complete, and the intensity of the tetragonal phase does not experiment any change in intensity during the rest of the experiment. It means that, in this case, there is a direct transformation between the cubic and tetragonal phases, where other species (such as the remaining CuO) do not participate. This temperature range is close to the expected for the cubic-to-tetragonal transition according to the previously mentioned references.

5.2.2. Co-precipitation sample

In Figure 4. 27 are shown some of the measurements done during the heating process, from room temperature to 950 °C. The represented temperatures are the same than those chosen for the sol-gel sample in order to facilitate their comparison.

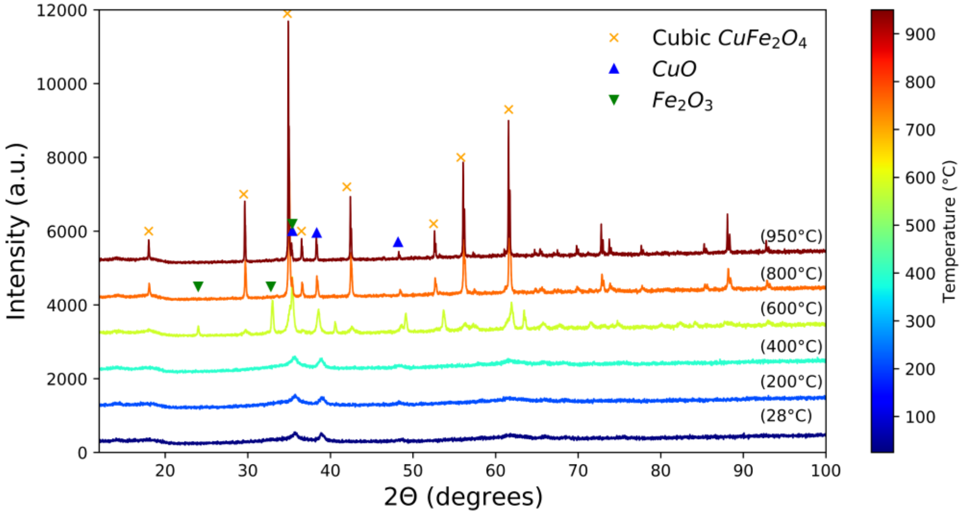

Figure 4. 27. Temperature–dependent XRD patterns for one sample prepared by co-precipitation. These measurements correspond to the heating process. All the patterns have been intentionally displaced 1000 units in intensity to facilitate their simultaneous visualization. The different markers indicate the 2θ positions of the main peaks of the present crystalline phases.

In this case, a poor crystalline structure is detected until 600 °C. The two peaks detected in the low-temperature range correspond to CuO and Fe_2O_3, the two precursor oxides. There is a transition where the crystallization of the system improves, as the peaks of CuO and Fe_2O_3 become more intense and well defined. However, the ferrite transformation has not already started, as these are the unique peaks detected. The $CuFe_2O_4$cubic phase is formed at 800 °C, reducing then the presence of CuO and Fe_2O_3. However, as in the previous case, at 950 °C there is still a certain amount of CuO. In order to have a more detailed idea of these two transitions, Figure 4. 28 shows all the measurements done – every 50 °C – during the heating process of this sample. The selected 2θ positions are the same than in the previous sample in order to allow their comparison.

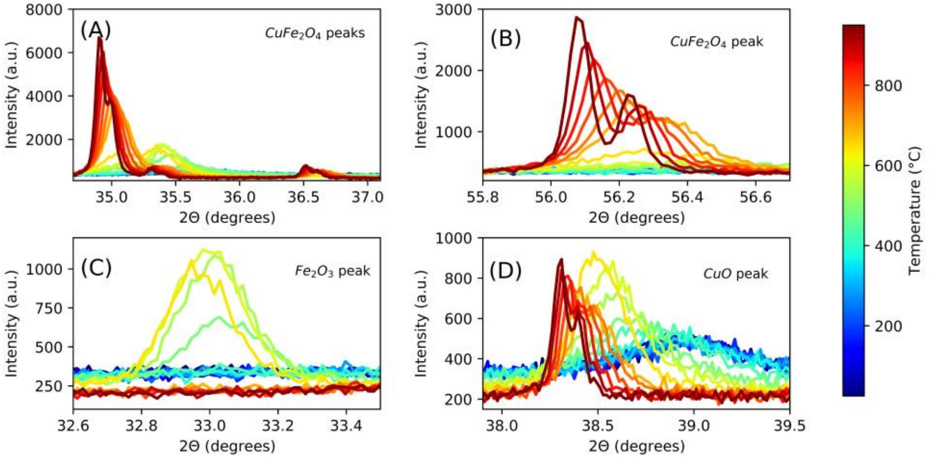

Figure 4. 28. Zoomed regions of the XRD patterns of the co-precipitation prepared sample. (A) and (B) contain tetragonal and cubic $CuFe_2O_4$ peaks, (C) contains a Fe_2O_3 peak, and (D) a CuO peak. These measurements correspond to the heating process.

In Figure 4. 28.A and Figure 4. 28.B two cubic $CuFe_2O_4$ peaks are represented. There it is possible to see how, around 600 °C and 650 °C, these peaks appear. Contrary to the previous sample, here the ferrite has not been previously formed and the peak appears when the reaction takes place. The low-temperature peak seen in Figure 4. 28.A corresponds to a CuO and a Fe_2O_3 peaks. In Figure 4. 28.B, the double peak due to $K_{\alpha 1}$ and $K_{\alpha 2}$ radiation can be clearly seen at high temperatures.

The crystalline transition and ferrite formation reaction can be visually detected in Figure 4. 28. The Fe_2O_3 peak - which is not the more intense for this phase - remains shielded by the background at low temperatures. It suddenly appears at 500°C when the crystallinity increases. However, the reaction between Fe_2O_3 and CuO takes place at 650 °C and it starts reducing its intensity at 650 °C. Finally, it completely disappears at 800 °C. Finally, CuO follows a similar behaviour, but with the main difference that this phase does not completely disappear at 950 °C. As it is shown in Figure 4. 28, the peak starts to be well resolved at 500 °C and decreases above 650 °C, confirming then the temperatures defined by the other two phases. Moreover, the temperature at which the reaction to form the ferrite takes place is the same as for the sol-gel sample, 650 °C. Furthermore, here it is also possible to see the $K_{\alpha 1}$ and $K_{\alpha 2}$ radiation effect at high temperatures.

As it is expected, the stable phase at high temperatures is the cubic one. However, there is an interesting first aspect that should be highlighted from these results: the cubic phase has been directly formed from the precursors oxides, without having first formed the tetragonal phase.

As has been seen in the previous section, co-precipitation leads to a stable cubic structure at room temperature. It means that, as can be checked in Figure 4. 29, the high-temperature cubic form remains stable during the cooling process.

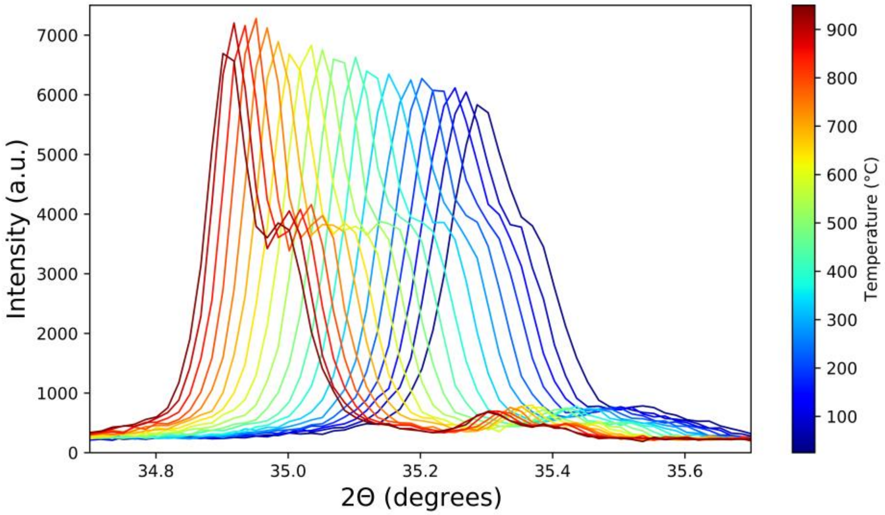

Figure 4. 29. Temperature–dependent XRD pattern between 34.7° and 35.7° - corresponding to a cubic $CuFe_2O_4$ Bragg position - for the co-precipitation prepared sample. These measurements correspond to the cooling process.

The only change that the cubic peak experiments is the shift to lower 2θ positions due to the sample contraction when cooling down. Additionally, it is seen a slight decrease of the peak intensity when reducing the temperature, and it can also be observed that the effect of $K_{\alpha 1}$ and $K_{\alpha 2}$ radiation is less visible at low temperatures. Finally, the composition at room temperature (28 °C) is the same than at 950 °C, cubic $CuFe_2O_4$ and smaller quantities of CuO.

5.2.3. Discussion

With these measurements, we actually know how the chemistry of the reaction is, and how crystalline phases are formed during the calcination process for both methods, sol-gel and co-precipitation.

First, our results are in accordance with those previous works [16], [19] that stated that copper ferrite may be formed during the gel burning process prior to the calcination. Moreover, the sol-gel prepared samples behave as expected: cubic phase is dominant at high temperatures, and it transforms to the tetragonal form under 400 °C. On the other hand, the reason why the cubic structure remains stable at room temperature when the co-precipitation method is used is not clear. The formation of the cubic phase at room temperature has only been explained by means of fast cooling rates [19] - which quenches the high temperatures cubic structure – or by controlling the oxidation of the sample through working under inert atmospheres [32]. Nevertheless, in the temperature dependent XRD measurements, the temperatures, the heating/cooling rates, and the atmosphere have been exactly the same in both cases. Thus, here it is reported an experimental evidence that this is not, at least, the unique factor determining the resulting structure.

The unique thermal difference between both samples has been the gel burning process applied to the sol-gel samples - and the subsequent formation of the cubic phase - before running the measurement. Thus, we associate the formation of one or the other phase to the history of the structure, more than the last cooling rate. According to our results, it seems that when the cubic phase is prematurely formed, it then has the capacity to return to the tetrahedral structure if enough thermal energy is applied; however, when the cubic structure is continuously formed by consuming the precursor oxides at high temperatures, the formed structure seems to be more stable and remains when it is cooled back down to room temperature. Probably, this difference in behaviour is related with the distribution and occupation of cation in the structure, and the resulting Jahn–Teller energy. The distribution of cations in the structure may be different when it is quickly (gel burning) or progressively (co-precipitation) formed. If the location of cations in the progressive thermal process is stable enough, it can energetically stay in equilibrium even when lowering the temperature. This assumption must be corroborated by other characterization methods that allow to precisely determine the cations distribution and coordination in the structure.

In order to provide an easier comparison between samples, Figure 4. 30 shows the characteristic peaks of the three phases found in both samples. In this figure are only represented the pattern at the beginning of the experiment at 28 °C, the one at the end of the heating process at 950 °C, and finally the one obtained at room temperature (28 °C) after cooling down. These temperatures have been selected to simplify the comparison between samples and structures. This figure first provides a clearer visualization of the behaviour previously discussed for each sample. Moreover, the phases' formation during the heating and cooling can be easily compared between samples. The initial presence of cubic phase, its growth until 950 °C, and its final transformation to the tetragonal one is evident for the sol-gel sample. Contrary, the cubic phase is not formed by co-precipitation until the reaction occurs at high temperature, but it is then stable when cooling down. Finally, this figure also provides another important information: the 2θ peak positions of the cubic phase present at 950 °C are different for each synthesis method. The sample prepared by co-precipitation has the cubic $CuFe_2O_4$ peaks placed in lower 2θ positions than the sol-gel sample, what could indicate a larger unit cell parameter. Therefore, these results proof that the cubic phase formed at high temperatures is different from a crystallographic point of view. This crystallographic difference is in good agreement with the previous arguments stating that, probably, there is a difference on the cation occupation (leading to the unit cell distortion) that makes one structure stable, but not the other.

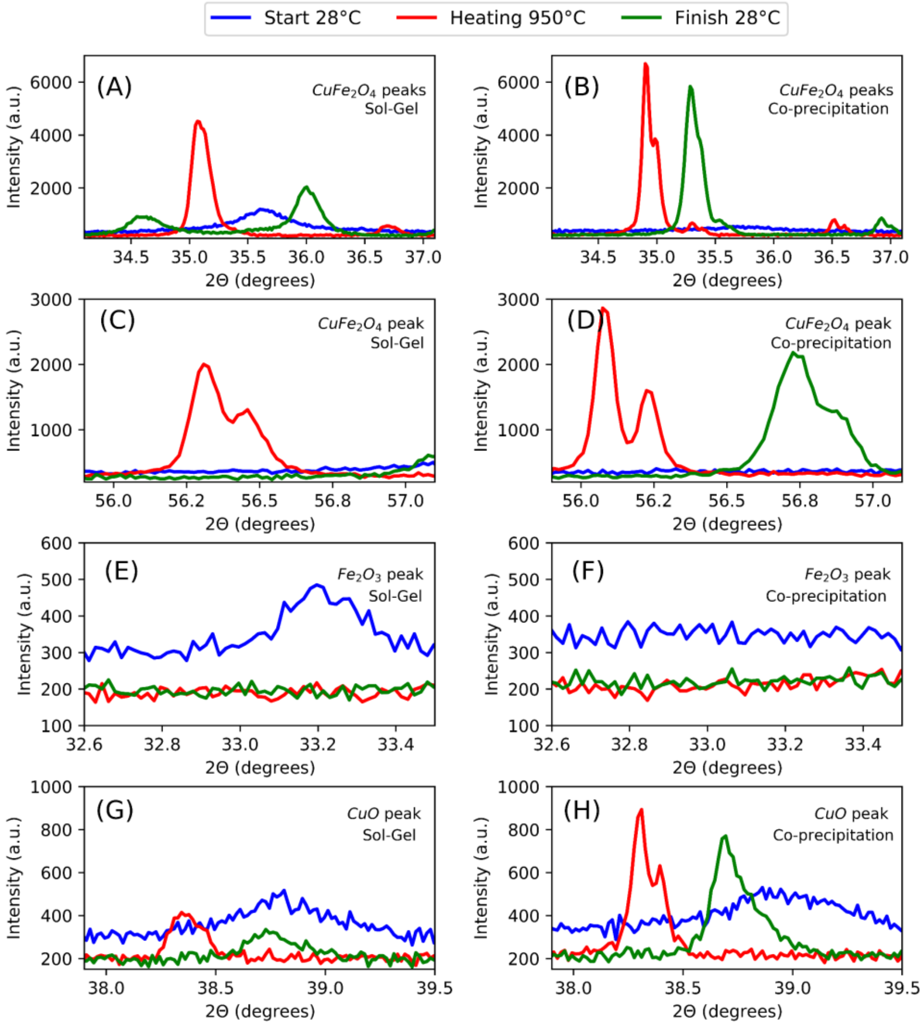

Figure 4. 30. Comparison of the main peaks of each phase, for both samples during the heating and cooling process. The figures in the left column correspond to the samples prepared by sol-gel, while the right column shows the patterns of the co-precipitation samples. (A) and (B) correspond to the $CuFe_2O_4$ (cubic + tetragonal) peak between 35° and 36°, (C) and (D) correspond to the cubic $CuFe_2O_4$ peak between 56 ° and 57 °, (E) and (F) correspond to the Fe_2O_3 peak around 33 °, and (G) and (H) correspond to the CuO peak between 38 ° and 39 °.

6. MECHANICAL AND MAGNETIC PROPERTIES IN BULK SAMPLES

In this section we investigate the mechanical and magnetic properties (both static and dynamic) of the previously sol-gel prepared powders.

6.1. Structural characterization

A total of twenty-two different pellets, of three different chemical compositions ($CuFe_2O_4$, CuO, and Fe_2O_3), have been fabricated in two different shapes: circular and toroidal. In all cases we have used our own powder, previously fabricated by the sol-gel method. However, it is important to mention that this powder has not been calcinated before the compaction, as it is later sintered at higher temperatures. The sintering temperatures have been of 1000 °C, 1100 °C, 1200 °C, 1300 °C, and 1400 °C. CuO pellets have been prepared only at 1000 °C because it has been experimentally detected that it softens or melts at higher temperatures. CuO and Fe_2O_3 have been prepared exactly by the same method described for $CuFe_2O_4$ but by using only the corresponding metal salt precursor. Table 4. 11 summarizes the main characteristics of each pellet.

Table 4. 11. Characteristics of all the prepared pellets. Each type of pellet has been fabricated twice, one circular and one toroidal-shaped. Both shapes show the same properties.

Pellet	Composition	Sintering temperature (°C)	Sintering time (h)	Apparent density, ρ_{app} (g/cm^3)	Porosity, *P* (%)
CFO_1	$CuFe_2O_4$	1000	6	1.36	74.9
CFO_2	$CuFe_2O_4$	1100	3	1.34	75.2
CFO_3	$CuFe_2O_4$	1200	3	1.49	72.5
CFO_4	$CuFe_2O_4$	1300	3	1.32	75.6
CFO_5	$CuFe_2O_4$	1400	3	1.06	80.4
CuO_1	CuO	1000	6	2.63	59.5
FeO_1	Fe_2O_3	1000	6	1.33	75.1
FeO_2	Fe_2O_3	1100	3	1.34	74.9
FeO_3	Fe_2O_3	1200	3	1.42	73.5
FeO_4	Fe_2O_3	1300	3	1.47	72.5
FeO_5	Fe_2O_3	1400	3	1.22	77.2

Porosity P values have been approximated by comparing the experimental apparent density (ρ_{app}) and the expected one (ρ_{exp}) for each phase ($P(\%) = \rho_{app}/\rho_{exp}$). The considered expected densities have been 5.402 g/cm^3 for tetragonal $CuFe_2O_4$, 6.530 g/cm^3 for CuO, and 5.357 g/cm^3 for Fe_2O_3. Figure 4. 31 graphically shows the apparent density and porosity dependence on the sintering temperature. It must be considered, for all the exposed results, that the sintering time for those samples prepared at 1000 °C is the double than at the rest of temperatures. We did so in order to ensure a good sintering and adhesion of the powder at the minimum temperature as it is the only one at which CuO pellets could be prepared.

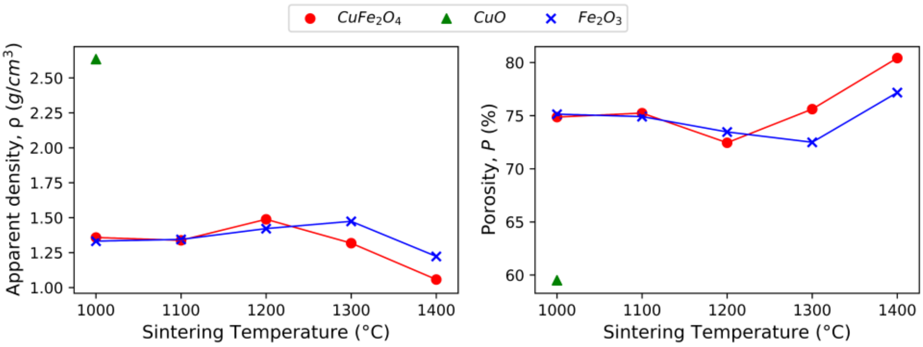

Figure 4. 31. (A) Apparent density, and (B) porosity dependence with sintering temperature for the different prepared pellets.

From these results, it is possible to observe different interesting aspects. First, CuO clearly presents the highest density and lowest porosity. Also, $CuFe_2O_4$ starts increasing its density with temperature (we may associate it to a higher solid-state diffusion that allow to fill the free spaces in the structure), but it then reduces above 1300 °C. These two effects can be related with the fact that we experimentally detected that those CuO pellets prepared above 1000 °C started to lose their shape or even to melt. It was even noticed that in those $CuFe_2O_4$ pellets prepared at higher temperatures, a fraction of the matter melt during the process and left the pellet, as it is seen in Figure 4. 32. Then, if CuO softens or melts, it is able to better fill the free spaces in the pellet and thus reduce the porosity. Moreover, if it melts and leaves the $CuFe_2O_4$ pellets, there is a generation of holes (pores) in those places previously occupied by CuO. On the other hand, other authors [33] have observed an expansion of the $CuFe_2O_4$

above 1000 °C that leads on a reduction of the density. Although in Fe_2O_3 it is also observed a decay in density, we did not notice any physical change in the sample. Moreover, there is only one point out of the general tendency, which can be understood as part of the measurement error as generally the density is almost constant in all the temperature range.

Figure 4. 32. $CuFe_2O_4$ circular and toroidal-shaped pellets after sintering. Part of the matter has left the pellet, probably because it melts.

All the prepared pellets have been analysed by XRD, but only quantitative information can be extracted from the results of the circular-shaped samples. In the case of the toroids, the X-ray beam does not only shine the sample due to its geometry, and the difference on the irradiated area may lead to considerable intensity differences between samples. Figure 4. 33 shows the results obtained by analysing the toroids with the three compositions.

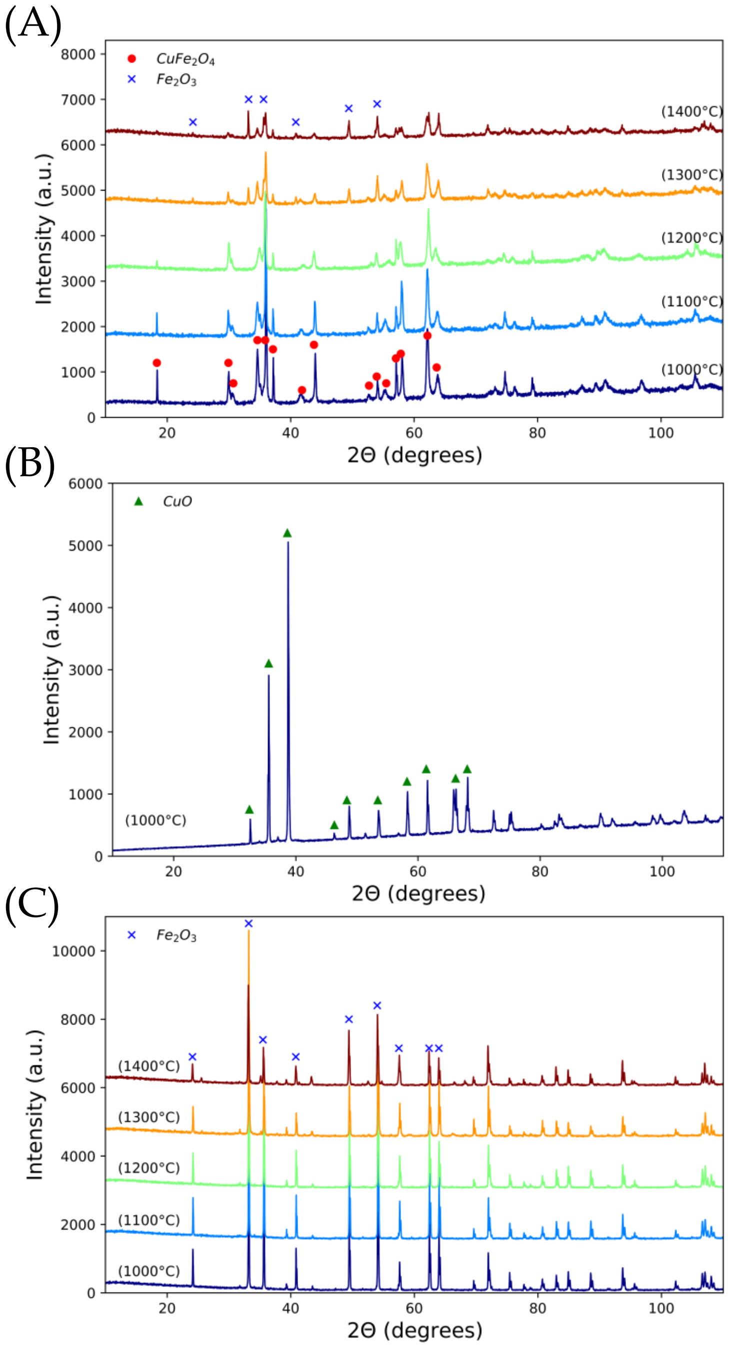

Figure 4. 33. XRD results for the different (A) $CuFe_2O_4$, (B) CuO, and (C) Fe_2O_3 circular-shaped toroids. All the patterns have been intentionally displaced in order to allow a better comparison.

First, by analysing Figure 4. 33.A, it is possible to notice that the sample is purely made by tetragonal $CuFe_2O_4$ (99.7% according to Rietveld results) from 1000 °C until 1200 °C; above this temperature, there is a clear reduction of the copper ferrite peaks and start to appear others originated by Fe_2O_3. This is in good agreement with the previous argument: if CuO leaves the structure above 1200 °C (where density starts to reduce), there must be an excess of Fe_2O_3 in the system. Moreover, there is also a notably reduction of the crystallinity of the structure, as the peaks are every time less resolved and the background signal increases.

Pure CuO is formed at 1000 °C, as it can be seen in Figure 4. 33.B. Furthermore, pure Fe_2O_3 is formed in the last set of samples (Figure 4. 33.C) and it is stable with temperature. Additionally, small traces of Al_2O_3 have been found in some of the pellets, which come from the aluminium oxide used to protect the crucible during the sintering process.

6.2. Mechanical properties

Nanoindentation tests have been performed in all the pellets. The presented results in this chapter are the average properties measured from 25 indentations at 2000 nm in depth. Moreover, it has been corroborated that the mechanical properties of the toroidal and circular pellets are exactly the same, so only the results from the circular pellets are shown here.

First, Figure 4. 34 provides a comparison of the elastic modulus (E) and hardness (H) of the three different compositions sintered at the same conditions, 6h at 1000 °C. From a general perspective we can say that the mechanical properties of $CuFe_2O_4$ are between those of CuO and Fe_2O_3. Elastic modulus is closer to the values measured for CuO, meanwhile hardness is more similar to the one shown by Fe_2O_3.

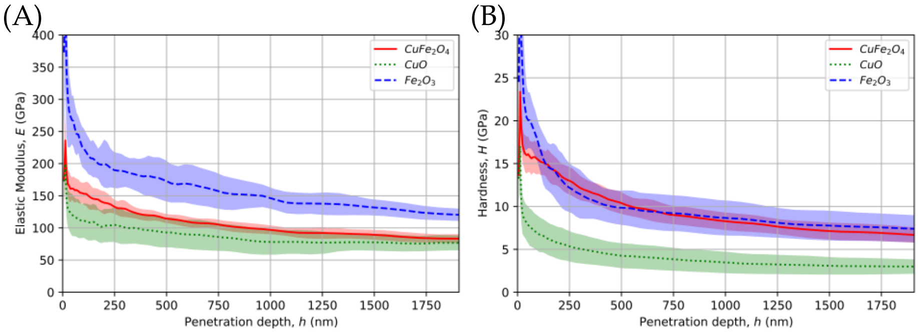

Figure 4. 34. Penetration depth dependence of the (A) elastic modulus (*E*), and (B) hardness (*H*) of the three different chemical composition pellets sintered during 6 hours at 1000 °C. Solid lines represent the mean values, while the shadowed areas represent the standard deviation.

Furthermore, Figure 4. 35 shows the mechanical properties as a function indentation depth for $CuFe_2O_4$ samples sintered at different temperatures. In both cases, the mechanical properties increase as the sintering temperature is higher. Moreover, it is possible to see how the sample sintered at 1000 °C is clearly the one with lower mechanical properties, but from 1100 °C there is not an evident gain of mechanical properties with temperature. Probably, once the sintering is efficient above 1000 °C, the particles become strongly attached and the mechanical properties are almost constant.

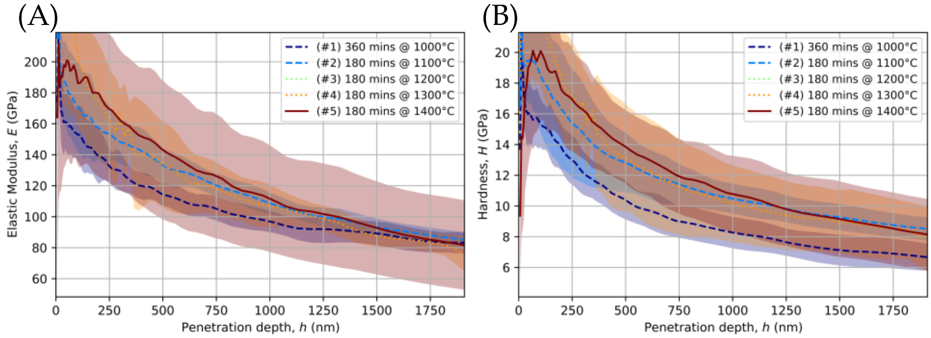

Figure 4. 35. Penetration depth dependence of the (A) elastic modulus (*E*), and (B) hardness (*H*) of the $CuFe_2O_4$ pellets sintered at different temperatures. Solid lines represent the mean values, while the shadowed areas represent the standard deviation.

In order to have a better idea about the evolution of the mechanical properties as a function of the sintering temperature, the mean value of these properties has been calculated in each sample between 600 nm and 1800 nm of penetration depth, a monotone region which is out of surface hardening effects. The results are shown in Figure 4. 36.

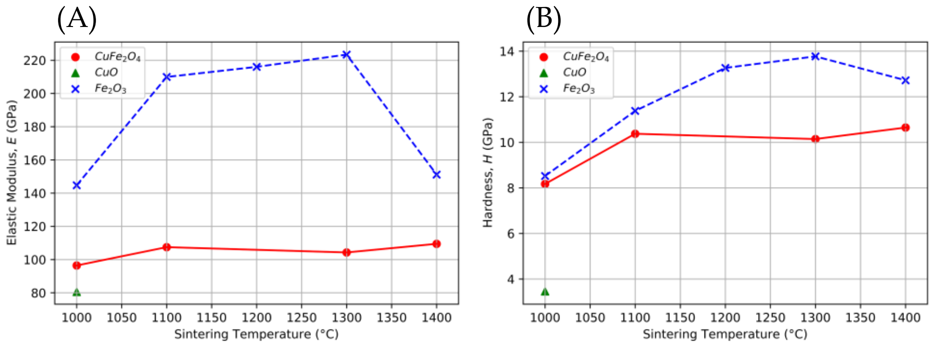

Figure 4. 36. Dependence of the (A) elastic modulus (*E*), and (B) hardness (*H*) with the sintering temperature. These are the main values calculated between 600 nm and 1800 nm of penetration depth.

Here we can confirm that the main increase on mechanical properties in both materials is made between 1000 °C and 1100 °C. Moreover, in copper ferrite, the *E* and *H* continuously increase with temperature. On the other hand, Fe_2O_3 experiments an increase of *E* and *H* that seem to arrive to a maximum or a plateau at 1300 °C, but then they suddenly drop down at 1400 °C. This decrease in mechanical properties agrees with the decrease in density at this temperature.

6.3. Static magnetic properties

A piece of each pellet used for nanoindentation has been measured by SQUID magnetometry. The *M*(*H*) cycle has been measured. The results obtained for the different $CuFe_2O_4$ samples are represented in Figure 4. 37. Due to the symmetric behaviour of the hysteresis cycle, only the first magnetization and demagnetization curves have been measured, as they already provide all the needed information.

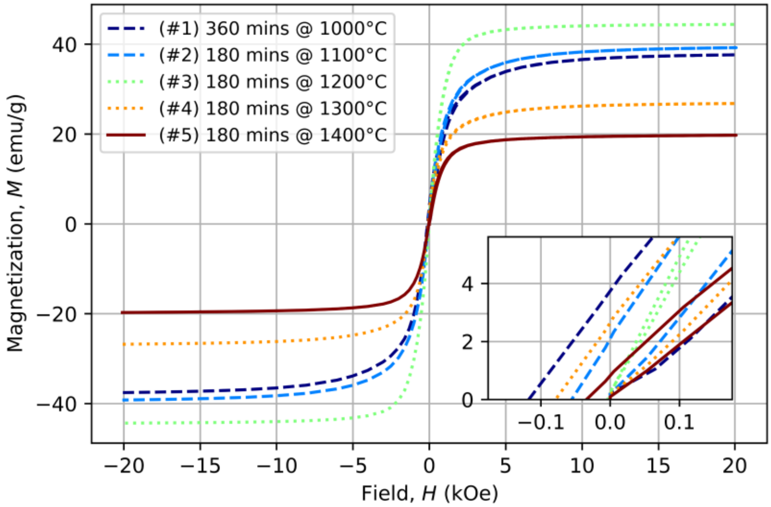

Figure 4. 37. *M*(*H*) measurements at 300 K for the different $CuFe_2O_4$ pellets sintered at different temperatures.

The saturation values reached by these materials are considerably higher than those previously obtained for the tetragonal $CuFe_2O_4$ in powder form, and much more similar to those obtained for the powder cubic phase. Nevertheless, it should be taken into account that the used temperatures in these samples are considerably higher than those in powders, and it has been already seen it may favour the increase of M_S. In this case, the M_S continuously increases until 1200 °C, where values above 40 emu/g are reached. These results are in good agreement with other bulk $CuFe_2O_4$ sintered at 1000 °C and characterized by other authors [33]. Above this temperature, it continuously decreases. This behaviour is in accordance with the results obtained by XRD, where a decrease of the $CuFe_2O_4$ content is found above 1200 °C due to the CuO removal. Furthermore, by looking to the inner plot one may see that as the temperature increases, the ferrite softens (the hysteresis cycle becomes thinner) and its permeability (μ) increases. Again, above 1200 °C - when we start to have a $CuFe_2O_4$+Fe_2O_3 mixture in the sample – this tendency is broken. The increase on permeability is understood to be a consequence of an increase of the purity and the crystal size, and a reduction of internal stresses and defects.

The *M*(*H*) behaviour of the two former oxides is illustrated in Figure 4. 38.

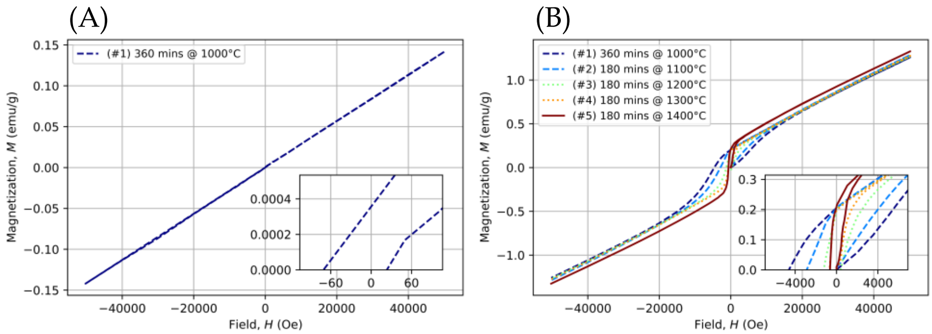

Figure 4. 38. $M(H)$ measurements at 300 K of the (A) CuO, and (B) Fe_2O_3 pellets sintered at different temperatures.

The paramagnetic behaviour of the Fe_2O_3 is corroborated, and the almost null magnetic response of CuO checked, as could be expected [4], [34]. The non-saturation, even at 40 kOe, may be the consequence of the existence of very small particles that are superparamagnetic at room temperature. By looking at the inner plot in Figure 4. 38.B, it is possible to clearly see how the magnetic permeability increases with the sintering temperature. Moreover, the magnetic response is softer with the increase of the sintering temperature. This tendency is similar to the one obtained by the $CuFe_2O_4$ pellets and can be also understood as a crystal growth and relaxation of the microstructure after the compaction process.

In order to summarize the magnetic properties of all the pellets and to allow an easier comparison, M_S, M_R, and H_C have been deduced in each case and the results are shown in Figure 4. 39.

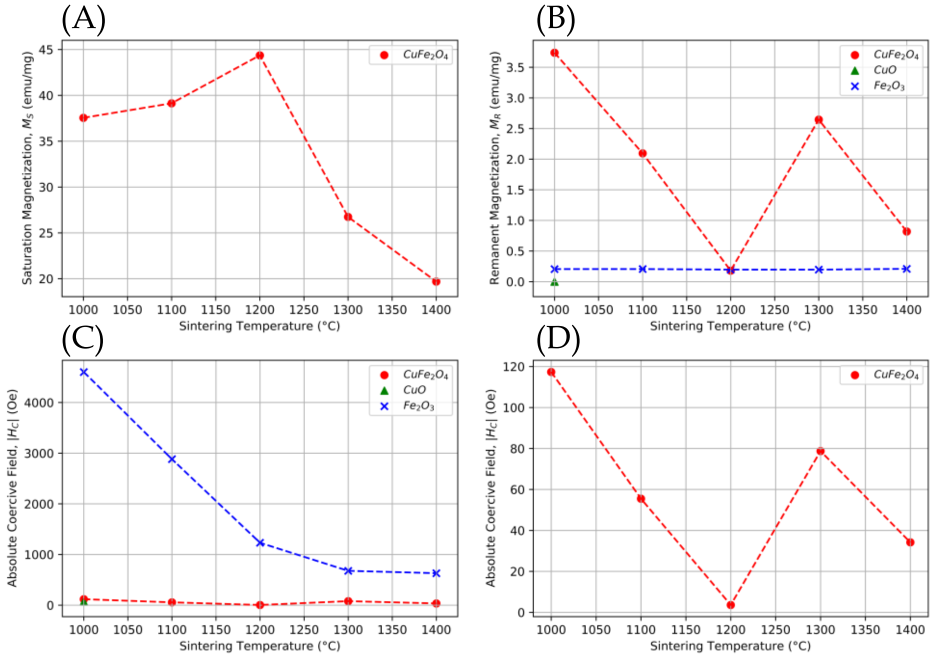

Figure 4. 39. Effect of the sintering temperature for all pellets on the (A) saturation magnetization M_S, (B) remanent magnetization (M_R), and (C) absolute value of coercive field (H_C). (D) Individual representation of the H_C evolution only for $CuFe_2O_4$.

In Figure 4. 39.A, it is clearly seen the change in behaviour tendency for $CuFe_2O_4$ previously commented. M_S continuously increases until the critical sintering temperature is reached; then, it is rapidly reduced due to the reduction of $CuFe_2O_4$ content in the pellet. The M_S behaviour could not be analysed for the other samples as the saturation was not reached in the $M(H)$ measurements.

The same tendency break at 1200 °C is observed for $CuFe_2O_4$ in Figure 4. 39.B, where the dependence of M_R with the sintering temperature is studied. The remanence initially decreases according to the properties' softening observed before. On the other hand, M_R is almost constant in this temperature range in the case of Fe_2O_3.

There is a clear H_C reduction tendency in Fe_2O_3, as it can be appreciated in Figure 4. 39.C. It continuously decreases with temperature until reaching constant values of around 650 Oe. It also decreases in $CuFe_2O_4$ until 1200 °C, where starts to be an excess of Fe_2O_3 in the sample and the coercivity increases. Once it has increased by the appearance of Fe_2O_3, it then keeps reducing with temperature.

Overall, the increase on M_S and the decrease on H_C (which are seen until 1200 °C), as well as the reduction on M_R observed here, are in agreement with other results obtained elsewhere [33].

6.4. Frequency-dependent magnetic properties

As it has been previously introduced, ferrite materials are of great interest in applications operating at high frequencies due to their high electrical resistivity, which reduced the eddy current losses in the material. They do not possess a magnetic permeability (μ) as large as metallic soft magnets, but they can reach higher operation frequencies due to their low power losses. For this reason, its frequency-dependent complex magnetic permeability ($\hat{\mu}(\nu) = \mu'(\nu) - j\mu''(\nu)$) has been measured in the kHz and MHz range by impedance spectroscopy. The toroidal-shaped pellets have been measured, and the Davidson-Cole (DC) model has been manually fitted to the experimental data. Figure 4. 40 shows the results obtained for the $CuFe_2O_4$ samples.

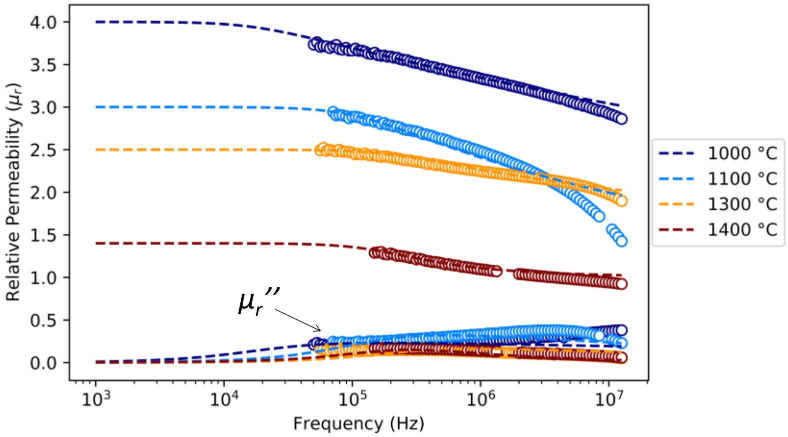

Figure 4. 40. Frequency-dependent complex magnetic permeability (μ) measured by impedance spectroscopy in the frequency range from 1 kHz to 13 MHz. Circular dots represent experimental data, while dashed lines is the DC model fitting. The curves at the top part of the figure corresponds to the real component, while those at the bottom are the imaginary parts.

In all cases, the relaxation has already started in this frequency range, as the real component decreases. This range of relaxation frequencies is of the same order of magnitude as those obtained in other works [35] performing complex impedance analyses of similar ferrites. Furthermore, the static magnetic permeability (μ_S), which is the μ_r' value at low frequencies, decreases as the sintering temperature grows. This is contrary to the behaviour seen in the $M(H)$ measurements; however, one should consider that these are dynamic results, instead of the static ones obtained in the $M(H)$. The response of the precursor oxides is shown in Figure 4. 41.

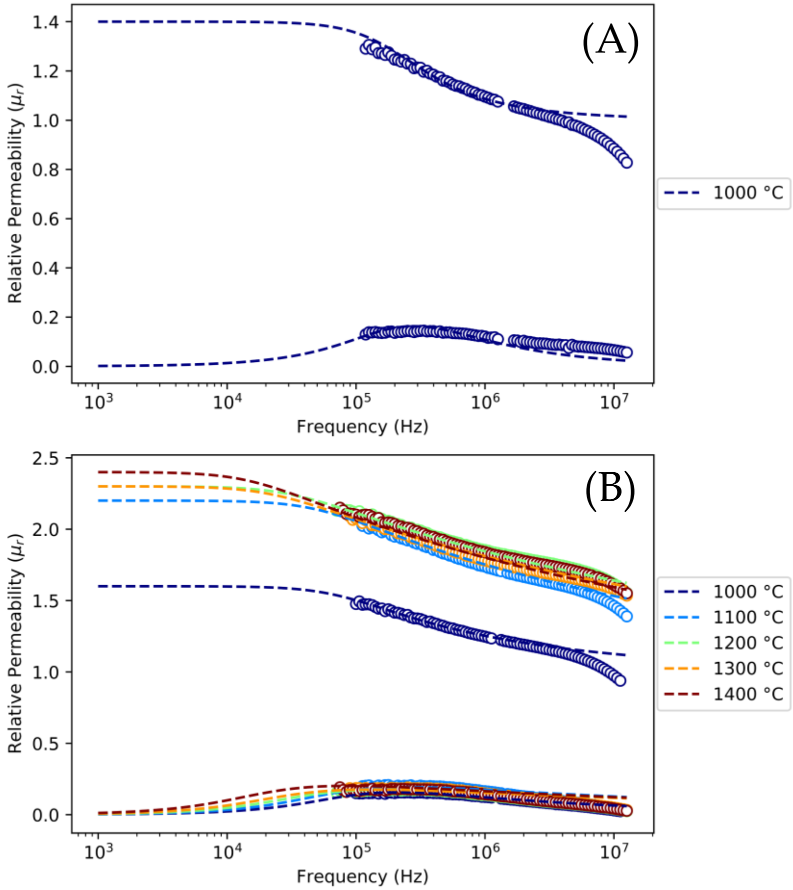

Figure 4. 41. Frequency-dependent complex magnetic permeability of the (A) CuO, and (B) Fe_2O_3 pellets sintered at different temperatures.

As it might be expected, the magnetic permeabilities are lower than those from $CuFe_2O_4$. The relaxation in CuO (Figure 4. 41.A) seems to start at 100 kHz, where μ_r' decreases and a maximum in μ_r'' is found. Furthermore, a second relaxation is intuited at 10 MHz.

Fe_2O_3 is already relaxing in the frequency range at which has been measured. It presents static magnetic permeabilities between 1.5 and 2.5. In this case, the tendency in the change of real permeability is the opposite of that in $CuFe_2O_4$: it now grows when increasing the temperature. Moreover, it can be seen how it notably increases between 1000 °C and 1100 °C, but then it is almost constant and only small differences are detected. In order to summarize these results and better compare the behaviour of each sample, Figure 4. 42 presents the values obtained from the DC model adjustment for each sample.

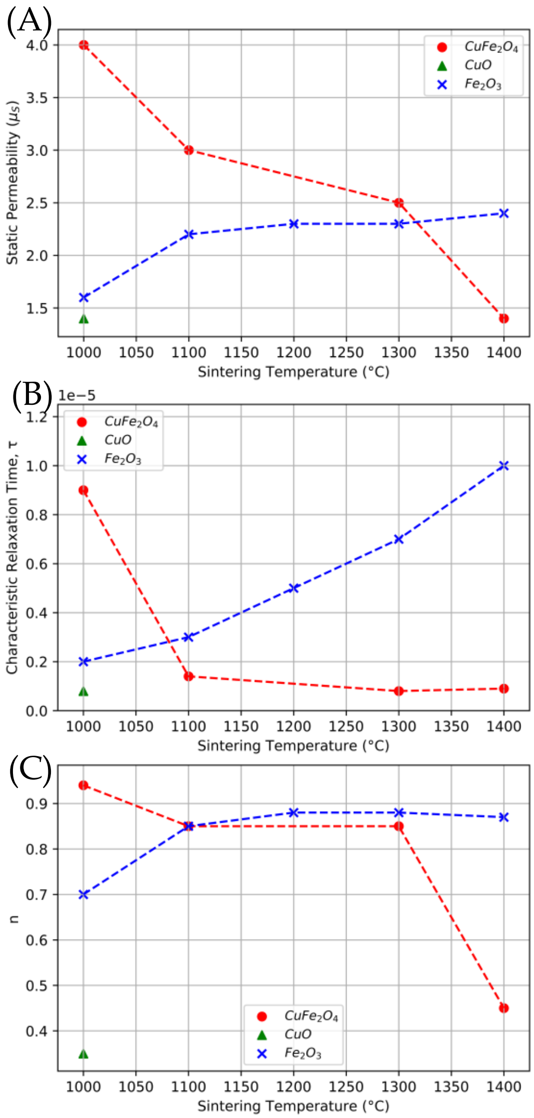

Figure 4. 42. Dependence of the DC fitted parameters with the sintering temperature. (A) Static permeability (μ_S), (*B*) characteristic relaxation time (τ), *and* (*C*) geometrical factor *n*.

The sintering temperature affects in a radical opposite way the frequency-dependent magnetic properties of $CuFe_2O_4$ and Fe_2O_3. The inverse effect on the evolution of the static magnetic permeability – which is shown in Figure 4. 42.A - has already been commented. On the other hand, the relaxation time of the samples sintered at 1000 °C is higher in the $CuFe_2O_4$ pellet than in the Fe_2O_3 one. This means that, in these conditions, $CuFe_2O_4$ relaxes - i.e. the power losses appear – at lower frequencies than in Fe_2O_3. However, when pellets are sintered at higher temperatures, $CuFe_2O_4$ shows better frequency stability than Fe_2O_3.

Finally, n parameter is reduced with temperature in $CuFe_2O_4$, while it increases until a maximum value for Fe_2O_3. n parameter describes the type of relaxation: the closer n is to zero, the closer is the relaxation to the ideal Debye model; as closer is n to one, more important is the DC influence on the relaxation. Larger n values correspond to smaller slopes in the decrease of μ_r', what is due to the presence of a distribution of relaxation times.

7. CORRELATION BETWEEN MECHANICAL AND MAGNETIC PROPERTIES IN BULK SAMPLES

Once the structural, mechanical, and magnetic properties have been separately studied and discussed as a function of the preparation conditions, we now aim to directly correlate them. As stated before, this may be an important step for materials' selection and design processes.

A large number of possible combinations between all the studied mechanical and magnetic parameters could be tested in order to find meaningful experimental relationships between properties. However, in this work we have used statistical tools to objectively check the relationship between variables [36].

By using a self-made *Python*® program, all the possible combinations between the magnetic and mechanical properties have been tested. The mechanical properties here considered have been H and E, while the magnetic ones are M_S, M_R, H_C, μ_S, τ, and n. It leads on twelve possible combinations, in each of the different eleven samples.

The Pearson's correlation coefficient (ρ) has been calculated for each of these combinations. This factor, which is defined between -1 and 1, provides information about the linear correlation between two variables. There is no correlation when the coefficient is 0, whereas there is a strong correlation when the coefficient is close to 1 or -1. The positive or negative nature of the index indicates if there is a positive or a negative correlation, i.e. if the variables are directly or inversely proportional. The calculation of this coefficient is defined by Equation 4. 1. Moreover, in this study we have also used the Spearman's correlation, which does not assume neither a Gaussian distribution of values nor a lineal relationship between variables. This is a good exercise to double-check the importance of the relationship between variables and to discuss its linear nature. The Spearman's factor (r_S) can be calculated by means of Equation 4. 2.

$$\rho = \frac{cov(X,Y)}{\sigma(X) \cdot \sigma(Y)}$$ Equation 4. 1

$$r_S = \frac{cov\big(rg(X), rg(Y)\big)}{\sigma\big(rg(X)\big) \cdot \sigma\big(rg(Y)\big)}$$ Equation 4. 2

where cov refers to the covariance, rg is the rank variables, and σ is the standard deviation.

The Pearson's coefficients for $CuFe_2O_4$ are shown in Table 4. 12, while Table 4. 13 shows the Spearman's factor for the same material.

Table 4. 12. Pearson's correlation between the magnetic and mechanical properties for $CuFe_2O_4$.

	Elastic Modulus, *E*	**Hardness, *H***
Saturation magnetization, M_S	-0.53	-0.55
Remanent magnetization, M_R	-0.94	-0.88
Coercive field, H_C	-0.99	-0.94
Static permeability, μ_S	-0.86	-0.85
Relaxation time, τ	-0.92	-0.98
n	-0.73	-0.64

Table 4. 13. Spearman's correlation between the magnetic and mechanical properties for $CuFe_2O_4$.

	Elastic Modulus, *E*	**Hardness, *H***
Saturation magnetization, M_S	-0.40	-0.40
Remanent magnetization, M_R	-1.00	-1.00
Coercive field, H_C	-1.00	-1.00
Static permeability, μ_S	-0.80	-0.80
Relaxation time, τ	-0.40	-0.40
n	-0.95	-0.95

The first aspect that should be highlighted is the negative nature of all the obtained parameters. It means that in all cases, an increase of the magnetic parameters leads to a decrease of the mechanical properties. On the other hand, it should be also stressed the strong correlation found between the magnetic and mechanical properties, as in general terms most of the factors are above 0.7 in absolute value. Additionally, the values obtained for Spearman's correlation are the same for E than H.

There are some differences between the values obtained by each method. On those cases where Pearson's coefficient is higher than Spearman's in absolute value, we can understand that the correlation is closely to be linear. On the other hand, when Spearman's coefficient is better than Pearson's one, another kind of correlation might be better.

Nevertheless, in general terms both methods agree on which are those properties with higher correlations. They specially are M_R, H_C, μ_S. Moreover, τ also seems to have a high correlation with E and H according to Pearson's criteria, while it is n the one that improves when using Spearman's.

Then, as the correlations apparently have a high degree of linearity, a linear regression have been individually done in all the possible combinations. The *r-squared* (R^2) coefficient obtained from each regression is annotated in Table 4. 14.

Table 4. 14. R^2 coefficients obtained from the linear regression between the magnetic and mechanical properties of $CuFe_2O_4$.

	Elastic Modulus, *E*	**Hardness, *H***
Saturation magnetization, M_S	0.28	0.30
Remanent magnetization, M_R	0.88	0.77
Coercive field, H_C	0.97	0.88
Static permeability, μ_S	0.74	0.73
Relaxation time, τ	0.85	0.96
n	0.53	0.41

The correlations are excellent in some cases. For instance, there is a R^2 of 0.97 between H_C and E, a R^2 of 0.96 between τ and H, or a R^2 of 0.88 when M_R vs E and H_C vs H are compared. With these results, we actually have an objective criterion to decide which properties are correlated.

In Figure 4. 43, the two stronger correlations found for the elastic modulus (*E*) are represented.

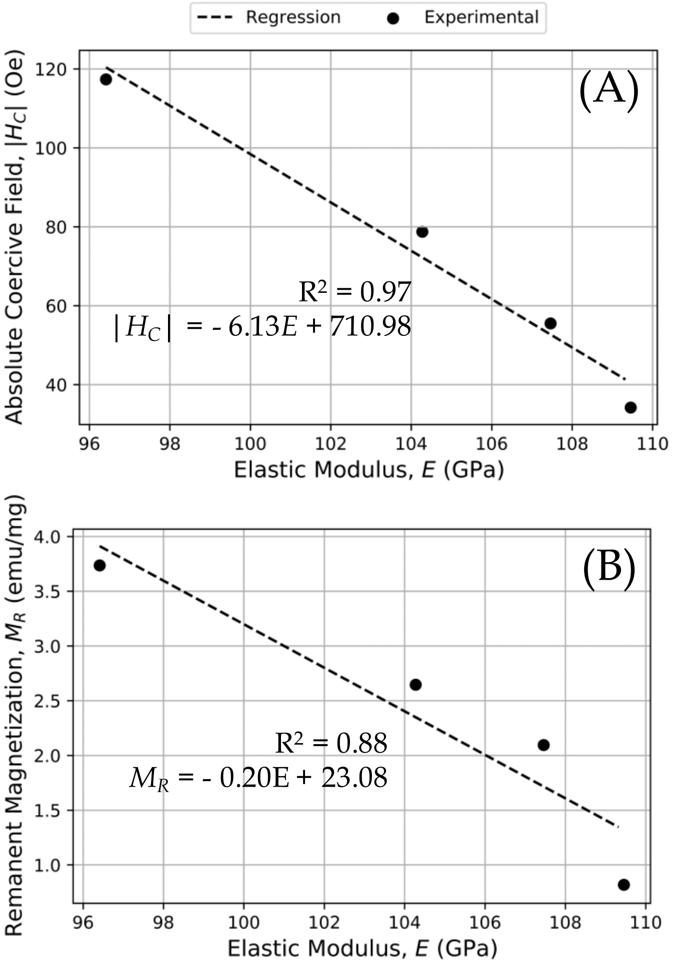

Figure 4. 43. (A) Elastic modulus – coercive field, and (B) elastic modulus – remanent magnetization correlations for $CuFe_2O_4$. The resulting R^2 values and the obtained regression functions are specified in each graph.

The correlation between all the properties shown in Figure 4. 43 is evident. Both the coercivity and the remanence of $CuFe_2O_4$ decrease with higher elastic modulus values. As both, H_C and M_R, provide information about the character of the magnetic properties, we can expect to fabricate a soft magnetic copper ferrite with an elevated elastic modulus, which would be formidable for the fabrication of pieces for high frequency applications because of the good mechanical properties and low hysteresis losses. On the other hand, the two more significant correlations for the hardness are presented in Figure 4. 44.

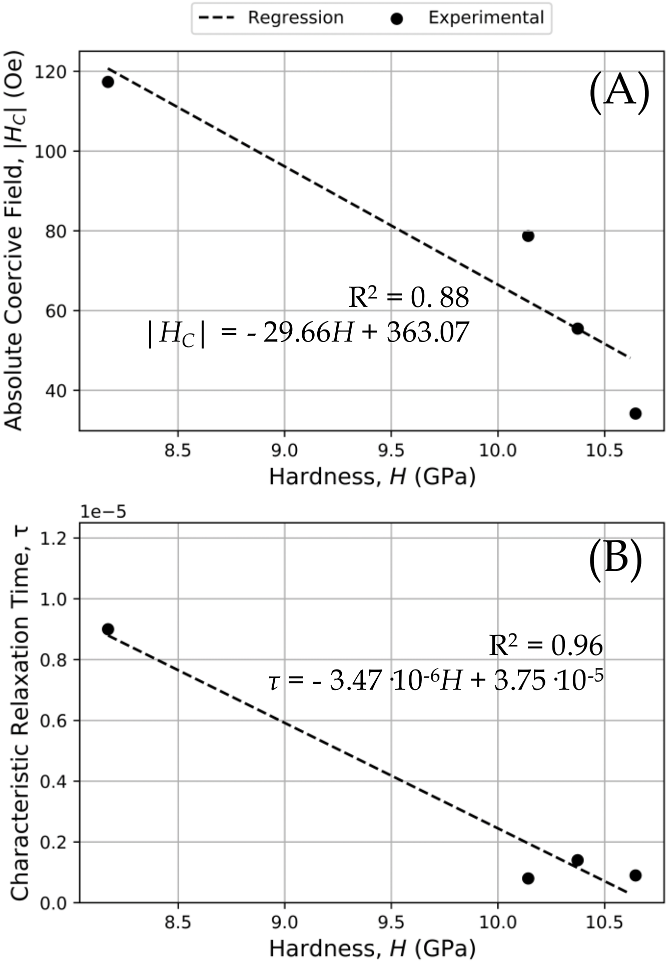

Figure 4. 44. (A) Hardness – coercive field, and (B) hardness – relaxation time correlations for $CuFe_2O_4$. The resulting R^2 values and the obtained regression functions are specified in each graph.

Again, we can see how the coercivity of the system reduces while we are able to increase the mechanical properties of the material. Thus, harder and softer copper ferrite pellet can be obtained by an appropriate fabrication method. Furthermore, in this case we can also see that the relaxation time decreases in harder materials. It means that harder materials relax at higher frequencies than the softer ones. Once more, these are promising results for the high-frequency technology sector as both, the mechanical properties and the frequency stability of the pellet, can be increased at the same time.

8. CHAPTER CONCLUSIONS

From all the results presented in this chapter, many conclusions may be extracted. The most important ones are commented below.

We have successfully synthesized $CuFe_2O_4$ nanoparticles, despite they sinter forming micrometric aggregates. Moreover, the purity of the products obtained are high (above 96 % by sol-gel and more than 88 % by co-precipitation), which are slightly higher than the ones reported for similar methods. The crystalline structure has been refined by the Rietveld method.

By analysing the sol-gel method, it has been proven that the chemical purity does not improve above 850 °C, while the particles' agglomeration keeps increasing at high temperatures and long times. It is therefore recommended to work in the softer conditions of the second DoE (30 minutes at 850 °C), where a maximum in $CuFe_2O_4$ content is reached. As a general trend, it has been found that high temperatures and short times seem to be an interesting direction to allow the formation of $CuFe_2O_4$ and to avoid sintering between nanoparticles.

On the other hand, co-precipitation method has also been upgraded according to our targets. By comparing both methods under the same temperature conditions, it has been reported that sol-gel provides purer samples, while the co-precipitation one leads on less-aggregated systems. The most important difference between the sol-gel and co-precipitation methods has been the production of two different crystal structures of $CuFe_2O_4$: tetragonal and cubic, respectively. The formation of the cubic and tetragonal phases has been clearly seen by temperature dependent XRD measurements. In the sol-gel sample, the cubic structure is already formed during the gel burning process prior to the calcination, which acts as a quenching of the high-temperature structure. During the cooling process, there is a cubic-to-tetragonal transition just below 400 °C. In the co-precipitation sample the cubic phase is formed at 650 °C and remains stable even when it is cooled down to room temperature. The explanation of why the cubic phase is stable at room temperature is not obvious. The cooling rate after heating to 950 °C must be discarded as the reason, as it has been the same for both samples. From the obtained results, we suggest that it could be due to the different distribution of cations when the cubic phase is formed during the fast gel burning process or during a continuous heating treatment.

Furthermore, we have fabricated bulk toroids with three different compositions: copper ferrite, and its corresponding former oxides (iron and copper oxides). Sintering problems have been detected due to the CuO melting, which has prevented us to fabricate CuO pellets at higher temperatures. It has also affected to the $CuFe_2O_4$ pellets as they have started to lose CuO above 1200 °C.

The apparent densities and porosities are in good agreement with the melting of CuO. By XRD measurements we have corroborated the removal of CuO from the $CuFe_2O_4$ samples at high temperatures, as well as the tetragonal crystal structure of the ferrite.

The intermediate mechanical properties of $CuFe_2O_4$ compared with its former oxides have been observed. On the other hand, this behaviour is different when we talk about the magnetic properties, as the copper ferrite is much more magnetic than its former oxides. The results from nanoindentation and SQUID magnetometry are consistent with the XRD measurements and porosity calculated for each sample, as a clear transition is often detected at 1200 °C for $CuFe_2O_4$.

The frequency dependent permeability measurements - by means of impedance spectroscopy - have revealed that the static permeability of $CuFe_2O_4$ decreases for higher sintering temperatures, just the opposite that happens in Fe_2O_3. All the measured samples present a perfect order of the static permeability with the sintering conditions, which gives an idea about the importance of the change of microstructure in these dynamic properties.

In this chapter, the magnetic and mechanical properties have been finally correlated. The use of Pearson's and Spearman's correlation coefficients has provided a general and objective view about which are those properties strongly correlated. Furthermore, by the comparison of these coefficients, the linear nature of the correlation seems to be clear. The linear regression between these properties has given R^2 values higher than 0.95, demonstrating a solid linear correlation between variables. Some of the variables strongly correlated are the $CuFe_2O_4$ coercivity with its mechanical properties (*E* and *H*), as well as the remanence or the relaxation time. In all cases, it has been proved that it is possible to fabricate magnetic pellets with lower magnetic losses and higher frequency stability, and to improve the mechanical properties at the same time. This is a promising result for high-frequency applications, but also for the materials selection process in general as it leads to a clear methodology to extract direct relationships between properties.

9. FUTURE WORK

Interesting conclusions have been obtained from this work; nevertheless, there are still many aspects that need to be investigated to solve some of the questions and challenges that remain to be done. This work is hoped to open a door to continue investigating in some synthesis aspects, the understanding of the tetragonal and phase structures formation, or the correlation between mechanical and magnetic properties for selection processes.

First, it needs to be found a solution to avoid the particles' agglomeration. The control over the gel burning and calcination process is mandatory. It seems that short and high-temperature processes could be useful in this regard. Also, the region between 750 °C and 850 °C should be better explored in order to determine if it is possible to reduce the temperature without a reduction of the maximum purity. The inversion factor in the synthetized spinel structures could be more deeply explored. The re-localization of Cu^{2+} and Fe^{3+} cations may have an important effect on the physical properties of these ceramic materials. Transmission Electron Microscopy (TEM) measurements by Electron Energy Loss Spectroscopy (EELS) are planned to be done in the short-future in order to determine the inversion factor [37]. Moreover, these results may be combined with the Rietveld method in order to get more adjusted refinements.

The sites occupation of the cubic structures formed by sol-gel and co-precipitation should be deeply explored in order to confirm or refuse the proposed explanation to the stability of the cubic form at room temperature. Rietveld refinement, TEM, or X-ray photoelectron spectroscopy (XPS) could be interesting techniques to be used.

The potential soft magnetic properties of the powder cubic samples prepared by co-precipitation should be deeply investigated. The investigation of the frequency-dependent magnetic permeability would provide important information. However, impedance spectroscopy measurements cannot be directly done in powder form and require bulk toroidal-shaped samples.

It would be also interesting to fabricate pellets from the co-precipitation products and to check if it is possible to fabricate $CuFe_2O_4$ pellets with a cubic structure. Also, calcinating the powder before the compaction and sintering of the pellets could be a way to keep the stoichiometry of $CuFe_2O_4$ at high temperatures. With this strategy, $CuFe_2O_4$ could be formed prior to the sintering, and the removal of CuO could, maybe, be avoided. Also, the addition of this thermal treatment could lead to a different structure, resulting then in different mechanical and magnetic properties of the same compound.

Moreover, the use of more advanced methods (such as tomography) would lead to a better understanding of the amount and morphology of the porosity, which affects both the mechanical and magnetic properties of the bulk. Furthermore, performing further magnetic measurements (such as ZFC – FC) would provide information about the material's energy barrier distribution.

In general, a larger number of samples would improve the statistical process here presented. With a larger number of experimental points (toroids sintered at other temperatures, times, or even exploring intermediate chemical compositions) it would be possible to get a more accurate correlation, or even to explore other types of relationships between those properties presenting a low linear correlation.

10.REFERENCES

[1] A. M. Balagurov, I. A. Bobrikov, M. S. Maschenko, D. Sangaa, and V. G. Simkin, "Structural phase transition in CuFe2O4 spinel," *Crystallogr. Reports*, vol. 58, no. 5, pp. 710–717, 2013.

[2] M. Kanagaraj, P. Sathishkumar, G. K. Selvan, P. Kokila, and S. Arumugam, "Structural and magnetic properties of CuFe 2 O 4 as-prepared and thermally treated spinel nanoferrites," *Indian J. Pure Appl. Phys.*, vol. 52, no. February 2016, pp. 124–130, 2014.

[3] P. Khemthong, C. Kongmark, N. Kochaputi, S. Mahakot, S. Rodporn, and K. Faungnawakij, "In Situ X-ray Absorption Fine Structure Probing-Phase Evolution of CuFe2O4 in Nanospace Confinement," *Inorg. Chem.*, vol. 58, no. 10, pp. 6584–6587, 2019.

[4] J. M. D. Coey, *Magnetism and Magnetic Materials*. Cambridge University Press, 2009.

[5] M. T. Dove, J. Singleton, A. M. Fox, S. J. Blundell, J. F. Annett, and R. A. L. Jones, *Magnetism in Condensed Matter Physics*. Oxford Master Series in Condensed Matter Physics, 2001.

[6] A. Hernando, P. Marín, M. Vázquez, and G. Herzer, "Thermal dependence of coercivity in magnetic nanostructures," *J. Magn. Magn. Mater.*, vol. 177–181, pp. 959–961, 1998.

[7] M. Yousefi, S. Sharafi, and a. Mehrolhosseiny, "Correlation between structural parameters and magnetic properties of ball milled nano-crystalline Fe-Co-Si powders," *Adv. Powder Technol.*, vol. 25, no. 2, pp. 752–760, 2014.

[8] S. Cazottes, a. Fnidiki, M. Coisson, D. Lemarchand, and F. Danoix, "Correlation between microstructure at fine scale and magnetic properties of magnetoresistive Cu80Fe10Ni10 ribbons: Modeling of magnetization," *J. Magn. Magn. Mater.*, vol. 333, pp. 22–29, 2013.

[9] V. Sebastian, N. Lakshmi, and K. Venugopalan, "Correlation between microstructure and magnetic properties in mechanically alloyed nanogranular FeAl," *Mater. Lett.*, vol. 61, pp. 4635–4638, 2007.

[10] M. Sedlacik *et al.*, "Correlation of structural and magnetic properties of Fe3O4 nanoparticles with their calorimetric and

magnetorheological performance," *J. Magn. Magn. Mater.*, vol. 326, pp. 7–13, 2013.

[11] R. K. Dwivedi, P. K. Jha, P. a. Jha, and P. Kumar, "Structural – Electrical property correlation in defect induced nanostructured off-stoichiometric bismuth ferrite: A defect analysis," *Mater. Chem. Phys.*, vol. 164, pp. 15–22, 2015.

[12] R. Ristić *et al.*, "Simple correlation between mechanical and thermal properties in TE–TL (TE=Ti,Zr,Hf;TL=Ni,Cu) amorphous alloys," *J. Non. Cryst. Solids*, vol. 357, no. 15, pp. 2949–2953, 2011.

[13] V. Zhukova *et al.*, "Correlation between magnetic and mechanical properties of devitrified glass-coated Fe71.8Cu1Nb3.1Si15B9.1 microwires," *J. Magn. Magn. Mater.*, vol. 249, no. 1–2, pp. 79–84, 2002.

[14] M. Morales *et al.*, "Correlation between electrical and mechanical properties in LaSrGaMgO ceramics used as electrolytes for solid oxide fuel cells," *J. Power Sources*, vol. 246, pp. 918–925, 2014.

[15] L. B. Zakiyah *et al.*, "Up-scalable synthesis of size-controlled copper ferrite nanocrystals by thermal treatment method," *Mater. Sci. Semicond. Process.*, vol. 40, pp. 564–569, 2015.

[16] M. V. López-Ramón, M. A. Álvarez, C. Moreno-Castilla, M. A. Fontecha-Cámara, Á. Yebra-Rodríguez, and E. Bailón-García, "Effect of calcination temperature of a copper ferrite synthesized by a sol-gel method on its structural characteristics and performance as Fenton catalyst to remove gallic acid from water," *J. Colloid Interface Sci.*, vol. 511, pp. 193–202, 2018.

[17] I. Sharifi, A. Zamanian, and A. Behnamghader, "Synthesis and characterization of Fe0.6Zn0.4Fe2O4 ferrite magnetic nanoclusters using simple thermal decomposition method," *J. Magn. Magn. Mater.*, vol. 412, pp. 107–113, 2016.

[18] W. Lv, B. Liu, Z. Luo, X. Ren, and P. Zhang, "XRD studies on the nanosized copper ferrite powders synthesized by sonochemical method," *Jorunal Alloy. Compd.*, vol. 465, no. 3, pp. 261–264, 2008.

[19] V. A. Zhuravlev, R. V. Minin, V. I. Itin, and I. Y. Lilenko, "Structural parameters and magnetic properties of copper ferrite nanopowders obtained by the sol-gel combustion," *J. Alloys*

Compd., vol. 692, pp. 705–712, 2017.

[20] T. P. Sumangala, C. Mahender, A. Barnabe, N. Venkataramani, and S. Prasad, "Structural, magnetic and gas sensing properties of nanosized copper ferrite powder synthesized by sol gel combustion technique," *J. Magn. Magn. Mater.*, vol. 418, pp. 48–53, 2016.

[21] S. Anandan, T. Selvamani, G. G. Prasad, A. M. Asiri, and J. J. Wu, "Magnetic and catalytic properties of inverse spinel CuFe 2 O 4 nanoparticles," *J. Magn. Magn. Mater.*, vol. 432, pp. 437–443, 2017.

[22] R. S. Yadav *et al.*, "Cation Migration-Induced Crystal Phase Transformation in Copper Ferrite Nanoparticles and Their Magnetic Property," *J. Supercond. Nov. Magn.*, vol. 29, no. 3, pp. 759–769, 2016.

[23] M. Salavati-Niasari, T. Mahmoudi, M. Sabet, S. M. Hosseinpour-Mashkani, F. Soofivand, and F. Tavakoli, "Synthesis and Characterization of Copper Ferrite Nanocrystals via Coprecipitation," *J. Clust. Sci.*, vol. 23, no. 4, pp. 1003–1010, 2012.

[24] P. Tailhades *et al.*, "Cation Migration and Coercivity in Mixed Copper-Cobalt Spinel Ferrite Powders," *J. Solid State Chem.*, vol. 141, no. 1, pp. 56–63, 1998.

[25] Y. Gao, Z. Wang, J. Pei, and H. Zhang, "Structural, elastic, thermal and soft magnetic properties of Ni-Zn-Li ferrites," *J. Alloys Compd.*, vol. 774, pp. 1233–1242, 2019.

[26] W. Zhang, Y. Xue, and Z. Cui, "Effect of Size on the Structural Transition and Magnetic Properties of Nano-CuFe2O4," *Ind. Eng. Chem. Res.*, vol. 56, no. 46, pp. 13760–13765, 2017.

[27] X.-X. Tang, A. Manthiram, and J. B. Goodenough, "Copper ferrite revisited," *J. Solid State Chem.*, vol. 79, no. 2, pp. 250–262, Apr. 1989.

[28] A. M. Balagurov, I. A. Bobrikov, V. Y. Pomjakushin, D. V. Sheptyakov, and V. Y. Yushankhai, "Interplay between structural and magnetic phase transitions in copper ferrite studied with high-resolution neutron diffraction," *J. Magn. Magn. Mater.*, vol. 374, pp. 591–599, 2015.

[29] A. K. S. Rocha *et al.*, "Copper local structure in spinel ferrites determined by X-ray absorption and Mössbauer spectroscopy and

their catalytic performance," *Mater. Res. Bull.*, vol. 109, no. October 2017, pp. 117–123, 2019.

[30] M. M. Rashad, R. M. Mohamed, M. a. Ibrahim, L. F. M. Ismail, and E. a. Abdel-Aal, "Magnetic and catalytic properties of cubic copper ferrite nanopowders synthesized from secondary resources," *Adv. Powder Technol.*, vol. 23, no. 3, pp. 315–323, 2012.

[31] Y. Slimani *et al.*, "Magneto-optical and microstructural properties of spinel cubic copper ferrites with Li-Al co-substitution," *Ceram. Int.*, vol. 44, no. 12, pp. 14242–14250, 2018.

[32] Z. Xing, Z. Ju, J. Yang, H. Xu, and Y. Qian, "One-step solid state reaction to selectively fabricate cubic and tetragonal CuFe2O4 anode material for high power lithium ion batteries," *Electrochim. Acta*, vol. 102, pp. 51–57, 2013.

[33] R. Köferstein, T. Walther, D. Hesse, and S. G. Ebbinghaus, "Crystallite-growth, phase transition, magnetic properties, and sintering behaviour of nano-CuFe2O4 powders prepared by a combustion-like process," *J. Solid State Chem.*, vol. 213, pp. 57–64, 2014.

[34] R. Valenzuela, *Magnetic Ceramics*. Cambridge University Press, 1994.

[35] E. Oumezzine, S. Hcini, F. I. H. Rhouma, and M. Oumezzine, "Frequency and temperature dependence of conductance, impedance and electrical modulus studies of Ni0.6Cu0.4Fe2O4 spinel ferrite," *J. Alloys Compd.*, vol. 726, pp. 187–194, 2017.

[36] A. L. Edwards, *Introduction to linear regression and correlation*, 1st ed. San Francisco: WILEY-VCH, 1976.

[37] P. Torruella Besa, "Development of novel EELS tools to unveil nanoparticle properties," University of Barcelona, 2019.

CHAPTER V

MAGNETIC RELAXATION EXPERIMENTS IN CNT-BASED NANOCOMPOSITE

1. INTRODUCTION

There is actually an important interest paid to the study of the properties of magnetic nanocomposites which consist on magnetic nanoparticles embedded in a matrix of another material. Additional degrees of freedom are created by the combination of each material's properties, such as particle size, shape, concentration, conductivity, or permeability [1]–[3]. New functionalities may be obtained by combining these parameters [4].

Carbon Nanotubes (CNT) magnetic nanocomposites are of great interest as they can provide a useful platform to study various types of nanoparticles interactions, as well as the impact of the CNT matrix on the nanoparticles arrangement and their interplay [5], [6]. These composites can be fabricated by producing CNT by chemical vapour deposition (CVD) methods using 3d metals (Fe, Co, Ni) as catalysts. By this way, magnetic nanoparticles are placed inside the CNT matrix. The location of the magnetic nanoparticles can be controlled by the concentration of catalyst: for low concentrations, nanoparticles are only placed inside the CNT, while they can be also placed outside the inner CNT channels and within the wall for high concentrations [5], [7]. Thus, it is possible to change the nature and the interparticle interaction of the composite by controlling the catalyst concentration. The particles formed with these conditions are of few tens of nanometres in size, so they can be considered as single domain objects.

It has been recently found that for high concentration of ferromagnetic nanoparticles uniformly distributed throughout the sample, the interparticle interaction can be described within the random anisotropy model (RAM) [5], [8]. The local magnetic moments of single domain particles (SDP) are randomly oriented, and their exchange interaction exceeds to gain in energy due to magnetic anisotropy. In the light of these results, it is interesting to study the influence of the distribution of orientations of the local magnetization vectors and of the barriers (due to magnetic anisotropy between metastable magnetic states) on the relaxation processes.

In this chapter, we study the magnetic relaxation of a CNT magnetic nanocomposite filled with Fe-based nanoparticles prepared by CVD. The work presented in this chapter is the result of an interesting collaboration with Dr. Serghej L. Prischepa from the Belarusian State University of Informatics and Radioelectronics, Minsk (Belarus). S. L. Pischepa has been the responsible of the nanocomposite synthesis and its characterization by XRD and transmission electron microscopy (TEM), and worked on the theoretical approach.

2. CHAPTER OBJECTIVES

The first goal in this chapter is to study this CNT-Fe magnetic nanocomposite from a structural point of view in order to confirm the chemical composition and size of the embedded nanoparticles.

Also, we aim to determine the static magnetic response of this material, as well as to observe its energy barrier distribution from the ZFC-FC curves.

Finally, the main objective of this chapter is to do a deep analysis on the magnetic relaxation process of this family of materials, which has not been previously done to our knowledge.

3. SYNTHESIS AND CHARACTERIZATION

The multiwalled CNTs powder has been produced by the atmospheric pressure floating catalyst CVD (AP FC CVD). The experimental setup represented an 8 mm inner diameter tubular-type quartz reactor, and the feeding system consisting of a syringe pump for injection of a solution of ferrocene ($Fe(C_5H_5)_2$) in xylene. The ferrocene concentration has been chosen to be 10 wt.%. This quantity corresponds to the upper limit of the solubility of ferrocene in xylene, ensuring maximum saturation of the sample with ferromagnetic iron-containing nanoparticles. The temperature in the reaction zone has been fixed to 1150 K and the process duration to 1 min. It has created a carpet of multi-walled CNTs of thickness of 50 μm and CNT inner diameter of approximately 30 nm. The average size of nanoparticles is in the range of 20 – 40 nm. Argon with 100 sccm/min flow has been used as a carrier gas. More details about CNTs fabrication can be found elsewhere [5], [7], [9], [10].

The obtained powder sample has been analysed by SEM in Jeol and Quanta microscopes. The obtained images (see Figure 5. 1) reveal the formation of micrometric blocks where the CNTs are aligned. There is a random relative orientation between the different blocks.

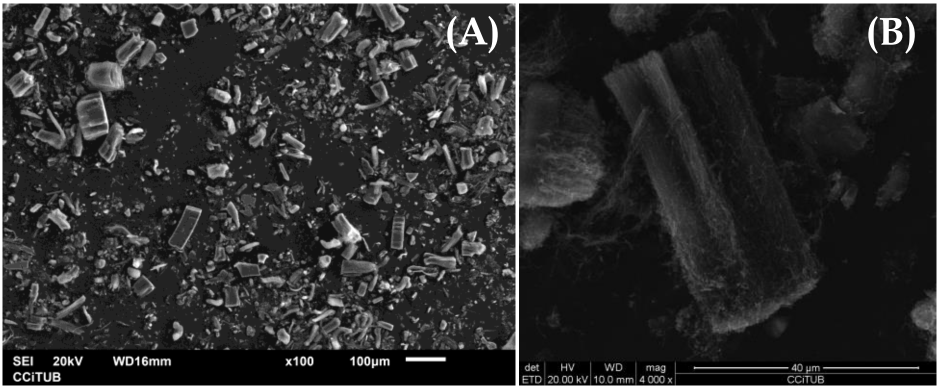

Figure 5. 1. SEM images of the CNT-based nanocomposite at (A) x100 magnification in the Jeol microscope, and (B) at x4000 magnification in the Quanta microscope.

We have also studied the sample by TEM with a *JEM-100CX TEM* (*JEOL*, Japan) microscope at an accelerating voltage of 100 kV. The results shown in Figure 5. 2 corroborate that the nanoparticles are distributed all over the sample's volume.

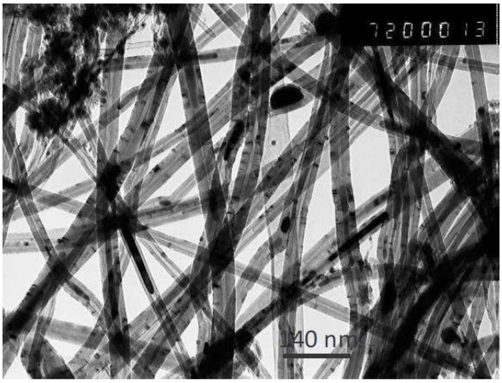

Figure 5. 2. TEM image of the CNT-based nanocomposite.

XRD measurements have also been done in order to determine the chemical composition and crystal structure of the different elements on the composite. The results presented in Figure 5. 3 confirm the majority presence of the cementite phase (Fe_3C), and the presence of lower quantities of graphite and iron. This is in good accordance with literature. The presence of Fe_3C phase was proved previously by Mossbauer spectroscopy [11] and by measurement of the saturation magnetization [5]. By means of the reference intensity ratio (RIR) approach the relative quantitative composition is of approximately 55% of cementite, 33% of graphite and 12% of iron. Moreover, this spectrum shows an important amorphous background signal, which might be due to the low long-term order to the CNTs.

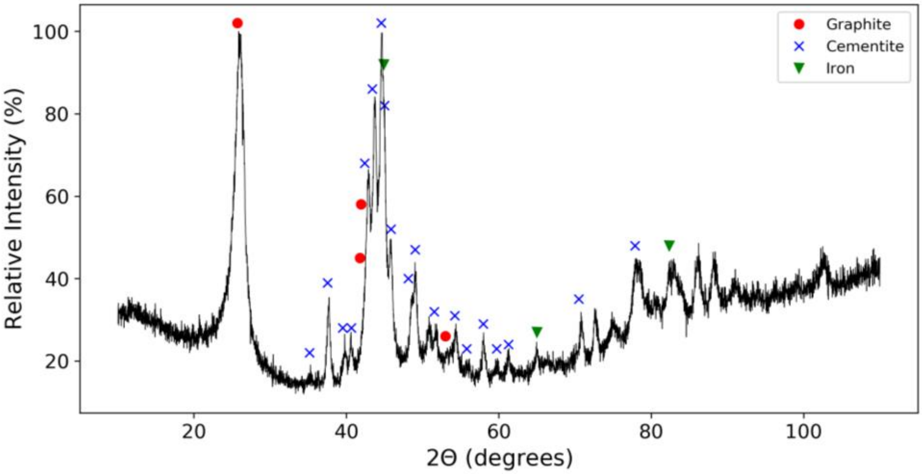

Figure 5. 3. XRD spectrum of the CNT-based nanocomposite. Each marker type indicates the main peaks of each phase.

4. MAGNETIC CHARACTERIZATION

The magnetic properties of the CNT-based nanocomposite have been studied by SQUID magnetometry. First, the *M*(*H*) curves have been analysed at different temperatures, from ultra-low (2 K) to room conditions (300 K).

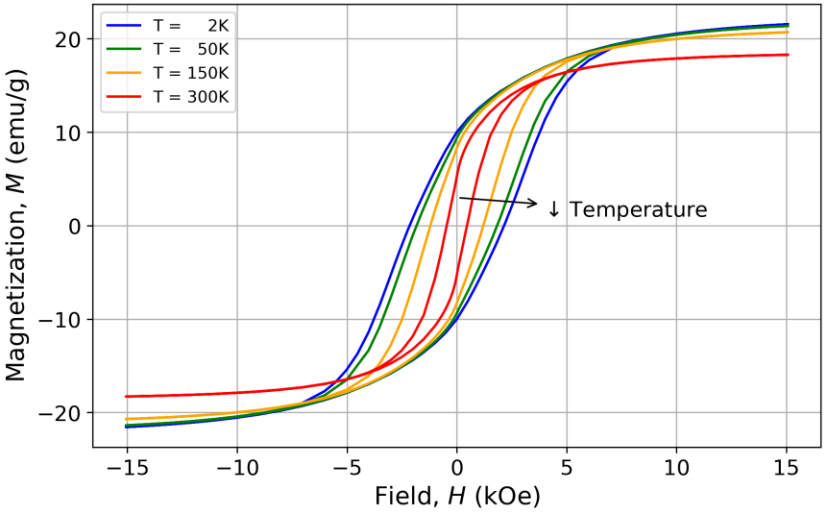

Figure 5. 4. $M(H)$ curves of the CNT-based nanocomposite at 2 K, 50 K, 150 K, and 300 K.

The comparative results are shown in Figure 5. 4. From these curves, one can clearly observe how the area of the hysteresis inversely depends on the temperature. From these results we have extracted the coercivity, which varies in the range from 0.5 to 2.2 kOe. These values are much greater than those usually reported for bulk Fe_3C [12]. We believe that this is a clear indication of small size effects on the H_C values, i.e. the coercivity of SDP is usually much greater than those of bulk [1]. For this case, and for the intermediate temperatures, H_C is expected to follow the empiric law expressed in Equation 5. 1.

$$H_c(T) = H_c(0)\left[1 - (T/T_B)^{\zeta}\right] \qquad \text{Equation 5. 1}$$

where T_B is the blocking temperature of the largest particles, and the exponent ζ depends on the alignment of the particles [1], which has a value of 0.77 in randomly oriented particles [13]. Figure 5. 5 shows the temperature dependence of H_C and the best fit with Equation 5. 1. The results show the good agreement between the experimental data with respect to $T^{0.77}$, that confirms the random distribution of local magnetic moments. Furthermore, from this fit it has also been estimated a T_B close to 415 K, which is lower than the Curie temperature of cementite, 418 K.

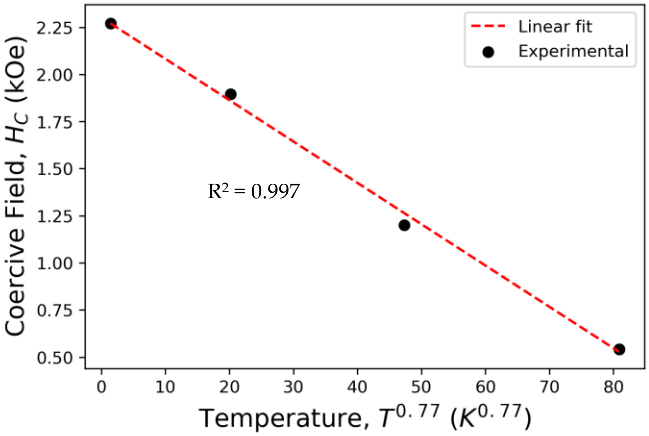

Figure 5. 5. Coercivity dependence on temperature from 3 K to 300 K. Dashed line represents the best linear fit.

The ZFC – FC curves from 2 K to 300 K have also been measured for this material, with magnetic fields applied of 100 and 3000 Oe. Results are shown in Figure 5. 6.

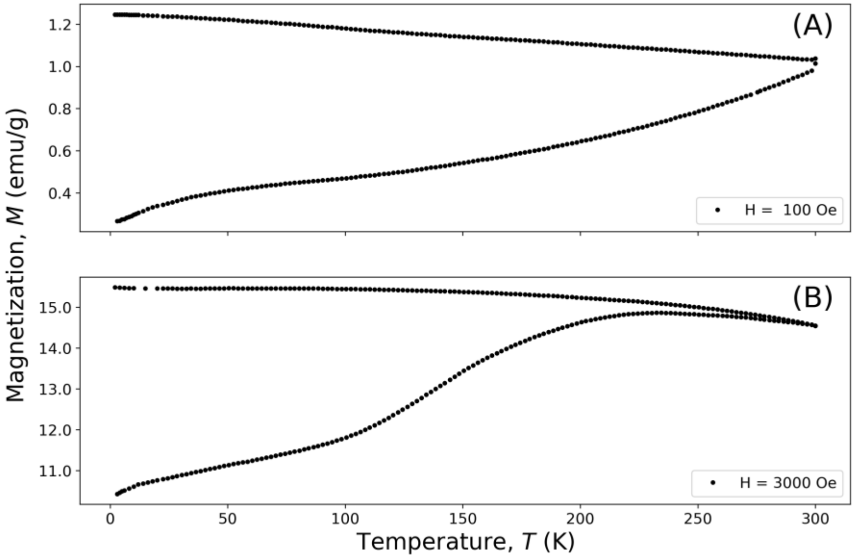

Figure 5. 6. ZFC - FC curves from 2 K to 300 K of the CNT-based nanocomposite with a magnetic field applied of (A) 100 Oe, and (B) 3 kOe.

In the measurement at 100 Oe (Figure 5. 6.A) the FC curve shows a small variation of the magnetization when lowering the temperature, which reflects the strong interaction between nanoparticles. A maximum in the ZFC magnetization versus T has not been achieved. This agrees with the previous estimated T_B value. On the other hand, if one measures ZFC - FC magnetizations at a greater magnetic field (H = 3 kOe, Figure 5. 6.B), there is a reduction of the barrier heights between the metastable states and a broad peak at ZFC curve becomes apparent. This indicates, clearly, the existence of a broad distribution of relaxation times for the metastable magnetic states, which are usually related to both the random orientations of the local effective anisotropy axes and the broad distribution of the anisotropy barrier heights. Furthermore, from these results it is possible to detect the presence of a second distribution located at lower temperatures, which indicate the presence of another anisotropy energy barrier. The origin of this second distribution may be the existence of a smaller particle size distribution of the same phase material, or the presence of a second magnetic phase with a lower anisotropy energy barrier. In order to elucidate this point, both maxima have been fitted to two Gaussian distributions, and the area under each one has been calculated. The results - which are graphically shown in Figure 5. 7 - reveal that the total area under the ZFC has a 94% of contribution of the distribution with T_B at 235 K, while the distribution centred at 2 K contributes a 6%. These results are in good agreement with the compositional results obtained from the XRD measurements, thus keeping open the possibility that the low temperature distribution corresponds to the Fe nanoparticles.

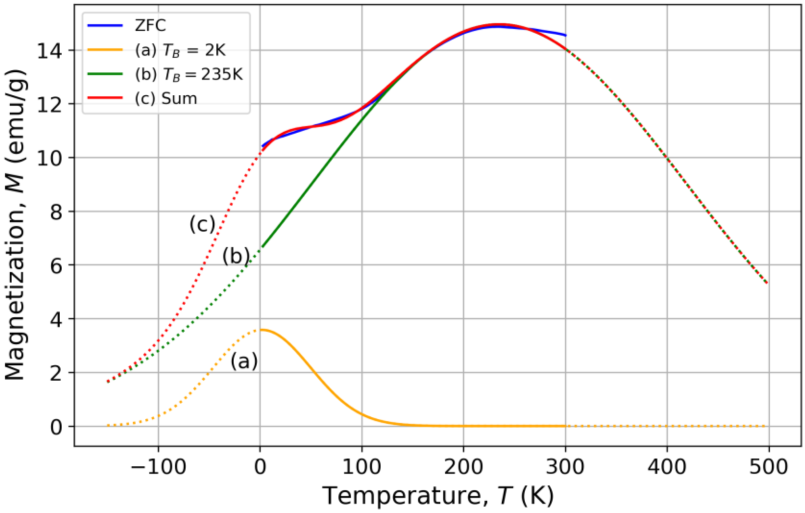

Figure 5. 7. Fitting of two Gaussian distributions to the ZFC curve measured with H = 3 kOe. (a) is a distribution with T_B = 2 K, (b) is a distribution with T_B = 235 K, and (c) and the sum of both distributions.

5. MAGNETIC RELAXATION

Magnetic relaxation experiments have been done, in which the dependence of the magnetization with time is measured once the magnetic field is removed after saturation. In our experiments, a small magnetic field (50 Oe) opposite to the magnetization has been applied in order to overcome the remanent magnetic field of the SQUID magnetometer. The obtained relaxation data at some of the measured temperatures is shown in Figure 5. 8, where the logarithmic decay in magnetization (M vs ln(t)) is represented.

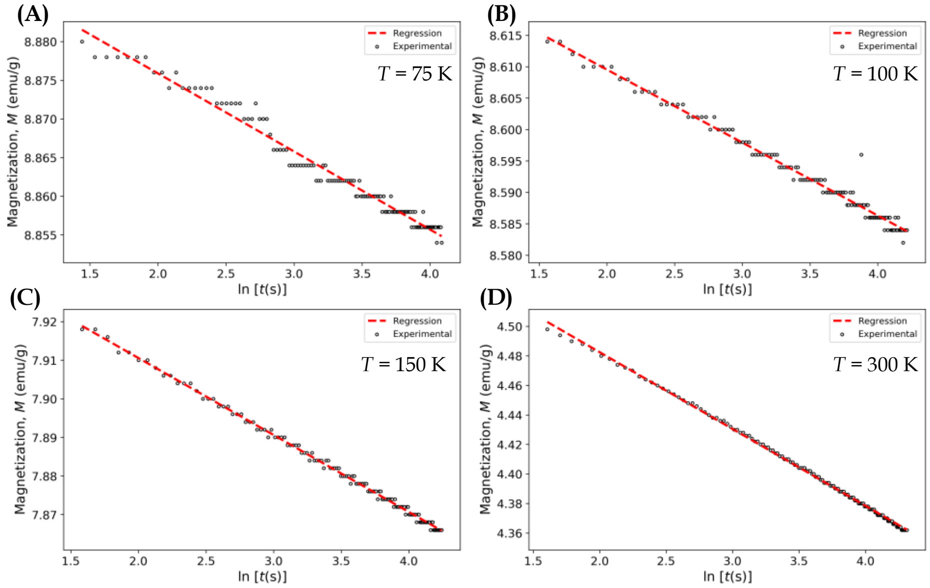

Figure 5. 8. Logarithmic decrease of the magnetization during relaxation at (A) 75 K, (B) 100 K, (C) 150 K, and (D) 300 K, with a reverse magnetic field of 50 Oe. Circles represent the experimentally measured points, while dashed lines are the best linear regression.

The logarithmic decay on time of the magnetization is seen in this figure. As the relationship between M and ln(t) is expected to be inversely proportional, a linear regression has been done at each temperature. It can be appreciated that the fitting with the experimental data improves with temperature, as the relaxation is larger. It happens because at low temperatures the relaxation time is greater than the SQUID measurement time. For this reason, the data is staggered in different levels. Although we have carried out measurements from 2 K to 300 K, we therefore only consider the data above 75 K, where the relaxation starts to be clearly defined.

From the slope of the M vs ln(t) regression curves, the magnetic viscosity (S) has been calculated by applying Equation 2.88 [14]. The calculated S value at each measured temperature is shown in Figure 5. 9.

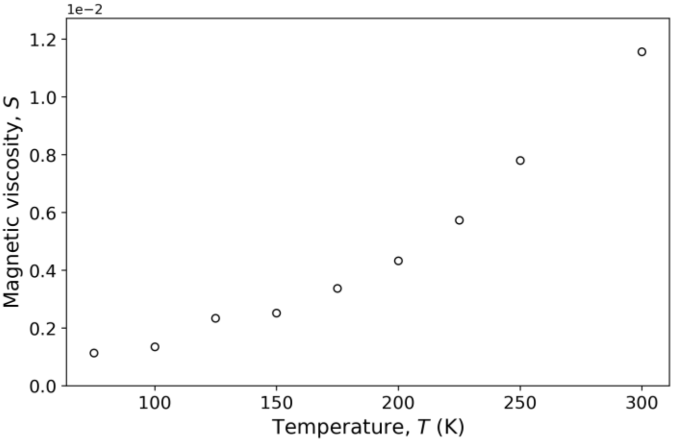

Figure 5. 9. Magnetic viscosity (S) values in the temperature range 75 – 300 K, calculated from the magnetic relaxations with a reverse magnetic field of 50 Oe.

From these results, it is possible to observe the expected decay of S when lowering temperature. It is due to the lower thermal energy that the system has to overcome the energy barrier and rotate the magnetic moment from the saturation direction to demagnetize [14], [15]. There is a nonlinear increasing tendency of S with respect to temperature, in agreement with the fact that there is not just a single barrier distribution on the sample, as it has been deduced from ZFC-FC measurements. As it has been previously discussed in Chapter II and Equation 2.90, $S(T)$ depends on the distribution function $f(V)$ of the magnetic nanoparticles, which can be described as

$$f(V) = \frac{1}{V} exp\left[-\varphi(T)\frac{V}{V_0}\right] \qquad \text{Equation 5. 2}$$

where $\varphi(T)$ is a test function that only depends on temperature. The presence of the function $\varphi(T)$ is explained by the fact that the parameters affecting the magnetic viscosity (such as the anisotropy constant, the saturation magnetization) depend on temperature in the considered temperature range. In addition, the experimental dependence $S(T)$ is essentially non-linear. By replacing $f(V)$ expression into Equation 2.90 and considering that $\langle V\rangle \int_0^\infty f(V)dV = V_0/\varphi(T)$, it is possible to obtain the following expression for the temperature–dependent viscosity:

$$S(T,t)\ln\left(\frac{t}{t_0}\right) = \varphi(T)\frac{T}{T_B}\frac{K_B}{K(T)}exp\left[-\varphi(T)\frac{T}{T_B}\frac{K_B}{K(T)}\right] \qquad \text{Equation 5. 3}$$

By considering the RAM [6], [7], Equation 5. 3 can be simplified as:

$$S(T,t)\ln\left(\frac{t}{t_0}\right) = F(T)exp(-F(T)) \qquad \text{Equation 5. 4}$$

being $F(T) = \varphi(T)\gamma_0\gamma(T)$. γ_0 and $\gamma(T)$ are, respectively, a constant that depends on coercivity and saturation at $T = 0$, and a temperature dependent factor that depends on the Bloch constant B and T_B. For a more detailed description of this approach, see reference [16]. On the basis of the obtained $S(T)$ dependence, and assuming $\ln(t/t_0) = 25$, it is possible to first find the function $F(T)$ and then deduce $\varphi(T)$. In Figure 5. 10 all these functions are represented and compared with the experimental data.

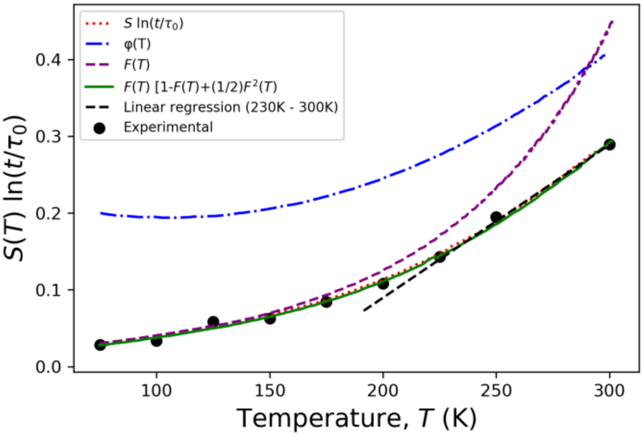

Figure 5. 10. Magnetic viscosity versus temperature with a reverse magnetic field applied of 50 Oe after the saturation (points). Functions used for the fitting procedure are compared with the experimental data.

The good agreement with the experiment confirms the proposed hypothesis about the distribution function given in Equation 5. 2. From Figure 5. 10, it is seen that the test function $\varphi(T)$ is almost temperature independent in the range 75 – 150 K, whereas the magnetic viscosity $S(T)$ times $\ln(t/t_0)$ follows $F(T)$. It means that the $S(T)$ dependence is determined only by $\gamma(T)$, in which the linear increase is modified by the temperature dependence of the anisotropy constant. That is, in the temperature range 75 – 150 K, the linear dependence of the magnetic viscosity is modified by the temperature dependence of the anisotropy constant *K*(*T*). This suggests that, in this temperature range, the relaxation process is mainly determined by the anisotropy of the sample. In the range 150 – 300 K the effect of the test function $\varphi(T)$ is manifested. Its influence leads to correction of the function *F*(*T*) in the direction of the increase with respect to γ (*T*), as described in Equation 5. *5*.

$$S(T,t)\ln\left(\frac{t}{t_0}\right) = F(T)\left[1 - F(T) + \frac{1}{2}F^2(T)\right] \qquad \text{Equation 5. 5}$$

in which the term in square brackets contributes only in the T > 150 K region. This approximation is more convenient for the experimental data fitting than Equation 5. 4.

When the *T* ln(*t*) plot is done (see Figure 5. 11) it is possible to see a clear ordering of the data measured at the different temperatures, although they are not perfectly aligned. This misalignment is common in high temperature measurements, where *T* is close to T_B. Thus, the relaxation is thermally governed in this temperature range. These conclusions are in good agreement with the ones that obtained from Figure 5. 9, where *S* is temperature-dependent in all the tested temperature range.

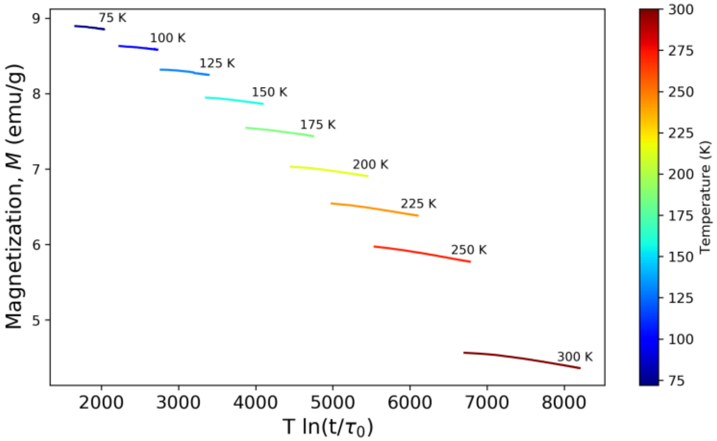

Figure 5. 11. *M* vs ln(*t*) plot for the magnetic relaxation of the CNT-based nanocomposite with a reverse magnetic field of 50 Oe for temperatures in the range 75 – 300 K.

In order to explore the low temperature region, the same experiments have been repeated from 2 K to 9 K by applying a reverse magnetic of 1 kOe, in order to solve the measuring resolution problems. A higher magnetic field is expected to accelerate the demagnetization process and thus a bigger difference on magnetization should be measured. As can be seen in Figure 5. 12, the variation on magnetization is now considerably higher and the logarithmic decay of *M* with time is better defined compared with the previous measurements. Furthermore, as in this case we are working in a more defined temperature range, it is possible to simultaneously compare all the relaxation. Figure 5. 13 shows how the relaxation increases at higher temperatures.

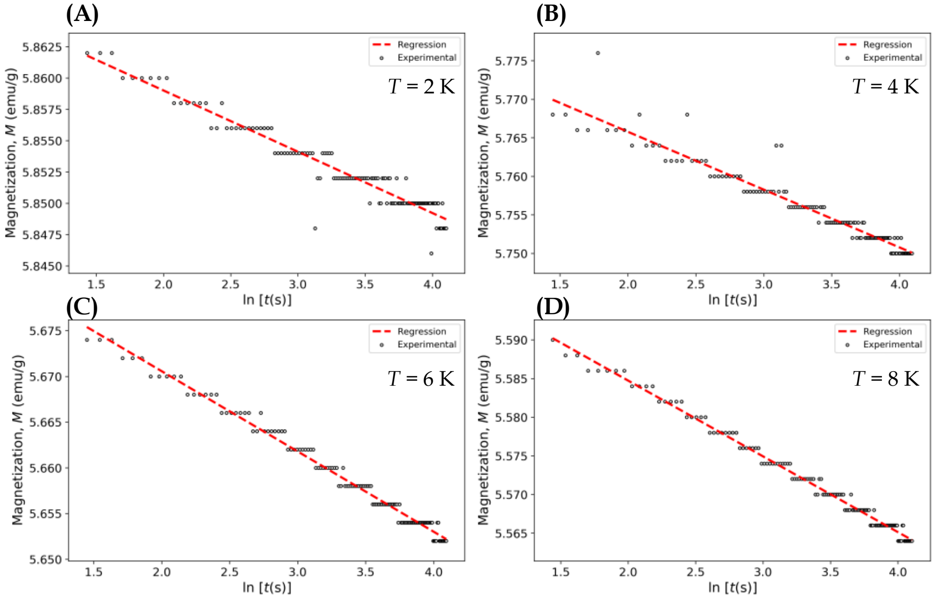

Figure 5. 12. Logarithmic decrease of the magnetization during relaxation at (A) 2 K, (B) 4 K, (C) 6 K, and (D) 8 K, with a reverse magnetic field of 1 kOe. Circles represent the experimentally measured points, while dashed lines are the best linear regression.

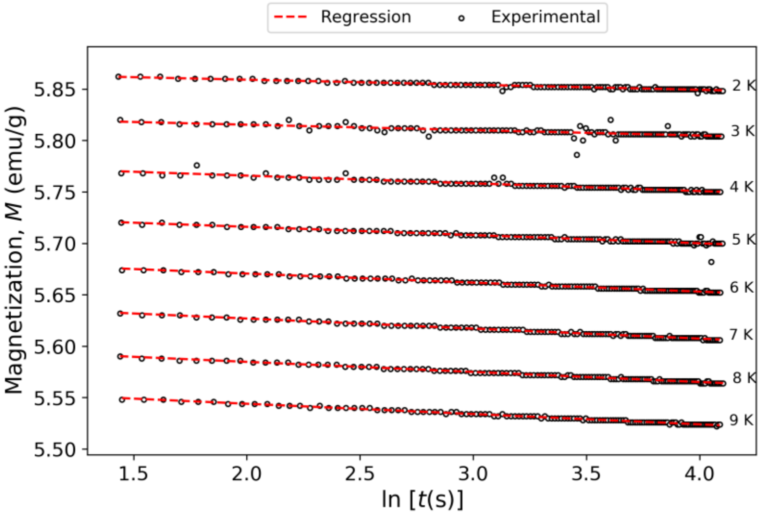

Figure 5. 13. The decay with time of the total magnetic moment versus ln(*t*) for various temperatures.

The magnetic viscosity *S* has also been calculated in these conditions, and its temperature dependence is shown in Figure 5. 14. As can be appreciated, it increases linearly with temperature, describing again a thermally governed relaxation process. These results are again in good agreement with the tendency seen in the *T* ln(*t*) plot shown in Figure 5. 15, where the data measured at different temperatures perfectly follows the same tendency.

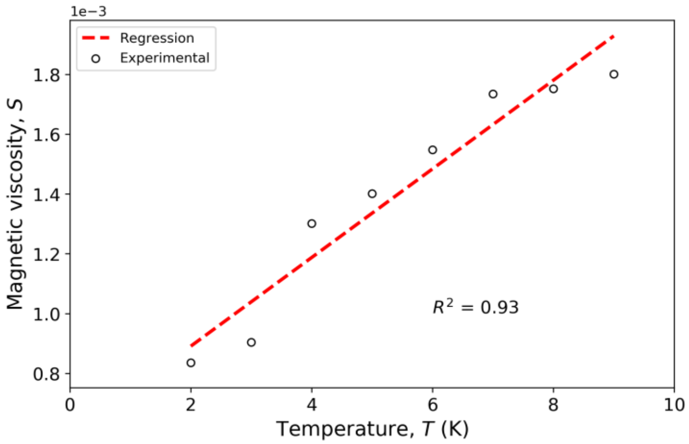

Figure 5. 14. Magnetic viscosity *S* values at each temperature calculated from the magnetic relaxations with a reverse magnetic field of 1 kOe. The best linear fit is represented by the dashed line.

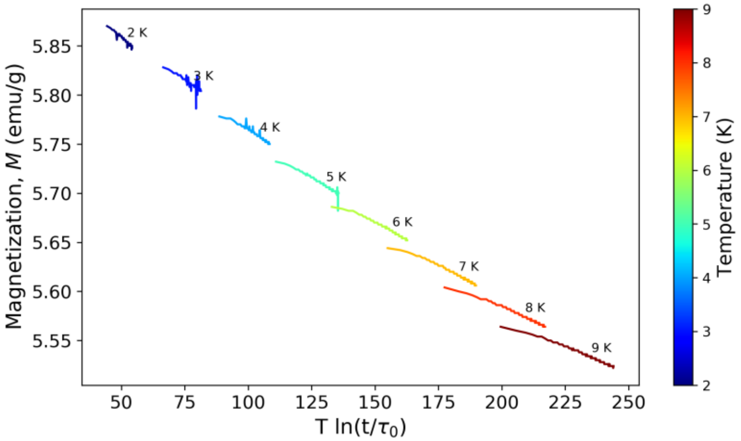

Figure 5. 15. *M* vs ln(*t*) plot for the magnetic relaxation of the CNT-based nanocomposite with a reverse magnetic field of 1 kOe.

The application of a reverse magnetic field unbalances the energy barriers between the two states (parallel or antiparallel with respect *H*). This unbalanced state makes easy the demagnetizing process, as the thermal energy needed to cross the barrier is smaller. Thus, as higher is the reverse magnetic field applied, lower is the required thermal energy to demagnetize.

6. CHAPTER CONCLUSIONS

In this chapter a novel CNT – Fe nanocomposite has been described and structurally characterized. The nanometric size of the Fe-based nanoparticles and their distribution all over the sample has been confirmed by TEM. SEM images have shown that the CNTs tend to form aggregates, which have a random orientation between each other. XRD measurements have revealed that the sample is composed by a predominant cementite phase, and smaller quantities of iron and graphite.

The magnetic properties of the material have been inspected by means of $M(H)$ measurements at different temperatures, and ZFC-FC experiments. The first kind of measurements have shown the dependence of the hysteresis area and H_C with respect the temperature. The $T^{0.77}$ dependence of H_C has proven the random distribution of the local magnetic moments. The second type of experiments have corroborated that T_B is above 300 K, confirming the value of 481 K calculated from the $M(H)$ results. Furthermore, a second energy barrier distribution has been found at low temperatures.

The magnetic relaxation of this nanocomposite has been studied. A non-linear increase of S with respect the T has been observed and related with the distribution of volumes. However, the low temperature region has not been examined at low reverse fields due to the small relaxation, and its associated resolution problems. In order to overcome with this problem, we have done further relaxation measurements from 2 K to 9 K with a reverse magnetic field of 1 kOe. In this second batch of measurements a clear linear temperature dependence of S has been observed.

7. FUTURE WORK

Once the material is structurally known and its main magnetic properties are understood, the effort should go in two main directions. First, it can be more deeply investigated the origin of the double energy distribution observed in the ZFC-FC measurements. Our results have kept open the possibility that the low temperature distribution may correspond to the Fe nanoparticles, but it needs to be better characterized to have a certainty. On the other hand, it could be interesting to investigate possible quantum phenomena (such as spin tunnelling during the relaxation) in this material. To do so, the low temperature resolution problems should be solved without needing to apply intense reverse magnetic fields.

8. REFERENCES

[1] J. L. Dormann, D. Fiorani, and E. Tronc, *Magnetic relaxation in fine-particle systems*, vol. 98. 1997.

[2] M. George, A. M. John, S. S. Nair., P. A. Joy, and M. R. Anatharaman, "Finite size effects on the structural and magnetic properties of solid-gel synthesized MFe2O4 powders," *J. Magn. Magn. Mater.*, vol. 302, pp. 190–195, 2006.

[3] S. Mørup, M. F. Hansen, and C. Frandsen, "Magnetic interactions between nanoparticles," *Beilstein J. Nanotechnol. Nanotechnol*, vol. 1, pp. 182–190, 2010.

[4] D. Xiao, T. Lu, R. Zeng, and Y. Bi, "Preparation and highlighted applications of magnetic microparticles and nanoparticles: a review on recent advances," *Microchim. Acta*, vol. 183, no. 10, pp. 2655–2675, 2016.

[5] A. L. Danilyuk *et al.*, "Interplay between exchange interaction and magnetic anisotropy for iron based nanoparticles in aligned carbon nanotube arrays," *Carbon N. Y.*, vol. 68, pp. 337–345, Mar. 2014.

[6] A. L. Danilyuk *et al.*, "Impact of CNT medium on the interaction

between ferromagnetic nanoparticles," *Epl*, vol. 117, no. 2, 2017.

[7] A. L. Danilyuk *et al.*, "Manifestation of coherent magnetic anisotropy in a carbon nanotube matrix with low ferromagnetic nanoparticle content," *New J. Phys.*, vol. 17, pp. 023073-1–12, 2015.

[8] S. V. Komogortsev, R. S. Iskhakov, A. D. Balaev, A. G. Kudashov, A. V. Okotrub, and S. I. Smirnov, "Magnetic properties of Fe3C ferromagnetic nanoparticles encapsulated in carbon nanotubes," *Phys. Solid State*, vol. 49, no. 4, pp. 734–738, 2007.

[9] S. L. Prischepa, A. L. Danilyuk, A. L. Prudnikava, I. V. Komissarov, V. A. Labunov, and F. Le Normand, "Exchange coupling and magnetic anisotropy for different concentration of iron based nanoparticles in aligned carbon nanotube arrays," *Phys. Status Solidi Curr. Top. Solid State Phys.*, vol. 11, no. 5–6, pp. 1074–9, 2014.

[10] A. C. Ferrari and J. Robertson, "Interpretation of Raman spectra of disordered and amorphous carbon," *Phys. Rev. B*, vol. 61, no. 20, pp. 14095–14107, 2000.

[11] A. L. Prudnikava, J. Fedotova, J. V. Kasiuk, B. G. Shulitsk, and V. A. Labunov, "Mössbauer spectroscopy investigation of magnetic nanoparticles incorporated into carbon nanotubes obtained by the injection CVD method," *Semicond. Physics, Quantum Electron. Optoelectron.*, vol. 13, no. 2, pp. 125–31, 2010.

[12] J. W. Byeon and S. I. Kwun, "Magnetic evaluation of microstructures and strength of eutectoid steel," *Mater. Trans.*, vol. 44, no. 10, pp. 2184–90, 2003.

[13] H. Pfeiffer and W. Schüppel, "Investigation of magnetic properties of barrium ferrite powders by remanence curves," *Phys. Status Solidi*, vol. 119, no. 1, pp. 259–69, 1990.

[14] E. M. Chudnovsky and J. Tejada, *Macroscopic Quantum Tunneling of the Magnetic Moment*. Cambridge University Press, 1998.

[15] J. Tejada and X. Zhang, "Experiments in quantum magnetic relaxation," *J. Magn. Magn. Mater.*, vol. 140–144, no. PART 3, pp. 1815–1818, 1995.

[16] J. Calvo-de la Rosa, A. L. Danilyuk, I. V. Komissarov, and J. Tejada, "Magnetic Relaxation Experiments in CNT-Based Magnetic Nanocomposite," *J. Supercond. Nov. Magn.*, 2019.

CHAPTER VI

CHARACTERIZATION AND DEVELOPMENT OF Fe-BASED SOFT MAGNETIC MATERIALS AND COMPOSITES

1. INTRODUCTION

The application of magnetic materials in today's technology is every time more important. With the goal of increasing the power, certain applications require to work at higher frequencies, resulting in an increase of the magnetic loses. This increase in the operating frequency leads, therefore, to a reduction of the system efficiency [1]. In this regard, Fe- based Soft Magnetic Materials (SMMs) are gaining every day more attention.

The total losses in a material (W_t, in J/m^3), which are also referred as *core loses*, are known to have three contributions [1]–[4]: (i) hysteresis losses (W_h), (ii) eddy current losses (W_e), and (iii) excess loses (W_{exc}). Therefore, the power dissipation P_t (in W/kg) can be calculated by Equation 6. 1.

$$P_t = W_h \frac{\nu}{\rho} + W_e \frac{\nu}{\rho} + W_{exc} \frac{\nu}{\rho} = P_h + P_e + P_{exc} \qquad \text{Equation 6. 1}$$

where ν is the frequency, and ρ the density of material.

The hysteresis loses are related with the hysteresis cycle area when a material is cyclically magnetized and demagnetized. SMMs are a great candidate to overcome this kind of losses due to their low magnetic anisotropy and coercivity, i.e. their resulting small hysteresis area.

However, these metallic structures are usually electrically conductive and the power losses due to eddy currents are high. This type of losses is originated by the inner and interparticle electrical current created by an alternating magnetic field. On the other hand, the excess losses appear only because the classical calculation of eddy current losses ignores the presence of domains and domain wall motion [5]. The combination P_e + P_{exc} represent the dynamic losses P_{dyn} [3]. In order to keep the low hysteresis losses of SMMs and at the same time reduce the eddy current losses, core-shell structured composites - known as Soft Magnetic Composites (SMCs) – have been developed. These materials consist on a ferrimagnetic core and a thin insulating layer, which provide the soft magnetic properties and electrical insulation between particles, respectively. Shells can be composed by inorganic (phosphates, oxides or soft ferrites for instance) or organic materials (epoxy resins, acrylic powders, polyester powders, etc.) as well [6]–[9].

Nowadays SMCs are common in plenty of applications as alternators, generators, electric motors [10], reactor cores for hybrid electric vehicles [4], solenoid valves and reactors for high capacity power supplies or check-coils and noise filters for small power supplies [11].

In this chapter the results obtained from the investigation of the magnetic properties of different SMMs and SMCs in the kHz and MHz frequency range are presented. Their structural properties are investigated in order to understand the origin of their magnetic response and, thus, be able to design novel materials with improved properties.

The present work has been carried out in collaboration with Dr. Arturo Lousa, from Universitat de Barcelona, who provided the impedance analyser and participated in the interpretation of the frequency-dependent permeability and power losses.

2. CHAPTER OBJECTIVES

In this chapter we first aim to investigate the SMMs and SMCs currently used in industry, both from a structural and functional point of view. We pretend to understand how the chemical and physical characteristics of these materials affect to their magnetic behaviour.

Furthermore, once these fundamental ideas are known, we aspire to design new laboratory-scale materials with competent magnetic properties in the kHz and MHz frequency range, as a potential alternative for the actual commercial materials.

Finally, the properties of the obtained new formulations want to be compared with the actual commercial ones. As these pieces are usually conformed by powder metallurgy methods [12], both the magnetic and the temperature stability response must be evaluated.

3. CHARACTERIZATION OF ACTUAL SMMs AND SMCs

3.1. Structural characterization

3.1.1. X-Ray Diffraction (XRD)

The powder samples of both materials, called as "SMM" and "SMC" during this chapter, have been first measured by powder XRD. The obtained results, which are shown in Figure 6. 1, show that both materials consist on the same crystalline phase. The observed pattern has been identified as a pure Fe cube structure, with unit cell parameter of a = 2.866A Å. These results are in accordance with what could be expected for the particle core from literature references [13], [14]. Therefore, the chemical differences between particles may only come from an amorphous - or really low in composition - shell, as was previously noticed by Huang and co-workers [13]. By using the Scherrer equation (previously defined by Equation 2.26) the crystallite size is approximated to 100 nm.

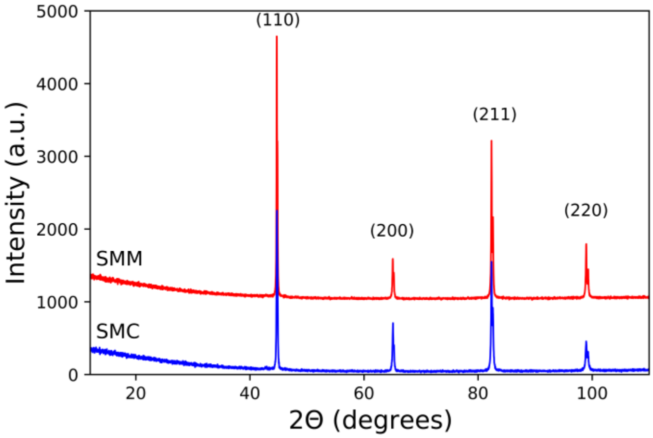

Figure 6. 1. XRD diffraction pattern of the SMM (red) and SMC (blue) samples. Both correspond to a pure Fe cubic phase. The SMM spectrum has been intentionally spaced 1000 units in intensity to allow a better comparison.

3.1.2. Fourier Transformed Infrared Spectroscopy (FT – IR)

Once the crystal structure of both samples is known, FT-IR has been used to investigate the nature of the shell. The obtained results are shown in Figure 6. 2.

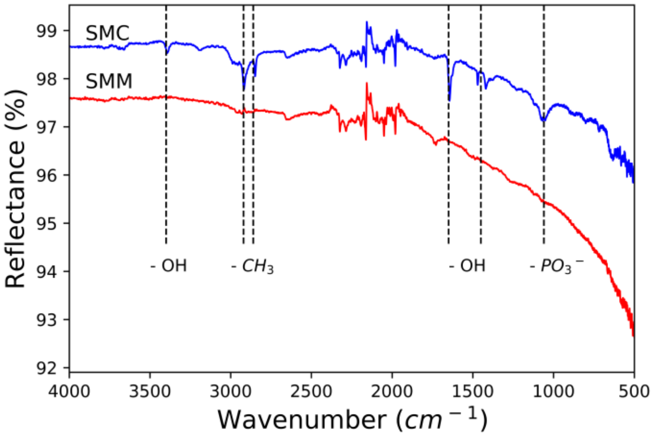

Figure 6. 2. FT-IR spectrum of the SMM (red) and SMC (blue) powder samples.

First, one can detect some common traces between both samples. There is a big irregularity between 2500 and 2000 cm^{-1} and a tendency in decreasing the reflectance at low energies, possibly due to the Fe-O vibrations which can be attributed to the formation of an oxide layer around the iron core. Nevertheless, as we are interested in characterizing the isolating shell of the SMC, more attention will be paid to the differences between samples.

Again, these results match very well with the ones obtained when studying similar materials [15]. Peaks around 3500 and 1500 cm^{-1} are typical for –OH groups, and those just below 3000 cm^{-1} are due to $–CH_3$ groups. Both are organic groups coming from the resin remainder [7]. Moreover, it is more interesting the $–PO_3^-$ peak that appears at 1040 cm^{-1}, which confirms that the coating around the iron core has a phosphate nature. On the other hand, with these results it is not possible to specify what kind of phosphate it consists on. Finally, the PO_4^{3-} peak that would be also expected for a phosphate around 570 cm^{-1} is not detected. Possibly the big decrease in transmittance in the same frequency region shields the peak.

3.1.3. Laser Diffraction (LD)

The particle size distribution of these powder samples has been investigated by means of Laser Diffraction. Both the volume and number fractions have been determined to have a global idea about the particles' size. The results are shown in Figure 6. 3.

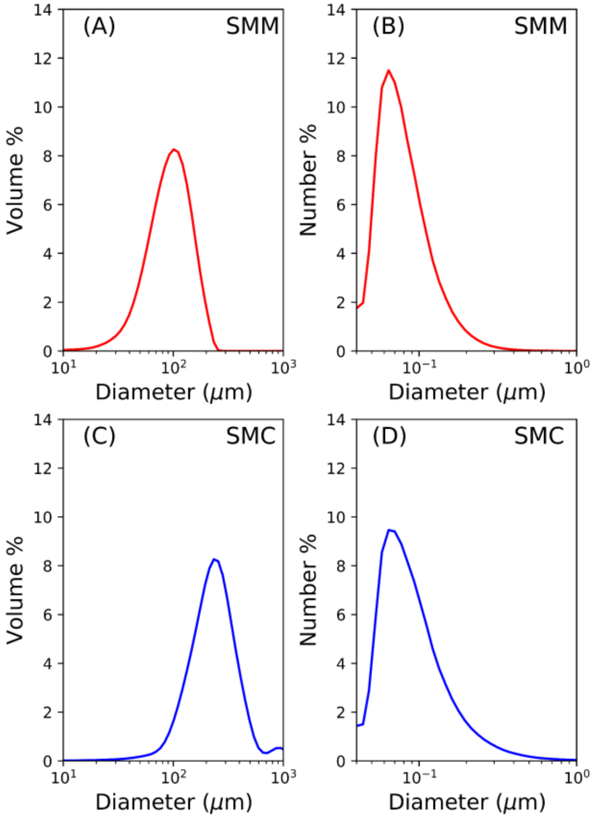

Figure 6. 3. Particle size distribution results. (A) Volume percentage results for SMM sample; (B) number percentage results for SMM sample; (C) volume percentage results for SMC sample; and (D) number percentage results for SMC sample.

First, it is possible to see that pure iron cores (SMM) studied in this paper have a volume particle size distribution centred at 100 μm. On the other hand, SMC sample has the distribution centred around 200 μm. The distribution is wide and there is some dispersion in diameter: only 8% of the volume is occupied by the mean diameter in both materials.

Therefore, it should be pointed out that - apart from the coating - there is a size difference between samples.

Furthermore, by analysing the Number % distribution one can see that both samples have a particle size distribution centred at 60 nm, involving around a 10% and a 12% of the particles in each case. It means that there is a coexistence of a micrometre and nanometre particle size distribution. Consequently, the main part of the volume is occupied by the 100 μm or 200 μm diameter particles, but they are surrounded by a bigger number of 60 nm particles. This coexistence between the two distributions may increase the density of the pressed pellet, because smaller particles can occupy free spaces between the bigger ones.

3.1.4. Scanning Electron Microscopy (SEM)

Particle size and morphology has been checked by SEM. Images from Secondary Electrons (SE) and Backscattered Electrons (BSE) have been obtained in the same position to have morphological and chemical information of the sample. Both powder samples have been embedded in a conductive resin, which has been finally polished in order to reveal their inner core. Some of the images obtained with the Quanta microscope are shown in Figure 6. 4.

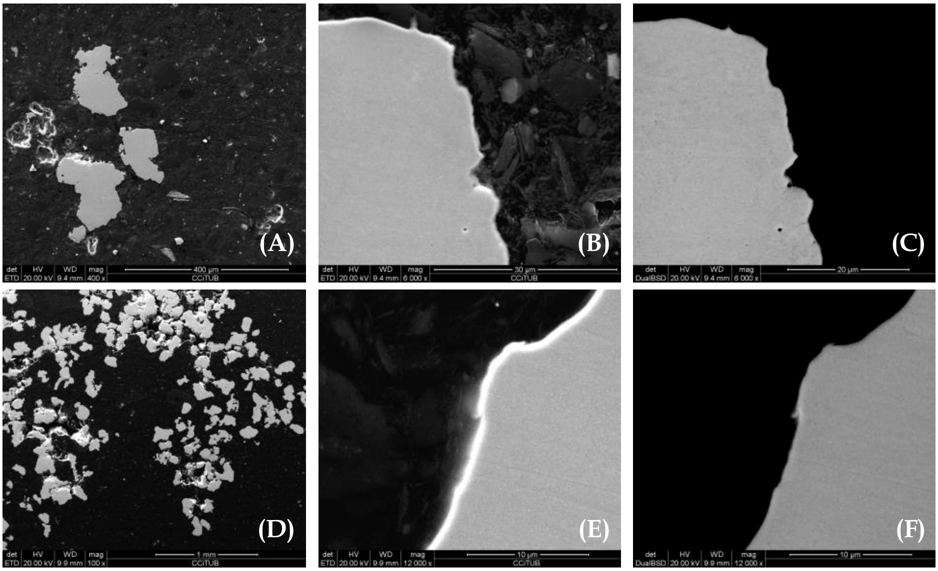

Figure 6. 4. SEM images of the powder particles embedded in a conductive resin. Upper images correspond to SMM sample, obtained by (A) SE at x400, (B) SE at x6000, and (C) BSE at x6000. Bottom images correspond to SMC sample, obtained by (D) SE at x100, (E) SE at x12000, and (F) BSE at x12000.

The particle size of the sample SMM is appreciated in Figure 6. 4.A, where it is also seen that the particles' morphology is not perfectly spherical. This irregular shape can lead to error in the LD calculations, as it considers spherical-shaped particles. it is possible to see the particle border by looking at higher magnifications (Figure 6. 4.B), where any difference compared with the centre of the particle is detected. Here, it should be stressed that all the particle shows a metallic behaviour, even though the sample has not been coated with a conductive material. It is in good agreement with the XRD results that have shown that pure Fe is the main phase in the sample. Furthermore, the BSE image in Figure 6. 4.C does not show any change in composition in the whole particle.

On the other hand, the three bottom images correspond to the SMC powder sample. In the low magnifications image (Figure 6. 4.D) it can be checked again that particles are not perfectly spherical and that their diameter is in general of few thousands of μm. However, the higher magnifications (Figure 6. 4.E) confirm a crucial fact: the presence of the shell in the SMC. Furthermore, as the sample has not been coated with an electrically conductive material, it is seen that the shell has an insulating character, as it retains the electrons and shines. Figure 6. 4.F - that is the same image than before but obtained by BSE - does not show any clear compositional change in the particle border despite it is worse defined than in SMM. It means that probably the shell thickness is lower than the one than can be seen by SE, which can be distorted by the shining effect. In order to get a more defined visualization of the isolating layer, the SMC has been coated with carbon and observed at higher magnifications (Figure 6. 5). The shining effect should be now avoided because of the conductive coating.

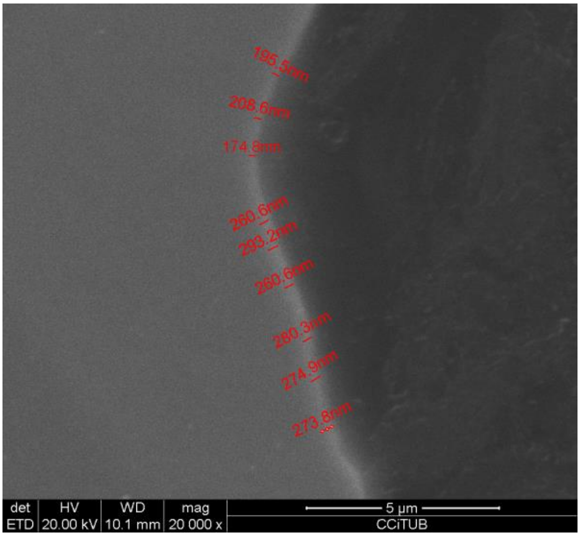

Figure 6. 5. Secondary Electrons SEM image of a carbon coated SMC sample at x20000 magnifications. Isolating shell thickness is measured at different points.

As the isolating effect producing brightness is not present, the shell thickness is much better resolved. Shell thickness has been measured at different points in this image, resulting in a mean value of 246.9 nm and a standard deviation of 42.5 nm.

The chemical composition of the shell has also been determined, by Energy-Disperse X-Ray Spectroscopy (EDS). Two different measurements have been performed: one in the centre of the particle, and another in the edge. Both results are shown in Figure 6. 6.

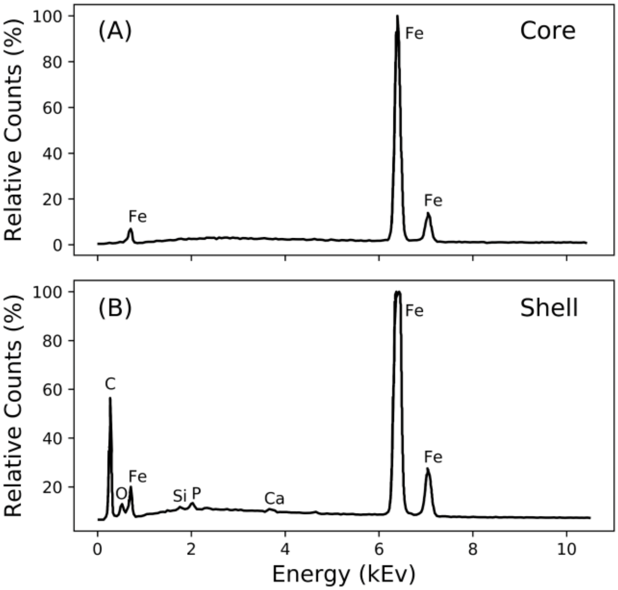

Figure 6. 6. EDS analysis of the SMC sample coated with carbon in the (A) centre, and the (B) border of the particle.

The results confirm the Fe nature of the core (Figure 6. 6.A), while the shell contains other elements (Figure 6. 6.B). Shell's analysis detects elements such as carbon (C), oxygen (O), iron (Fe), silicon (Si), phosphor (P) and calcium (Ca). Carbon, oxygen and calcium have been identified as resin elements by doing another EDS analysis out of the particle. Iron signal may come from the SMC core. It is also possible that the phosphate coating contains iron, but it cannot be ensured by this measurement. In addition, the presence of these elements can be attributed to the fact that EDS analysis is not perfectly punctual and involves a certain volume of the sample. The only element that is not present neither in the resin or the SMC core is phosphor; this is another proof for the phosphate-based nature of the coating. These results are in good agreement with those stated in other works [9].

3.2. Static magnetic properties

Despite SMMs and SMCs are used for applications in the kHz and MHz frequency range, the static magnetic characterization can reveal important information about the material's physics, such as its susceptibility or energy barrier distribution. With this goal, *M*(*H*) and ZFC-FC measurements have been performed by SQUID magnetometry.

3.2.1. *M*(*H*) measurements

The dependence of the magnetization with the magnetic field has been measured for both samples at room temperature.

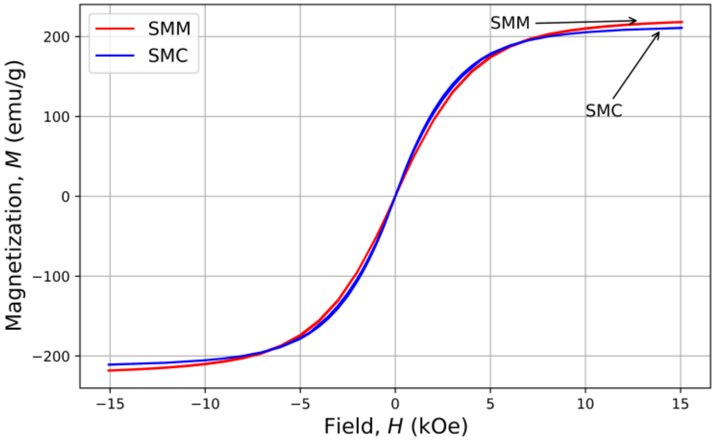

Figure 6. 7. *M*(*H*) measurement at 300 K, with a maximum magnetic field applied of 1.5 T. SMM (red) and SMC (blue) are represented.

As it can be appreciated in Figure 6. 7, both samples almost have an ideal soft magnetic behaviour: the susceptibility is high, and the remanence and coercivity is virtually zero. Furthermore, it sticks out the similarity between both samples originated by the common Fe core. The slight difference experimentally detected is not significant and could only be explained by the presence of the non-magnetic phosphate shell in the SMC.

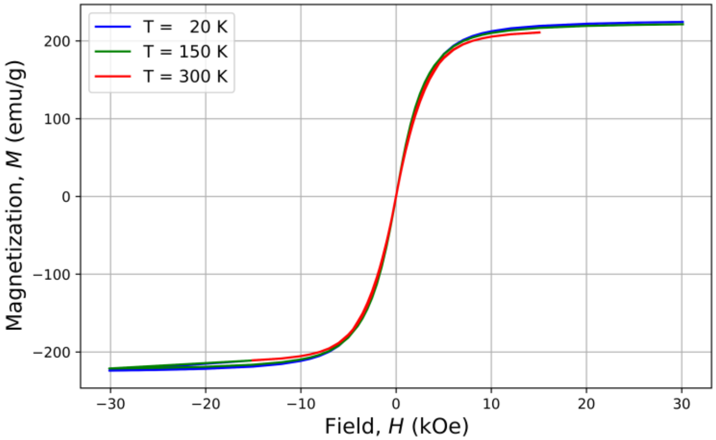

Figure 6. 8. $M(H)$ measurements of the SMC sample at 20 K (blue), 150 K (green), and 300 K (red).

The zero-area of the hysteresis cycle (there is no hysteresis, in fact) is an excellent characteristic for a soft magnet in order to avoid power losses. Despite it is not of technological direct interest, the hysteresis of the SMC has been tested at different temperatures. The results are shown in Figure 6. 8.

Even though the remanence and coercivity (i.e. the hysteresis area) is expected to increase at low temperatures - due to the increased difficulty to overcome the energy barrier when demagnetizing - the SMC shows exactly the same reversibility at low temperatures (20 K) than at room temperature (300 K).

3.2.2. Pulsed $M(B)$ measurements

In order to go one step further to understand the question above discussed, pulsed magnetic field hysteresis measurements have been measured using a 2 MJ capacitor bank at the pulsed field facility of *Katholieke Universiteit Leuven*, Leuven (Belgium). The results are shown in Figure 6. 9.

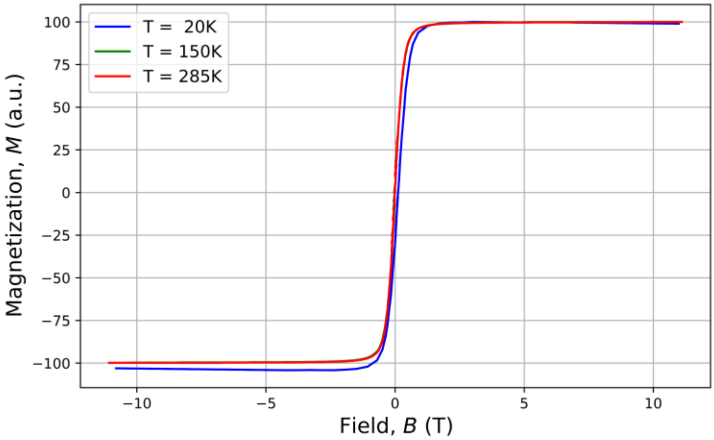

Figure 6. 9. Pulsed $M(B)$ measurements of the SMC sample at 20 K (blue), 150 K (green), and 285 K (red).

These are awesome results, as the hysteresis keeps being virtually zero despite the magnetic field has been applied in an extremely fast rate and at different temperatures. These results highlight the excellent soft magnetic properties of the SMC sample, which does not show hysteresis even though the high rate magnetic field applied. Moreover, the properties are again maintained at low temperatures (20 K).

3.2.3. Zero Field Cooled – Field Cooled (ZFC – FC)

The energy barrier distribution has been studied by means of the ZFC – FC curves. The applied magnetic field (5 kOe) is below the H_K, thus ensuring that the sample does not reach the saturation.

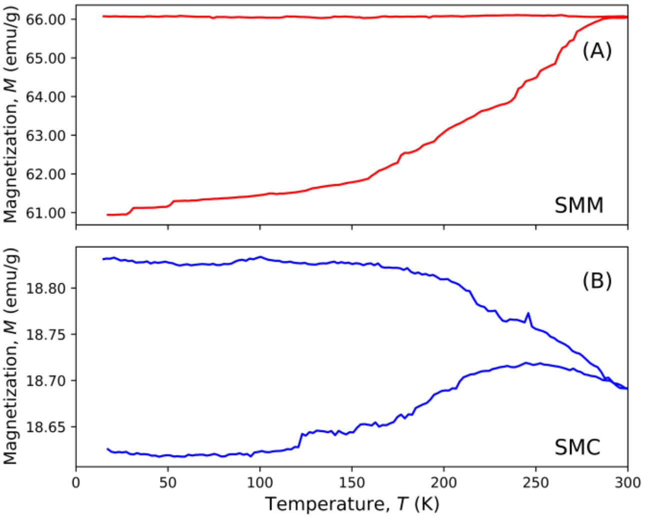

Figure 6. 10. ZFC-FC curves between 15 K and 300 K with H = 5 kOe. SMM sample results are shown in the top part (A), while those from the SMC sample are in the bottom part (B).

The ZFC curve of the SMM sample (Figure 6. 10.A) continuously increases until 300 K. This monotone increase in M with T supports the idea that there is a wide distribution of sizes, each one with a different energy barrier. The blocking temperature T_B - where all the particles are unblocked, and the superparamagnetic state begins - is not clearly detected. However, the reduction of the curve slope suggests that it is close to 300 K. The FC curve constantly returns to low temperatures, as the particles are still blocked at these temperatures. In the case of the SMC (Figure 6. 10.B) the tendency is the same, but blocking is reached around 250 K. However, the increase is again monotone, confirming the results expected from LD.

The most surprising result from these measurements is the opposite reversibility behaviour obtained from the $M(H)$ measurements and those from ZFC-FC. While all the M(H) data shows a complete reversibility of the system (from 20 K to 300 K), the ZFC – FC of both samples is irreversible in the entire temperature range. We are still working to find an explanation to justify these very curious and unexpected results, which would be an important fact to understand the magnetization dynamics of these materials.

3.3. Frequency-dependent magnetic properties

3.3.1. Differences between SMMs and SMCs

Impedance spectroscopy was used to study the complex magnetic permeability $\hat{\mu}$ from 1 kHz to 13 MHz. To do so, the powder materials have been uniaxially pressed with 700 kg/cm^2 at room temperature to form toroidal-shaped bulk samples. Further details on their fabrication are provided in Chapter III. Additionally, three replicates have been fabricated for each sample in order to have better statistics. The mean characteristics of each kind of toroid are described in Table 6. 1.

Table 6. 1. Mean physical characteristics of the toroids made of each material. Height and density values represent the mean and standard deviation values of the three replicates for each sample. Electrical resistance are approximated values.

Material	**Height, *h* (mm)**	**Density, ρ (g/cm^3)**	**Electrical resistance, *R* (Ω)**
SMM	3.61 ± 0.04	7.55 ± 0.03	5
SMC	3.61 ± 0.03	7.51 ± 0.03	92000

Dimensional and density values are roughly the same for both materials, while the electrical resistance is diametral opposed. Despite the provided values are dimensionally dependent, the difference in order of magnitude and the similarity on dimensions allow to corroborate the practical difference in resistivity between both materials.

The complex magnetic permeability spectra in the kHz and MHz frequency range of each material are shown in Figure 6. 11.

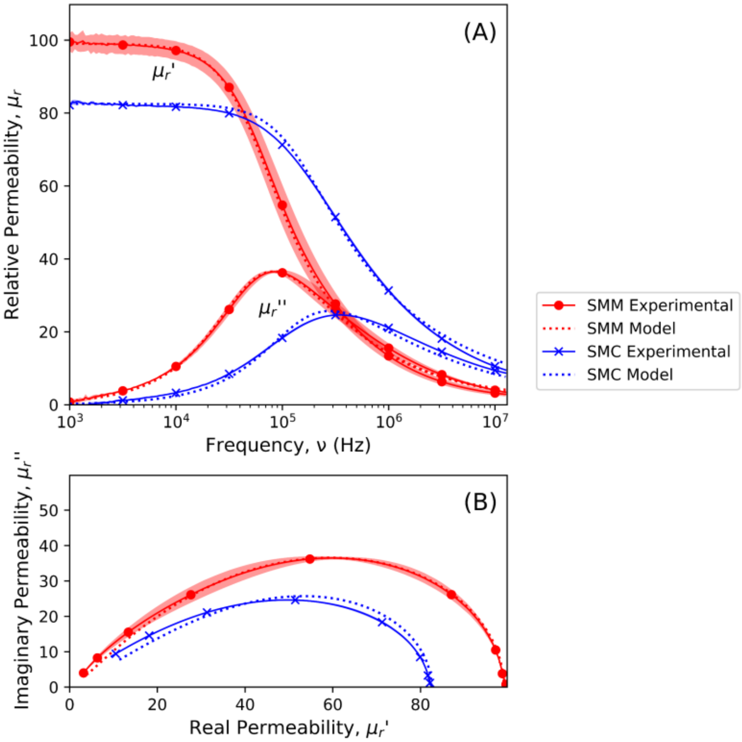

Figure 6. 11. (A) Complex magnetic permeability spectra from 1 kHz to 13 MHz from the SMM (red) and SMC (blue) samples, and (B) Cole-Cole diagram for the same samples. In both parts of the figure, the solid line represents the mean experimental data, the shaded region tis he standard deviation, and the dashed data is the best fit with the Davidson–Cole relaxation model.

Both materials show an initial plateau at low frequencies (static permeability, μ_S) in which they are able to absorb energy without experimenting losses. After this plateau, the real component decreases while the imaginary part increases until a maximum, corresponding to the relaxation frequency ν_r. Furthermore, the broad and asymmetric distribution of relaxation times corresponds to the characteristic Davidson-Cole (DC) behaviour due to the existence of a broad distribution of particles. It has been proved that the damping constant depends on the conductivity, volume, and shape of the particles [16]. This is also in good agreement with the results previously discussed from LD and ZFC-FC magnetic measurements.

In general terms, the magnetic permeability of the SMM is larger than the one for the SMC in this frequency range. It may be understood by the presence of the thin isolating shell in the SMC, which does not magnetically contribute. This combination of functional properties in composite materials has been studied in many works [17]–[19]. On the other hand, the SMC sample is capable to maintain its μ_S value until higher frequencies. This relationship between the quasi–static permeability and the relaxation frequency is in good agreement with the Snoek's law [20]–[22] for both samples. The ν_r is of 100 kHz for SMM, while SMC resists until 300 kHz. Consequently, the SMC is adequate to work at higher frequencies than the SMM, as it does not show magnetic losses until higher frequencies. Globally, phosphate coating is reducing the magnetic response of the material by reducing the magnetic permeability, but it is also shifting the start of losses to higher frequencies.

The other difference between SMM and SMC samples (particle size) can be discarded as the reason why ν_r shifts to higher frequencies. Some attempts [16], [23] have been made in order to estimate the value of τ (and thus the position of the peak of $\mu"$) as a function of the parameters of the material. Despite the lack of a general theory, different models predict that for similar values of the electrical conductivity, an increase on the particle size would shift the loss peak to lower frequencies. Equation 6. 2 and Equation 6. 3 define the expressions obtained for the damping constant (α) and relaxation time (τ) in each paper, respectively. Both magnitudes are inversely proportional to ν_r.

$$\alpha^{sphere}_{eddy,max} = \mu_0 \gamma M_s \sigma V^{2/3} S^{sphere}_{max} \tag{Equation 6. 2}$$

$$\tau_{00} = \frac{\sigma\mu}{\pi^2}\left(\frac{1}{a^2} + \frac{1}{b^2}\right)^{-1} \tag{Equation 6. 3}$$

where σ is the total material conductivity, μ_0 is the vacuum permeability, γ is the gyromagnetic ratio, V is the particle volume and S, a and b are the shape factor and dimensions, respectively. Overall, analysing Equation 6. 2 and Equation 6. 3 it becomes clear that the relaxation frequency should be reduced for either big particles' size or by high conductivity values.

Considering these concepts toghether with the results from Figure 6. 11.A, different considerations should be pointed out: (i) ν_r is three times bigger for SMC than SMM; (ii) SMC particles have approximately the double diameter than SMM ones; (iii) the magnetic permeability of the SMC is about an 80% of the one for SMM. It is therefore possible to conclude that although SMC should present a lower relaxation frequency due to its larger particle size, it relaxes at higher frequencies than SMM due to a lower conductivity. These results emphasize the role that the isolating shell plays on the composite materials. The difference on resistance has been previously measured (see the data provided in Table 6. 1).

In Figure 6. 11.B the Cole–Cole diagram is shown, which represents the relationship between the real and imaginary components of the complex magnetic permeability. This spectrum shows the characteristic asymmetry of a DC relaxation approach.

The experimental data has been fitted to the DC model by adjusting the τ and n parameters, apart from the experimental parameter C_p. The best fit has been considered as the combination of values that minimizes the residual R parameter described by Equation 3.6. The parameters that best fit the experimental data are annotated in Table 6. 2, and the resulting simulated spectra is represented in Figure 6. 11 by dashed lines.

Table 6. 2. Relaxation time (τ), n constant, and residual R parameters obtained from the fitting of the experimental data with the Davidson – Cole model.

Material	τ (μs)	n	R
SMM	3.10	0.45	0.81
SMC	1.15	0.59	1.43

The obtained τ value for the SMM is three times larger than the one for SMC, in good agreement with the results discussed from Figure 6. 11. Moreover, n parameter provides information about the relaxation behaviour: as closer it is to zero, closer it is to the ideal Debye model; when n tens to 1, more important is the DC influence on the relaxation. Therefore, these results suggest that the distribution of relaxation times τ is smaller in SMM than in SMC.

3.3.2. Particle size effect

In the previous sections we have referred many times to the possible effect that the particle size may have on the magnetic properties. To do so, the initial powder samples have been screened with different mesh sieve sizes and their particle size distribution has been checked by LD. Then, this powder has been used to fabricate a new set of toroids to measure their complex magnetic permeability by impedance spectroscopy. The obtained results are shown in Figure 6. 12.

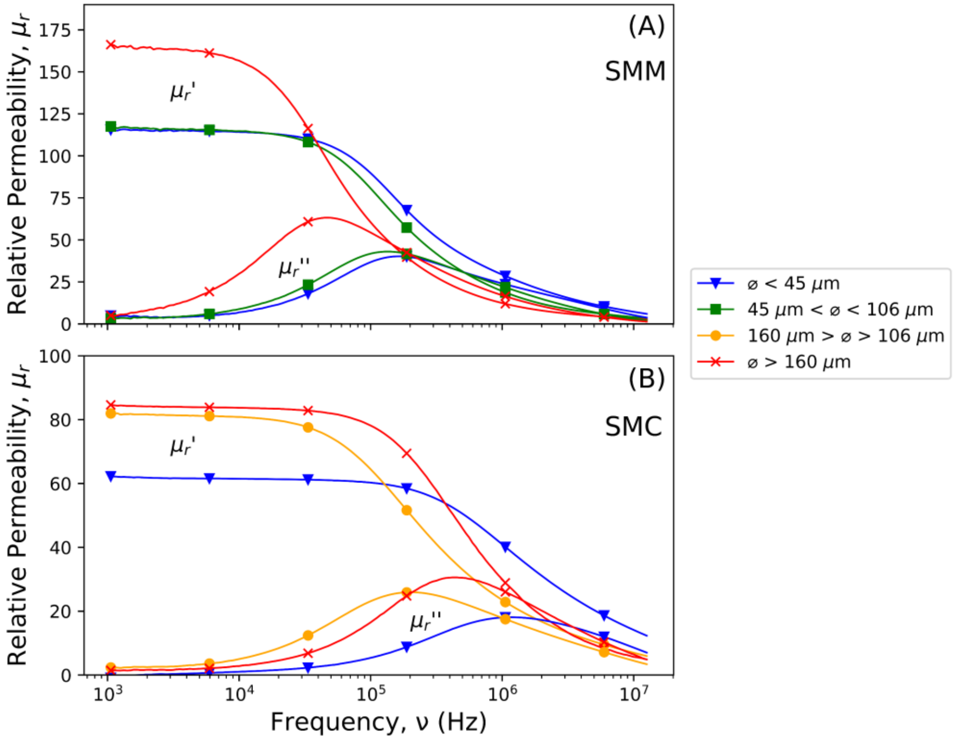

Figure 6. 12. Frequency–dependent complex permeability of different size distributions measured by impedance spectroscopy in the frequency range from 1 kHz to 13 MHz. (A) shows the results for the (A) SMM, and (B) SMC samples. One distribution is missing in each subplot due to technical difficulties.

From these results, it is possible to globally see again that the magnetic permeability of SMM is larger than the one of SMC, as well as the higher relaxation frequency of the SMC compared to SMM. However, here we will focus our attention on the changes on $\hat{\mu}$ due to particle size. It is a common trend for both samples that μ_S increases for bigger particles. In the case of SMM, it reaches values around 170. On the other hand, the relaxation frequency decreases when increasing the particle size. These trends are in notable agreement with Equation 6. 2, Equation 6. 3, and Snoek's law. Only the intermediate particle size in the SMC sample breaks this clear tendency.

3.3.3. Magnetic losses

The magnetic losses are related with the imaginary component of the complex permeability. For this reason, a common resource to evaluate the relationship between the lost and stored energies consists on calculating the loss tangent *tan(δ)*. This concept has been previously defined in Chapter II (Equation 2.93). Figure 6. 13 shows the results of this calculation for SMM and SMC samples.

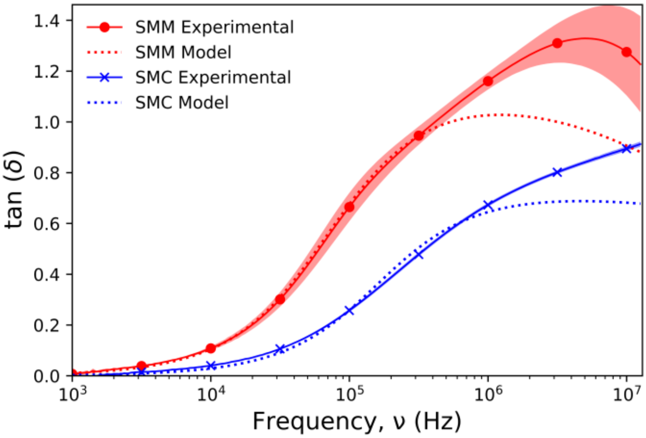

Figure 6. 13. Loss tangent factor for SMM (red) and SMC (blue), calculated from the experimental complex permeability measured by impedance spectroscopy from 1 kHz to 13 MHz. Solid lines represent the mean of the experimental results, the shaded region is the standard deviation, and the dashed lines are the best fitting oj *tan (δ)* calculated by the Davidson–Cole model.

The reduction of the lost part of the SMC compared to the SMM is evident in this figure. It starts close to zero until 10 kHz, but it then rapidly increases - especially in the case of the SMM - as a result of its lower relaxation frequency. These results emphasize again the importance of the phosphate coating in order to delay the energy losses.

However, *tan (δ)* is only an indicator of the relationship between the imaginary and real components of the permeability, but not of the energy losses itself. The dissipated power has to be calculated by means of Equation 2.7, where the $L_0 \nu \mu_r''(\nu)$ is an intrinsic parameter for each material. Figure 6. 14 shows the results according to this criterion.

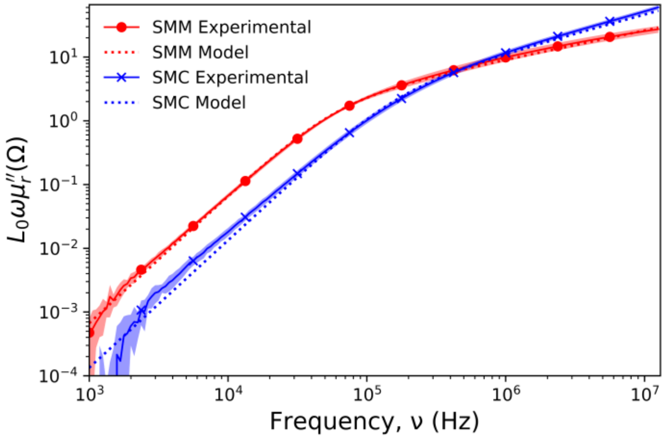

Figure 6. 14. Log-log magnetic losses plot of the SMM (red) and SMC (blue) samples in the frequency range from 1 kHz to 13 MHz. Solid lines represent the mean of the experimental results, the shaded region is the standard deviation, and the dashed lines are the best fitting of $L_0 \nu \mu_r''(\nu)$ calculated by the Davidson – Cole model.

These results first show how the power losses increase with frequency. As we could expect from the relaxation results, SMM experiments larger magnetic losses than SMC until 300 kHz, which is the relaxation frequency of SMC. Once the SMC relaxes, the energy losses are higher than those for SMM. However, the SMC keeps the low-loss level along a wider frequency-range. Finally, the excellent fit with the DC suggests that the loses are mainly of relaxation nature.

4. DESIGN OF NEW SMCs

With the light of the above presented results, it has been then pretended to design and fabricate a self-made and laboratory-scale SMC with competitive magnetic properties compared with the SMM and SMC analysed in the previous section. With this goal, the formulation and the characterization of two new types of SMCs are described.

4.1. Description and material's targets

According to the effects that we have seen that each element in a SMCs has on its magnetic properties, we have looked for:

- Pure Fe core to provide the maximum permeability and soft magnetic properties possible.
- Use the entire particle size distribution, in order to have an easy and economic fabrication process.
- Magnetic oxide isolating shell. By this way, we pretend the shell to play a double role: (i) avoid eddy currents, and (ii) contribute to the magnetization of the sample.
- The presence of an oxide isolating shell could also contribute to improve the mechanical properties of the material. A cermet composite would be created when compacting the powder.
- Thin and uniform shell around Fe. It must be uniform in order to neglect the contact between Fe cores, and thin in order to keep as much as possible the magnetic response as possible from the Fe core.
- Thermally stable. It needs to withstand the typically used annealing temperatures (around 400 °C [8], [15]).

With that in mind, we propose two different strategies:

- Oxidize the Fe cores to form a uniform iron oxide shell surrounding the core. These family of materials will be following noted as "OX".
- Surround the Fe cores with magnetic Fe_3O_4 nanoparticles (purchased from *SigmaAldrich*), in order to take profit of its good

magnetic properties. The term “NM” will refer to this families of samples during the rest of the work.

In both cases, the 100 μm Fe cores used in the previous section (referred as SMM) have been used as the composite core.

4.2. Mixture with nanomaterials

4.2.1. Description

A first approximation consists on surrounding the Fe cores with magnetic nanomaterials, Fe_3O_4 in this case. A schematic representation is shown in Figure 6. 15.A.

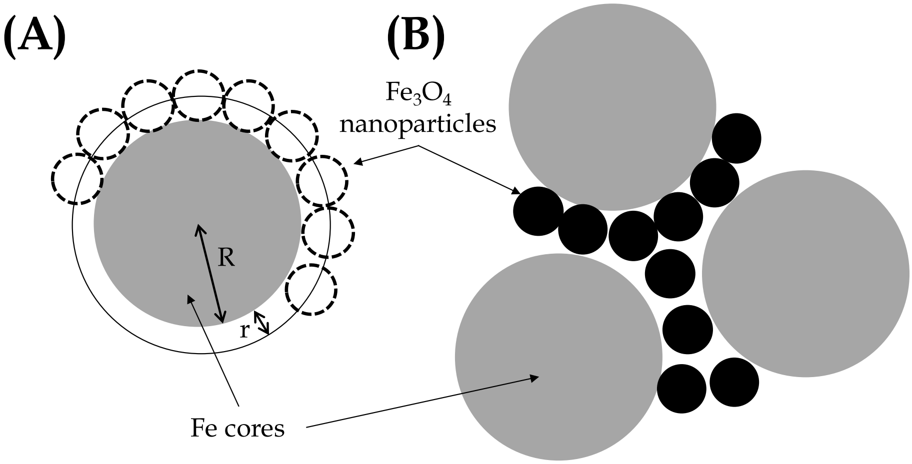

Figure 6. 15. Illustration of the nanomaterials mixture SMCs. (A) Scheme of the distribution of nanoparticles surrounding a single Fe core; (B) Global distribution with the Fe cores separated by a single Fe_3O_4 nanoparticles layer shell.

By considering an order of magnitude of 100 μm and 100 nm for the Fe core and Fe_3O_4 nanoparticles radius, respectively, we have approximated that $4 \cdot 10^6$ nanoparticles are needed to surround each Fe core. Also, taking 7.87 g/cm^3 and 5.18 g/cm^3 as their respective densities, an ideal mixture should have 380 times the Fe mass compared with the Fe_3O_4 one. However, as it can be seen in Figure 6. 15.B, in a real design two particles can share the shell nanoparticles; otherwise, there would be a double layer of nanoparticles isolating the Fe cores. As one of our goals is to produce a thin shell, the optimum formulation is probable below the proportion of 380 before calculated.

These mixtures have been prepared at a lab-scale by two different methods: (i) simple manual mixing; (ii) microwave mixing by suspending the powder precursors in a minimal quantity of ethanol. Thus, the nomenclature that we will use to refer to this type of SMC during the rest of this work is: *NM_prop_mix*, where the term *prop* refers to the weight proportion between Fe and Fe_3O_4, and *mix* is the mixture process (*MA* for manual agitation, and *MW* for microwave assisted method).

4.2.2. Static magnetic properties

Two samples close to the calculated ideal proportion (ratios of 300 and 400) has been prepared by manual agitation. Their hysteresis cycle has been measured at room temperature in order to see the effect of the added nanoparticles.

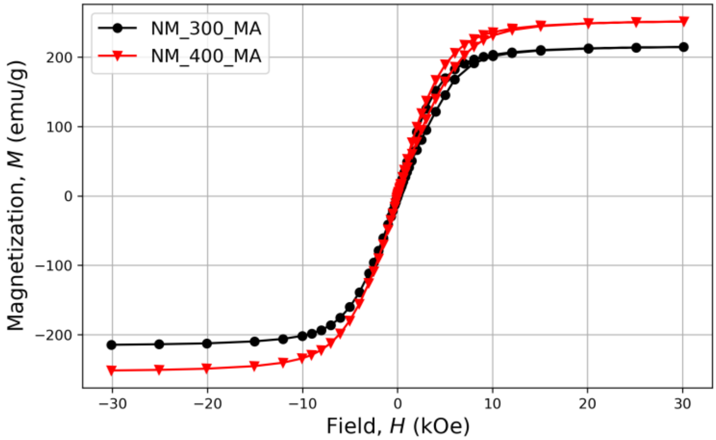

Figure 6. 16. *M*(*H*) hysteresis cycles of NM_300_MA (black) and NM_400_MA (red) measured at 300 K. It has been measured the first magnetization and demagnetization curves.

It can be seen that for the higher Fe content (NM_400_MA) the saturation magnetization is similar to the one previously shown in Figure 6. 7. Furthermore, it can be checked that the addition of Fe_3O_4 nanoparticles reduces both, the saturation magnetization and the magnetic permeability.

4.2.3. Nanoparticles distribution

Achieving an adequate dispersion of nanoparticles around the Fe cores is crucial in order to ensure a full electrical isolation between particles. The quality of this dispersion has been qualitatively checked by SEM (in a Quanta microscope) for each of the mixing methods.

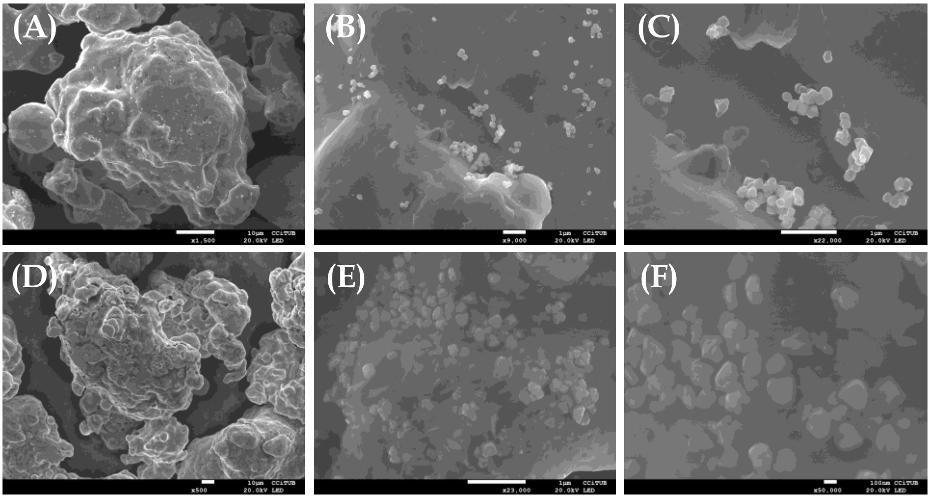

Figure 6. 17. SEM images of the manually (top) and microwave (bottom) mixture of the Fe_3O_4 nanoparticles and Fe cores with a ratio of 300 in mass. The magnifications are (A) x1500, (B) x9000, (C) x22000, (D) x500, (E) x23000, and (F) x50000.

The surface covering is not complete in any of the cases. However, the amount of coated surface is qualitatively higher when the microwave mixing method is used. The low magnification images (Figure 6. 17.A and Figure 6. 17.D) do not allow to clearly see the nanoparticles on the surface. Alternatively, Figure 6. 17.B and Figure 6. 17.C reveal that by using the manual agitation the number of nanoparticles remaining on the surface is very low, and only some particles forming aggregates remain stable. On the other hand, Figure 6. 17.E and Figure 6. 17.F show that when the microwave agitation method is used the number of particles attached to the iron core surface increases, and the nanoparticles are less aggregated than before. This is an important result in order to achieve a homogeneous thin shell of nanoparticles.

Despite the covering degree seen in Figure 6. 17 is far from a 100%, it should be pointed out that, in order to ensure that particles do not leave the sample in the SEM vacuum conditions, they have been blown with air before the observation. It means that only those particles strongly attached to the core are observed, while those softly attracted by electrostatic forces have left. Thus, we can expect a higher degree of covering in our samples than the one observed by SEM.

4.3. Oxidized iron cores

4.3.1. Description

This approach pretends to make a controlled oxidation of the Fe core in air atmosphere to produce a thin iron oxide shell surrounding the core. The schematic representation of this approach is also shown in Figure 6. 18. In this case, it is important to consider that an increase of the produced oxide leads to a decrease on the Fe content on the core, so it is crucial to have a good control over the process. However, despite in Figure 6. 18 it has been simplified, the oxide thickness generation does not directly correspond to the reduction of Fe core diameter, as the densities of each phase should be first considered.

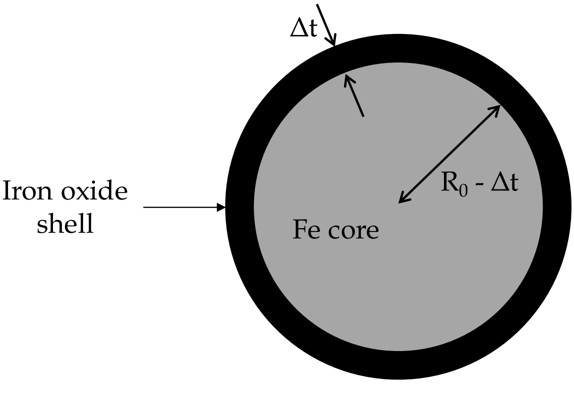

Figure 6. 18. Schematic representation of the oxidized Fe SMC. *Δt* represents the generated shell thickness, and *R_0* the initial Fe core radius.

This family of samples will be noted with the code *OX_temp_time* during the rest of the work. The term *temp* indicates the oxidation temperature in degrees, and *time* refers to the oxidation time, in minutes.

4.3.2. Oxidation process

The control of the oxide layer by placing the podwer sample in a furnace with air atmosphere is not trivial. For this reason, we have performed a first set of samples prepared in a wide range of temperatures (300, 400, 500, and 600 °C) and times (30 and 120 minutes). The oxide formation has been characterized by XRD in order to know the nature and quantity of the formed oxides. The results for the samples prepared for 120 minutes are shown in Figure 6. 19.

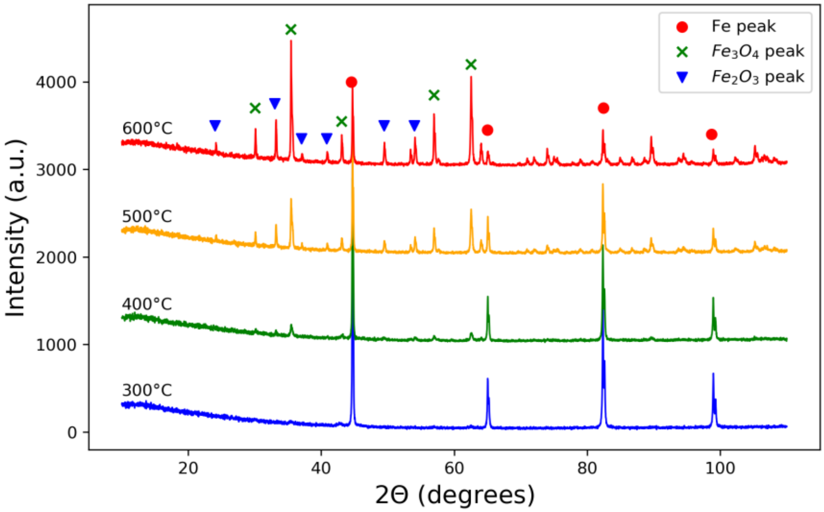

Figure 6. 19. XRD pattern of the Fe cores oxidized during 2 hours at 300 °C (blue), 400 °C (green), 500 °C (orange), and 600 °C (red). The markers represent the main peak positions of the phases identified. All the patterns have been intentionally spaced 1000 units in intensity in order to allow a better comparison.

This figure shows how the pure Fe structure starts to oxidize and to produce higher quantities of iron oxide as the temperature raises. In this case, the first iron oxide peaks are detected at 400 °C, but it may change depending on the oxidation time. Furthermore, two different oxide phases have been formed: Fe_3O_4 (magnetite) and Fe_2O_3 (hematite). The intensity of the Fe_3O_4 is higher than the one of Fe_2O_3, suggesting a higher amount of magnetite. We aim to form Fe_3O_4, as it has a larger magnetic moment than Fe_2O_3 [24].

The XRD spectra of the samples oxidized for 30 minutes show the same trends. The RIR criteria has been used to semi-quantify the amount of Fe at each oxidation conditions. In Figure 6. 20 it is seen a higher reduction in Fe content (i.e. oxide production) at higher temperatures and longer times, as could be expected.

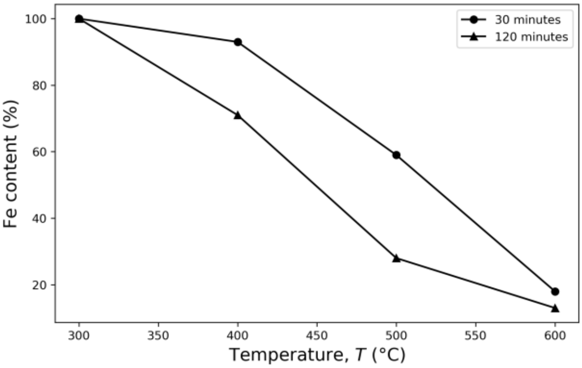

Figure 6. 20. Fe content versus temperature for the oxidation processes performed during 30 (circles) and 120 (triangles) minutes.

At 300 °C there is almost no oxide formation for these oxidation times. However, there is an important decrease on iron content at 400 °C (93% for 30 minutes, and 71% for 120 minutes). If we pretend to form a thin shell (in the nano-micro range), these oxidations are already too severe. At higher temperatures it is possible to see how, in both cases, the iron content stabilizes at around a 15%, as the formed oxide shell protects the core from further oxidation. From these results, our first guess is that the most appropriate oxidations will be those done at low temperatures (around 300 °C) in order to have a good control on the shell thickness.

4.3.3. Oxide shell thickness and uniformity

As it has been previously done with the NM samples, we have also investigated the aspect of the formed shell by SEM. The powder samples have been embedded in a conductive resin and polished until the core is revealed. In the light of the results seen from the XRD measurements, three samples with softer oxidation processes (350 °C and 450 °C for different times) have been prepared. By this way, in Figure 6. 21 the formed core-shell structure is seen.

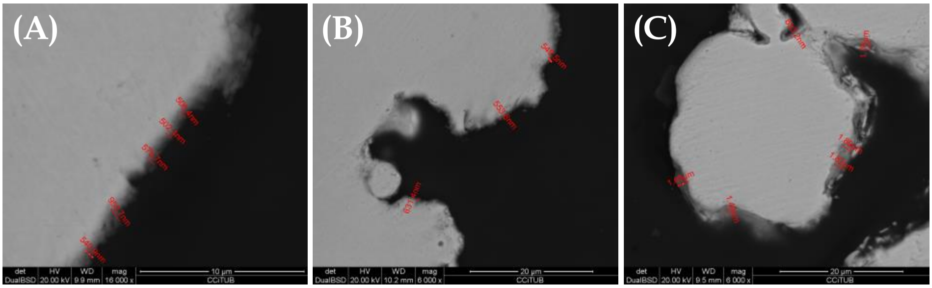

Figure 6. 21. Backscattered electrons SEM images of Fe cores oxidized for(A) 15 minutes at 350 °C, (B) 45 minutes at 350 °C, and (C) 45 minutes at 450 °C.

The BSE images allow us to detect the differences in chemical composition, and thus to see the oxide shell. In general terms, we can see that the shell uniformity worsens from the softer oxidation conditions to the harder ones, which are respectively represented in Figure 6. 21.A and Figure 6. 21.C. Furthermore, in Figure 6. 21.B it is seen that there is no oxidation in hidden regions due to the particle geometry. The shell thickness has been measured in different random points in each sample. The mean results are 616.0 nm ± 189.7 nm for 15 minutes at 350 °C, 578.2 nm ± 46.1 nm for 45 minutes at 350 °C, and 1537.2 nm ± 465.2 nm for 45 minutes at 450 °C. Due to the low statistics in these measurements it is not possible to extract precise conclusions, but it is clear the difference in order of magnitude on the shell thickness between those samples oxidized at 350 °C and 450 °C. Furthermore, the standard deviation of the measurement is also lower in those samples prepared at 350 °C, what represents a more homogeneous layer formation. With all that in mind, the ideal conditions seem to go in the direction of low temperatures, which allows to form thin shells in a homogeneous way. The obtained thicknesses at 350 °C are approximately the double than the one previously measured for the currently used SMC, but there is still room to work at lower temperatures to achieve similar results.

4.4. Frequency-dependent magnetic properties

Now, we know the constitution of both materials (NM and OX) and we have an idea about the effect that the preparation conditions have on their characteristics. Now it is time to investigate the frequency-dependent magnetic properties of these new materials, and to compare them with those of the SMMs and SMCs currently used in technological applications. This is the key aspect to evaluate their applicability in the kHz and MHz frequency range. Furthermore, the understanding of the effect that the preparation conditions have on the final magnetic properties of these materials is of great importance to be used as guidelines for further research.

Toroidal-shaped bulk samples have been prepared with the NM and OX samples obtained under the same previous conditions. In order to facilitate the comprehension of the results, the work done with the NM samples will be first presented, and lately the one done with the OX ones. In all cases the samples have been studied in green form, without annealing them, as it has been done in all the previously presented results. The annealing could differently affect each kind of materials, so we are ensuring to compare them in the same conditions.

4.4.1. Nanomaterials mixture SMCs (NM)

We have prepared five different samples to be analysed by impedance spectroscopy. We have first planned four samples prepared with two clearly differentiated ratios (in order to undoubtedly see the effect of the nanoparticles) prepared by the two different agitation methods. Moreover, after considering the dispersion observed by SEM, it has been decided to add another sample (NM_200_MW) with an extra charge of nanoparticles by microwaves agitation, in order to try to have a sample with the maximum number of nanoparticles surrounding the Fe core. The characteristics of the five toroids are described in Table 6. 3.

Table 6. 3. Characteristics of the NM toroids prepared for impedance spectroscopy measurements. All of them have been compacted under a uniaxial pressure of 700 kg/cm^3.

Sample	Mass ratio (Fe/Fe_3O_4)	Agitation	Density, ρ (g/cm^3)
NM_200_MW	200	Microwaves	7.43
NM_250_MA	250	Manual	7.52
NM_250_MW	250	Microwaves	7.48
NM_500_MA	500	Manual	7.56
NM_500_MW	500	Microwaves	7.44

These characteristics reveal that those samples prepared by microwave agitation present lower density values than those manually agitated. A possible reason might be the fact that a lower degree of surface covering with oxide particles may allow the Fe cores to freely deform. The complex permeability spectra obtained for these samples is represented in Figure 6. 22.

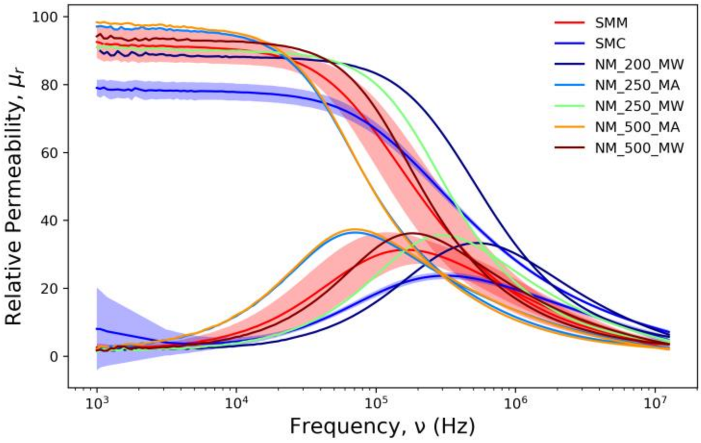

Figure 6. 22. Complex permeability spectra of the NM samples from 1 kHz to 13 MHz measured by impedance spectroscopy. Results are compared with the mean results previously obtained for SMM and SMC samples. Shaded areas correspond to the standard deviation in those measurements calculated from the mean of more than one replicate.

A first aspect that may be highlighted from these results is the fact that all the samples present higher μ_S than the SMC; some of them are even above the SMM, but always inside the standard deviation region. This supports the argument that the Fe_3O_4 may be favourably contributing to the global magnetic moment. Furthermore, it seems to be a tendency of increasing the permeability when decreasing the number of nanoparticles in the system, in good agreement with the results obtained for the $M(H)$. On the other hand, only the sample NM_200_MW is capable to exceed the relaxation frequency of the SMC. In order to allow an easier comparison and analysis of the effect of each variable, Figure 6. 23 presents some statistics of these results.

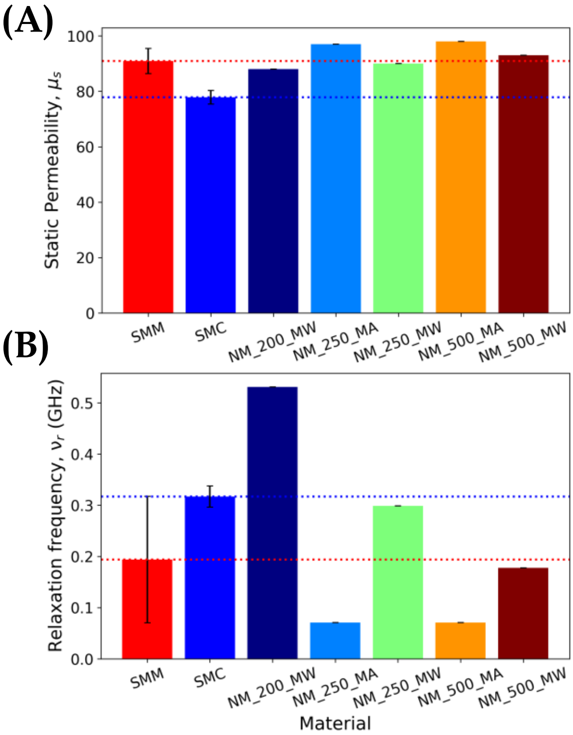

Figure 6. 23. Statistical analysis of the (A) static permeability μ_S, and (B) relaxation frequency ν_r of the NM samples.

In Figure 6. 23.A it is confirmed that all the NM formulations improve the permeability of the SMC, i.e. providing a better magnetic response. Those samples manually agitated seem to have values even slightly higher than those of the SMM, but the difference is minimum, and they are inside the error region of the SMM measurements. However, there is a clear difference between the manually and microwave agitated samples in terms of frequency stability. The samples prepared by using microwaves have considerably higher ν_r values than those manually prepared and can even be higher than those of the SMC. Moreover, there is a perfect correspondence between the number of nanoparticles present in the samples agitated by microwaves and their relaxation frequency: the larger number of oxide nanoparticles, the better isolation. The low relaxation frequency in those samples manually prepared is explained by the poor surface covering achieved, as it has been seen by SEM before.

Overall, manual agitation may be discarded as a viable option due to the bad frequency stability that these samples present. Microwave agitated samples with ratios between 200 and 250 show promising properties as they improve both, the magnetic permeability and frequency stability compared with actual used SMCs.

4.4.2. Oxidized Fe cores (OX)

With these samples the problem is even more complicated, as we must play with a larger number of variables. With the NM samples, one of the variables (agitation method) only could present two states, and from the firsts results the microwave agitation have shown better results. On the other hand, now we must define adequate conditions in terms of time and temperature. First of all, we have examined the first eight powder samples that we have previously characterized by XRD. Despite we already know that some of these samples contain unacceptable oxide quantities, the wide range of conditions used become an excellent opportunity to see their effect on complex permeability. The characteristics of this set of samples are described in Table 6. 4. From this data, it is possible to see how the density of the toroid decreases at higher oxidation temperatures, due to the iron oxide formation. The complex spectrum is shown in Figure 6. 24.

Table 6. 4. Characteristics of the first set of OX toroids prepared for impedance spectroscopy measurements. All of them have been compacted under a uniaxial pressure of 700 kg/cm^3.

Sample	Temperature, *T* (°C)	Time, *t* (minutes)	Density, *ρ* (g/cm^3)
OX_300_30	300	30	7.26
OX_300_120	300	120	7.32
OX_400_30	400	30	7.29
OX_400_120	400	120	7.25
OX_500_30	500	30	6.82
OX_500_120	500	120	6.43
OX_600_30	600	30	5.76
OX_600_120	600	120	5.30

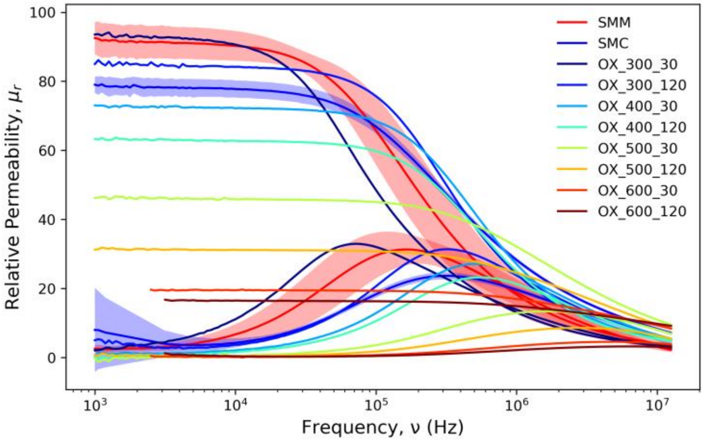

Figure 6. 24. Complex permeability spectra of the first set of OX samples from 1 kHz to 13 MHz measured by impedance spectroscopy. Results are compared with the mean results previously obtained for SMM and SMC samples. Shaded areas correspond to the standard deviation in those measurements calculated from the mean of more than one replicate.

There is an evident order of the samples' static permeability regarding their oxidation conditions in Figure 6. 24. Magnetic permeability decreases for harder and larger oxidation processes, according to the reduction on Fe content observed in XRD measurements. Moreover, the increase of oxides in the sample also leads to an increase of the sample stability against frequency due to the increase of resistivity in the system. In this figure the Snoek's law is exemplified. The analysis of the static permeability and frequency stability for each sample is shown in Figure 6. 25.

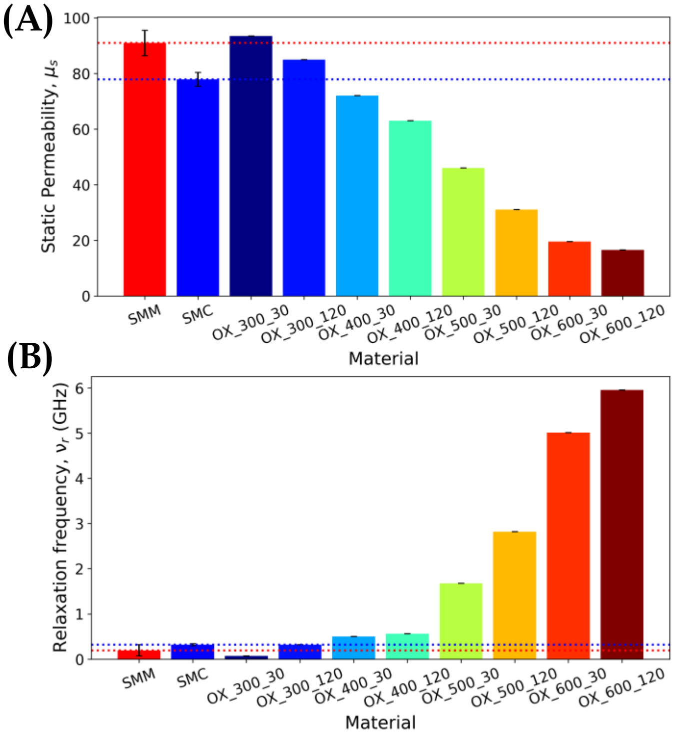

Figure 6. 25. Statistical analysis of the (A) static permeability μ_S, and (B) relaxation frequency ν_r of the first set of OX samples.

Again, one can appreciate the perfect dependence of the material performance with the synthesis conditions. In Figure 6. 25.A the magnetic permeability decreases when increasing oxidation temperatures, while the inverse effect is seen in Figure 6. 25.B. Although the major part of these samples would not be of interest for applications in the kHz and MHz frequency range because of their low magnetic permeability, it is possible to extract potentially interesting conclusions from these figures. Those samples oxidized at 300 °C for 30 and 120 minutes have an equilibrated balance of properties: their μ_S is higher than the one of the SMC, and is even similar to the SMM when the sample is oxidized only 30 minutes. The frequency stability of the sample oxidized for 120 minutes is comparable with the currently used SMCs.

In the light of these results, a second ser of samples has been prepared, considering that the region under interest is the one around 300 °C. The oxidation times used in this second set of samples are slightly larger in order to give enough time to form a homogeneous shell around the Fe core. It has been observed by SEM that high temperature and short oxidation processes can lead to a high degree of inhomogeneity in the shell. The new set of samples is described in Table 6. 5.

Table 6. 5. Characteristics of the second set of OX toroids prepared for impedance spectroscopy measurements. All of them have been compacted under a uniaxial pressure of 700 kg/cm^3.

Sample	Temperature, *T* (°C)	Time, *t* (minutes)	Density, *ρ* (g/cm^3)
OX_275_60	275	60	7.59
OX_275_180	275	180	7.46
OX_325_30	325	60	7.45
OX_325_180	325	180	7.50

The results obtained from the impedance spectroscopy measurement of these samples are shown in Figure 6. 26.

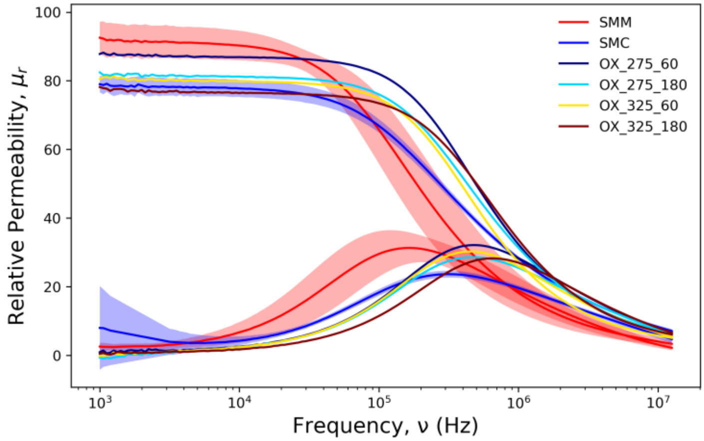

Figure 6. 26. Complex permeability spectra of the second set of OX samples from 1 kHz to 13 MHz measured by impedance spectroscopy. Results are compared with the mean results previously obtained from the SMM and SMC samples. Shaded areas correspond to the standard deviation in those measurements calculated from the mean of more than one replicate.

In this case, any of these samples has a higher static permeability than the pure Fe core (SMM), as could be expected. However, sample OX_275_60 – the one with the softer oxidation – presents a similar magnitude. The other samples, which come from harder oxidations, show μ_S similar to the SMC. In terms of frequency stability, the results are excellent: all the new formulations relax at higher frequencies than SMC and, of course, SMM. These results are clearly exposed in Figure 6. 27.

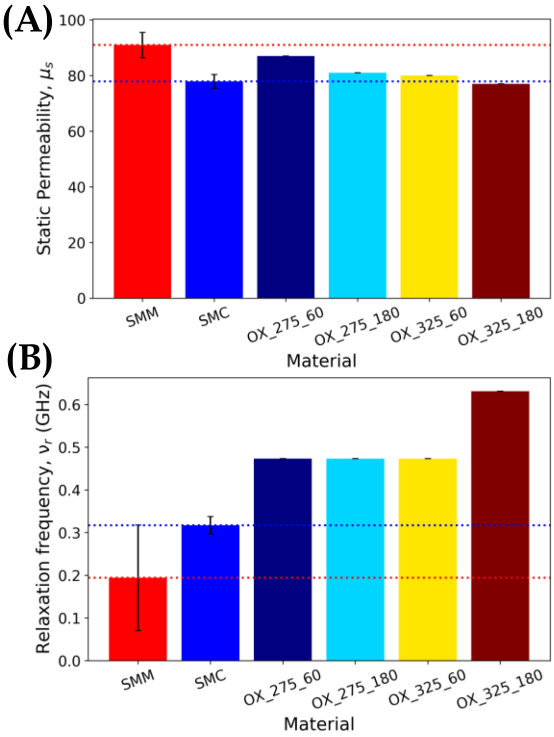

Figure 6. 27. Statistical analysis of the (A) static permeability μ_S, and (B) relaxation frequency ν_r of the second set of OX samples.

These results confirm the promising properties of this family of materials, and, at the same time, highlight that the criteria of reducing temperature and enlarge times can lead to thinner (i.e. higher permeability) and more uniform (i.e. higher frequency stability) shells. The uniformity of the shell is demonstrated by the fact that, in the OX_275_60 sample, the ν_r is not reduced compared with harder oxidations, while the static permeability increases. This sample has better stability than the SMC sample, and similar permeability than pure Fe. For this reason, we have lastly examined another set of samples below 275 °C and larger times. Their characteristics are provided in Table 6. 6.

Table 6. 6. Characteristics of the third set of OX toroids prepared for impedance spectroscopy measurements. All of them have been compacted under a uniaxial pressure of 700 kg/cm^3.

Sample	Temperature, *T* (°C)	Time, *t* (minutes)	Density, ρ (g/cm^3)
OX_200_120	200	120	7.50
OX_200_240	200	240	7.59
OX_250_120	250	120	7.53
OX_250_240	250	240	7.53

The complex permeability spectra, that is shown in Figure 6. 28, shows again that the permeability of all samples is much closer to the one for SMM than for SMC. The relaxation frequencies are also similar to the ones for SMM, and only the sample oxidized at 250 °C for 4 hours improves the stability of the SMC. Due to the high degree of similarity between all these curves, it is easier to analyse the results from Figure 6. 29.

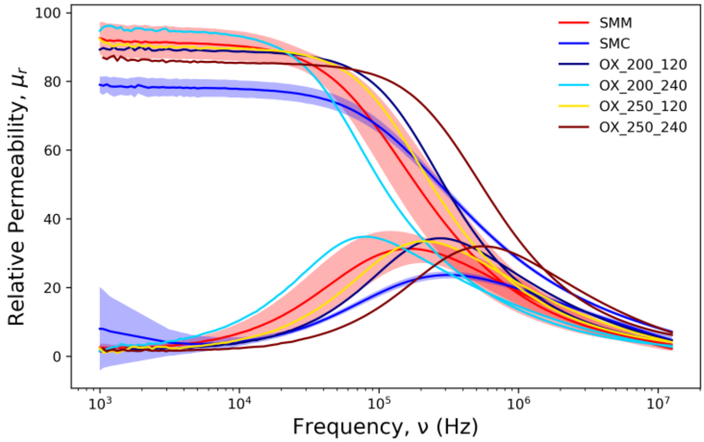

Figure 6. 28. Complex permeability spectra of the third set of OX samples from 1 kHz to 13 MHz measured by impedance spectroscopy. Results are compared with the mean results previously obtained for SMM and SMC samples. Shaded areas correspond to the standard deviation in those measurements calculated from the mean of more than one replicate.

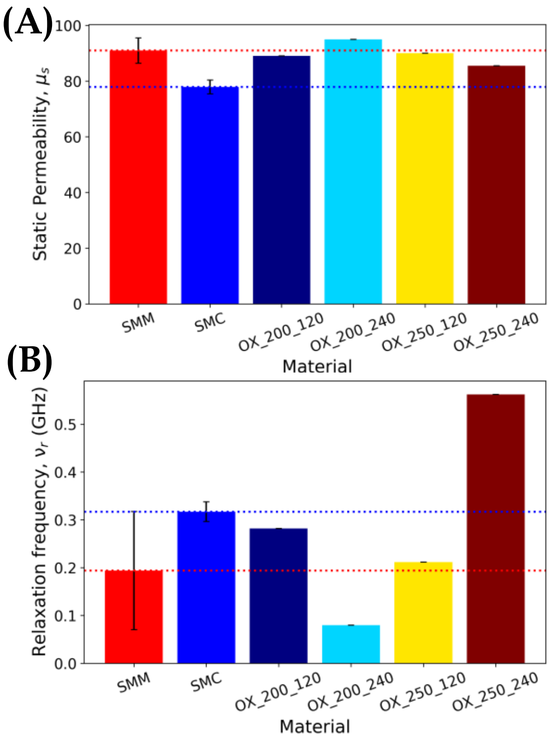

Figure 6. 29. Statistical analysis of the (A) static permeability μ_S, and (B) relaxation frequency ν_r of the third set of OX samples.

The tendency in fulfilling the Snoek's law is clear in all samples, unless for OX_200_120 that presents an anomalous behaviour. Considering the error bars of the measurements with good statistics (SMM and SMC), it could be due to experimental deviation. However, the general trends in this set of samples show elevated permeability values (comparable with the ones for pure Fe), but low relaxation frequencies. These results indicate a low degree of oxidation of the Fe core in these conditions. Nevertheless, the sample oxidized under harder conditions presents promising properties: higher magnetic permeability and frequency stability than the SMC.

In the light of all these results, it has been seen than the oxidation of Fe cores under air atmosphere is a promising approach which can lead to improved magnetic response and frequency stability properties even compared with current SMCs. The most suitable conditions consist on low temperatures and long times, which allow the formation of a thin and uniform oxide layer. The temperatures that have shown better properties are those in the range between 250 °C and 275 °C.

5. STUDY OF THE ANNEALING PROCESS

The properties of the designed new SMCs are encouraging from a technological point of view and seem to compete against current SMCs. However, there is one more step prior to their application: the annealing process. This thermal process is applied after the compaction in order to reduce internal stresses from the previous cold work, leading to an increase of the magnetic permeability [9], [15]. As it has been commented before, all the results of the previous section correspond to green toroids. It is therefore of vital importance to study how all these materials respond to the annealing treatment and, if it is possible, to find the most suitable conditions to treat each kind of material.

5.1. Annealing design

One formulation of each type of material has been selected in order to perform these experiments. These samples are SMC, SMM, OX_250_240, and NM_200_MW, as they are those with better properties in their families.

The effect that the annealing has on the properties of each material has not been just tested under single conditions. A matrix of experiments has been designed surrounding the typical annealing conditions (15 minutes at 400 °C in N_2 atmosphere). Thus, the four corners defined by 350 °C – 450 °C, and 10 – 20 minutes have been investigated. 6 samples of each material have been prepared (24 in total) in order to check the four corners, and to do 2 replicates in the central point. The characteristics of each toroid are described in Table 6. 7.

Table 6. 7. Characteristics of the prepared samples and the applied annealing conditions. Corner conditions are defined by T_{min} = 350 °C, T_{max} = 450 °C, t_{min} = 10minutes, and t_{max} = 20 minutes. Central conditions are T = 400 °C, and t = 15 minutes. All the annealing treatments have been done in N_2 atmosphere, and the toroids have been previously compacted under a uniaxial pressure of 700 kg/cm^3.

Sample	**Temp, T (°C)**	**Time, t (min)**	**Initial Density, ρ (g/cm^3)**	**Final Density, ρ (g/cm^3)**	**Density variation, $\Delta\rho$ (%)**
SMM_1	350	10	7.35	7.30	-0.69
SMM_2	350	20	7.19	7.31	1.63
SMM_3	450	10	7.22	7.28	0.75
SMM_4	450	20	7.20	7.22	0.37
SMM_5	400	15	7.24	7.24	-0.08
SMM_6	400	15	7.30	7.28	-0.28
SMC_1	350	10	7.11	7.30	2.58
SMC_2	350	20	7.24	7.22	-0.21
SMC_3	450	10	7.30	7.28	-0.31
SMC_4	450	20	7.25	7.26	0.15
SMC_5	400	15	7.18	7.24	0.80
SMC_6	400	15	7.26	7.27	0.12
OX_250_240_1	350	10	7.15	7.26	1.50
OX_250_240_2	350	20	7.09	7.21	1.72
OX_250_240_3	450	10	6.54	7.16	9.60
OX_250_240_4	450	20	7.12	7.25	1.80
OX_250_240_5	400	15	7.23	7.31	1.11
OX_250_240_6	400	15	7.07	7.21	2.06
NM_200_MW_1	350	10	6.71	6.76	0.69
NM_200_MW_2	350	20	6.67	6.71	0.68
NM_200_MW_3	450	10	7.30	6.72	-7.92
NM_200_MW_4	450	20	6.60	6.72	1.88
NM_200_MW_5	400	15	6.63	6.68	0.84
NM_200_MW_6	400	15	6.62	6.69	1.05

It has not been found a clear tendency on the density change, which could be representative of contraction or expansion of the sample.

5.2. Change in frequency-dependent magnetic properties

All the toroids have been measured before and after being annealed, in order to individually see the caused changes. Their magnetic response in green form is shown in Figure 6. 30. The mean and standard deviation have been calculated because all the samples are under the same conditions before the annealing process.

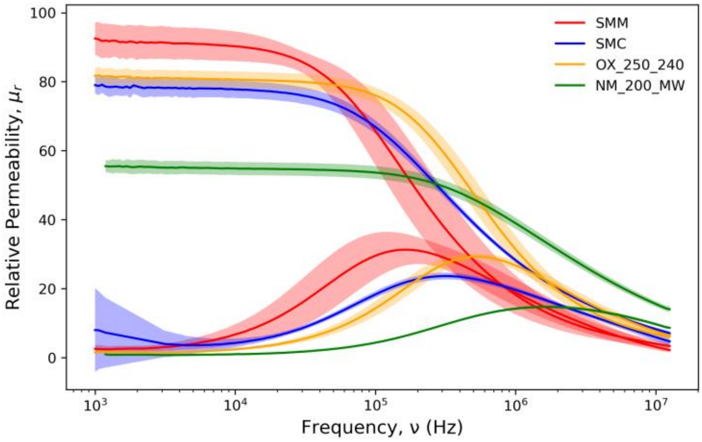

Figure 6. 30. Frequency–dependent complex magnetic permeability spectra of the four samples under study. Each curve represents the main values of six replicated of the same material, while shaded regions are the standard deviation.

As a starting point, these results agree with those seen in the previous sections. SMM has higher μ_S than SMC, but lower ν_r. NM with high Fe_3O_4 nanoparticles content is highly stable against frequency, while OX samples have better properties than SMC. The statistical analysis of these results is provided in Figure 6. 31.

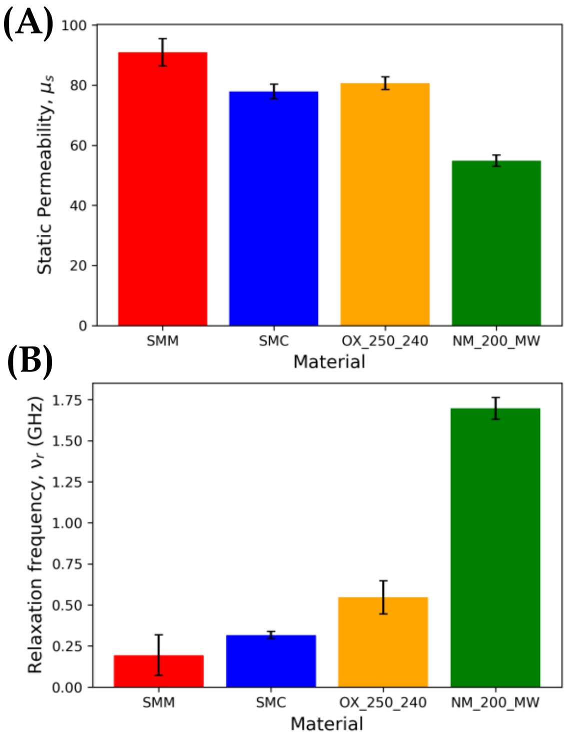

Figure 6. 31. Comparison of the (A) static permeability μ_S, and (B) relaxation frequency ν_r of the SMM (red), SMC (blue), OX_250_240 (orange), and NM_200_MW (green) samples.

Starting by the most elemental sample, which is SMM (pure Fe cores), its magnetic properties are highly sensitive to the annealing conditions, as Figure 6. 32 demonstrates.

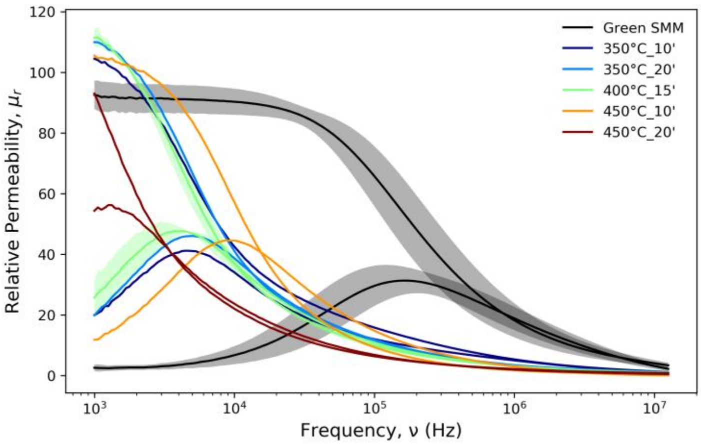

Figure 6. 32. Complex magnetic permeability spectra of the SMM sample after performing different annealing treatments. The black plot corresponds to the green form of the sample.

There is a clear shift of the spectrum towards lower frequencies even for the softer annealing conditions. It is true that the permeability values increase as we expected, but the associated reduction on frequency stability is notable and makes this material difficult to be applied in engineering situations. Furthermore, a progressive shift of the spectrum is observed, according to the annealing conditions, except for the case of the one treated at 450 °C for 10 minutes. The harder annealing conditions seem to reach μ_S values of around 120, despite it cannot be clearly seen because the reduction on ν_r is so high that it is defined in the lower frequency limit of the measurement (1 kHz). By comparing these two properties before and after the annealing process in each one of the toroids, we get Figure 6. 33.

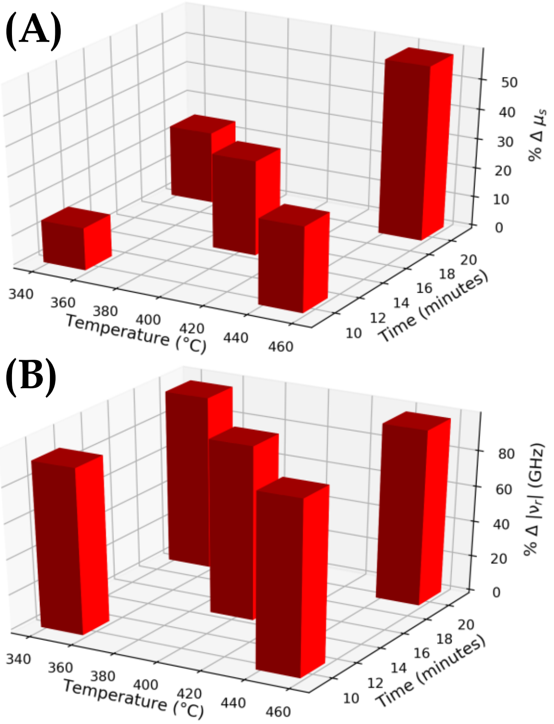

Figure 6. 33. Analysis of the variation of (A) static permeability μ_S, and (B) relaxation frequency ν_r at different annealing conditions of the SMC sample. Both results are expressed as a percentage variation. The variation of ν_r is negative, so the absolute value has been represented in order to facilitate its visualization.

From Figure 6. 33.A can it be observed that the increase of permeability is regular with the increasing annealing temperature and time. On the other hand, Figure 6. 33.B shows that there is an almost complete loss of frequency stability in all the conditions.

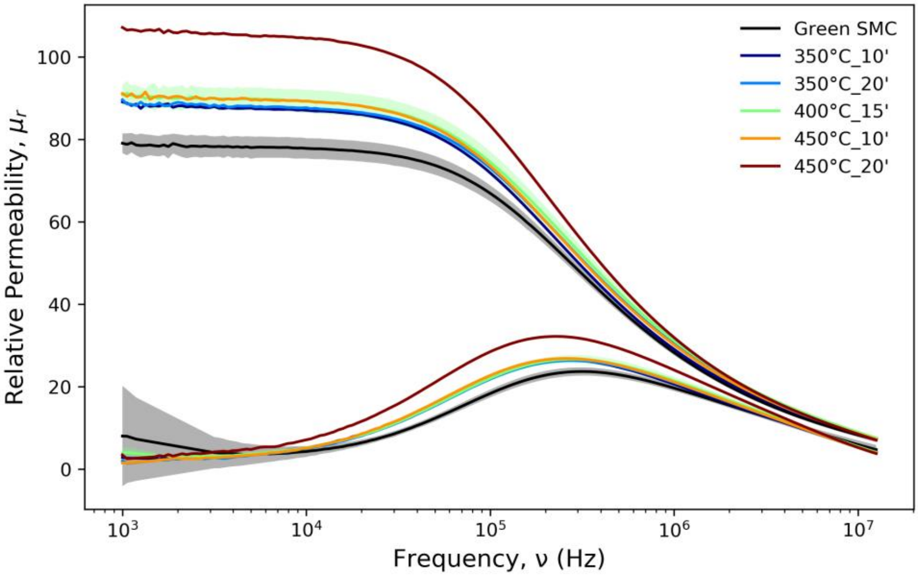

Figure 6. 34. Complex magnetic permeability spectra of the SMC sample after performing different annealing treatments. The black plot corresponds to the green form of the sample.

The same test has been done with the SMC samples, and the results are completely different. In this case, as can be seen in Figure 6. 34, the permeability continuously increases as the annealing conditions become harder. The temperature stability of this material is excellent, and this makes it so interesting from a technological perspective. The properties' variation has also been calculated, and it is shown in Figure 6. 35.

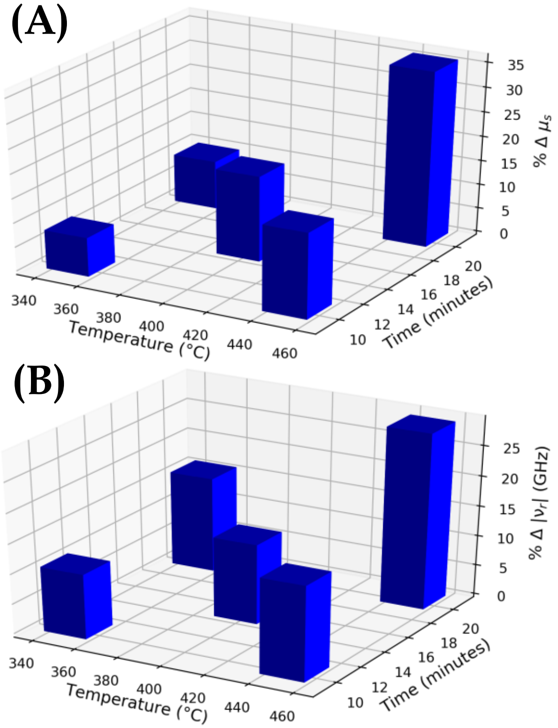

Figure 6. 35. Analysis of the variation of (A) static permeability μ_S, and (B) relaxation frequency ν_r at different annealing conditions of the SMC sample. Both results are expressed as a percentage variation. The variation of ν_r is negative, so the absolute value has been represented in order to facilitate its visualization.

It can be observed the progressive increase of the static magnetic permeability with respect to temperature and time in Figure 6. 35.A. Contrary to the previous case, in this sample the reduction on relaxation frequency is minimum, reaching a maximum value of around 25% when the gain in permeability has been a 35%. These results highlight even more the importance of the phosphate coating in these composites. The Fe core is common in the SMM and SMC, and its properties are only stable during the annealing if the shell is present.

Then, it is time to examine the response of the new SMC formulations under the same conditions. Figure 6. 36 shows the variation on the complex permeability spectrum of the NM sample.

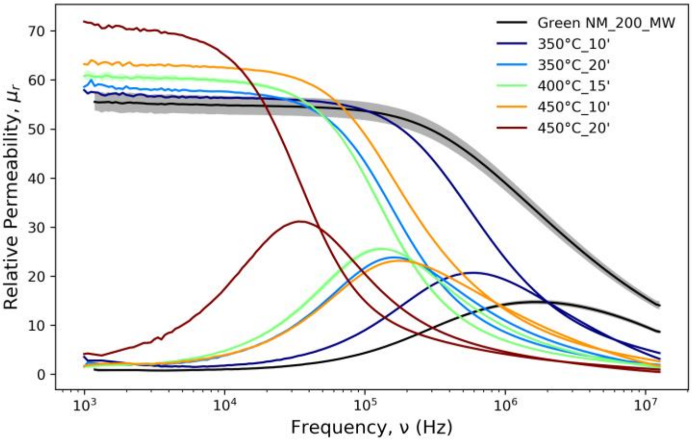

Figure 6. 36. Complex magnetic permeability spectra of the NM_200_MW sample after performing different annealing treatments. The black plot corresponds to the green form of the sample.

The expected increase on μ_S is produced, reaching relative values around 70. On the other hand, there is a clear shift to lower frequencies of the relaxation mechanism. However, this shift is smaller than the one observed for the pure Fe particles. Despite the nanoparticles surface covering is not perfect, part of them are protecting the core. Therefore, better thermal stability could be achieved by improving the distribution of Fe_3O_4 nanoparticles around the Fe cores. Finally, it should be also mentioned that as the green relaxation frequency is elevated (around 2 GHz), the resulting relaxation frequencies are still correct.

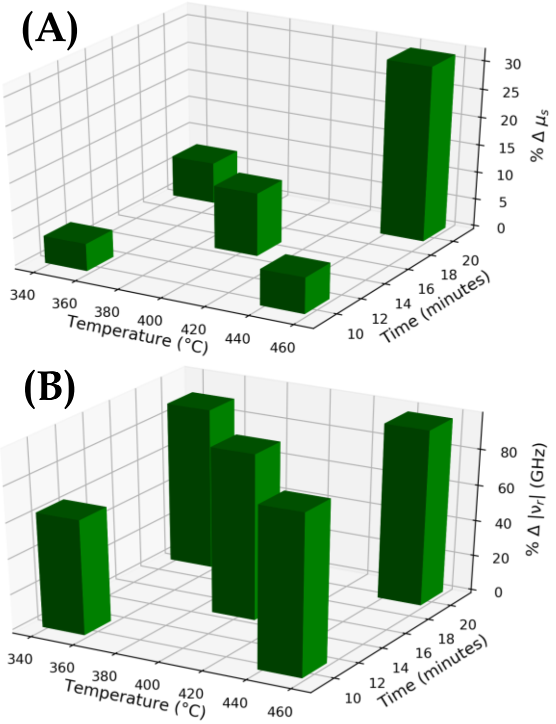

Figure 6. 37. Analysis of the variation of (A) static permeability μ_S, and (B) relaxation frequency ν_r at different annealing conditions of the NM_200_MW sample. Both results are expressed as a percentage variation. The variation of ν_r is negative, so the absolute value has been represented in order to facilitate its visualization.

The analysis in Figure 6. 37 shows an important gain in magnetic permeability for treatments of 20 minutes at 450 °C. In general, the improvement in magnetic properties is not significant, despite there is an important decrease of the relaxation frequency. In Figure 6. 37.B it is possible to see that it rapidly decays around an 80% of its initial value.

Finally, the oxidized Fe core sample has been studied. The spectra shown in Figure 6. 38 describes a strong starting loose of frequency stability when the annealing treatments are done, while the gain on permeability is more progressive. The μ_S values achieved are higher than 120, well above the SMC's levels. Furthermore, the relaxation frequencies are not as low as those obtained for the SMM sample and keep constant at around 10 kHz. This behaviour might be describing a process in which the oxide shell is not homogeneous at the beginning and the core is not fully protected, leading to a rapid decrease of ν_r. Then another species might be formed on the surface, passivating and protecting the Fe core. From this moment, the relaxation frequency stabilized, and the permeability keeps growing, as in the case of the SMC.

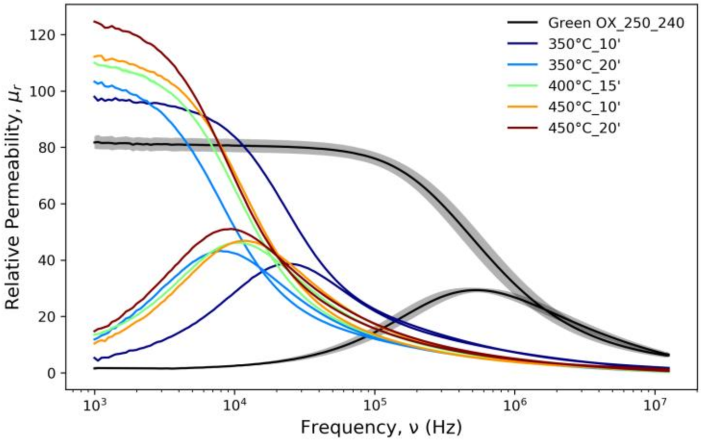

Figure 6. 38. Complex magnetic permeability spectra of the OX_250_240 sample after performing different annealing treatments. The black plot corresponds to the green form of the sample.

The analysis shown in Figure 6. 39 reinforce this argument, as the increase on permeability is perfectly continuous and monotone. However, the relaxation frequency rapidly decreases around an 80% of its starting value, but it then stabilizes.

By comparing these results with the ones of the SMC, it seems that the key aspect is the homogeneity of the isolating shell around the Fe core. The green-form properties of the oxidized sample are better than those of the SMC, but the SMC responds much better to the annealing process and its properties improve. A ceramic shell must be stable at temperatures of 350 °C and 450 °C, so the problems may come from irregularities in the shell. Therefore, having a precise control over the oxide formation is crucial for making this material thermally stable during the annealing process.

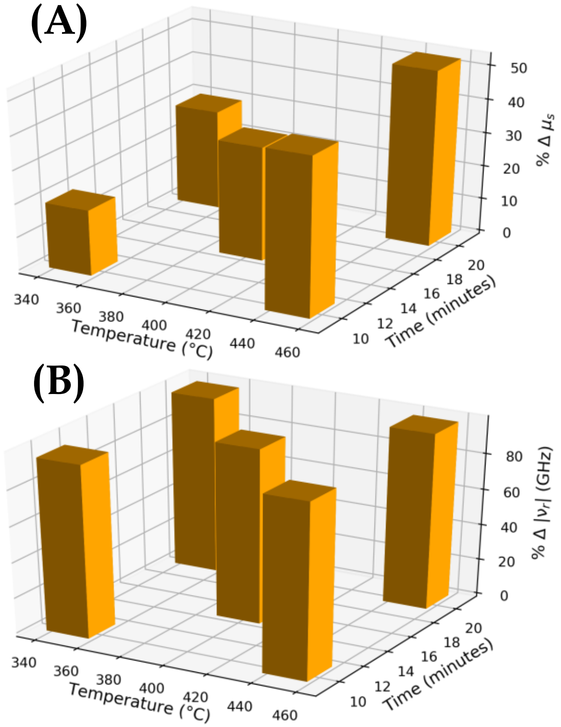

Figure 6. 39. Analysis of the variation of (A) static permeability μ_S, and (B) relaxation frequency ν_r at different annealing conditions of the OX_250_240 sample. Both results are expressed as a percentage variation. The variation of ν_r is negative, so the absolute value has been represented in order to facilitate its visualization.

5.3. Compositional changes

The annealing processes has been done under inert N_2 atmosphere and no chemical reactions were expected during this process. However, due to the important loss of frequency stability we have performed XRD measurements in the inner and outer part of the toroids to check if there is any compositional or microstructural change. The results of the analysis of both materials are shown in Figure 6. 40.

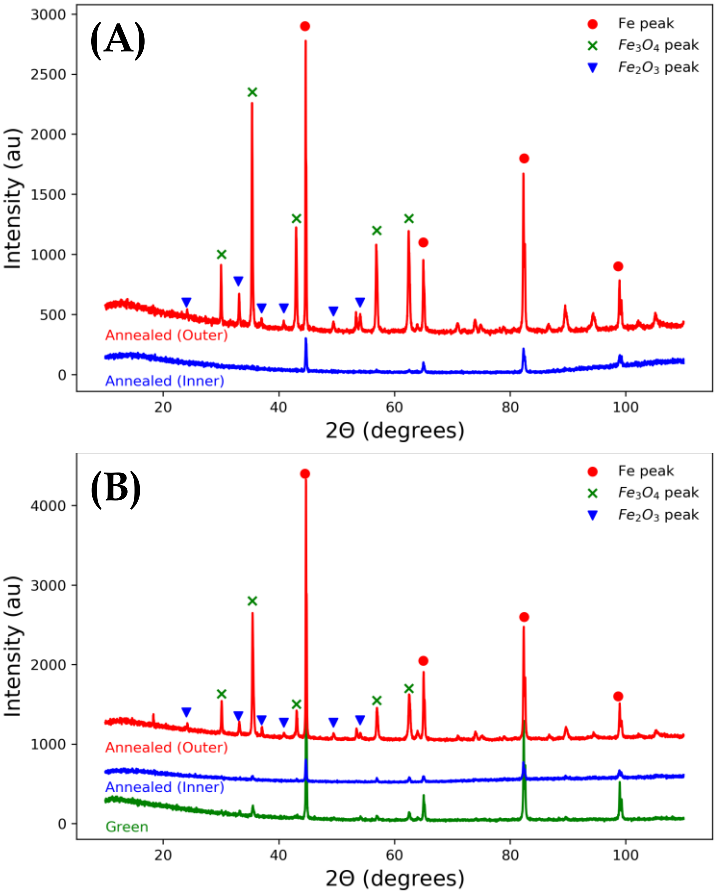

Figure 6. 40. XRD measurement of the annealed toroid in its inner (blue) and outer (red) parts of the (A) NM, and (B) OX samples. The diffraction patterns have been intentionally spaced 1000 units in intensity in order to allow a better comparison. The markers represent the main peak positions of each of the identified phases.

Surprisingly in both cases iron oxide has been formed in the surface of the toroids. Really small quantities are also detected in the inner part only in the OX sample. Therefore, a first conclusion is that the sample is reacting with oxygen even though the process has been carried out under N_2 atmosphere. It may have two causes: (i) oxygen is entering inside the furnace during the treatment, or (ii) sample oxidizes during the transportation from the furnace to the vacuum chamber. Probably the origin corresponds to the second reason, as the sample leaves the furnace at high temperature, and it requires some time to move it to the chamber and have an effective vacuum.

Another surprising aspect is that the formation of the oxide is causing a decrease on the relaxation frequency. As it has been seen during the oxidation process of the Fe powder, an increase of the oxide content reduces the permeability and increases the relaxation frequency, due to its higher electric resistivity. However, the oxidation has been performed in the powder form and a higher homogeneity may be expected. Thus, the origin of the appearance of magnetic losses at lower frequencies might be more related to the generation of a chemically and structurally inhomogeneous structure rather than the direct effect of the oxide in the structure.

6. CHAPTER CONCLUSIONS

This work leads to a large list of conclusions with both scientific and technological interests. Nevertheless, some of the most relevant conclusions and thoughts are now exposed.

Two technologically applied materials - one SMM and a SMC – have been first structurally studied. It has been found a difference on particle diameter (100 μm for the SMM, and 200 μm for the SMC), but the core composition is exactly the same (pure Fe). However, the SMC sample contains a phosphate-based shell with proved isolating behaviour. From the static magnetic measurements, a wide distribution of energy barriers has been detected in both samples, and an almost identical *M*(*H*) behaviour. Furthermore, the hysteresis area was not observed in any of these samples, what is of great interest to be applied as a soft magnet.

The most surprising result has been to find that these samples do not show any hysteresis from 20 K to 300 K. Even with the application of pulsed magnetic fields, their *M*(*H*) cycle keeps univariable. The complete reversibility of the *M*(*H*) measurements is opposed to the irreversibility measured in the ZFC-FC all over the temperature range. We have still not found a physical explanation to this phenomenon and we will keep working on that.

The magnetic properties of the SMM and SMC have been characterized from 1 kHz to 13 MHz. There, the higher permeability of the Fe core has been proved, whereas the SMC has a better frequency stability due to the isolating phosphate shell. This shell reduces the formation of eddy currents between particles, thus lowering the energy losses. The effect of the particle size has been observed: bigger particles increase the static permeability, while the smaller ones shift the spectra to higher frequencies. It is explained as an increase of the interparticle resistance due to the break on the crystal homogeneity when particles are small. The power losses of the SMM and SMC have also been characterized. As it could be expected from the previous results, SMM has higher energy losses until the SMC relaxation at around 0.3 GHz.

An interesting contribution to this field has been the formulation of two novel SMCs by using the basic Fe micrometer cores. The first, based on the mixture of these Fe cores with magnetic Fe_3O_4 nanoparticles, has shown better distribution of the nanoparticles when the mixture process has been assisted by microwaves. Furthermore, this material has presented a high relaxation frequency (higher than that of the SMC) but low permeability. On the other hand, the second design has consisted on the oxidation under air atmosphere of the iron power to produce an oxide shell. These samples have shown a large variety of properties depending on the preparation conditions (temperature and time), that make them a versatile material which can be adapted to specific requirements. Moreover, it is competitive in green form with the current SMC when the oxidation is produced in the range from 250 °C to 275° for long times (from 1 to 3 hours).

The stability of the proposed materials during the annealing process is not as good as the one of the SMC, which is able to increase its permeability and almost maintain the relaxation frequency. The two new formulation have increased its static permeability during the annealing, but the frequency stability has considerably decreased.

An important conclusion here is the importance of the phosphate shell in the SMC and its homogeneity. Despite the new materials are competitive with the SMC in the green form, their shell is not able to protect the core and the properties are lost. At this point, it is crucial to fabricate a homogeneous shell around the core.

7. FUTURE WORK

The number of interesting conclusions obtained from this chapter is comparable with the opportunities that have emerged and the questions that remain unresolved. If three main working routes should be chosen for going on with this research field, they would be the ones described below.

First, an immense question mark remains on the understanding of the reversibility paradigm. Its reversibility has been found in many different experiments in extreme conditions, in terms of temperature and sweeping rates of H. Additional measurements should be performed to understand the magnetization dynamics of this system from a low scale point of view in order to give some light to this question.

Secondly, it is mandatory to find a suitable process to have homogeneous shells surrounding the Fe cores in the new formulations, either by nanoparticles or oxidation mechanisms. In the first case, organic ligands could be useful in order to attach the nanoparticles to the Fe core. Furthermore, it would be excellent if these ligands could be removed during the annealing process. In the case of the oxidation of Fe cores, it seems from our results that the direction that must be investigated goes through small temperatures and long oxidation times. However, we need to ensure a regular oxidation of the particle surface. Here, gas flow mechanisms - where the particles are suspended in hot air - could be useful.

Finally, it is important to understand why the frequency stability is damaged during the annealing process. This is a key step in order to be able to design an adequate annealing process for the new materials, which have shown better properties than the SMC in green form.

Therefore, this is the last step that needs to be achieved before they can be technologically applied.

8. REFERENCES

[1] A. M. Leary, P. R. Ohodnicki, and M. E. Mchenry, "Soft magnetic materials in high-frequency, high-power conversion applications," *Jom*, vol. 64, no. 7, pp. 772–781, 2012.

[2] L. Hegedus *et al.*, "Energy Losses in Composite Materials Based on Two Ferromagnets," *IEEE Trans. Magn.*, vol. 53, no. 12, 2017.

[3] P. Kollár, Z. Birčáková, J. Füzer, R. Bureš, and M. Fáberová, "Power loss separation in Fe-based composite materials," *J. Magn. Magn. Mater.*, vol. 327, pp. 146–150, 2013.

[4] N. Igarashi, M. Uozumi, T. Kosuge, A. Sato, K. Kusawake, and K. Yamaguchi, "Pure iron based soft magnetic composite core that enables downsizing automotive reactors," *SEI Tech. Rev.*, no. 80, pp. 98–103, 2015.

[5] B. D. Cullity and C. D. Graham, *Introduction to Magnetic Materials*, 2nd ed. New Jersey: John Wiley & Sons, Inc, 2009.

[6] K. J. Sunday and M. L. Taheri, "Soft magnetic composites: recent advancements in the technology," *Met. Powder Rep.*, vol. 72, no. 6, pp. 425–429, 2017.

[7] V. Girman, "Characterization of composite materials based on Fe powder (core) and phenol – formaldehyde resin (shell) modified with nanometer- sized SiO 2," vol. 37, no. 2, pp. 167–177, 2014.

[8] D. Liu, S. Gao, Y. Zhang, S. Yu, and F. Wang, "Microstructural and compositional evolution of core-shell FeSiAl composites during high-temperature annealing," *Ceram. Int.*, no. July, pp. 0–1, 2019.

[9] A. H. Taghvaei, H. Shokrollahi, and K. Janghorban, "Properties of iron-based soft magnetic composite with iron phosphate-silane insulation coating," *J. Alloys Compd.*, vol. 481, no. 1–2, pp. 681–686, 2009.

[10] H. Shokrollahi and K. Janghorban, “Soft magnetic composite materials (SMCs),” *J. Mater. Process. Technol.*, vol. 189, no. 1–3, pp. 1–12, 2007.

[11] T. Ueno, H. Tsuruta, T. Saito, A. Watanabe, T. Ishimine, and K. Yamada, “Practical and potential applications of soft magnetic powder cores with superior magnetic properties,” *SEI Tech. Rev.*, no. 82, pp. 9–15, 2016.

[12] J. A. Bas, J. A. Calero, and M. J. Dougan, “Sintered soft magnetic materials. Properties and applications,” *J. Magn. Magn. Mater.*, vol. 254, no. 255, pp. 391–398, 2003.

[13] M. Huang, C. Wu, Y. Jiang, and M. Yan, “Evolution of phosphate coatings during high-temperature annealing and its influence on the Fe and FeSiAl soft magnetic composites,” *J. Alloys Compd.*, vol. 644, pp. 124–130, 2015.

[14] O. Gutfleisch, M. A. Willard, E. Br??ck, C. H. Chen, S. G. Sankar, and J. P. Liu, “Magnetic materials and devices for the 21st century: Stronger, lighter, and more energy efficient,” *Adv. Mater.*, vol. 23, no. 7, pp. 821–842, 2011.

[15] M. Huang, C. Wu, Y. Jiang, and M. Yan, “Evolution of phosphate coatings during high-temperature annealing and its influence on the Fe and FeSiAl soft magnetic composites,” *J. Alloys Compd.*, vol. 644, pp. 124–130, 2015.

[16] E. Martinez, L. Lopez-Diaz, and L. Torres, “Nonphenomenological damping constant due to eddy current losses in uniformly magnetized samples,” *J. Appl. Phys.*, vol. 99, no. 12, 2006.

[17] L. Jylhä and A. Sihvola, “Equation for the effective permittivity of particle-filled composites for material design applications,” *J. Phys. D. Appl. Phys.*, vol. 40, no. 16, pp. 4966–4973, 2007.

[18] H.-M. Chang and C. Liao, “A Parallel Derivation to the Maxwell-Garnett Formula for the Magnetic Permeability of Mixed Materials,” *World J. Condens. Matter Phys.*, vol. 01, no. 02, pp. 55–58, 2011.

[19] G. R. Gavalas, “Comparison of effective conductivities calculated by the effective medium approximation and the self consistent approximation for core-shell particulate composites,” *AIP Adv.*,

vol. 7, no. 9, p. 095222, 2017.

[20] J. L. Snoek, "Dispersion and absorption in magnetic ferrites at frequencies above one Mc/s," *Physica*, vol. 14, no. 4, pp. 207–2017, 1948.

[21] R. Lebourgeois, C. Le Fur, M. Labeyrie, M. Paté, and J. P. Ganne, "Permeability mechanisms in high frequency polycrystalline ferrites," *J. Magn. Magn. Mater.*, vol. 160, pp. 329–332, 1996.

[22] T. Nakamura, "Snoek's limit in high-frequency permeability of polycrystalline Ni – Zn , Mg – Zn , and Ni – Zn – Cu spinel ferrites," *J. Appl. Phys.*, vol. 88, no. 1, p. 348, 2000.

[23] F. Colaiori, G. Durin, and S. Zapperi, "Eddy current damping of a moving domain wall: Beyond the quasistatic approximation," *Phys. Rev. B - Condens. Matter Mater. Phys.*, vol. 76, no. 22, pp. 1–7, 2007.

[24] V. P. Ponomar, "Synthesis and magnetic properties of magnetite prepared by chemical reduction from hematite of various particle sizes," *J. Alloys Compd.*, vol. 741, pp. 28–34, 2018.

CHAPTER VII

OPTICAL PROPERTIES IN THE THz FREQUENCY RANGE

1. INTRODUCTION

As it has been previously discussed in Chapter II, metal oxides comprise a broad family of materials with wide variety of properties depending on their chemical composition and crystal structure. Their applications go from precursors for further chemical process to more advanced applications as energy storage, gas sensors, pigments, or food packaging, for instance [1]–[3]. More specifically, CuO and ZnO are two different semiconductor oxides, p-type and n-type respectively. ZnO most stable structure is *wurtzite*, which is a hexagonal structure where both the oxygen and zinc are tetrahedrally coordinated [4]. On the other hand, CuO presents a monoclinic structure known as *tenorite* [5].

Despite the dielectric properties of these oxides are of interest across the electromagnetic spectrum, their characterization in the terahertz (THz) frequency range is of interest for several applications in non-destructive evaluation, process monitoring, sensing, and spectroscopy. THz time-domain spectroscopy (THz-TDS) is commonly used to determine their optical constants, in particular the refractive index, absorption coefficient, complex permittivity, and frequency-dependent conductivity. Numerous works in this field have used this technique to characterize explosives [6], [7], drugs [8], organic [9]–[11], ceramic [12]–[14], and composite materials [15].

At the same time, it is important to note that measuring the optical constants of powders is not without difficulty of interpretation. Due to the high attenuation of this kind of materials, powder samples are usually dispersed in a well characterized matrix material. For low filling factors, scattering and diffuse effects are minimized and for particle size much smaller than the optical wavelength - and assuming spherical particles – one can apply Maxwell- Garnet (MG) theory or other Effective Medium Models (EMMs) to extract the optical constants of the powder constituent. The values inferred for the powder may differ from those of the bulk material. This may be in part be due to modification of the optical constants linked to the micro or nanostructure but may also be due to limited applicability of the EMM theory to a given sample.

In this chapter, the optical constants of two semiconductor powder samples (ZnO and CuO) are investigated by means of THz-TDS. A set of different samples have been prepared by dispersing different oxide quantities in polyethylene (PE) powder to fabricate pellets. The particle size of the powder samples, as well as their dispersion in the PE matrix, is analysed by SEM and EDS in order to discuss the respective contributions to the THz measurement. The analysis provides frequency-dependent complex dielectric constant from ~180 GHz to 3 THz. Furthermore, the repercussion of the pellets’ porosity on the THz-TDS results is analysed and discussed.

Despite we have also measured magnetic samples (Fe_3O_4), here only the results obtained for the semiconductor samples are presented. The magnetic results are discarded because the Fresnel model [16] - which is the basis for the interpretation of the signal attenuation – assumes $\mu_r = 1$. That is manifestly wrong for Fe_3O_4, and by this way all the signal attenuation would be associated to the dielectric component, and thus omitting the magnetic contribution.

All the processes and results presented in this chapter are the result of a 5-months research internship in the European campus of the Georgia Institute of Technology (Georgia Tech Lorraine) in Metz (France). This internship was done under the supervision of Prof. David S. Citrin and Dr. Alexandre Locquet. All the experiments have been carried out in the facilities of the Photonics and Terahertz Group, a research group from the School of Electrical and Computer Engineering.

Moreover, in this research project we had the opportunity to collaborate with Dr. Denis Bouscaud and Dr. Sophie Berveiller from the Laboratoire d'Etude des Microstructures et de Mécanique des Matériaux of the Université de Lorraine in Metz, who were the responsible for manufacturing the pellets and performing their structural characterization.

2. CHAPTER OBJECTIVES

The most important goal in this part of the work is to define a methodology for the sample preparation, measurement, and signal processing to precisely calculate the optical and dielectric properties of the sample. Then, we wish to know and analyse the optical response of ZnO and CuO in the THz frequency range.

Additionally, we pretend to discuss the suitableness of the MG theory to deduce the inclusions' properties from the measured mixture with our samples. With that in mind, we also aim to understand which are the strengths and limitations of this approach.

Finally, the potential effect of the intrinsic porosity in the fabricated pellets wants to be checked. As the size and shape of the pores in the sample is difficult to be predicted, we also wish to test which of the most common EMMs functions best accounts for this effect.

3. PELLETS FABRICATION AND INSPECTION

The ZnO and CuO powder samples have been manually mixed with PE powder and filled into a 13-mm diameter evacuable pellet die. A force of 25 kN has been used to compress the powders and fabricate the pellets. The pellets' height tends to be around 3.5 mm, but it depends on the exact mass used. For a more detailed description of the process and materials used, see Chapter III.

A batch of pellets with different filling factors has been prepared for each material in order to study how the optical properties depend on the oxide fraction. In Table 7. 1 the characteristics of these pellets are specified.

Table 7. 1. Physical characteristics of the fabricated pellets. All are made of PE and pressed under 25 kN.

Sample Name	**Oxide Inclusions**	**Weight Filling Factor, f_W (%)**	**Volume Filling Factor, f_V (%)**	**Experimental Density, ρ (g/cm^3)**	**Porosity, P (%)**
PE_ref	None	0.0	0.0	0.81	13.8
ZnO_02.5	ZnO	2.5	0.4	0.82	16.0
ZnO_05.0	ZnO	5.0	0.9	0.84	15.3
ZnO_10.0	ZnO	10.0	1.9	0.85	18.0
ZnO_20.0	ZnO	20.0	4.1	0.93	19.1
ZnO_30.0	ZnO	30.0	6.8	0.99	21.9
ZnO_40.0	ZnO	40.0	10.2	1.09	23.7
CuO_02.5	CuO	2.5	0.4	0.81	16.4
CuO_05.0	CuO	5.0	0.8	0.83	16.6
CuO_07.5	CuO	7.5	1.2	0.85	16.4
CuO_10.0	CuO	10.0	1.7	0.87	16.7
CuO_20.0	CuO	20.0	3.6	0.96	16.8
CuO_30.0	CuO	30.0	6.1	1.06	17.4
CuO_40.0	CuO	40.0	9.2	1.17	18.8

During the fabrication, the amount of oxide powder in each pellet has been controlled by the weight fraction (*weight filling factor*, f_W), but it has then been converted to volume fraction (*volume filling factor*, f_V) by using Equation 3.8. The porosity P can be calculated by comparing the experimentally measured density with the one expected for the oxide + PE mixture (see Equation 3.9 and the related constants used).

Before performing the THz-TDS measurements, the as-received powders have been investigated by SEM in order to know the particles' size and morphology. We need to do that to estimate the importance of the scattering and to ensure that the assumptions done by the MG theory are consistent with the morphology of the particles. Figure 7. 1 shows the SEM images of the PE, CuO, and ZnO powders.

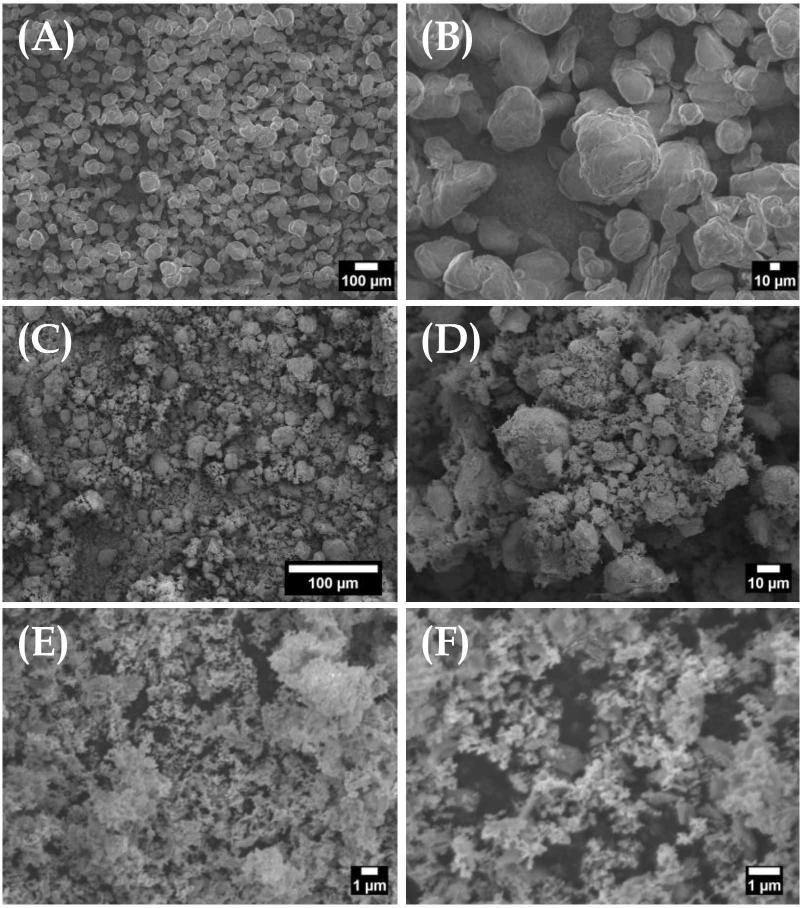

Figure 7. 1. SEM images of the PE (A and B), CuO (C and D) and ZnO (E and F) unconsolidated powders at various magnifications.

The initial particle shape in all cases is roughly spherical with a diameter lower than 100 µm. The PE particles (Figure 7. 1.A and B) are the largest, and we expect it to deform during the compaction and to provide an approximately uniform (though porous) matrix. In addition, the particles are almost spherical shaped in this case. In Figure 7. 1.C and D, which shows the CuO powder, it is possible to appreciate that all the particles are below 50 µm in diameter. Note that these particles are non-spherical and form porous aggregates, which probably appear by sintering of the smaller particles during thermal processes. Despite their aspherical shape, we assume the validity of the MG theory due to their isotropic distribution. Lastly, in Figure 7. 1.A and B we observe that ZnO particles are much smaller than the CuO ones. These particles are of nanometric dimensions, and in most cases form aggregates of 10 µm in size. Despite the nanometric particles seem to be spherical shaped, the formed aggregates have dispersed morphologies. This may impact the validity of the MG theory in this sample.

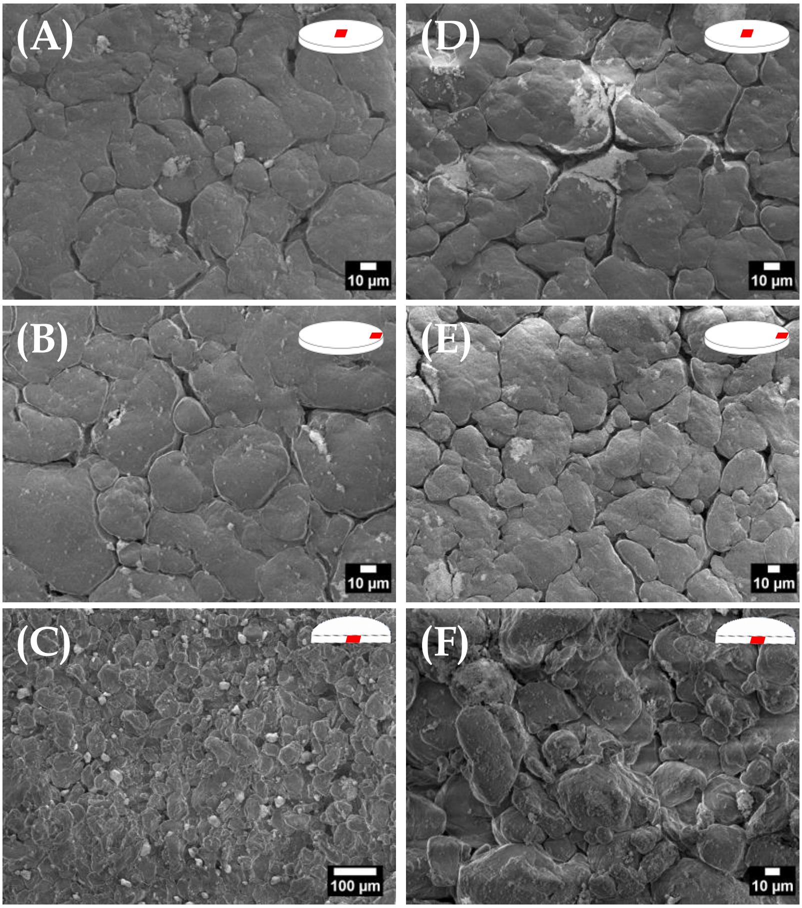

Figure 7. 2. SEM images of the pressed CuO_10.0 sample in the centre (A) and the edge (B) of the pellet surface, and on the cross section on a cut through the pellet (C). ZnO_10.0 sample SEM images in the centre (D) and the edge (E) of the pellet surface, and the cross section on a cut through the pellet (F).

The fabricated pellets have also been investigated in order to determine the dispersion of the oxide powder, and the results are shown in Figure 7. 2. In these images, the distribution of the powder particles is observed through different surfaces in the pellet. In the CuO_10.0 pellet (Figure 7. 2.A-C) the porosity seems qualitatively consistent with the calculated *P* in Table 7. 1. The CuO powder appears to be reasonably homogeneously distributed throughout the sample volume. On the other hand, Figure 7. 2.D-F show the disposal of the ZnO on the ZnO_10.0 pellet. Despite the size of the aggregates is lower than 10 µm, here their distribution is not as regular as in the previous case. The cross section (Figure 7. 2.F) suggests a high degree of homogeneity of the oxide particle distribution within the pellet.

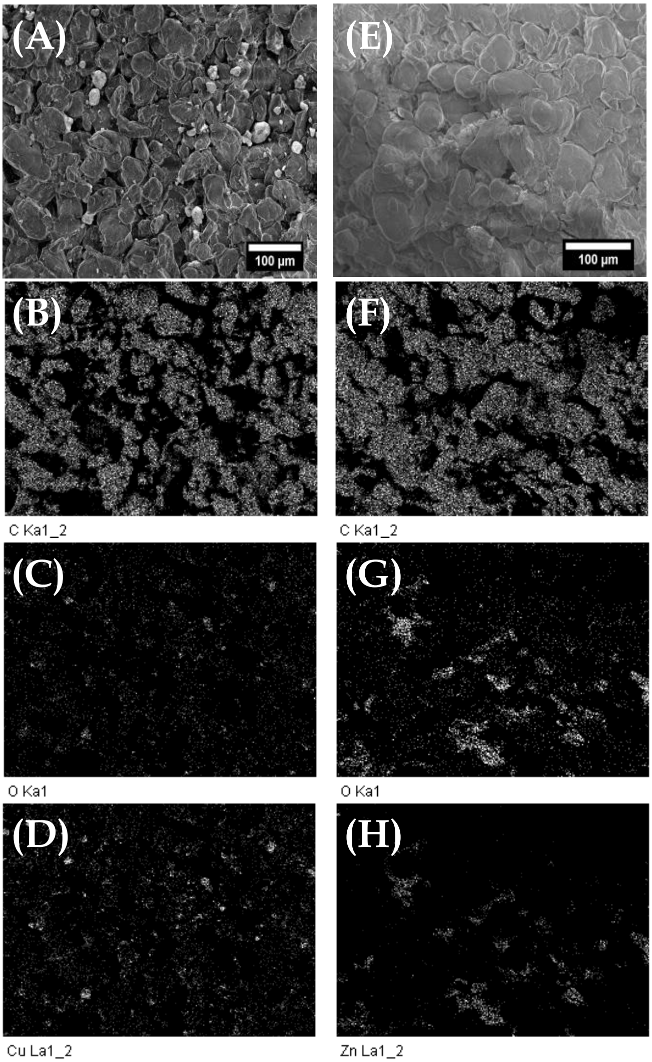

Figure 7. 3. Cross-section SEM and EDS images. CuO_10.0 pellet: (A) SEM, (B) EDS map of C distribution, (C) EDS map of O distribution, and (D) EDS map of Cu distribution; ZnO_10.0 pellet: (E) SEM, (F) EDS map of C distribution, (G) EDS map of O distribution, and (H) EDS map of Cu distribution. EDS maps have the same magnification as their corresponding SEM images.

Finally, we performed a two-dimensional EDS analysis on the cross-section surface of each one of these pellets in order to study the distribution of the chemical species on the sample. The results are shown in Figure 7. 3, where the left columns (Figure 7. 3.A-D) correspond to the CuO_10.0 pellet, while the one in the right side (Figure 7. 3.E-H) contains the images obtained for the ZnO_10.0 sample.

The carbon distribution (corresponding to the PE matrix) is regular and homogeneous in all the analysed surface in both samples. Furthermore, notice that the oxygen and the metal (Cu and Zn, respectively) distributions agree in each sample, thus mapping the metal oxide though the sample. A high degree of homogeneity is seen in CuO_10.0. The overall homogeneity is also high in ZnO_10.0, despite we note some small-scale features corresponding to the aggregation previously seen in secondary electrons' images.

We therefore conclude that homogeneity of the oxide particle dispersion in PE is sufficiently high so that measurements obtained from a specific point on the pellet (constrained by the sample holder) are representative of the entire pellet.

4. TERAHERTZ CHARACTERIZATION

The optical and dielectric properties in the THz frequency range of the fabricated pellets have been finally measured in the transmission mode by means of a *TeraView TPS Spectra* device. The cavity where the sample is placed has been always purged with N_2 to avoid water absorption abortion lines. Moreover, 1800 measurements have been averaged in each analysis. For further details about the procedure and conditions used in the measurement, see Chapter III. The time domain (TD) spectra obtained from the measurements are presented in Figure 7. 4.

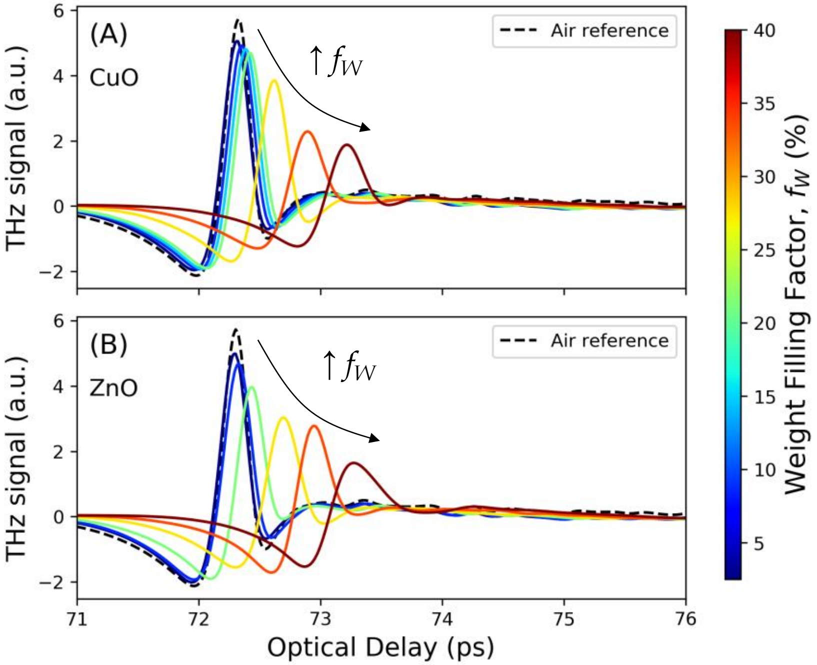

Figure 7. 4. THz signals of (A) CuO and (B) ZnO particles dispersed in PE pellets for various weight filling factors f_w.

Not surprisingly, the THz pulse amplitude decreases as f_W increases, thus indicating attenuation as well as increased reflection associated with the Fresnel coefficient; the pulse time delay also raises proving an increased refractive index in those pellets with a higher oxide content. Additionally, pellets containing either oxide powder are less transmissive than pure PE, as it was expected. The frequency dependence of the transmitted THz pulses is shown in Figure 7. 5.

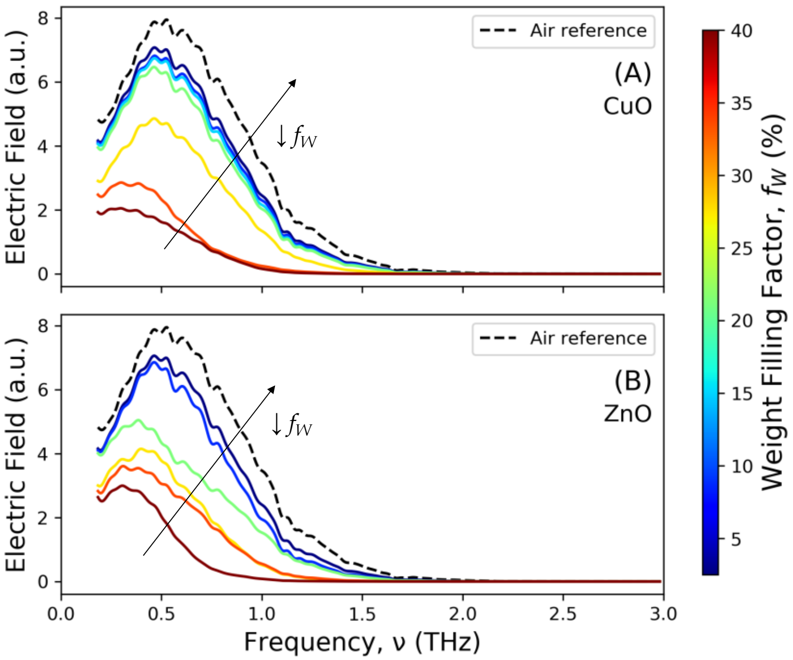

Figure 7. 5. Frequency-dependence power spectrum of the transmitted THz pulses for (A) CuO and (B) ZnO powders in PE pellets for various f_w.

In both samples it is seen a clear reduction tendency of the signal amplitude when increasing f_W, which reflects the higher attenuation of the oxides compared with PE, and the importance of having worked in the low filling factor region. It is important to mention that no pronounced absorption lines are detected for any of the pellets in this frequency range, as the lowest far-infrared-active modes in CuO are at and above 12.96 THz [17], while those in ZnO are at or above 13.11 THz [18], [19]. THz absorption features in PE are expected to be spectrally diffuse as polymers rarely show pronounced features in the measurement bandwidth.

From the FD data is now possible to deduce the optical constants. Equation 2.107 and Equation 2.108 have been used to calculate the refractive index n and the absorption coefficient α, respectively. In the following, the term *effective* is used to describe the apparent optical constants for the pellets (PE + oxide) in contrast to the values extracted for the oxides (inclusions).

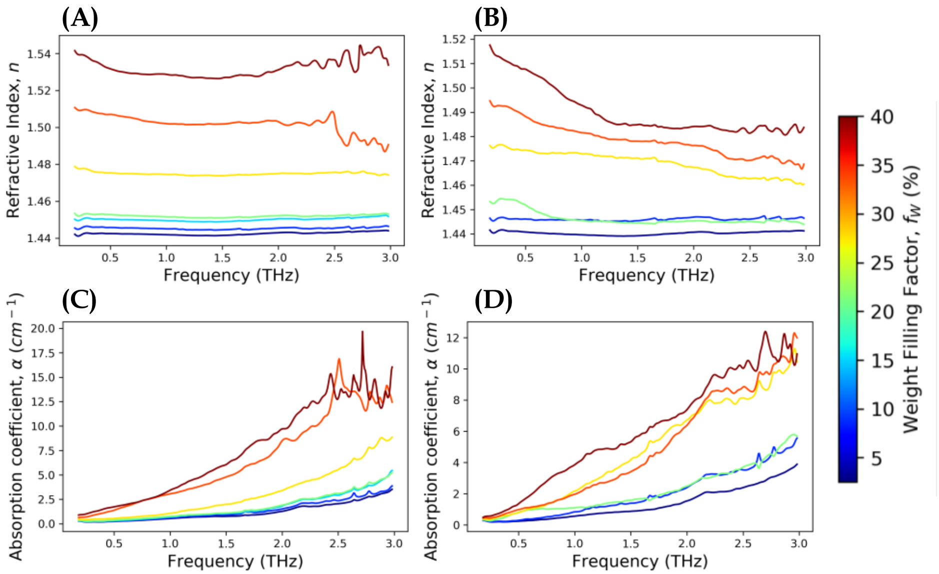

Figure 7. 6. Effective optical constants for the pellets directly extracted from experimental data. Effective refractive index *n* for (A) CuO and (B) ZnO pellets, and effective absorption coefficient α for (C) CuO and (D) ZnO pellets with various weight filling factors f_w.

Figure 7. 6.A and B show refractive indices $n(\nu)$ which are almost constant within the experimental bandwidth. On the other hand, it is seen a characteristic power-law increase of the absorption coefficient $\alpha(\nu)$ with frequency [11], [12]. Of note, features observed above ~2 THz are attributed largely to the low SNR.

The real and imaginary components of the relative dielectric permittivity ($\varepsilon_r'(\nu)$, $\varepsilon_r''(\nu)$) have been then calculated by means of Equation 2.100 and Equation 2.111, and the results are shown below. As it can be seen in Figure 7. 7, the real component $\varepsilon_r'(\nu)$ presents a similar behaviour than $n(\nu)$, with practically no change along the measured frequency range. On the other hand, Figure 7. 8 reveals that the imaginary component $\varepsilon_r''(\nu)$ has the same power-law increase as it has been previously seen for $\alpha(\nu)$. Then, these effective values have been used in the MG theory to calculate the inclusions' (i.e. oxides') permittivity all along the measured frequency range. One inclusions' value is obtained from the f_V effective permittivity at each frequency by the MG model. The mean and standard deviation has been calculated at each point. The results, which represent the dielectric properties of the pure oxide, are represented in the top part of each figure.

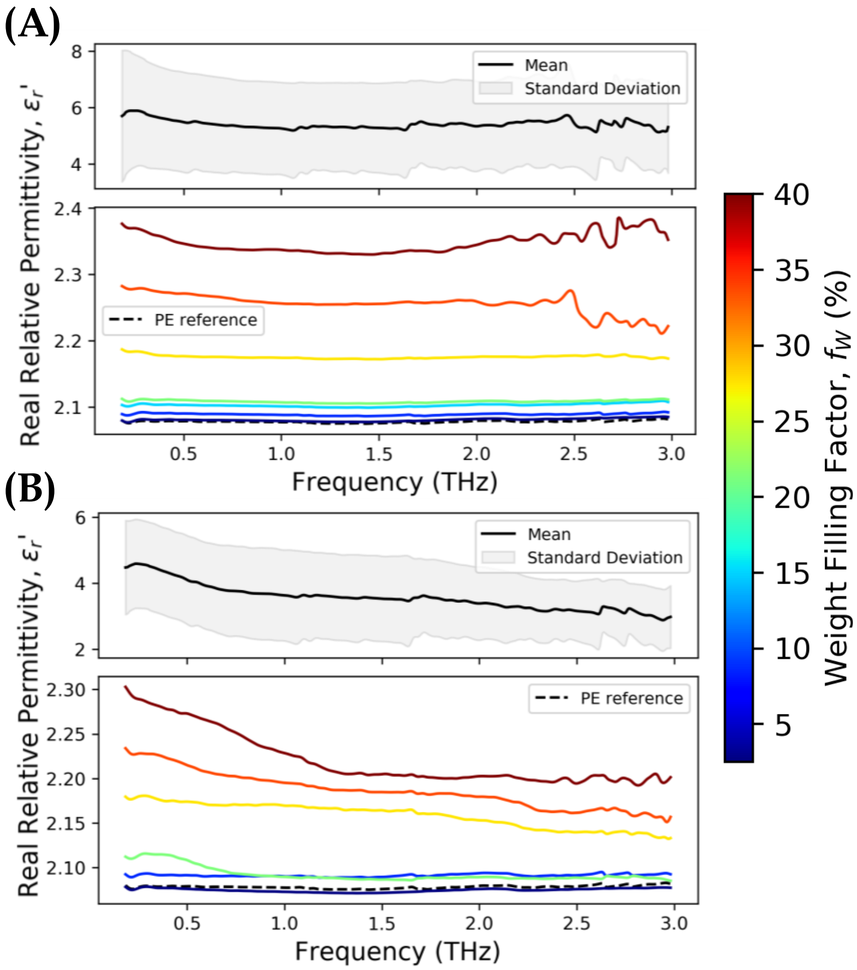

Figure 7. 7. ε_r' for (A) CuO and (B) ZnO pellets, for various f_w. In the top plots the properties of the inclusion oxides are represented after being calculated by MG theory. The standard deviation of mean values is represented by the shaded grey area in the top panels.

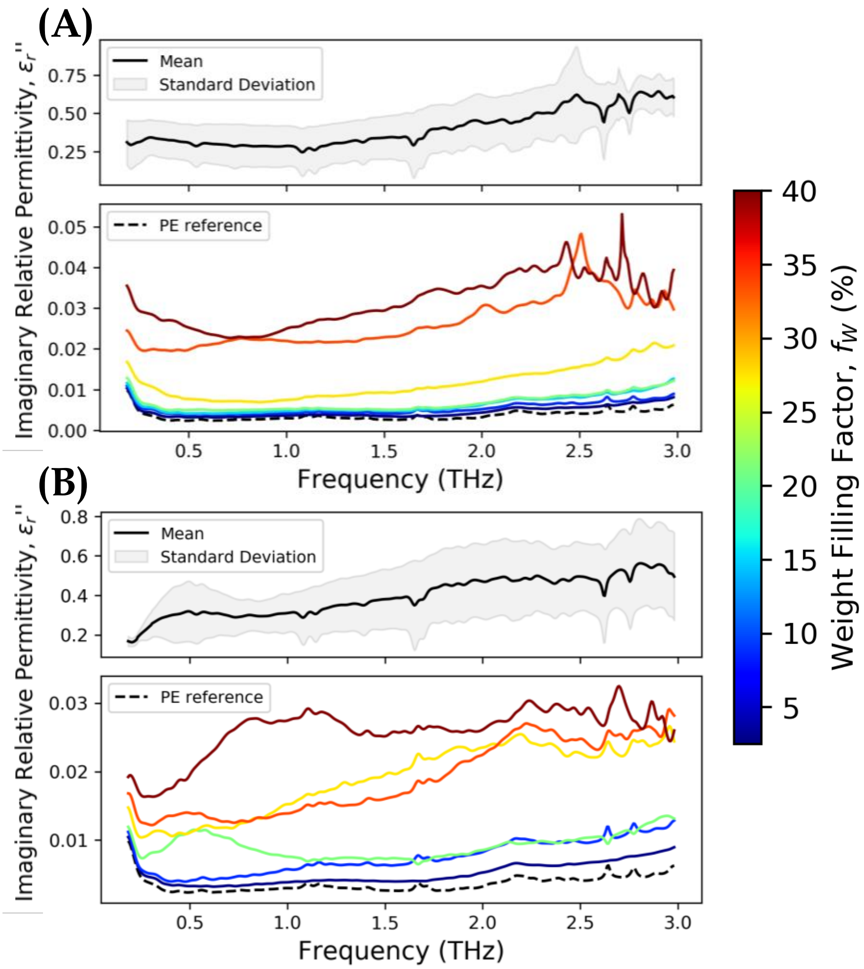

Figure 7. 8. ε_r'' for (A) CuO and (D) ZnO pellets, for various f_w. In the top plots the properties of the inclusion oxides are represented after being calculated by MG theory. The standard deviation of mean values is represented by the shaded grey area in the top panels.

Moreover, a graphical comparison between the obtained dielectric properties for CuO and ZnO is given in Figure 7. 9. There, the constant tendency of $n(\nu)$ and $\varepsilon_r'(\nu)$, and the power-law increase in $\alpha(\nu)$ and $\varepsilon_r''(\nu)$ are better observed. Furthermore, CuO has higher $n(\nu)$ and $\varepsilon_r'(\nu)$ values than ZnO. The extracted mean values for these - almost frequency independent - properties are given in Table 7. 2. On the other hand, ZnO presents higher absorption coefficient values than CuO in this frequency range. Both materials have a similar behaviour in $\varepsilon_r''(\nu)$.

Table 7. 2. Inclusions' mean real permittivity ε_r' and refractive index n calculated by the MG model.

Material	ε_r'	n
CuO	5.41	2.30
ZnO	3.55	1.85

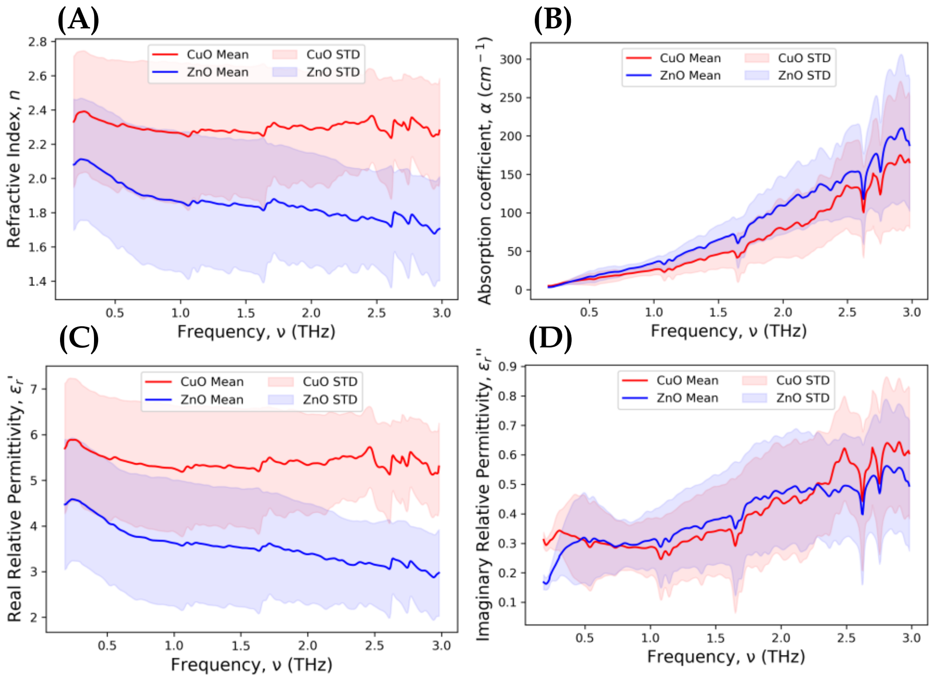

Figure 7. 9. CuO and ZnO optical properties between 0.18 and 3 THz: (A) refractive index n, (B) absorption coefficient α, (C) real relative permittivity ε′, and (D) imaginary relative permittivity ε′′. All the represented optical properties correspond to the oxide inclusions.

Both CuO and ZnO are anisotropic crystals, which means that the dielectric properties must be described by tensors, and a number of measurements of the optical constants in the THz regime have been made on single crystals of these materials [20]–[24]. Since our powder samples are randomly oriented (as it has been previously proved by SEM) they can be considered macroscopically isotropic, leading to an absence of birefringence.

Reference [23] reports room temperature ordinary and extraordinary refractive indices close to 3 with birefringence ≲ 2% with total dispersion

$\lesssim 2\%$ in the frequency range from 500 GHz to 2 THz. Contrary to the behaviour we have described in Figure 7. 9, this reference describes an increase of refractive index with frequency. The reported values for refractive index in CuO [23], [24] tend to be higher than our calculated value (2.3). Birefringence in single crystals is small, so that our neglect of anisotropy of the underlying crystals does not appear to be able to account for the discrepancies.

In recent studies on CuO films, Alqahtani *et al.* [25] obtained values of n around 1.5; meanwhile Dolai *et al.* [26] found values around 3.5 and ε_r' close to 11. Clearly, there is a large range of values reported for various types of samples, and morphology as well as the method of parameter extraction surely play a role in contributing to this range.

The absorption coefficients in [23] appear to obey Jonscher's universal power law (see below). They report a similar frequency dependence of the absorption coefficient for CuO to the one we have, reaching values around 25 cm^{-1} at 1 THz.

Fujii *et al.* [22] report $\varepsilon_r' \sim 8$, and in Azad *et al.* [21] $n \sim 2.8$ for ZnO. The room-temperature ordinary and extraordinary refractive indices of ZnO in the THz range have been measured to be 2.67 and 2.84, respectively, from 180 GHz to 1.25 THz with little dispersion [20]. There appears thus to be a discrepancy between these reported values and ours (Table 2). The absorption coefficient of ZnO measured in reference [20] also obeys Jonscher's law, but overall with considerably lower absorption. Again, scattering as well as the different crystal structure may play a role in the differences in the values.

In the paper [20], however, reported values for α are almost an order of magnitude lower than ours. The role of scattering in our experiment due to the intrinsically inhomogeneous nature of particles pressed into pellets may account for the much higher value of attenuation we infer for ZnO.

Another possible source of the differences between the values we infer from the pressed pellets and measurements made on single crystals may stem from differences in the optical constants of the particles themselves with respect to bulk. Onwudiwe *et al.* [27] and Rehman *et al.* [28] both reported ε_r' values around 3.5 in the MHz and GHz ranges for ZnO nano- and microspheres, respectively, which is close to the value we infer from the pressed pellets. Measurements of particles well outside our frequency range exist [29] though comparisons with our work may have limited meaning.

Finally, $\varepsilon_r''(\nu)$ and Equation 2.112 have been used to calculate the electric conductivity of the material. The obtained σ data has been fitted to the *Jonscher's universal power law* (Equation 7. 1), which is generally used to describe the frequency dependence of conductivity [30].

$$\sigma_{AC} = \sigma_0 + A\omega^n \qquad \text{Equation 7. 1}$$

where σ_0 is the zero-frequency electrical conductivity, and the pre-factor A (not electric-field amplitude here) and exponent n (not refractive index here) depend on the material and temperature. The value of n is smaller than unity when the conductivity is dominated by the long-range movement of charge carriers; meanwhile it is larger than 1 when short-range hopping dominates transport [31]–[34] . The experimental data, as well as the best fit with this law, for each material are shown in Figure 7. 10.

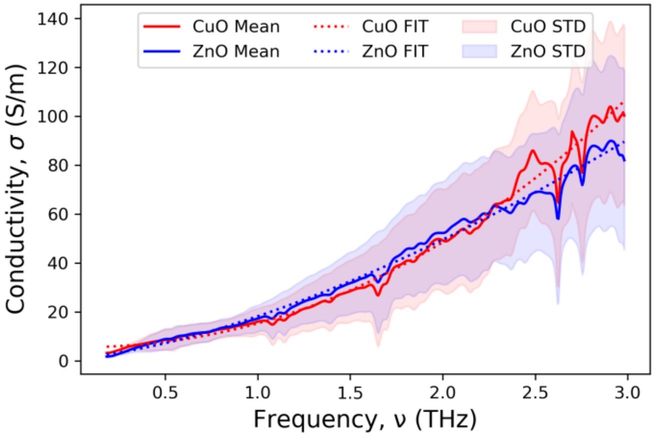

Figure 7. 10. Oxide conductivity σ inferred from pressed-pellet samples. Solid lines represent the average values, shaded regions indicate the standard deviation, and dashed lines show the fit to Jonscher's model for each oxide.

The agreement between the experimental data and the Jonscher's power law is notable. As it could be expected from the previously exposed results for α, ZnO presents a slightly higher electrical conductivity until approximately 2.3 THz. The best-fit parameters obtained from the Jonscher's model fitting are listed in Table 7. 3.

Table 7. 3. Jonscher's law fitting values.

Material	**σ_0 (S/m)**	**A**	**n**
CuO	9.26	17.0	2.10
ZnO	4.66	28.7	1.47

The obtained n values reveal that the conductivity is mainly dominated by short-range hopping in both materials. Finally, we have checked the accuracy and adequacy of the MG calculation with our experimental results. To do so, in Figure 7. 11, the experimentally measured effective permittivity values with the ones calculated by the MG at each f_V are compared. For doing the calculation, we have considered an average PE real permittivity of 2.08, and CuO or ZnO inclusions, giving the parameters of Table 7. 2. With this simulation we are predicting the effective values that the pellets with different f_V should have to obtain the calculated inclusions' permittivity by the MG theory. We note a significant agreement between the experimental values and MG theory.

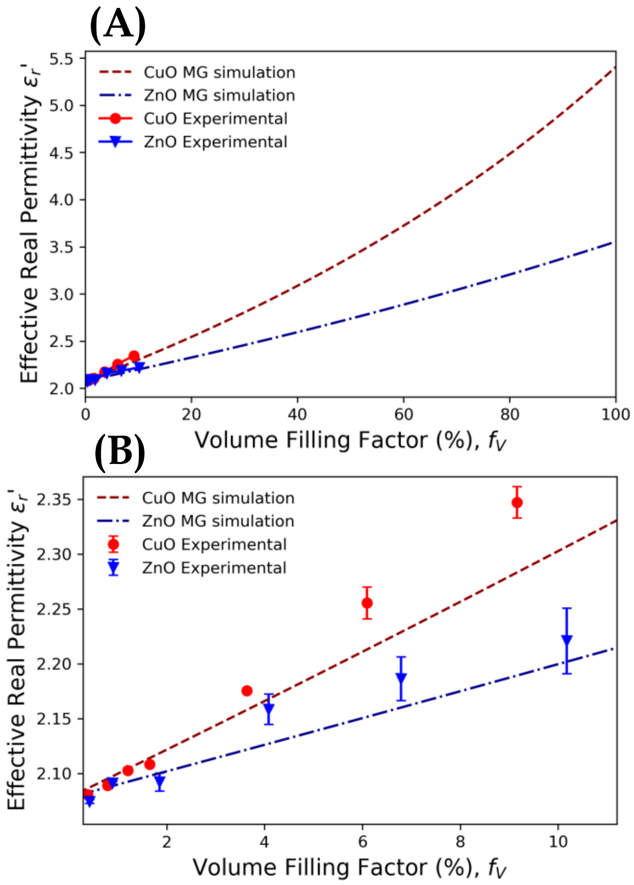

Figure 7. 11. Comparison between experimentally measured effective permittivity values for different f_v and MG theory for the entire range of f_v (A), and a zoomed image around the experimental values studied here (B).

A good agreement between the experimental data and the model is seen in Figure 7. 11.A. However, when the low f_V region is magnified (Figure 7. 11.B) it is possible to observe small deviations. This difference might be due to the non-perfectly spherical particles' shape (which is assumed by the MG model), scattering, or uncertainties due to the presence of air trapped in the pores inside the pellets. In general, the model slightly underestimates the permittivity of the oxide inclusions.

5. DISCUSSION ON THE POROSITY EFFECT

In the previous section the optical properties of both oxides have been investigated considering a biphasic system composed of PE and the corresponding oxide. However, there is a certain amount of air trapped in the pellets corresponding to the porosity reported in Table 7. 1. The values listed there are significant, as they represent between the 15% and 24% of the pellet volume. The dependence of the porosity *P* with f_W is shown in Figure 7. 12.

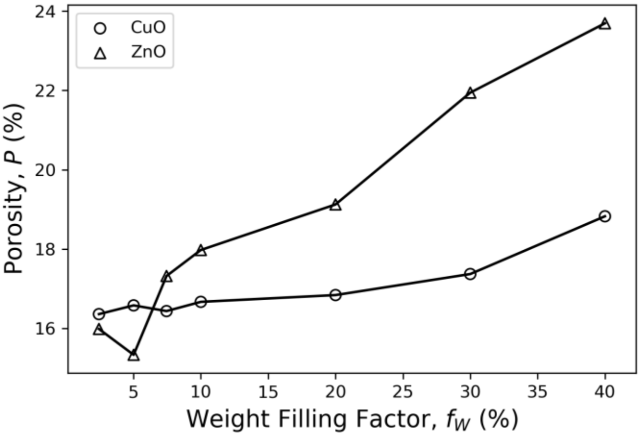

Figure 7. 12. Porosity *P* dependence on the weight fill factor f_W for the CuO (circles) and ZnO (triangles) pellets.

The porosity is similar at low f_W for both materials and tends to the one of the pure PE pellet (13.8%). Then, the higher amount of oxide the higher porosity in the pellet. This may be due to the lower elastic deformation that oxides suffer during the compaction, compared with PE. Once the pressure is removed, PE recovers part of the deformation while oxides keep unchanged. Despite the porosity could be almost null in the compaction instant, it can lead to empty spaces (pores) once it is removed and different recovery mechanisms take place.

Parrot *et al*. [35] previously discussed the repercussion of the remaining porosity on the measured THz optical properties. They proved differences of a 5% on the refractive index *n* when MG theory was applied on samples containing an 8 – 9 % of porosity. The obtained parameters tend to increase when the calculation considers it, because the absorbing phase represents a lower volume fraction.

In the case of our samples, where the porosity values go from 15% to 24%, the effect could be even more significant. This may be part of the reason why our results - reported in Table 7. 2 - are smaller than those found in literature. It can also explain the underestimation that the MG theory makes of the effective experimental results, in Figure 7. 11. For this reason, we propose a protocol - based on the application of the EMMs - to account for the trapped air in the pellet.

Our new approach consists on considering each pellet as a ternary system made of PE+oxide+air. Consequently, the f_V listed in Table 7. 1 are no longer true when describing the whole pellet. These f_V values corresponded to the volume fraction of oxide in the PE+oxide mixture. We now define the *real volume filling factor* f_V^R, which considers the relative oxide volume (f_V) only over the non-porous (100-P) volume. This new parameter is defined in Equation 7. 2.

$$f_V^R(\%) = (100 - P) \cdot f_V(\%) \qquad \text{Equation 7. 2}$$

Therefore, the filling factor in this new conception is smaller than before, and the sum of the volume fractions of the oxide [$f_V^R(\%)$], PE, and porosity [$P(\%)$] must result in a 100% of the volume. The new interpretation of volume distribution is graphically represented in Figure 7. 13.

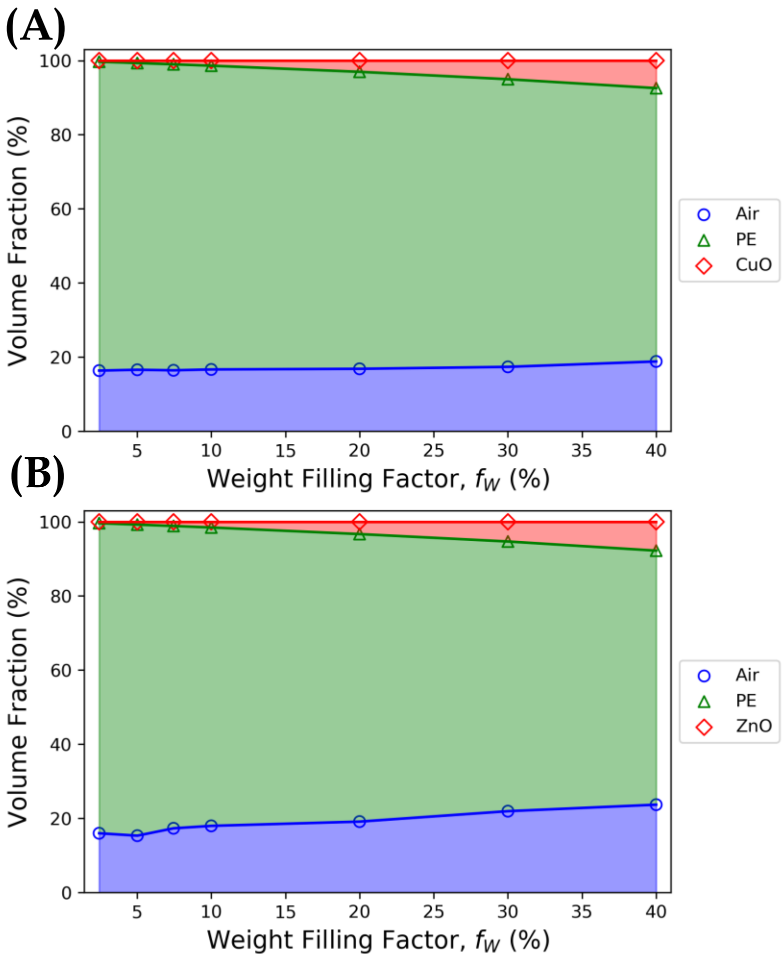

Figure 7. 13. Pellet's volume occupancy in (A) CuO, and (B) ZnO samples as a function of the weight filling factor.

In this figure, the % volume occupancy of each phase is clearly seen. Now we are considering that part of the volume in the sample is occupied by air. As stated before, this volume increases with f_W. In Table 7. 4 the new f_V^R values are listed and compared with f_V and P for each sample.

Table 7. 4. Re-calculated volume filling factors for the inclusions considering the porosity in each pellet.

Sample Name	**Volume Filling Factor, f_V (%)**	**Porosity, P (%)**	**Real Volume Filling Factor, f_V^R (%)**
PE_ref	0.0	13.8	0.0
ZnO_02.5	0.4	16.0	0.3
ZnO_05.0	0.9	15.3	0.7
ZnO_10.0	1.9	18.0	1.0
ZnO_20.0	4.1	19.1	1.4
ZnO_30.0	6.8	21.9	3.0
ZnO_40.0	10.2	23.7	5.0
CuO_02.5	0.4	16.4	7.4
CuO_05.0	0.8	16.6	0.4
CuO_07.5	1.2	16.4	1.1
CuO_10.0	1.7	16.7	1.5
CuO_20.0	3.6	16.8	3.3
CuO_30.0	6.1	17.4	5.3
CuO_40.0	9.2	18.8	7.8

Once the volume occupancy is clear, we have started to work with the EMMs models to calculate the dielectric properties of the oxides under the new consideration. The calculation consists in a two-steps process: (i) remove the air contribution from the sample in order to deduce the effective properties of the PE+oxide mixture (denoted as $\varepsilon_{eff}^{PE+Oxide}$). To do so, the corresponding EMM has been applied by considering the air as the inclusions (ε_r = 1), the porosity P as the filling factor, and the properties of the host are deduced. In this case, the host corresponds to the solid fraction of the pellet (PE+oxide) where the pores are distributed. Three different EMMs have been tested to account for the air: direct linear proportionality between phases $[f_V \cdot \varepsilon_i + (1 - f_V) \cdot \varepsilon_h]$, MG, and Bruggeman (BG). (ii) Deduce the oxide's properties from the $\varepsilon_{eff}^{PE+Oxide}$ previously deduced. The $\varepsilon_{eff}^{PE+Oxide}$ mixture results obtained by each model are considered as the effective permittivity in the EMM model later used to calculate the properties of the inclusions (ε^{Oxide}). As the situation has been reduced to a biphasic system in this second step, the filling factor considered here is f_V. This process is graphically schematized in Figure 7. 14. Notice that the second step is the one used for the standard ε^{Oxide} deduction. Thus, we simply propose to add a pre-calculation to remove the air contribution prior to the ε^{Oxide} deduction. If one does not want to account for the porosity, Step 1 should be removed and apply only Step 2 with the measured effective data.

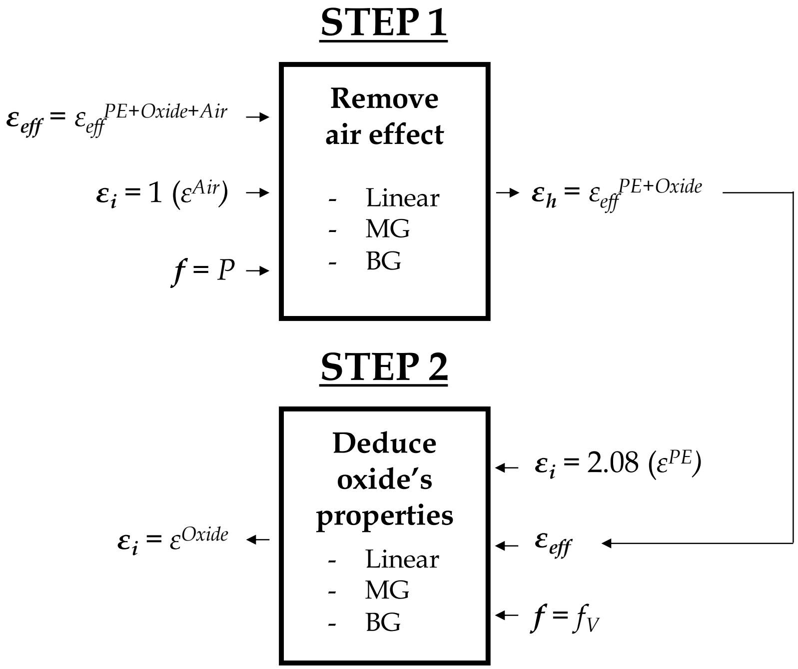

Figure 7. 14. Scheme of the two-steps process to remove the air effect in the pellets and then calculate the properties of the oxides.

The obtained $\varepsilon_{eff}^{PE+Oxide}$ results from the first step are shown in Figure 7. 15. First, the measured effective values ($\varepsilon_{eff}^{PE+Oxide+Air}$) are represented, which contain the porosity effect, and then the values obtained after removing the air contribution by the three proposed models. The difference in the effective real permittivity (ε_r') increases around a 10% when the air permittivity is considered. This is in good agreement with the increase observed by Parrot *et al.* [35]. Furthermore, the increase in ε_r' is higher when the porosity is considered by MG or BG than by a linear model. Overall, these results corroborate that the consideration of the air in the pellet may have a significant effect on the effective real permittivity.

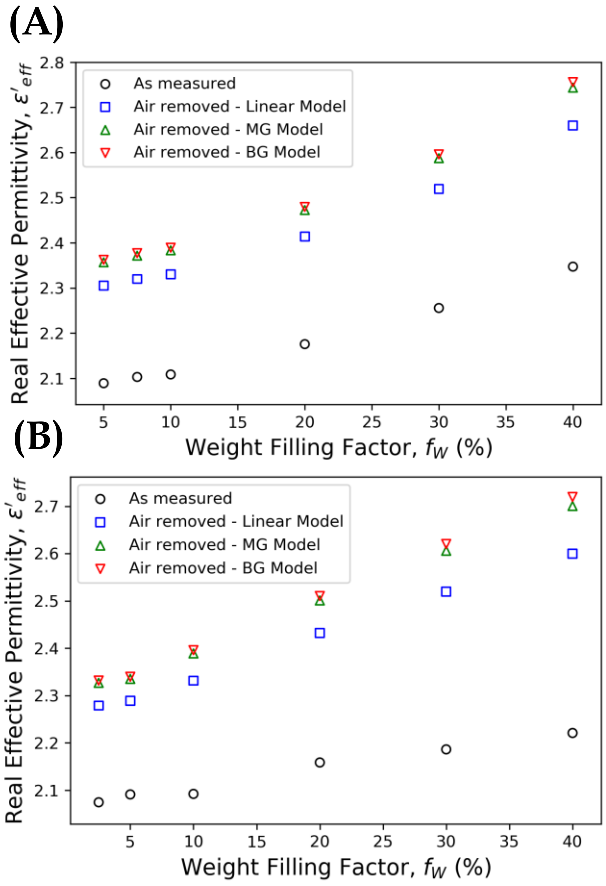

Figure 7. 15. Effective permittivity of the as measured pellets (black circle), and the linear (blue square), MG (green upper triangle), and BG (red lower triangle) EMMs considerations of the porosity, for (A) CuO and (B) ZnO samples.

The next step is to evaluate how this change in the effective properties affects to the deduced dielectric properties of the oxide after applying again an EMM. To do so and to determine which EMM better considers the oxide inclusions, we have searched for the inclusions' permittivity ε_i (i.e. ε^{Oxide}) that minimizes the difference between the experimental and the calculated effective values at each f_V. The host permittivity (ε_h) used for this calculation corresponds to the PE permittivity obtained by each of the models in Step 1. ε_i is the variable parameter that is tested until reaching the best fit. To compute the difference between the calculated and the experimental data, the *fitting error* (*FE*) parameter has been defined in Equation 7. 3.

$$FE = \frac{\sum_{j=1}^{n}\left(\varepsilon_j^{exp} - \varepsilon_j^{cal}\right)^2}{n} \quad \text{Equation 7. 3}$$

where n is the total number of samples, and ε_j^{exp} and ε_j^{cal} are the experimental and calculated values at each f_V.

The three EMMs here considered have been fitted to each set of $\varepsilon_{eff}^{PE+Oxide}$ values obtained from the air consideration in Step 1, i.e. leading to 9 different model calculations. Furthermore, the three models have also been adjusted to the measured raw effective data, where the air contribution has not been removed. Therefore, 12 different combinations of models have been investigated.

In order to check the adequacy of each combination of models, Figure 7. 16 compares the measured effective permittivity with the calculated one by each of the models.

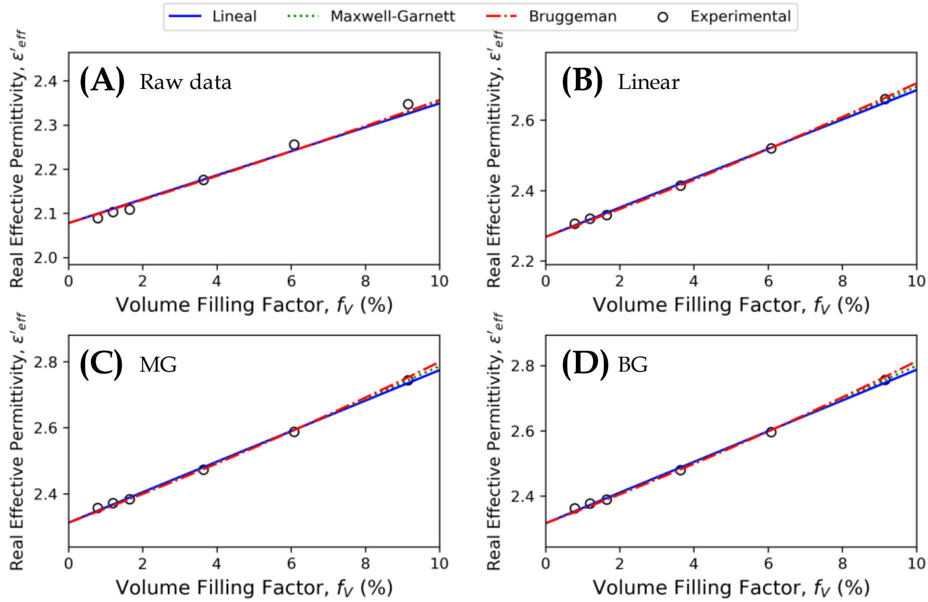

Figure 7. 16. Comparison between the models' simulations and the experimental data for CuO pellets. Linear (blue), Maxwell-Garnett (green), and Bruggeman (red) models are fitted with the effective experimental data. Each subplot contains the experimental values obtained from different air considerations: (A) without removing air contribution; (B) Linear; (C) Maxwell-Garnett; and (D) Bruggeman.

The agreement between the calculated and experimental data is good in all cases. It becomes difficult to determine which is the best model in each subplot (corresponding to one porosity interpretation). However, by comparing the fitting between subplots, it is possible to see how the fit is less accurate in Figure 7. 16.A than in the others. This subplot corresponds to the models' fitting to the measured raw data (without previously accounting for the air effect). Therefore, calculations of the optical and dielectric properties are less accurate if the air contribution is not first removed. Apart from this point, it is impossible to extract objective conclusions from these adjustments just by looking to the plots. For this reason, we have statistically interpreted the results by analysing the *FE* for each combination. Table 7. 5 summarizes the results' matrix, containing the calculated CuO real permittivity and *FE* values (in brackets) for each combination of models in the two steps.

Table 7. 5. Results' matrix with the CuO ε_r'' calculated by the different EMMs. The fitting error (*FE*) of each calculation is expressed in brackets.

		INCLUSIONS MODEL		
		Lineal	**Maxwell - Garnett**	**Bruggeman**
AIR MODEL	**None**	4.79 ($1.6\cdot10^{-4}$)	6.65 ($1.4\cdot10^{-4}$)	6.50 ($1.2\cdot10^{-4}$)
	Lineal	6.44 ($0.3\cdot10^{-4}$)	12.08 ($0.2\cdot10^{-4}$)	11.22 ($0.2\cdot10^{-4}$)
	Maxwell - Garnett	6.93 ($0.5\cdot10^{-4}$)	14.62 ($0.3\cdot10^{-4}$)	13.22 ($0.5\cdot10^{-4}$)
	Bruggeman	7.02 ($0.5\cdot10^{-4}$)	15.22 ($0.4\cdot10^{-4}$)	13.68 ($0.3\cdot10^{-4}$)

Bigger differences on the CuO permittivity are seen in this matrix compared with the results in Figure 7. 16. This is because the figure only shows the low-f_V region where the experiments have been performed. The models tend to separate when increasing f_V, and the differences can be significant at f_V = 100%. For this reason, it is crucial to select the appropriate model.

There is a wide variety in the obtained ε_r' values, ranging from a minimum value of 4.79 to a maximum one of 15.22. As it was expected from previous results, the values obtained without removing the air contribution underestimate the permittivity. On the other hand, the BG model seems to be the more severe when considering the air effect as it provides the higher permittivity values. In terms of agreement between the models and the experimental data, we see that the linear model is the one that better accounts for the air content, whereas it is not accurate for extracting the inclusions' properties. Moreover, MG and BG behave similarly, and their accuracy depends on the model previously used to consider the air effect.

The same comparative analysis between the calculated and experimental values has been done with the ZnO samples. Figure 7. 17 shows the graphic comparison for the different combinations of models.

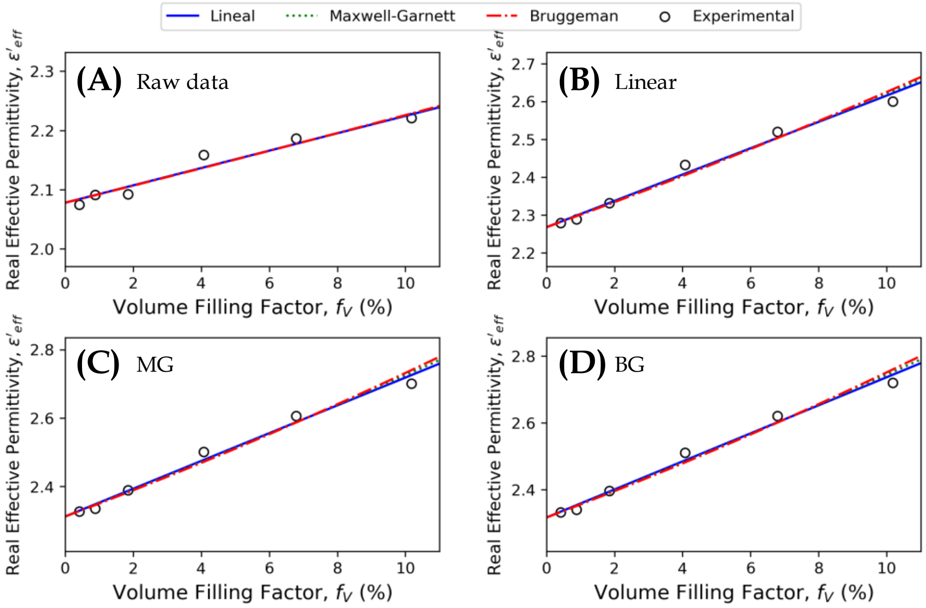

Figure 7. 17. Low-f_V region of the comparison between the models' simulations and the experimental data for ZnO pellets. Linear (blue), Maxwell-Garnett (green), and Bruggeman (red) models are fitted with the effective experimental data. Each subplot contains the experimental values obtained from different air considerations: (A) without removing air contribution; (B) Linear; (C) Maxwell-Garnett; and (D) Bruggeman.

It is possible to appreciate that the agreement between the experimental and calculated data is qualitatively worse in this case. Now it becomes much more difficult to visually define which approach agrees more with the experimental data. One may detect that some measured points are placed above or below the calculation in all the subplots. The results' matrix containing the calculated ZnO real permittivity and the *FE* is described in Table 7. 6.

Table 7. 6. Results' matrix with the ZnO ε_r'' calculated by the different EMMs. The fitting error (*FE*) of each calculation is expressed in brackets.

		INCLUSIONS MODEL		
		Lineal	**Maxwell-Garnett**	**Bruggeman**
AIR MODEL	**None**	3.54 $(1.4\cdot10^{-4})$	3.95 $(1.4\cdot10^{-4})$	3.94 $(1.4\cdot10^{-4})$
	Lineal	5.75 $(2.3\cdot10^{-4})$	8.89 $(2.9\cdot10^{-4})$	8.51 $(3.5\cdot10^{-4})$
	Maxwell - Garnett	6.37 $(2.8\cdot10^{-4})$	11.22 $(3.7\cdot10^{-4})$	10.47 $(4.9\cdot10^{-4})$
	Bruggeman	6.52 $(2.8\cdot10^{-4})$	11.91 $(3.8\cdot10^{-4})$	11.02 $(5.0\cdot10^{-4})$

Surprisingly, in this case the agreement between the experimental and the calculated data is worse when the air effect is considered. Although the quality of the calculation is similar to the previous case - when the air effect is not removed - now the *FE* is significantly higher for any of the models considering the porosity.

This failure in the porosity consideration may be due to the higher porosity (see Figure 7. 12) in the ZnO pellets, leading to bigger air volumes and higher signal scattering. This makes the air phase to be out of the EMMs basic considerations. The similar *FE* when the air effect is not removed suggests that the models fail due to the air inclusions and not for the ZnO powder itself. On the other hand, this approximation has worked much better for the CuO pellets, which have a lower degree of porosity and its characteristics may fit better on the EMMs requirements.

6. CHAPTER CONCLUSIONS

In this chapter, the method for performing THz-TDS analysis of powder samples has been described. Higher filling factors of the PE matrix by the powder oxides have resulted in higher attenuation of the THz pulse through the pellet.

The frequency dependence of optical and dielectric properties - such as refractive index n, absorption coefficient α, complex permittivity $\hat{\varepsilon}$, or electrical conductivity σ - have been deduced for the CuO and ZnO samples. n and ε_r' have shown a constant behaviour all along the experimental bandwidth, while α, ε_r' and σ have a power-law increase with frequency. Moreover, σ has been successfully fitted to the Jonscher's universal power law for both materials.

From these analyses, we have deduced a mean ε_r' of 5.41 and n of 2.30 for the CuO powder, and ε_r' of 3.55 and n of 1.85 for ZnO. These results are in general slightly lower than those found in literature. We attribute this difference to the scattering occurring due to the intrinsically inhomogeneous nature of the particles and the difference in optical constants between particles and bulk, as well as size effects.

Additionally, the influence of the pellet porosity on the calculated optical properties has been checked. The high volume fractions of the pellets occupied by air (around a 20%) suggest that it can play an important role. Furthermore, a real oxide volume filling factor has been calculated for each pellet in order to correct the standard volume filling factor, considering now the space occupied by air.

We have proposed a method to account for the air effect in the calculated optical properties. This method consists in two steps: the first in which an EMM considers the air as inclusions and returns the effective values of the PE+oxide mixture. The second step is the traditionally used to deduce the inclusions' (i.e. oxides') properties by means of an EMM. The obtained results lead to increased permittivity values, in good agreement with the paper of Parrot *et al.* [35], who already studied this effect in other samples.

Finally, the linear, MG and BG models have been tested as candidate EMMs to first remove the air effect, and then extract the oxides' optical properties. All the possible combinations between these models have been tested, and the fitting accuracy with the experimental data has also been quantified. An improvement in the results' accuracy has been obtained for the CuO sample, whereas it worsens for ZnO. We attribute this opposite success of the method to the different porosity levels of each kind of samples. Higher porosities may lead in bigger and more irregular air pores, producing higher signal scattering. These conditions limit the applicability of the EMMs.

7. FUTURE WORK

The first aspect in which we should work on is in performing more accurate porosity measurements. We have corroborated that porosity may have a considerable impact on the calculated optical properties, so it is crucial to improve the information we have about them. A better characterization would lead to more accurate optical results. In this regard, tomographic techniques would be of great interest, as they can provide information about the % of porosity, but also about the pores' morphology and their distribution. It would lead to a deeper discussion about the adequacy of each EMM to account for the air effect.

Moreover, it would be interesting to explore a wider f_V region. In this work we have fitted each model to the experimental data, but only in the low-f_V region. By this way it is difficult to account for the change in tendency that each model has at higher f_V. Thus, with a wider distribution of f_V we could analyse the ε_{eff} - f_V dependence and associate it to a specific EMM model. However, the attenuation should be controlled for higher f_V pellets, in order to ensure having enough transmitted intensity for the later signal processing.

We should also clarify why our proposed methodology to account for the porosity effect has improved or worsen the results depending on the sample analysed. The results suggest that it may be related with the sample porosity level, so it would be interesting to prepare a set of pellets with different porosities but with the same oxide inclusions. By this way we could deeply discuss if there are limitations on the applicability of the EMMs at certain porosity levels. Moreover, the previously commented improvement on the porosity characterization would also be useful in this point.

Furthermore, and just from a practical point of view, it would be interesting to identify which is the best data processing mechanism to deduce the properties of the oxides. In this chapter, we have used two methods, leading to different permittivity values. The first has consisted on calculating the ε_i for each of the pellets with different f_V, and then simply calculate the mean value. Later - when our goal has been to check the consistency of the EMMs accounting for the pellet porosity - we have switched ε_i until finding the best agreement with the experimental data. Probably, having samples in a wider f_V range would be also useful for this goal, as the ε_{eff} - f_V dependence of the experimental data would be better defined, leading in a more precise analysis of the methods.

Finally, independently from the other points, being able to theoretically quantify the signal scattering depending on the physical properties of the powder and pores would signify a great advance. It would improve the calculations done with the EMMs when the sample does not have the model ideal characteristics.

8. REFERENCES

[1] X. Guo, G. Zhang, Q. Li, H. Xue, and H. Pang, “Non-noble metal-transition metal oxide materials for electrochemical energy storage,” *Energy Storage Mater.*, vol. 15, no. February, pp. 171–201, 2018.

[2] A. Dey, “Semiconductor metal oxide gas sensors: A review,” *Mater. Sci. Eng. B Solid-State Mater. Adv. Technol.*, vol. 229, no. November 2017, pp. 206–217, 2018.

[3] C. V. Garcia, G. H. Shin, and J. T. Kim, “Metal oxide-based nanocomposites in food packaging: applications, migration, and regulations,” *Trends Food Sci. Technol.*, vol. 82, no. February, pp.

21–31, 2018.

[4] E. L. Brosha *et al.*, *Metal Oxides*. Taylor & Francis Group, LLC, 2000.

[5] Ç. Oruç and A. Altındal, "Structural and dielectric properties of CuO nanoparticles," *Ceram. Int.*, vol. 43, no. 14, pp. 10708–10714, 2017.

[6] M. R. Leahy-Hoppa, M. J. Fitch, X. Zheng, L. M. Hayden, and R. Osiander, "Wideband terahertz spectroscopy of explosives," *Chem. Phys. Lett.*, vol. 434, no. 4–6, pp. 227–230, 2007.

[7] M. J. Fitch, M. R. Leahy-Hoppa, E. W. Ott, and R. Osiander, "Molecular absorption cross-section and absolute absorptivity in the THz frequency range for the explosives TNT, RDX, HMX, and PETN," *Chem. Phys. Lett.*, vol. 443, no. 4–6, pp. 284–288, 2007.

[8] A. G. Davies, A. D. Burnett, W. Fan, E. H. Linfield, and J. E. Cunningham, "Terahertz spectroscopy of explosives and drugs," *Mater. Today*, vol. 11, no. 3, pp. 18–26, 2008.

[9] Y. Wang, Q. Wang, Z. Zhao, A. Liu, Y. Tian, and J. Qin, "Rapid qualitative and quantitative analysis of chlortetracycline hydrochloride and tetracycline hydrochloride in environmental samples based on terahertz frequency-domain spectroscopy," *Talanta*, vol. 190, no. August, pp. 284–291, 2018.

[10] T. Chen, Q. Zhang, Z. Li, X. Yin, and F. Hu, "Experimental and theoretical investigations of tartaric acid isomers by terahertz spectroscopy and density functional theory," *Wuhan Univ. J. Nat. Sci.*, vol. 11, no. 6, pp. 1633–1635, 2018.

[11] C. Du, X. Zhang, and Z. Zhang, "Quantitative analysis of ternary isomer mixtures of saccharide by terahertz time domain spectroscopy combined with chemometrics," *Vib. Spectrosc.*, vol. 100, no. November 2018, pp. 64–70, 2019.

[12] N. S. Almodovar, J. Portelles, O. Raymond, J. Heiras, and J. M. Siqueiros, "Characterization of the dielectric properties and alternating current conductivity of the SrBi5-xLaxTi4FeO 18(x=0, 0.2) compound," *J. Appl. Phys.*, vol. 102, no. 12, pp. 3–10, 2007.

[13] L. S. Kadyrov *et al.*, "Terahertz-infrared spectroscopy of overdoped manganites La1-xCaxMnO3," *Phys. B Condens. Matter*, vol. 460, pp. 199–201, 2015.

[14] S. B. Kang *et al.*, “Terahertz characterization of Y2O3-added AlN ceramics,” *Appl. Surf. Sci.*, vol. 388, pp. 741–745, 2016.

[15] G. B. Jung *et al.*, “Terahertz spectroscopy of nanocrystal-carbon nanotube and -graphene oxide hybrid nanostructures,” *J. Phys. Chem. C*, vol. 114, no. 25, pp. 11258–11265, 2010.

[16] A. I. Lvovsky, “Fresnel Equations,” in *Encyclopedia of Optical Engineering*, no. August, New York: Taylor & Francis, 2013, pp. 37–41.

[17] M. Balık, V. Bulut, and I. Y. Erdogan, “Optical, structural and phase transition properties of Cu2O, CuO and Cu2O/CuO: Their photoelectrochemical sensor applications,” *Int. J. Hydrogen Energy*, pp. 1–12, 2018.

[18] R. Udayabhaskar and B. Karthikeyan, “Optical and phonon properties of ZnO:CuO mixed nanocomposite,” *J. Appl. Phys.*, vol. 115, no. 15, 2014.

[19] M. Sathya and K. Pushpanathan, “Synthesis and Optical Properties of Pb Doped ZnO Nanoparticles,” *Appl. Surf. Sci.*, vol. 449, pp. 346–357, 2018.

[20] Y. Kim, J. Ahn, B. G. Kim, and D. S. Yee, “Terahertz birefringence in zinc oxide,” *Jpn. J. Appl. Phys.*, vol. 50, no. 3, 2011.

[21] A. K. Azad, J. Han, and W. Zhang, “Terahertz dielectric properties of high-resistivity single-crystal ZnO,” *Appl. Phys. Lett.*, vol. 88, no. 2, pp. 1–3, 2006.

[22] T. Fujii, A. Ando, and Y. Sakabe, “Characterization of dielectric properties of oxide materials in frequency range from GHz to THz,” *J. Eur. Ceram. Soc.*, vol. 26, no. 10–11, pp. 1857–1860, 2006.

[23] S. P. P. Jones *et al.*, “High-temperature electromagnons in the magnetically induced multiferroic cupric oxide driven by intersublattice exchange,” *Nat. Commun.*, vol. 5, 2014.

[24] C. D. W. Mosley, M. Failla, D. Prabhakaran, and J. Lloyd-Hughes, “Terahertz spectroscopy of anisotropic materials using beams with rotatable polarization,” *Sci. Rep.*, vol. 7, no. 1, pp. 1–9, 2017.

[25] M. S. Alqahtani, N. M. A. Hadia, and S. H. Mohamed, “Effect of oxidation time on structural, optical and electrical properties of

mixed copper oxides nanocrystallites," *Optik (Stuttg).*, vol. 173, no. June, pp. 101–109, 2018.

[26] S. Dolai, R. Dey, S. Das, S. Hussain, R. Bhar, and A. K. Pal, "Cupric oxide (CuO) thin films prepared by reactive d.c. magnetron sputtering technique for photovoltaic application," *J. Alloys Compd.*, vol. 724, pp. 456–464, 2017.

[27] D. C. Onwudiwe, T. Arfin, and C. A. Strydom, "Surfactant mediated synthesis of ZnO nanospheres at elevated temperature, and their dielectric properties," *Superlattices Microstruct.*, vol. 81, pp. 215–225, 2015.

[28] S. ur Rehman, J. Liu, R. Ahmed, and H. Bi, "Synthesis of composite of ZnO spheres with polyaniline and their microwave absorption properties," *J. Saudi Chem. Soc.*, pp. 0–6, 2018.

[29] P. Vincent, D. K. Kim, J. H. Kwon, J. H. Bae, and H. Kim, "Correlating the nanoparticle size dependent refractive index of ZnO optical spacer layer and the efficiency of hybrid solar cell through optical modelling," *Thin Solid Films*, vol. 660, no. June, pp. 558–563, 2018.

[30] A. K. Jonscher, "The 'universal' dielectric response," *Naturevolume*, vol. 267, pp. 673–679, 1977.

[31] K. Funke, "Jump relaxation in solid electrolytes," *Prog. Solid State Chem.*, vol. 22, no. 2, pp. 111–195, Jan. 1993.

[32] L. Biswal, P. R. Das, and B. Behera, "Frequency dependent electrical properties of Na2Pb2R2W2Ti4Nb4O30(R = Nd, Sm) ceramics," *J. Adv. Ceram.*, vol. 3, no. 3, pp. 215–223, 2014.

[33] S. Sen and R. N. P. Choudhary, "Impedance studies of Sr modified BaZr 0.5 Ti 0.95 O 3 ceramics," *Mater. Chem. Phys.*, vol. 87, no. 2–3, pp. 256–263, 2004.

[34] M. Vijayakumar *et al.*, "Synthesis and ion dynamics studies of nanocrystalline Mg stabilized zirconia," *Phys. B Condens. Matter*, vol. 334, no. 3–4, pp. 390–397, 2003.

[35] E. P. Parrott, J. A. Zeitler, and L. F. Gladden, "Accurate determination of optical coefficients from chemical samples using terahertz time-domain spectroscopy and effective medium theory," *Opt. Lett.*, vol. 34, no. 23, p. 3722, 2009.

CHAPTER VIII

SWITCHING OF MAGNETIC MOMENT BY SURFACE ACOUSTIC WAVES

1. INTRODUCTION

The magnetic, mechanical, and even other functional properties of different materials have been studied in this Thesis. However, in this chapter we pretend to investigate the interaction between the magnetic moment and a mechanical stimulus, *surface acoustic waves* (SAWs) in this case.

SAWs are guided waves having their associated energy density confined to the surface in a narrow spatial region [1]. The frequency range of SAWs usually range from 50 MHz to almost 20 GHz [2]. In recent years it has been a growing interest paid to develop new mechanism to manipulate the magnetic moment, and SAWs are good candidates to produce magnetic excitations in a local and selective manner. Previous works have already studied the magnetization dynamics due to SAW-induced magnetostriction in a ferromagnetic layer [3]–[8]. This effect is explained by the change in the magnetic anisotropy generated by the elastic strain induced by the SAW. Typical SAWs used in these experiments are of hundreds of MHz, and therefore the ferromagnetic layer thickness is comparable with the SAW wavelength. Furthermore, SAW assisted magnetization switching from the single domain to the vortex state has been recently reported in mesoscopic Co elliptical disks [9].

In this chapter we investigate the possibility of switching the magnetic moment of an array of isolated magnetite (Fe_3O_4) nanoparticles in a piezoelectric by means of SAWs. The experimentally observed differences on the magnetization when the nanoparticles are subjected to SAWs are discussed. Furthermore, a physical explanation is provided to explain the observed phenomena.

The work presented in this chapter is the result of a collaboration between different actors: das-Nano company in Pamplona (Spain) prepared the Fe_3O_4 nanoparticles and performed the TEM and XRD characterization; Dr. Paulo Santos and Dr. Alberto Hernández-Mínguez from the Paul-Drude-Institut für Festkörpelektronik in Berlin (Germany), who were the responsible to fabricate the piezoelectric substrate; Prof. Eugene M. Chudnovsky from the City University of New York in New York (USA) and Dr. Ricardo Zarzuela from the University of California in Los Angeles (USA) worked on the theoretical understanding of the phenomena and development of a theory. Our group from Universitat de Barcelona in Barcelona (Spain), composed by Prof. Javier Tejada, Dr. Nahuel Statuto and me, did all the magnetic measurements. For this reason, this chapter is mainly devoted to the discussion of the experimental results more than in the other aspects, which are also described.

2. CHAPTER OBJECTIVES

The main target on this chapter is to manipulate the magnetic moment of the array of nanoparticles by using SAWs. Moreover, we aim to observe the repercussion that the power and frequency of the microwaves used to generate the SAWs have on the variation of the magnetic moment. This could lead to a novel way to control the magnetic moment. Finally, if a significant variation of the magnetic moment is observed, we expect to understand which physical mechanism is responsible on this phenomenon.

3. NANOPARTICLES' CHARACTERIZATION AND EXPERIMENTAL SETUP DESCRIPTION

Magnetite nanoparticles have been synthesized via a thermal decomposition process of iron oleate at high temperatures in high-boiling point organic solvent [10]. The obtained suspension of nanoparticles in organic solvent is dissolved in acetone, shaken and centrifugated at 4000 rpm for 20 minutes in order to obtain the powder Fe_3O_4.

The transmission electron microscopy (TEM) inspection of the samples shown in Figure 8. 1.A reveal the formation of (quasi-)spherical and triangular particles. The statistical image analysis of 1050 particles results in the size distribution presented in Figure 8. 1.B. The mean diameter is of 13 nm.

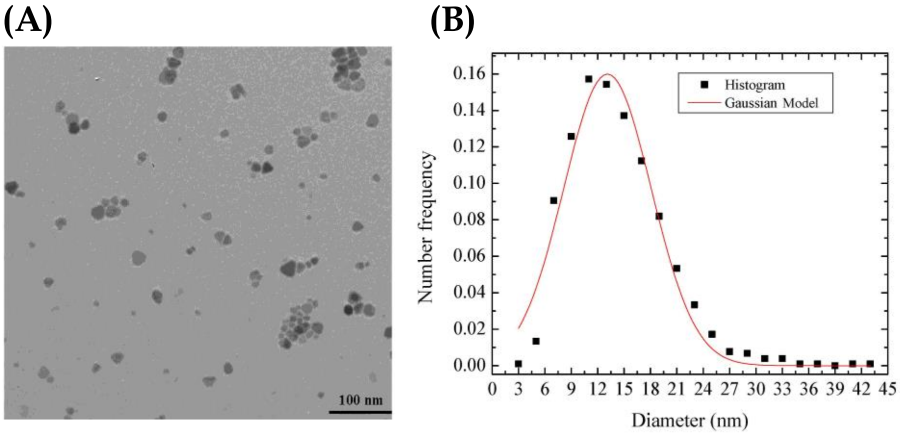

Figure 8. 1. (A) TEM image of the synthesized nanoparticles, and (B) size-distribution deduced from the measurement of 1050 particles from TEM images.

The powder sample has been also analysed by means of XRD. The result, which is presented in Figure 8. 2, confirms the Fe_3O_4 composition of the sample.

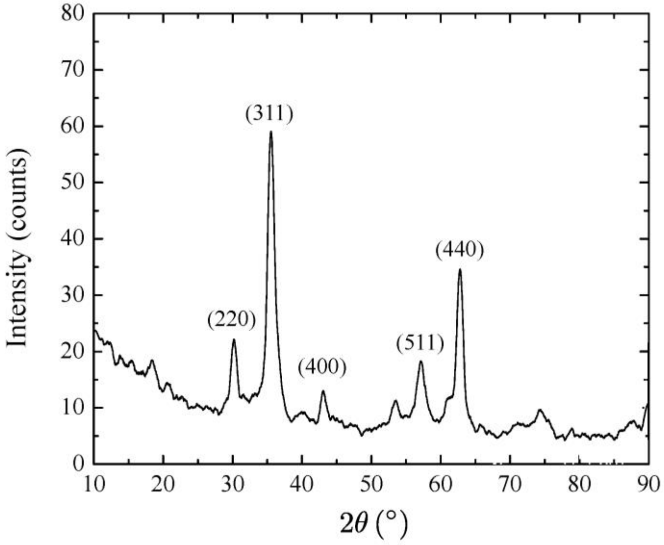

Figure 8. 2. XRD pattern of the synthesized Fe_3O_4 nanoparticles.

The nanoparticles have been the deposited on a LiNbO3, 128° Y-cut, substrate (see Figure 8. 3). SAWs are generated by means of hybrid piezoelectric interdigital transducers (IDT) patterned on the substrate. The spacing between fingers has been chosen to generate resonances with fundamental frequency f_0 = 111 MHz. Microwave excitation of the fundamental IDT resonance at f_0 = 111 MHz and of its harmonic at $3f_0$ = 333 MHz has been achieved with the help of a commercial Argilent signal generator able to generate frequencies in the range from 250 kHz to 4 GHz. An Argilent network analyser (PNA) has been used to measure the reflection coefficient S_{11} of the sample.

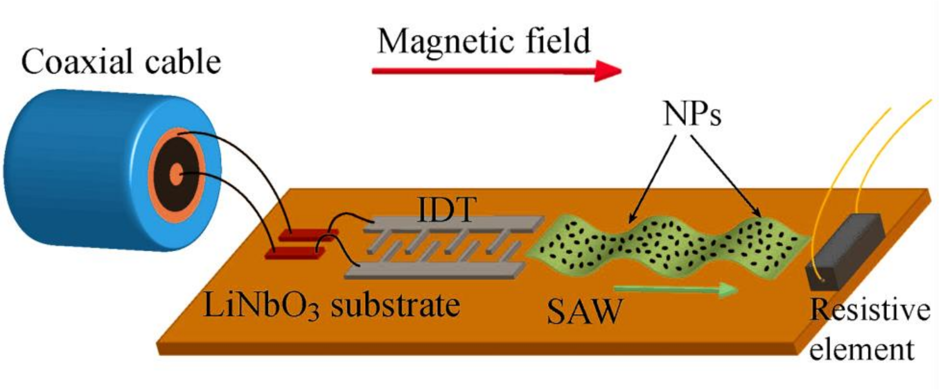

Figure 8. 3. Experimental setup.

4. MAGNETIC MEASUREMENTS

The measurement protocol, performed in a SQUID magnetometer, consists on the saturation of the sample along the SAW propagation direction with a positive magnetic field of 5 kOe. Then, the field is reduced to zero and later increased in the opposite direction up to – 50 Oe. The magnetization of the sample is measured as a function of time, simultaneously with the reflection coefficient S_{11}. This protocol has been repeated at all temperatures (from 2 K to 40 K) in the absence and presence of SAW, with a low-temperature stability better than 0.01 K and a magnetization sensitivity of 10^{-8} emu. Experiments with SAWs has been done at two available resonant frequencies: f_0 and $3f_0$ ($2f_0$ has been discarded as it was strongly supressed).

Figure 8. 4 shows the analysis of the power dependence of the *magnetization jump ΔM* when SAWs are applied at each harmonic frequency in the temperature range 7.5 K – 22 K. *ΔM* has been calculated as the difference in magnetization in the first relaxation point when SAWs are, or are not, applied. It can be observed that the higher the SAWs power (P_{SAW}/P_0) the higher *ΔM*. The power of SAW is defined as $P_{SAW} = P_{out} \cdot \left[10^{S_{11}(non-res)/10} - 10^{S_{11}(res)/10}\right]$, with $P_{out} = 10^{L[dB]/10}$ mW being the power at the output of the generator. *L* is decibel level of

the output power, and $S_{11}^{(\mathrm{res})}$ and $S_{11}^{(\mathrm{non\text{-}res})}$ denote the values in decibels of the reflection coefficient S_{11}. It is therefore seen that the magnetization relaxation of the Fe_3O_4 nanoparticles can be accelerated by applying SAWs with different powers. Furthermore, the magnetization jump increases at lower temperatures: the lower thermal energy barrier makes the normal relaxation (without SAW) to be small, leading then to bigger changes when SAWs are applied. An analogous experimental protocol has been followed along the ascending branch of the hysteresis cycle. Symmetric values of the magnetization have been obtained at all temperatures in the absence and in the presence of a SAW.

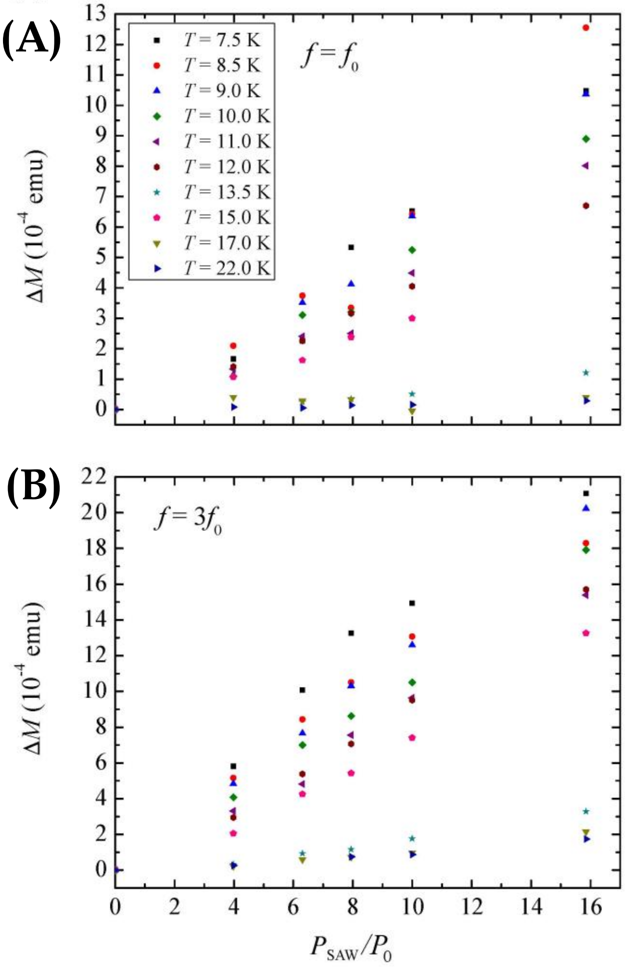

Figure 8. 4. Power dependence of the magnetization jump at the (A) fundamental frequency of SAW, $f = f_0 = 111$ MHz, and (B) the third harmonic $f = 3f_0 = 333$ MHz.

FC and ZFC curves have also been measured in the range from 9 K to 300 K at different magnetic fields, followed by an isothermal magnetic relaxation along the descending branch from the saturation state. As it can be realized from Figure 8. 5.A, SAWs tend to decrease the magnetization along the ZFC and to accelerate the relaxation dynamics (Figure 8. 5.B).

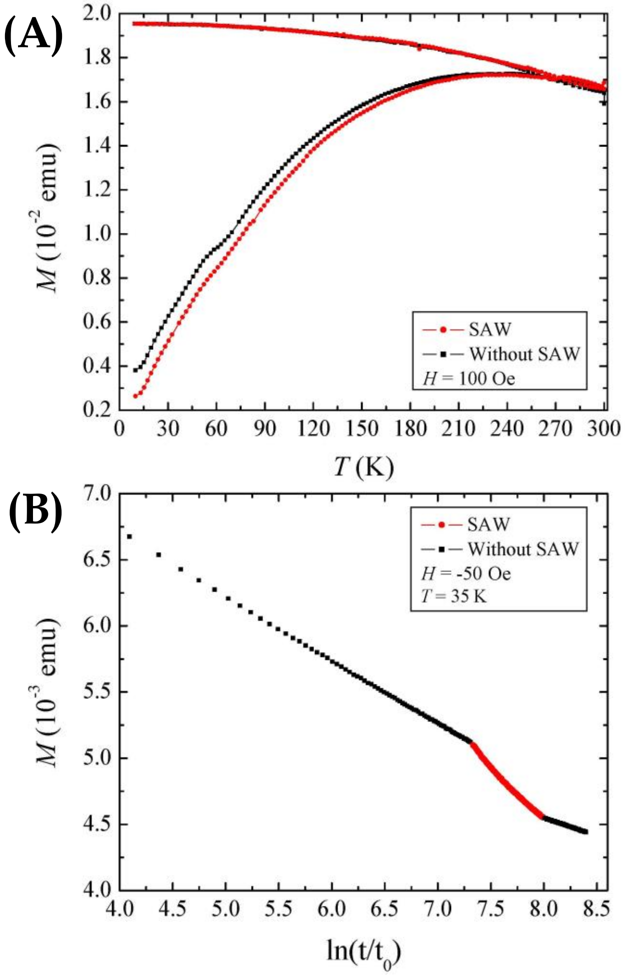

Figure 8. 5. (A) ZFC-FC curves at *H* = 100 Oe in presence (red dots) and absence (Black dots) of SAW. (B) Isothermal (*T* = 35 K) magnetic relaxations measurements from saturation (*H* = 5 kOe) to *H* = - 50 Oe in the presence (red dots) and the absence (Black dots) of SAW.

5. THEORETICAL APPROACH

5.1. Effect of the saw in magnetic relaxation of nanoparticles

The temperature of the system has been controlled with the SQUID thermometer. Moreover, in order to measure the temperature of the substrate a resistive element has been attached (see Figure 8. 3). Within their sensitivity limits, no heating of the substrate has been observed while SAWs are applied. Also, the reading of both thermometers coincided and remained constant in all individual measurements.

Discarding the heating of the substrate, we account for two possible mechanisms to be responsible for these switching effects: (i) magnetostriction on the magnetization due to the effect of the tensile stress on the magnetic anisotropy tensor, and (ii) the spin rotation switching mechanism, which arises as a manifestation of the Einstein-de Haas effect at the nanoscale [11], [12]. The second mechanism has been previously studied in applications to magnetic microcantilevers [13]–[17] and molecules sandwiched between conducting leads [18]. More recently it was also proposed for the enhancement of the magnetization reversal by spin polarized currents [19].

We argue that field-induced magnetostriction can be discarded as the main mechanism for the observed effect: contrary to ferromagnetic layers, the dispersed nanoparticles have a small contact area with the substrate [20]. Additionally, the nanoparticles used in this experiment are very small compared to the SAW wavelength, having thus elastic resonant frequencies much higher than the SAW frequency. Therefore, the nanoparticle is displaced and rotates – rather than be internally deformed by SAW – leading to the generation of an effective ac field [21], which is the responsible of the enhanced magnetic relaxation. This mechanism is schematically represented in Figure 8. 6.

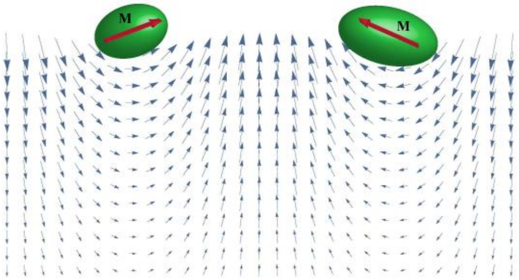

Figure 8. 6. Magnetic nanoparticles undergoing torsional oscillations due to surface acoustic waves. Blue arrows show the phonon displacement field generated by SAW in the substrate.

The power of the effective ac magnetic field of frequency f absorbed per particle of volume V at a temperature T is given by Equation 8. 1 [22].

$$P(V,T,F) \propto f^{2}\chi''(V,T,f)P_{SAW}$$

Equation 8. 1

where χ'' is the imaginary component of the magnetic susceptibility. When the power is turned on, the enhanced superparamagnetic transitions produced by the SAW create a jump in magnetization that can be expressed as:

$$\Delta M \propto \int dVF(V)\,P(V) \propto f^{2}P_{SAW}\chi''_{tot}(T,f)$$

Equation 8. 2

where $F(V)$ is the volume distribution function, and χ''_{tot} is the imaginary part of the total susceptibility of the system of nanoparticles. The detailed deduction of this mechanism and Equation 8. 2 can be found in [23].

5.2. Analysis of the data

By considering the particle size distribution shown in Figure 8. 1.B, the thermal prefactor $f^2\chi''_{tot}(T,f)$ has been calculated and is depicted in Figure 8. 7. It can be seen a monotonic decrease at both fundamental frequency and third harmonic, in good agreement with the tendency shown by the slopes on the magnetization jumps in Figure 8. 4.

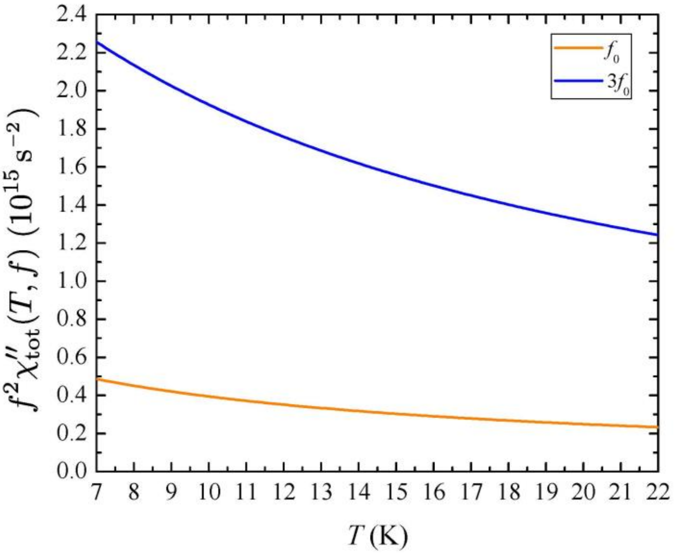

Figure 8. 7. Temperature dependence of the prefactor $f^2\chi''_{tot}(T,f)$ in Equation 8. 2 at the fundamental frequency of SAW, $f = f_0$, (orange line) and the third SAW harmonic, $f = 3f_0$ (blue line).

Furthermore, we have done a direct comparison of the experimental results with theory by calculating the ratio $\Delta M[T]/\Delta M[7.5K]$ at constant power, where the unessential prefactors of Equation 8. 2 cancel. The results shown in Figure 8. 8 demonstrate the good agreement between the experimental and calculated data, especially at the fundamental frequency of 111 MHz.

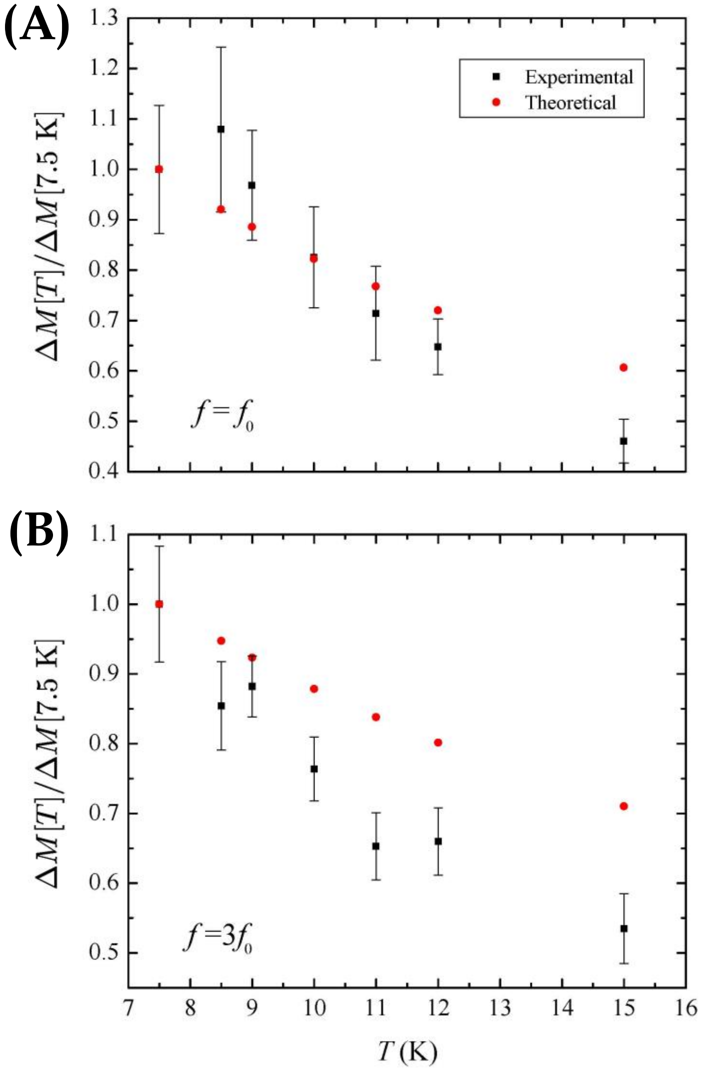

Figure 8. 8. Experimental (black) and theoretical (red) thermal dependences of the ratios ΔM[T]/ΔM [7.5K] (at a fixed SAW power) at the first (A) and third (B) harmonic.

6. CHAPTER CONCLUSIONS

We have experimentally proved that surface acoustic waves accelerate transition between magnetic states in nanoparticles. The accurate control on the sample temperature has allowed us to discard thermal effects of the SAW that would accelerate superparamagnetic transitions. Despite the previously published works [3]–[7] associated the magnetization switching in ferromagnetic layers to the change on magnetostriction produced by SAW, we propose that the Einstein-de Haas mechanism is the responsible of this effect in nanoparticles is due to ac field generated by the particles' rotation. Moreover, we have seen that the variation on magnetization scales as square of SAW frequency and linearly with SAW amplitude.

By relating the effect of SAW to the effect of ac field we have been able to reproduce its dependence on the power and frequency. There are no exiting models based on magnetostrictive effects capable of reproducing our experimental results.

Overall, our observation opens the way of manipulating the magnetic moment on nanoparticles by using SAW instead of a magnetic field, which reduces five orders of magnitude the wavelength. This could, in principle, open the way of individual manipulation of densely packed nanoparticles by SAWs.

7. FUTURE WORK

As the work presented in this chapter corresponds to a first experimental observation of the manipulation of magnetic moment in nanoparticles by SAW, there is plenty of work to do in order to have enough control of this mechanism to be applied in real technological devices.

The next step could be to design new setups to work at different frequencies in order to check the validity of our model in these new conditions. Moreover, performing the experiment with nanoparticles of different chemical composition would help to explore the SAW effect in materials with different physical properties.

8. REFERENCES

[1] A. P. Mayer, "Surface acoustic waves in nonlinear elastic media," *Phys. Rep.*, vol. 256, no. 4–5, pp. 237–366, 1995.

[2] F. Hadj-Larbi and R. Serhane, "Sezawa SAW devices: Review of numerical-experimental studies and recent applications," *Sensors Actuators, A Phys.*, vol. 292, pp. 169–197, 2019.

[3] S. Davis, A. Baruth, and S. Adenwalla, "Magnetization dynamics triggered by surface acoustic waves," *Appl. Phys. Lett.*, vol. 97, no. 23, 2010.

[4] O. Kovalenko, T. Pezeril, and V. V. Temnov, "New concept for magnetization switching by ultrafast acoustic pulses," *Phys. Rev. Lett.*, vol. 110, no. 26, pp. 1–5, 2013.

[5] L. Thevenard *et al.*, "Irreversible magnetization switching using surface acoustic waves," *Phys. Rev. B - Condens. Matter Mater. Phys.*, vol. 87, no. 14, pp. 1–9, 2013.

[6] L. Thevenard *et al.*, "Surface-acoustic-wave-driven ferromagnetic resonance in (Ga,Mn)(As,P) epilayers," *Phys. Rev. B - Condens. Matter Mater. Phys.*, vol. 90, no. 9, pp. 1–8, 2014.

[7] S. Davis, J. A. Borchers, B. B. Maranville, and S. Adenwalla, "Fast strain wave induced magnetization changes in long cobalt bars: Domain motion versus coherent rotation," *J. Appl. Phys.*, vol. 117, no. 6, 2015.

[8] L. Thevenard *et al.*, "Strong reduction of the coercivity by a surface acoustic wave in an out-of-plane magnetized epilayer," *Phys. Rev. B*, vol. 93, no. 14, pp. 1–5, 2016.

[9] V. Sampath, N. D'Souza, D. Bhattacharya, G. M. Atkinson, S. Bandyopadhyay, and J. Atulasimha, "Acoustic-Wave-Induced Magnetization Switching of Magnetostrictive Nanomagnets from

Single-Domain to Nonvolatile Vortex States," *Nano Lett.*, vol. 16, no. 9, pp. 5681–5687, 2016.

[10] J. Park *et al.*, "Ultra-large-scale syntheses of monodisperse nanocrystals," *Nat. Mater.*, vol. 3, no. 12, pp. 891–895, 2004.

[11] E. M. Chudnovsky, D. A. Garanin, and R. Schilling, "Universal mechanism of spin relaxation in solids," *Phys. Rev. B - Condens. Matter Mater. Phys.*, vol. 72, no. 9, pp. 1–11, 2005.

[12] D. A. Garanin and E. M. Chudnovsky, "Angular momentum in spin-phonon processes," *Phys. Rev. B - Condens. Matter Mater. Phys.*, vol. 92, no. 2, pp. 1–6, 2015.

[13] A. A. Kovalev, G. E. W. Bauer, and A. Brataas, "Magnetovibrational coupling in small cantilevers," *Appl. Phys. Lett.*, vol. 83, no. 8, pp. 1584–1586, 2003.

[14] A. A. Kovalev, G. E. W. Bauer, and A. Brataas, "Nanomechanical magnetization reversal," *Phys. Rev. Lett.*, vol. 94, no. 16, pp. 1–4, 2005.

[15] T. M. Wallis, J. Moreland, and P. Kabos, "Einstein-de Haas effect in a NiFe film deposited on a microcantilever," *Appl. Phys. Lett.*, vol. 89, no. 12, pp. 10–13, 2006.

[16] R. Jaafar, E. M. Chudnovsky, and D. A. Garanin, "Dynamics of the Einstein-de Haas effect: Application to a magnetic cantilever," *Phys. Rev. B - Condens. Matter Mater. Phys.*, vol. 79, no. 10, pp. 1–7, 2009.

[17] M. F. O'Keeffe, E. M. Chudnovsky, and D. A. Garanin, "Landau-Zener dynamics of a nanoresonator containing a tunneling spin," *Phys. Rev. B - Condens. Matter Mater. Phys.*, vol. 87, no. 17, 2013.

[18] R. Jaafar, E. M. Chudnovsky, and D. A. Garanin, "Single magnetic molecule between conducting leads: Effect of mechanical rotations," *Europhys. Lett.*, vol. 89, no. 2, 2010.

[19] L. Cai, R. Jaafar, and E. M. Chudnovsky, "Mechanically Assisted Current-Induced Switching of the Magnetic Moment in a Torsional Oscillator," *Phys. Rev. Appl.*, vol. 1, no. 5, pp. 1–9, 2014.

[20] N. Boechler, J. K. Eliason, A. Kumar, A. A. Maznev, K. A. Nelson, and N. Fang, "Interaction of a contact resonance of microspheres

with surface acoustic waves," *Phys. Rev. Lett.*, vol. 111, no. 3, pp. 1–5, 2013.

[21] E. M. Chudnovsky and R. Jaafar, "Manipulating the Magnetization of a Nanomagnet with Surface Acoustic Waves: Spin-Rotation Mechanism," *Phys. Rev. Appl.*, vol. 5, no. 3, pp. 1–5, 2016.

[22] E. M. Chudnovsky and J. Tejada, *Lectures on Magnetism*. Princeton, New Jersey: Rinton Press, 2008.

[23] J. Tejada *et al.*, "Switching of magnetic moments of nanoparticles by surface acoustic waves," *EPL*, vol. 118, no. 3, 2017.

CHAPTER IX

CONCLUSIONS

In this Thesis we have presented results from a wide variety of materials and techniques. However, all of them have provided interesting information to understand the structure and the properties that we have investigated. A complete view of the materials has been achieved, and the mechanical and functional properties have been related with the physical characteristics of each material. This work results in interesting conclusions from both, the fundamental and technological point of view.

First, copper ferrite nanoparticles have been successfully synthesized, reaching high purity values, which lead to improved magnetic properties compared with other references. We have also seen that the sol-gel synthesis forms the tetragonal spinel ferrite, whereas the co-precipitation approach results in the cubic structure. The formation of each phase has been observed by temperature dependent XRD measurements. Finally, the mechanical and magnetic properties of solid pellets have been investigated, and experimental direct correlations between both properties have been found. These correlations may be an important tool for designing and materials' selection processes.

A novel CNT-based magnetic nanocomposite has also been investigated, from a structural and magnetic point of view. Magnetic measurements have revealed the presence of a double energy barrier distribution. Moreover, the magnetic relaxation has been studied in a wide temperature range. The results at low field show a non-linear dependence of the magnetic viscosity with temperature, confirming the double energy barrier distribution.

The currently used SMM and SMC have been structurally and magnetically characterized. Moreover, their frequency-dependent magnetic properties in the kHz and MHz frequency range have shown the importance of the isolating shell in the SMC. Then, our new SMC formulations have shown competitive properties with respect the actual materials. These results are potentially interesting from a technological point of view.

THz-TDS has allowed us to deduce the optical and dielectric constants of two semiconductor oxides in the THz frequency range. The signal processing has been described, and the effect of the filling factor in the effective measured properties has been observed. Moreover, we have proved that porosity in the samples has a big impact on the results. In this regard, we have proposed a mechanism to account for this effect that offers good results for low porosity samples.

Finally, we have experimentally proved that the magnetic moment can be manipulated by means of SAWs. Furthermore, we have found the relationship between power and frequency of the applied SAWs and the change in magnetization.

Overall, our results give a complete knowledge of different materials as a whole, from the very beginning synthesis to the determination of their final properties. The conclusions may be of interest from a scientific and technological point of view and leads to an even more exciting future work to develop materials with novel properties.

APPENDIX

SCIENTIFIC CONTRIBUTIONS

1. LIST OF PUBLICATIONS

[1] J. Tejada *et al.*, “Switching of magnetic moments of nanoparticles by surface acoustic waves,” *EPL*, vol. 118, no. 3, 2017.

[2] J. Calvo-de la Rosa, J. Tejada, and A. Lousa, “Structural and impedance spectroscopy characterization of Soft Magnetic Materials,” *J. Magn. Magn. Mater.*, vol. 475, pp. 570–578, 2019.

[3] J. Calvo-de la Rosa, A. L. Danilyuk, I. V. Komissarov, and J. Tejada, “Magnetic Relaxation Experiments in CNT-Based Magnetic Nanocomposite,” *J. Supercond. Nov. Magn.*, 2019.

[4] C. Barreneche, M. Martín, J. Calvo-de la Rosa, M. Majó, and A. Fernández, “Own-Synthetize Nanoparticles to Develop Nano-Enhanced Phase Change Materials (NEPCM) to Improve the Energy Efficiency in Buildings,” *Molecules*, vol. 24, no. 7, p. 1232, 2019.

[5] J. Calvo-de la Rosa and M. Segarra, “Optimization of the synthesis of Copper Ferrite nanoparticles by polymer-assisted Sol-Gel method,” *ACS Omega*, 2019. (Accepted)

[6] J. Calvo-de la Rosa, A. Locquet, S. Bouscaud, D. Berveiller, and D. S. Citrin, “Optical Constants of CuO and ZnO Particles in the Terahertz Frequency Range,” *J. Alloys Compd.*, 2019. (Submitted)

2. CONFERENCE CONTRIBUTIONS

1. “Interaction of SAW with the magnetic moment of nanomagnetic particles”, Calvo-de la Rosa, J; Statuto, N.; Tejada, J.; Zarzuela, R.; **IEEE Summer School** (2017). Poster.
2. “Interaction of SAW with the magnetic moment of nanomagnetic particles”, Tejada, J.; Chudnovsky, E. M.; Zarzuela, R.; Statuto, N.; Calvo-de la Rosa, J.; **13th International Workshop on Magnetism and Superconductivity at the Nanoscale** (2017). Poster.
3. “Method comparison in the synthesis of magnetic nanoparticles”, Calvo - de la Rosa, J.; Segarra, M.; Ruiz-Izuriaga, D.; **The 19th International Sol-gel Conference** (2017). Poster.
4. “High Frequency Characterization of different Soft Magnetic Materials”, Calvo - de la Rosa, J.; Tejada, J.; **23rd Soft Magnetic Materials Conference** (2017). Poster.
5. “Particle size effect in MHz and GHz properties of different Soft Magnetic Materials”, Calvo-de la Rosa, J.; Tejada, J.; **14th International Workshop on Magnetism and Superconductivity at the Nanoscale** (2018). Poster.
6. “Magnetic properties of new Fe-CNT composites and Fe micrometer particles”; Calvo-de la Rosa, J.; Tejada, J.; Prischepa, S.; **14th International Workshop on Magnetism and Superconductivity at the Nanoscale** (2018). Oral.
7. “Investigation of Magnetic and Frequency Dependent Properties of Soft Magnetic Materials and Composites”, Calvo-de la Rosa, J.; Tejada, J.; **V Congreso Hispano-Luso de Cerámica y Vidrio** (2018). Oral.
8. “Soft Magnetic Composites: structure, magnetic properties and new formulations”, Calvo-de la Rosa, J.; Tejada, J.; **15th International Workshop on Magnetism and Superconductivity at the Nanoscale** (2019). Poster.